SAND89-2773
Unlimited Release
Printed June 1992

Distribution
Category UC-236

SAND--89-2773

DE92 018932

SODIUM REFLUX POOL-BOILER SOLAR RECEIVER ON-SUN TEST RESULTS

Charles E. Andraka
James B. Moreno
Richard B. Diver
Timothy A. Moss
Solar Thermal Electric Technology

Sandia National Laboratories
Albuquerque, New Mexico 87185

ABSTRACT

The efficient operation of a Stirling engine requires the application of a high heat flux to the relatively small area occupied by the heater head tubes. Previous attempts to couple solar energy to Stirling engines generally involved directly illuminating the heater head tubes with concentrated sunlight. In this study, operation of a 75-kW_t sodium reflux pool-boiler solar receiver has been demonstrated and its performance characterized on Sandia's nominal 75-kW_t parabolic-dish concentrator, using a cold-water gas-gap calorimeter to simulate Stirling engine operation. The pool boiler (and more generally liquid-metal reflux receivers) supplies heat to the engine in the form of latent heat released from condensation of the metal vapor on the heater head tubes. The advantages of the pool boiler include uniform tube temperature, leading to longer life and higher temperature available to the engine, and decoupling of the design of the solar absorber from the engine heater head. The two-phase system allows high input thermal flux, reducing the receiver size and losses, therefore improving system efficiency.

The receiver thermal efficiency was about 90% when operated at full power and 800°C. Stable sodium boiling was promoted by the addition of 35 equally spaced artificial cavities in the wetted absorber surface. High incipient boiling superheats following cloud transients were suppressed passively by the addition of small amounts of xenon gas to the receiver volume. Stable boiling without excessive incipient boiling superheats was observed under all operating conditions. The receiver developed a leak during performance evaluation, terminating the testing after accumulating about 50 hours on sun.

The receiver design is reported here along with test results including transient operations, steady-state performance evaluation, operation at various temperatures, infrared thermography, x-ray studies of the boiling behavior, and a post-mortem analysis.

DISCLAIMER

Acknowledgments

The reflux pool-boiler receiver on-sun test required a team effort within Sandia. The authors would like to thank the many people at Sandia that provided input and support to the receiver design, test, and analysis.

Craig Ginn was a jack-of-all-trades, designing many of the fixtures, designing and implementing the support structure and housing, assisting in the calorimeter design, and working closely with the shops to get the receiver system built. Craig's practical insights were valuable in keeping the project on schedule.

Vern Dudley provided data acquisition support and reduction, and operated the test site equipment to facilitate the testing.

This hardware intensive project required the support of many specialists. Jim Muir designed and analyzed the calorimeter system. Liz Roherty-Osmun provided brazing support for the calorimeter and the thermocouples. Bob Henning applied the copper to the calorimeters. Bill Aldrich provided fast turnaround on many small parts and fixtures. Jeff Rickey and Herman Molina drafted and built the housing. Gary Boruff provided skilled welding support. Daniel Ray, Walt Einhorn, and Roy Tucker provided final assembly and test support at the National Solar Thermal Test Facility.

The pool-boiler project also required a great amount of analytical support. Scott Rawlinson provided dish calorimetry and aim verification. Ed Hoffman, Mike Stone, and Mike Neilsen provided pre- and post-test stress analysis. We also received analyses from Roy Hogan (thermal), Vince Romero (optical), and Doug Adkins (cost). Jim VanDenAvyle provided materials selection and analysis support, with help from John Munford and John Stephens. Mark Nissen provided infrared thermography test support. Kyle Thompson and Gerald Stoker provided x-ray testing support.

The materials and methods evaluation for the next-generation receiver included additional input from Mike Ceislak and Mike Maguire (weld analysis) and Henry Peebles and Nelda Creager (laser cavity development).

Memos from many of the above contributors have been included with permission.

Table of Contents

Table of Contents (continued)

Table of Contents (continued)

Table of Contents (continued)

Figures

Table of Contents (continued)

Table of Contents (continued)

Table of Contents (continued)

Table of Contents (concluded)

Tables

Introduction

Dish-Stirling systems have demonstrated the potential to produce economical environmentally acceptable electric power from the sun. In 1984, the Advanco-Vanguard dish-Stirling module (Figure 1) demonstrated a world record sunlight-to-electricity peak net conversion efficiency of 29.4% (Washom, 1984a). McDonnell Douglas Corporation further developed and nearly commercialized a system based on the Advanco module (Coleman and Raetz, 1986). Recently, dish-Stirling system development by the Department of Energy (DOE) and industry has emphasized advanced components to improve system performance, cost, life, and reliability.

Figure 1. Advanco-Vanguard dish-Stirling module in operation. This module currently holds the world record for sunlight-to-grid-power conversion efficiency at 29.4%.

The modules demonstrated by Advanco and McDonnell Douglas used a United Stirling of Sweden engine with its heater head directly illuminated by concentrated solar flux. The nonuniform flux and temperature distributions severely limit the lifetime and performance of the engine and receiver (Washom, 1984b), and require accurate (costly) concentrators. To reduce peak flux intensities, the heater head tubes were extended, which increased engine dead volume and reduced engine performance (Figure 2). Heat balance among the four engine cylinders was difficult to maintain, further reducing performance. Hybridization (addition of fossil fuel heating) without compromising the solar receiver design of a tube receiver is also difficult.

The reflux receiver was conceived as an improvement over directly illuminated tube receivers (Diver et al., 1990). Sandia National Laboratories, Albuquerque, New Mexico (hereafter referred to as Sandia) has been conducting a dish-Stirling receiver development program to support design, development, and testing of the reflux receiver concept. In conjunction with NASA Lewis Research Center and industry, Sandia is supporting the development of Advanced Stirling Conversion Systems (ASCS) based on free-piston Stirling engines and reflux receivers. Sandia has also been supporting Stirling Thermal Motors, Inc.'s solarization of a kinematic Stirling engine with a matched reflux receiver. Sandia and the DOE are also supporting the development of cost-effective stretched-membrane solar concentrators for 25-kW_e dish-Stirling systems. The goal of these programs is to improve performance, cost, reliability, and durability of dish-Stirling systems. Cummins Power Generation, a subsidiary of Cummins Engine Corporation, has privately pursued the commercialization of a 5-kW_e dish-Stirling system that incorporates a reflux receiver, a free-piston Stirling engine, and a stretched membrane dish (Bean and Kubo, 1990). Sandia and Cummins are continuing development of this system on a cost-shared basis.

Figure 2. United Stirling of Sweden heater head used on the Advanco dish-Stirling Module. The heater head tubes were expanded to make the solar flux levels lower and more uniform.

The Reflux Receiver Concept

In the reflux receiver, liquid metal (sodium and/or potassium) evaporates at the solar absorber and condenses at the engine heater tubes, supplying the latent heat of vaporization to the engine. The liquid at the absorber can be a pool that floods the surface (pool boiler) or a wick saturated with liquid metal that covers the absorber surface (heat pipe). The condensate is returned to and distributed over the absorber by gravity (refluxing), wick capillary forces, or a combination thereof. The reflux receiver has the important advantage of nearly isothermal operation even with nonuniform incident solar-flux distributions. In addition, the reflux receiver permits independent design and optimization of the absorber (receiver) and the engine heater tubes. Finally, the reflux receiver has the potential to be readily hybridized, partly because of flexibility where the fossil-fuel burner can be located.

Sandia's reflux receiver program is currently evaluating both pool-boiler and heat-pipe receivers (Andraka and Diver, 1988). The pool-boiler receiver is simpler than the heat-pipe receiver, but uses a larger quantity of liquid metal. Compared to heat pipes, the physics governing pool-boiler performance is poorly understood. Although heat pipe technology has been extensively studied and is relatively well understood, its application to solar receivers introduces new elements to design and fabrication including the unique geometry and the large vertical and areal extent of the heated surface. Figure 3 shows an artist's conception of the Sandia reflux pool boiler receiver. This Sandia geometry is also being applied to a heat-pipe receiver by Stirling Thermal Motors under contract to Sandia.

In a previous report (Moreno and Andraka, 1989), bench-scale proof-of-concept testing of the pool-boiler receiver concept was presented. The present report relates the on-sun design and proof-of-concept test results for a full-scale, pool-boiler receiver tested at Sandia.

On-Sun Test Objectives

This first on-sun pool-boiler test's primary objective was to demonstrate the technical feasibility of the pool-boiler concept. A successful demonstration includes stable boiling and the ability to operate under all solar orientations and conditions. Demonstrating the advantages of the reflux receiver concept, including isothermal operation and high thermal efficiency was also desired. In addition, the test results would assist in the development of design and analysis tools to aid in the optimization of such receivers.

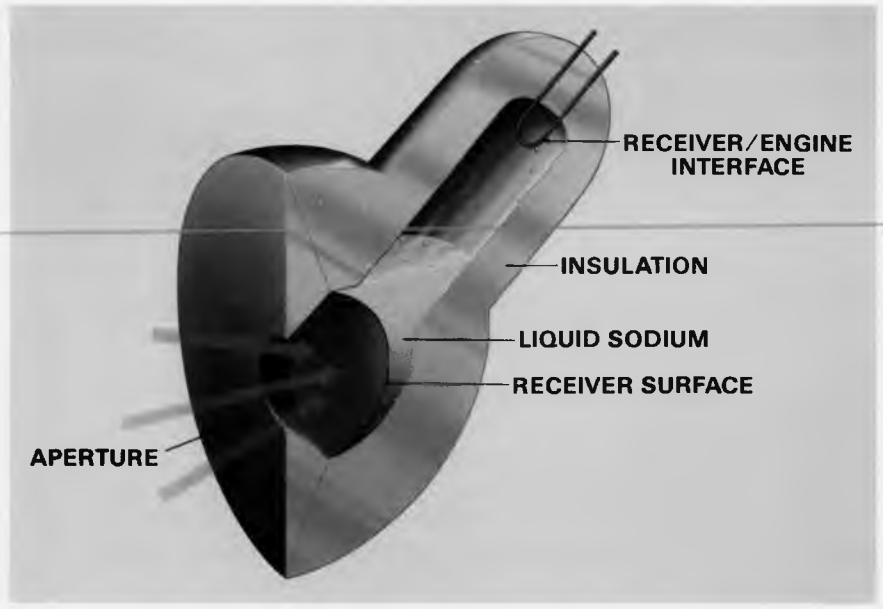

Figure 3. Artist's conception of the Sandia reflux pool-boiler receiver.

On-Sun Pool-Boiler Receiver Design

The pool-boiler receiver was designed for proof-of-concept testing, performance evaluation during solar operation, and also for comparison with alternate approaches such as the heat pipe receiver. Figure 4 is a cross-sectional view of the receiver attached to the Test Bed Concentrator (TBC) mounting ring. The gas-gap calorimeter used to simulate the engine during the tests is shown schematically, and is detailed in Appendix F of this report. The absorber surface is a 0.032-inch (in.) thick spherical shell segment with a radius of curvature of 8.6 in. and a base diameter of 16 in. (Appendix A of this report). The relatively small size permits testing at high heat fluxes to establish the limits of the technology. Thirty-five "artificial" cavities were machined into the absorber to promote stable boiling. The cavities were equally spaced, about 0.006 in. diameter and 0.020 in. deep. The incident concentrated solar flux is expected to be about 70 W/cm^2 based on CIRCE2 analysis (Appendix G of this report). The design power delivered by the concentrator was 75 kW_t, but calorimetry prior to receiver testing indicated that the actual dish power was about 65 kW_t (Appendix Q of this report). The receiver's small size also permits a sodium inventory of only 5.77 kilograms (kg) (12.7 pounds [lb]). A minimal inventory is desirable for both cost and safety reasons.

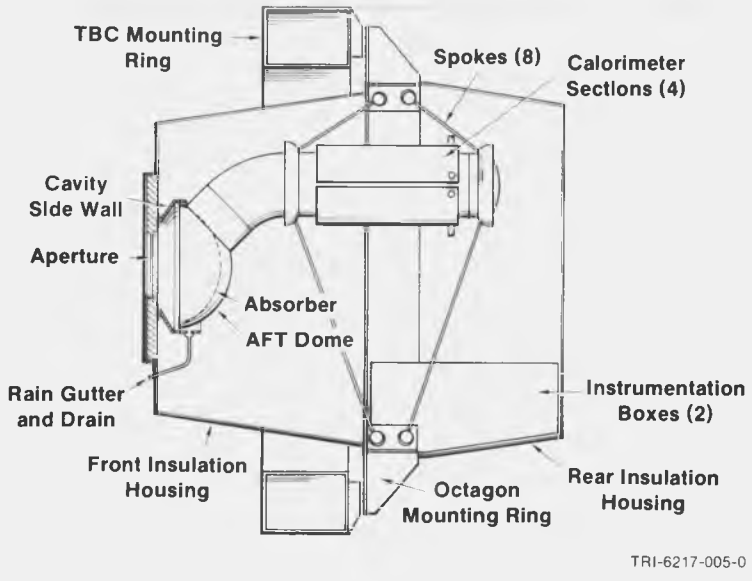

Figure 4. Schematic of the Sandia reflux pool-boiler receiver in the TBC mounting ring and the receiver insulation package.

Numerous considerations influenced the full-scale receiver design. The first full-scale receiver was fabricated out of type 316L stainless steel; this material was selected based on availability and adequacy for short-term tests (Lukens et al., 1988; Appendix C of this report). Finite-element stress analysis was used to determine required material thicknesses. In the stress analysis, the high operating temperature and the expected magnitude and radial distribution of the incident heat flux were considered. Starting transients were analyzed and the possibility of creep and fatigue damage was considered. The steady-state stresses were calculated and are acceptable for the short-term (100-hour [hr]) tests (Appendix H of this report).

On-Sun Receiver Testing

The pool-boiler receiver was tested on 18 separate days between August 31, 1989 and May 30, 1990 for a total of 48 hrs at or above 600°C and 33 hrs above 700°C. Normal operating temperatures included 700°, 750°, and 800°C. Well-behaved boiling was demonstrated at half, three-quarter, and full input power (approximately 65 kW_t). Receiver thermal efficiency was about 90% when the input power was 65 kW_t and the sodium temperature was 800°C (see Appendixes M and Q of this report). Figure 5 shows the receiver mounted on TBC-1 at Sandia during the testing. Figure 6 shows temperature and power data taken during an all-day performance verification test on October 19, 1989, which demonstrated the operation of the receiver at all orientations and flux levels that occur on a normal day.

Beyond these first successful demonstrations, much of the test time was spent studying the "hot restart" problem. This problem was initially seen in our bench-scale simulations of cloud transients, in which heat applied to the boiler was interrupted for a short period and then resumed. Very high incipient-boiling wall superheats sometimes occurred before boiling resumed. In the full-scale tests, the shutter was used to simulate cloud transients. Several methods to eliminate the hot restart problem were tested. The simplest method was the addition of a small amount of xenon to the boiler headspace (see Appendix N of this report). This method worked best at low sun elevations. Testing in May, 1990 was aimed in part at determining why this method was less effective at high dish-elevation angles.

Real-time video thermography was performed to qualify the areal temperature distributions and to compare the distribution with Sandia's thermal models. The results and analysis of the thermography are presented in Appendix P of this report. Real-time x-ray cinematography was attempted to study the boiling behavior of the liquid metal. In addition, discrete x-ray sensors were used to attempt to determine the vapor void fraction in the critical parts of the receiver during operation. The x-ray results are summarized in Appendix O of this report and detailed in Moreno et al. (1991).

On May 30, during a hot restart, the receiver absorber developed a leak approximately 1/8 x 1/4 in. Approximately 2.27 kg (5 lb) of the 5.77-kg (12.7-lb) inventory of sodium was consumed during subsequent fire. Figure 7 shows data taken during the test. The start of the leak is believed to coincide with the decrease in slope of the condenser temperature during the hot restart. Indicated temperatures during the fire were not greater than those seen in normal operation, and damage to the receiver was confined to the immediate vicinity of the leak.

Postmortem Analysis and Next-Generation Design

During the postmortem analysis of the receiver, materials, stress, fatigue, and loss of heat transfer were considered as possible causes of failure. These efforts are detailed in Appendix S of this report and are outlined below.

The failure was in the upper half of the absorber, halfway between two artificial cavities. A small heat-affected zone was noted around the failure, with a highly localized melt zone. No evidence of cracking that may have preceded the failure was found, but such evidence could have been consumed by the melt zone. No cracks or melted material were found in an inspection of the remainder of the absorber. Air-side oxidation of the receiver was minimal.

Prior to testing, finite-element analysis had not revealed any stresses during startup or steady operation that would exceed the yield stress of the material at its instantaneous temperature. During the postmortem analysis, the various stress cycles occurring during the test were considered with respect to their potential to cause fatigue failure. In each case, the combination of stress magnitude and number of cycles was found to be too small to cause failure. Of particular note is the fact that the failure did not occur at an artificial cavity, which is a stress concentration.

Figure 5. The Sandia reflux pool-boiler receiver during the on-sun testing.

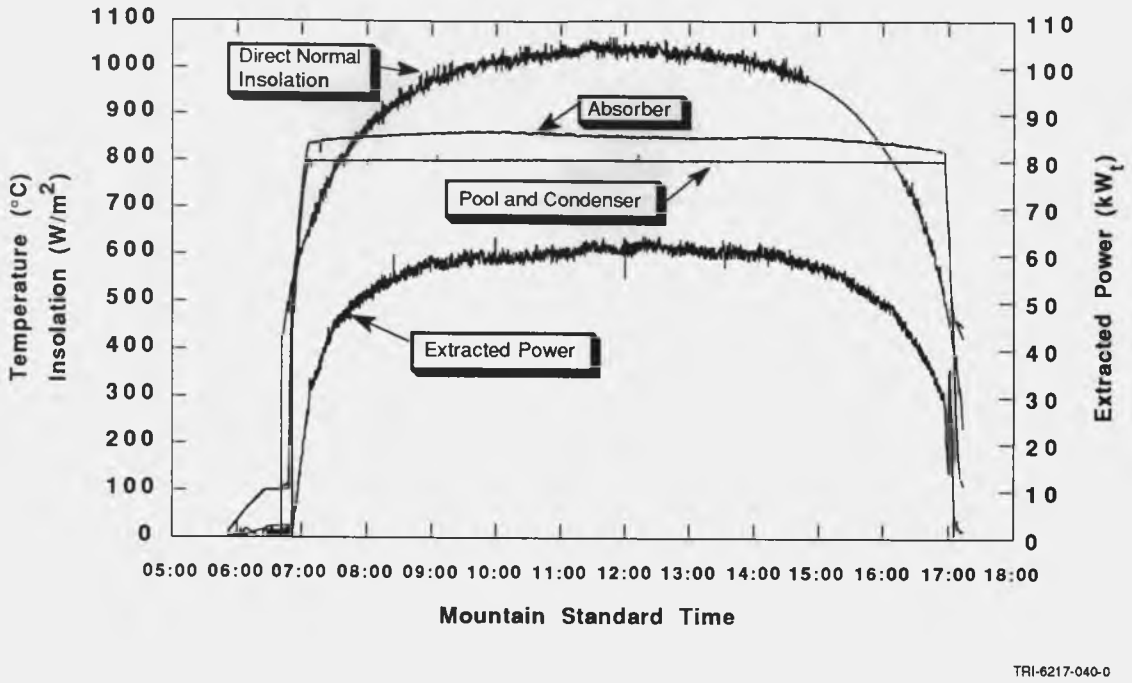

Figure 6. Power and temperature data taken during the all-day performance demonstration test on October 19, 1989.

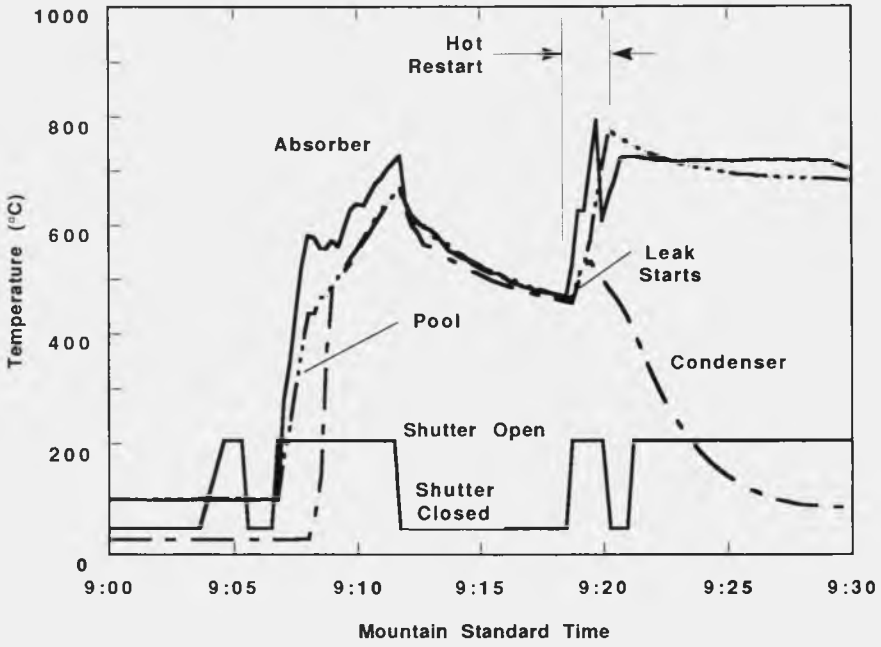

Figure 7. Temperature history during the May 30, 1990 receiver test and subsequent failure. Boiling, as evident by the microphone sounds, occurred during each start-up. No receiver thermocouples experienced an over-temperature indication during the failure.

An optical analysis supported by flux measurements confirmed that the area in which the failure occurred was a peak flux region (Appendix G of this report). While the fluxes were comfirmed to be below the design value, postmortem analysis suggests that a loss of heat transfer may have occurred under conditions not anticipated in the design. Two mechanisms can cause loss of heat transfer: localized film boiling and flooding. Localized film boiling would cause a small local dry spot at the peak flux location, resulting in burnout at that point. Flooding occurs when the liquid return from the condenser is restricted by the volumetric vapor flow. Dryout in this case would extend over a larger area, with burnout occurring again at the peak flux location. During the restart at the time of the failure, a unique condition occurred in which the pool was less sub-cooled than during a normal start-up (Appendix S). This is known to enhance both film boiling and flooding, and has been identified as the most likely cause of failure.

Based on the postmortem analysis, a next generation pool-boiler receiver has been designed. The new design is larger, reducing the peak flux and therefore improving the film boiling safety factor. A larger gap between domes provides a higher flooding limit. The shell material has been changed to Haynes-230 (Appendix D of this report) for improved high temperature strength, and the working fluid has been changed to NaK-78 for better operation at lower temperatures (700°C rather than 800°C) and because NaK-78 is liquid at room temperatures. Sandia is planning several bench-scale tests to investigate the elevation-angle dependence of hot restarts with xenon added to the receiver headspace and to test several new boiling stability enhancement surfaces.

Conclusions

A pool-boiler reflux receiver has been tested on-sun at Sandia. The receiver provided a thermal power throughput (available at the engine heater heads) of up to 62 kW, which is the most to date for a reflux receiver. The power was limited by the test dish capabilities, but was sufficient for full-power operation of current and planned 25-kW_e Stirling engines.

The receiver demonstrated measured thermal efficiencies of over 90% at operating temperatures of 800°C, while providing relatively low stress isothermal operation. The receiver was tested for about 50 hrs, and several operational concerns were addressed and solved.

The receiver failed during a unique hot restart. The failure was probably due to a loss of coolant (sodium), resulting in the formation of a 1/8 x 1/4 in. melt zone in the stainless steel absorber. Loss of coolant could be due to exceeding the flooding limit or local film boiling.

A next-generation receiver will be constructed based on the results of these tests and additional laboratory-scale receiver tests. Based on these results, reflux receivers appear to be a viable heat transport system for application to dish-Stirling generation systems, and will provide longer life and higher efficiency than current receiver designs.

References

Andraka, C. E., and R. B. Diver. 1988. "Reflux Heat-Pipe Solar Receivers for Dish-Electric Systems," paper no. 889213. *Proceedings of the 23rd IECEC, August, 1988.* SAND87-2976C. Albuquerque, NM: Sandia National Laboratories.

Bean, J. R., and I. Kubo. 1990. "Development of the CPG 5-kW Dish/Stirling System," paper no. 906298. *Proceedings of the 25th IECEC, Reno, NV, August, 1990.*

Coleman, G. C., and J. E. Raetz. 1986. "Field Performance of Dish Stirling Solar Electric Systems," paper no. 869136. *Proceedings of the 21st IECEC, San Diego, CA, August, 1986.*

Diver, R. B., C. E. Andraka, J. B. Moreno, D. R. Adkins, and T. A. Moss. 1990. "Trends in Dish Stirling Solar Receiver Design," paper no. 905303. *Proceedings of the 25th IECEC, Reno, NV, August, 1990.*

Lukens, L. L., C. E. Andraka, and J. B. Moreno. 1988. *Liquid Metal Thermal Electric Converter.* SAND88-0458. Albuquerque, NM: Sandia National Laboratories.

Moreno, J. B., and C. E. Andraka. 1989. *Test Results from Bench-Scale Sodium-Pool-Boiler Solar Receiver.* SAND89-0899. Albuquerque, NM: Sandia National Laboratories.

Moreno, J. B., G. C. Stoker, and K. T. Thompson. 1991. *X-Ray Observations of Boiling Sodium in a Solar Reflux Pool-Boiler Receiver.* SAND91-1538. Albuquerque, NM: Sandia National Laboratories.

Washom, B. J. 1984a. "Parabolic Dish-Stirling Module Development and Test Results," paper no. 849516. *Proceedings of the 19th IECEC, San Francisco, CA, August, 1984.*

Washom, B. J. 1984b. *Vanguard I Solar Parabolic Dish-Stirling Engine Module Final Report.* DOE-AL-16333-2 (84-ADV-5).

APPENDIX A

ON-SUN TEST RECEIVER DESIGN

APPENDIX A
ON-SUN TEST RECEIVER DESIGN

This appendix describes the mechanical design of the reflux pool-boiler receiver. The materials issues are discussed in Appendix C of this report, and the supporting stress analysis is presented in Appendix H of this report.

Figure A-1 shows a layout of the sodium-containing portion of the receiver, including the condenser pipe. The receiver absorber consists of a section of a sphere, on which optical analysis (Appendix G of this report) has shown a flux distribution with relative uniformity compared to conventional cylindrical receivers. This dome size provides a peak flux goal of 70 to 75 watts/square centimeter (W/cm^2), based on early calculations from CAV2 (Andraka and Diver, 1988) (see Appendix G). The total power was expected to be about 75 kW_t at a receiver temperature of 800°C. Seventy degrees was selected for the half-sphere angle, based on manufacturability issues. A deeper dome (greater half-sphere angle) reduces the peak fluxes, but is harder to form, increases material costs, and provides a very small vapor flow cross-sectional area for vapor formed near the rim. The dome thickness is a compromise between membrane stresses due to the internal pressure, thermal stresses due to the flux through the dome wall, and corrosion issues. The membrane (pressure) stress is low compared to the thermal stresses, which drives the design toward a thin absorber, with an "ideal" thickness of about 0.01 inches (in.). However, the selected material, 316L stainless steel, has a relatively high corrosion rate in air, driving the design toward a thicker absorber. In addition, forming the dome may result in a nonuniform absorber thickness. The dome design specification stipulates a nominal 0.040 in. thickness, with an 8.62-in. inner radius of curvature and a 70-degree half-sphere angle (Figure A-2). This provides a receiver cavity diameter of about 16 in. The domes used were hydroformed rather than spun, and resulted in a 0.032 in. thickness uniform within 0.001 in. over the entire absorber dome.

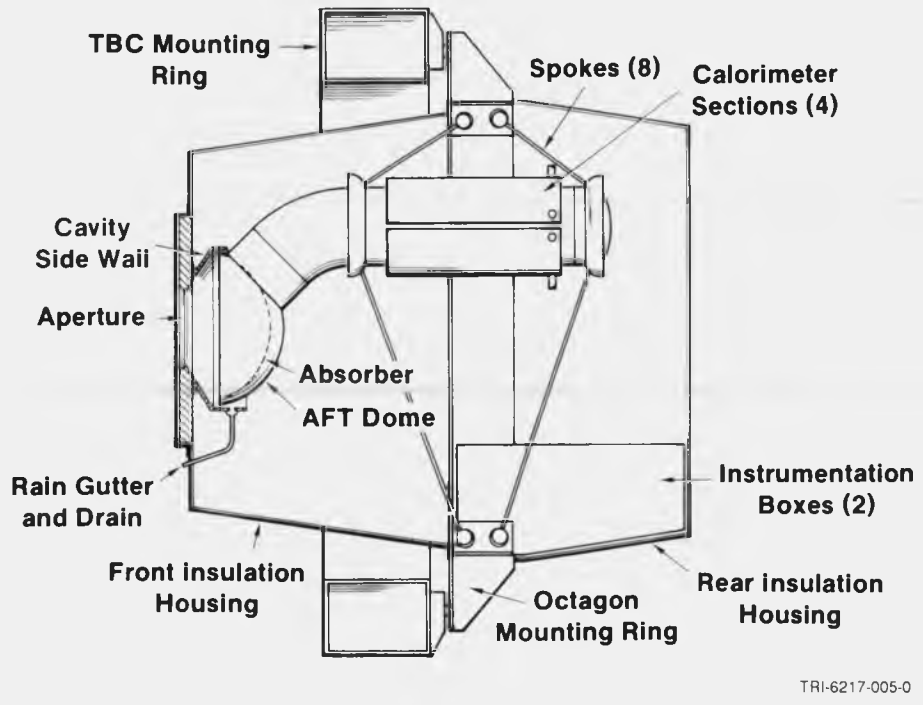

Figure A-1. Schematic of the pool-boiler receiver in the mounting ring.

The absorber support consists of a slightly larger dome in which the absorber nests. This design offers simplicity when compared to a weld-ring design, and a significantly lower liquid metal inventory than a cylindrical support design. In addition, because of the low angle at the edge joint, the support is almost in line with the membrane stresses, reducing any additional stresses caused by the support. Because of low solar flux near the edges, the small vapor passage near the edges is not critical. The aft dome is 0.125 in. thick, providing a substantial support for the absorber. The edge weld joint was machined for a close fit, with the intention of using an electron-beam welding technique. However, the actual weld was a manual fusion TIG operation.

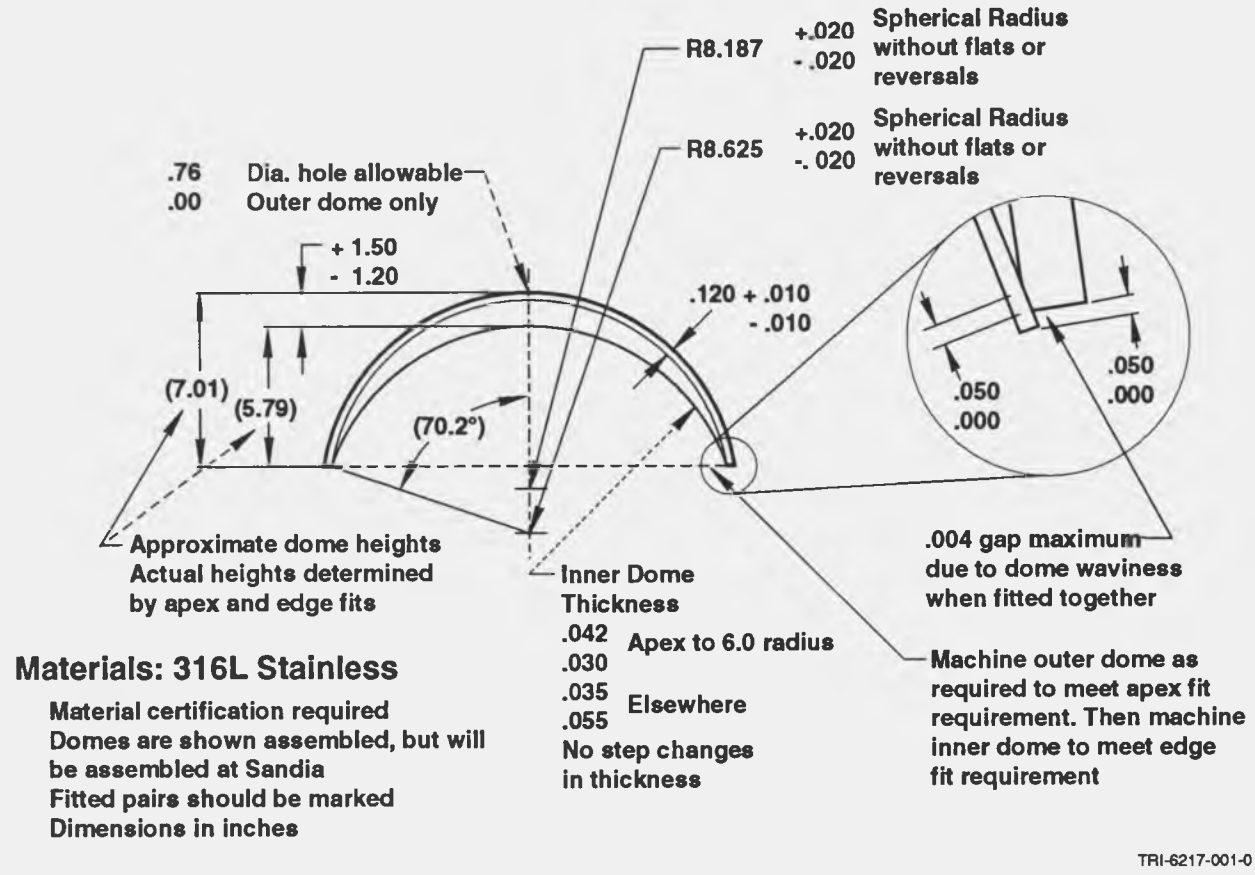

Figure A-2. Receiver dome specification drawing for Sandia pool-boiler receiver.

The gap between the apexes of the two domes should be sufficient to allow vapor to flow to the condenser while liquid flows back to the absorber. Stirling Technology Corporation's (STC) preliminary design of a pool-boiler receiver suggested using a modified Kutataladze flooding limit criterion (Stirling Technology Corporation, 1988). STC suggested a modification to add the predicted effect of flow angles other than vertical. The relationship was developed for flow in a circular tube, while here it is applied to a noncircular flow cross-section. Nonetheless, the criterion can be used for a relative idea of the flooding limit. Using the STC form of the equation

$$\phi = \frac{h_v c^2 \left[\rho_v^2 g(\sin\alpha)\gamma(\rho_l - \rho_v)\right]^{0.25}}{\left[1 + \left(\frac{\rho_v}{\rho_l}\right)^{0.25}\right]^2}$$

where

h_v = heat of vaporization
ρ_v = vapor mass density
ρ_l = liquid mass density
γ = surface tension
α = angle of flow to horizontal
g = gravitational constant
c^2 = dimensionless constant = 3.2
ϕ = allowable heat flux

the safety factor at 600°C is about 6.3 at the horizon and 4.3 at high noon on the longest day. The sodium inventory required to maintain a liquid layer on the absorber in all orientations is 12.7 pounds.

The condenser section was assembled from 8-in.-diameter schedule-10 304L stainless steel pipe and fittings. The large diameter allowed low vapor velocities, and simplified mating to the rear dome by eliminating the need for a conical vapor-collection section. An elbow allows the condenser to be above the pool surface for all anticipated orientations, while keeping the calorimeter section within the confines of the TBC mounting ring.

A 3/4-in. stainless steel tube was attached to the aft dome to provide a vacuum pumpout port. This tube also contained a feedthrough for nine 1/16-in.-diameter sheathed type-K thermocouples. The tubing was bent 90 degrees downward after exiting the aft dome to prevent vapor from entering and transferring heat to the valve and feedthrough. Another 3/8-in. tube was attached to the condenser cap, and was used for filling the receiver. This tube contained a feedthrough with five thermocouples, and was similarly bent to provide a liquid pool thermal barrier to the valve. The tube and feedthrough details are shown in Figures A-3 and A-4. The two thermocouple feedthroughs consisted of a stainless steel plug with 1/16-in. diameter holes for each thermocouple. The thermocouples were furnace-brazed into the feedthroughs using BNi-3 brazing alloy. BNi-7 furnace braze alloy was used to attach the thermocouple tips to the inside surfaces. Incuro-60 braze alloy was used for external thermocouples.

Based on results from bench-scale pool-boiler testing (Moreno and Andraka, 1989), "artificial" cavities were formed in the absorber dome, spaced approximately four inches apart (Figure A-5). The cavities were formed by electric-discharge machining, and were specified 0.020 in. deep, and 0.006 in. in diameter. Checking 30% of the actual cavities yielded diameters from 0.005 to 0.0095 in. and depths from 0.018 to 0.022 in. Figure A-6 shows a polished and etched cross section of a cavity removed from the dome after testing. These cavities supply stable nucleation sites for bubble formation.

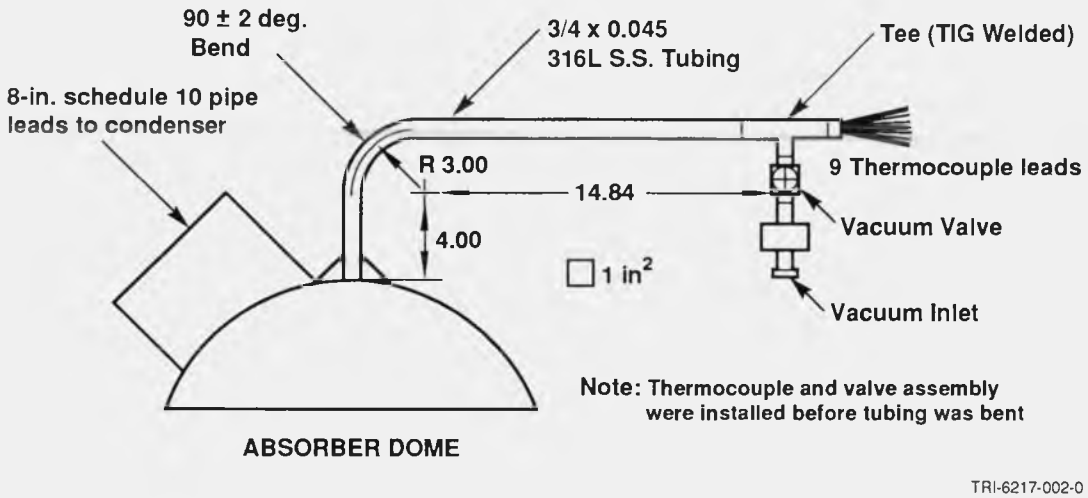

Figure A-3. Details of the aft dome and vacuum pumpout port with thermocouple feedthrough. Nine type-K stainless steel sheathed thermocouples entered through the brazed port and were attached to the absorber dome.

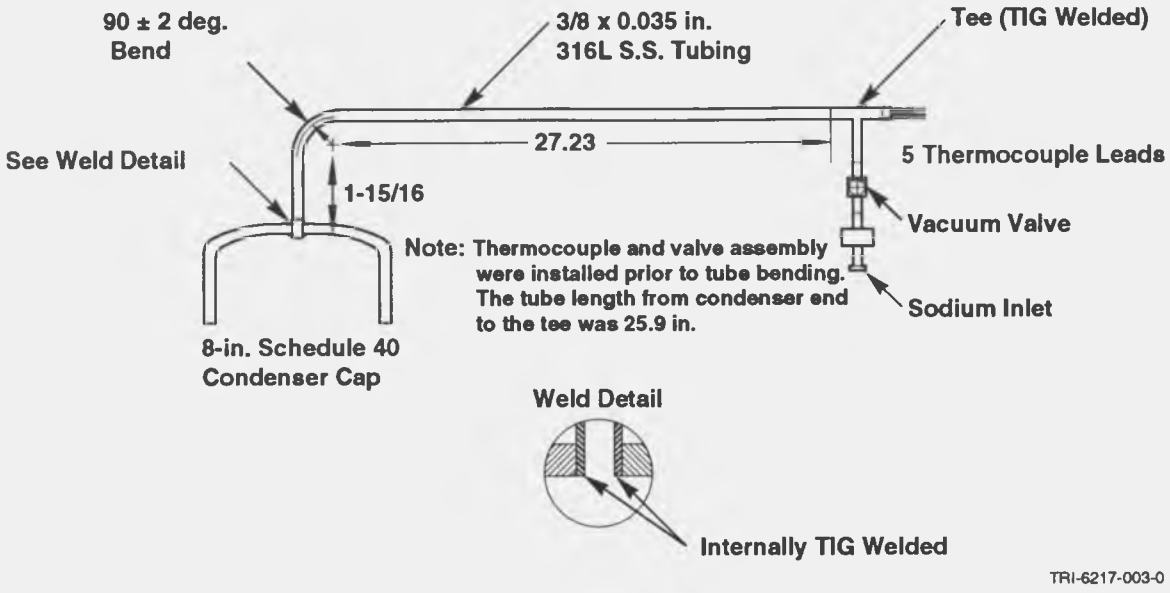

Figure A-4. Condenser endcap, sodium fill port, and thermocouple feedthrough details. Five thermocouples entered here and were applied to the condenser, vapor space, and the top of the pool. This tube was also used in later tests for introduction of xenon into the receiver.

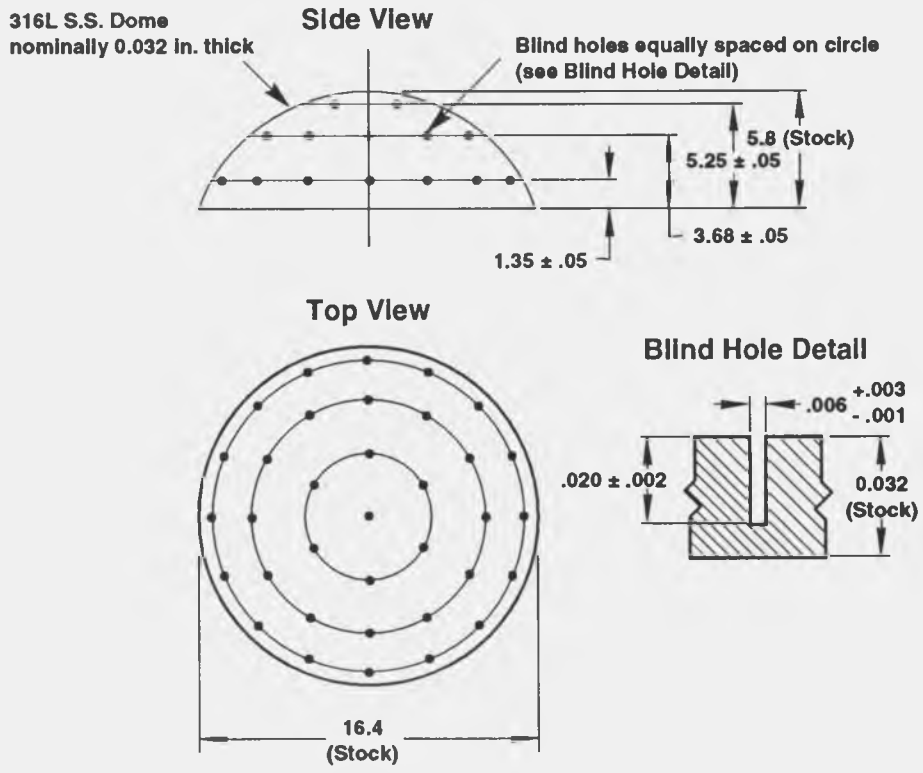

Figure A-5. Locations of the 35 "artificial" cavities in the surface of the absorber dome.

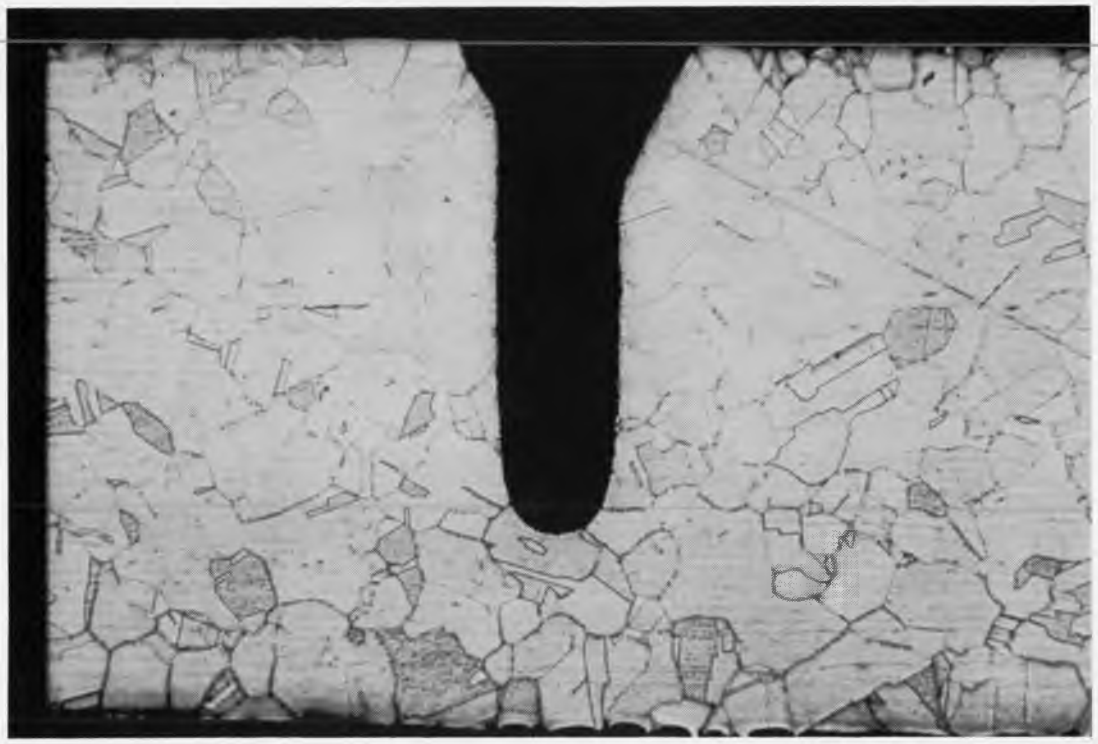

Figure A-6. Polished and etched section of an artificial cavity. This section was taken from the receiver after testing. The conical opening of the cavity is probably due to fatigue caused by bubble departure (see Appendix S of this report).

Three inconel-sheathed heaters were attached to the receiver to preheat and melt the sodium. Two heaters were attached to the aft dome and elbow area, while a third, smaller heater was attached to the condenser cap. The aft-dome heaters were rated at 1200 W each and were 0.188 in. diameter (ARI PN BXX-19B-94-24T). The condenser-cap heater was rated at 1000 W and was 1/8 in. in diameter (ARI PN BXX-13B-50-10T). The heaters were held in place by spot-welded stainless steel shim stock.

Table A-1 lists the assembly sequence for the receiver. This sequence allowed staging of the brazes used for attaching instrumentation, and protected the inner surfaces from oxidation during welding operations. All welds were purged with argon, were leak-checked to less than 10^{-9} standard cm^3/s, and were manual TIG welds. The fill and vacuum tubes and the rim weld were fusion welds with no filler, and the tube welds were backed up with external gussets for bending strength. The welds on the 8-in. pipes were performed with filler. The weld of the pipe to the aft dome was fixtured with an external skip weld, and then welded from the inside with filler rod.

TABLE A-1. ASSEMBLY SEQUENCE

1.	Attach interior thermocouples to absorber dome
2.	Attach interior thermocouples to condenser
3.	Assemble instrumentation feedthroughs
	-Braze interior TCs and feedthroughs (BNi-3)
4.	Apply outer surface thermocouples to absorber dome (INCURO 60 braze)
5.	Cut hole and weld relief in cap for instrumentation and fill port
6.	Cut hole in aft dome for instrumentation and vacuum port
7.	Weld fill port tubing from inside to cap
8.	Weld 8-in. condenser to elbow; weld short section to aft dome
9.	Cut hole in aft dome for condenser
10.	Weld 3/4-in. vacuum port tubing from inside aft dome
11.	Weld condenser-elbow assembly to aft dome
12.	Attach interior pool and vapor thermocouples to proper positions (spot weld)
13.	Weld cap to condenser
14.	Weld feedthrough to end of 3/8-in. tubing
15.	Position and tack weld absorber dome
16.	Trim absorber dome as needed (hand grinder)
17.	Weld absorber dome to aft dome
18.	Weld feedthrough to end of 3/4-in. tubing
19.	Attach support structure brackets to cap and elbow (weld)
20.	Leak test
21.	Apply additional outer surface thermocouples and heaters (spot-weld)
22.	Terminate thermocouples
23.	Assemble insulation, housing, and mounting struts to receiver
	-Includes side wall and aperture plate
24.	Perform any additional bakeout while monitoring internal gases (leak check)
25.	Fill with sodium
26.	Attach calorimeter
27.	Leak-test water system
28.	Complete insulation (vermiculite)
29.	Mount to TBC
30.	Connect and test instrumentation and controls

References

Andraka, C. E., and R. B., Diver. 1988. "Reflux Heat-Pipe Solar Receivers for Dish-Electric Systems," paper no. 889213. *Proceedings of the 23rd IECEC, Denver, CO, August, 1988.* SAND87-2976C. Albuquerque, NM: Sandia National Laboratories.

Moreno, J. B., and C. E. Andraka. 1989. *Test Results from Bench-Scale Sodium-Pool-Boiler Solar Receiver.* SAND89-0899. Albuquerque, NM: Sandia National Laboratories.

Stirling Technology Company. 1988. *25-kWe Solar Thermal Stirling Hydraulic Engine System, Final Conceptual Design Report.* DOE/NASA/0371-1, NASA CR- 180889. Cleveland, OH: National Aeronautics and Space Administration, Lewis Research Center.

APPENDIX B

SUPPORT STRUCTURE AND INSULATION HOUSING

APPENDIX B
SUPPORT STRUCTURE AND INSULATION HOUSING

A support structure and insulation housing were designed to interface the reflux receivers with the Test Bed Concentrator (TBC) mounting ring. The primary design objectives for the support structure and insulation housing were (1) flexibility in accommodating a large variety of receiver configurations, (2) positional flexibility, and (3) minimization of conduction heat loss. We knew that protecting the insulation from rain was an important part of minimizing conduction heat loss and critical to assessing receiver performance.

A schematic of the reflux pool-boiler receiver mounted in its support structure on the TBC mounting ring is shown in Figure B-1. The receiver insulation housing, aperture and side-wall, instrumentation boxes, and calorimeter are also shown in the figure. The support structure is also designed to accommodate reflux heat-pipe receivers using a condenser positioned coaxial with the receiver, Figure B-2. Figures B-3 and B-4 show nominal dimensions for the receiver geometry used in on-sun tests for both configurations. Photographs of the mounted receiver, showing the support structure details, insulation housing, instrumentation boxes, aperture, etc., are shown in Figures B-5 through B-10. Figures B-11 through B-15 are engineering drawings of major components. A receiver support fixture was also constructed to facilitate assembly and can be seen in some of the photographs.

Hot receiver parts, including the aperture cone, aft dome, elbow, calorimeter/condenser, and condenser end cap, were wrapped with at least two layers of 2-inch (in.) (5-centimeter [cm]) thick Cerablanket (aluminum oxide fibers) insulation. The last step in the assembly process involved filling the remainder of the receiver housing with vermiculite. A panel located on the top of the rear insulation housing was used for this purpose.

Receiver Support

The octagon support ring was constructed from 0.250-in. (0.63-cm) thick 6061-T6 aluminum, and provides the primary structural interface for attachment of the receiver to the TBCs. In addition, the insulation and instrumentation housings are supported from the octagon support ring. Feed-through connections for calorimeter cooling water and electrical preheat were made through the octagon ring.

The receiver was supported by eight 0.5-in. (1.27-cm) diameter stainless steel 316L stainless steel spokes. They were attached to the aluminum octagon support ring through spoke pins that were held in place by retaining rings. Recessed within the spoke pin, a spherical washer set and four Schnorr Disk Springs (Belleville Springs) were secured by a 1/2 in. x 13 thread/in. nut. Approximately one turn of pretension was applied to each nut. The disk spring assembly was designed to allow thermal expansion differences between the spokes and condenser while maintaining approximately 100 to 500 pounds of axial preload force in the spokes. Two support hubs were skip welded to the receiver condenser section to provide attachment pads for the spokes. Spherical washer assemblies (one spherical washer was welded to the spoke end) provided latitude for up to 5 degrees of spoke misalignment to the hubs. The receiver support hubs were machined from 304L stainless steel 10-in. schedule-40 pipe end caps. Following the test, it was observed that all but one or two of the skip welds on each hub had cracked. However, the weld bead interference between the hub and condenser was adequate to maintain position.

Insulation Housing

The insulation housing was constructed of 0.060-in. (0.15-cm) thick T6061-T6 aluminum and attached directly to the octagon support ring. The riveted seams along the joints of the eight-sided enclosures were silicone caulked and weather stripping was applied at the octagon support ring interface. Prior to final assembly, housing integrity was verified by dousing it with water from a garden hose. During testing, it was necessary to attach additional equipment to the housing for xenon addition and x-ray studies. No evidence of rain penetration or performance degradation due to wet insulation was observed.

Receiver Cone and Aperture

The uncooled portion of the receiver cavity was formed from 0.0630-in. (0.16-cm) thick 316L stainless steel and was supported from the front receiver housing. A rain collection gutter was incorporated behind the wide end of the

cone, just under the receiver absorber. The annular stainless steel ring, which was welded to the receiver cone and bolted to the receiver housing, proved to be unsuitable. Thermal gradients between the cavity (approximately 900°C) and the relatively cool perimeter (near the attachment points) resulted in severe buckling and movement of the aperture away from the receiver. This design deficiency was fixed by cutting radial slits from the edge of the annular ring to near the cone. The close position of the water cooled aperture ring on TBC-1 constrained the aperture movement to within acceptable limits.

The receiver aperture was machined from Fiberfrax 3000 board and was held in place with an aluminum support bracket. Its aperture diameter was 8.65 in. (22-cm). Melting of the aperture and part of the receiver cone occurred during an x-ray test in December 1989 when the TBC-1 tracking system experienced an intermittent malfunction. Subsequently, the aperture was enlarged to approximately 10.2 in. (26-cm) diameter, corresponding to the small diameter of the receiver side-wall cone. The aperture was enlarged to accommodate the IR camera studies and to help validate the receiver heat-loss models.

Instrumentation Housing

Receiver instrumentation, primarily type-K thermocouples, was terminated inside two instrumentation boxes that were attached to the octagon support ring and physically located inside the rear insulation housing. Four 12-pair thermocouple extension cables, approximately 12 ft (3.7 m) long were used to connect to the TBC instrumentation boxes located on the bipod support just below the receiver mounting ring.

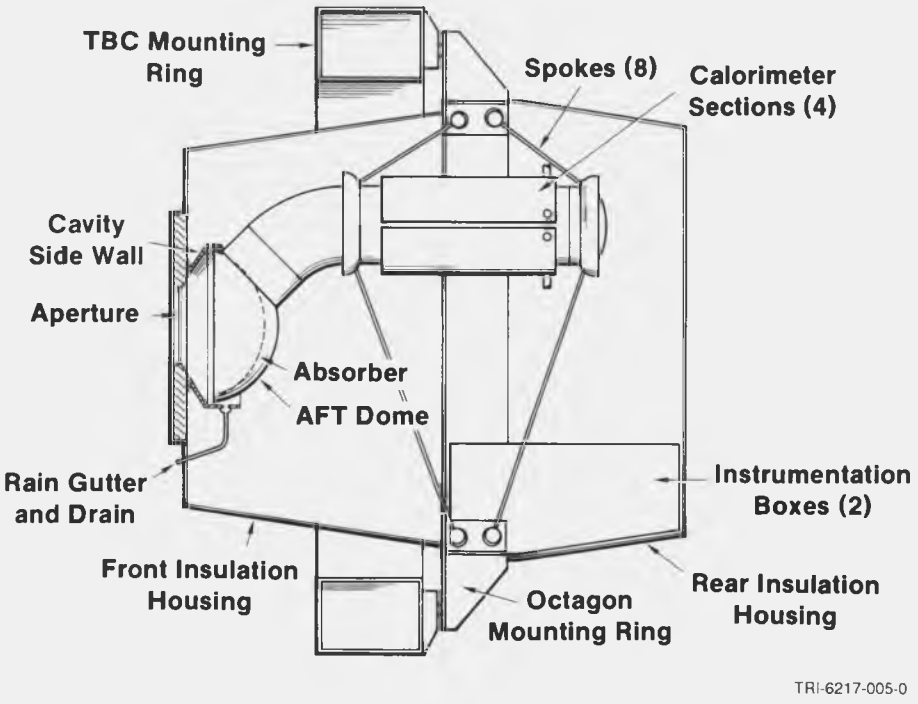

Figure B-1. Schematic of the pool-boiler receiver mounted in the support structure.

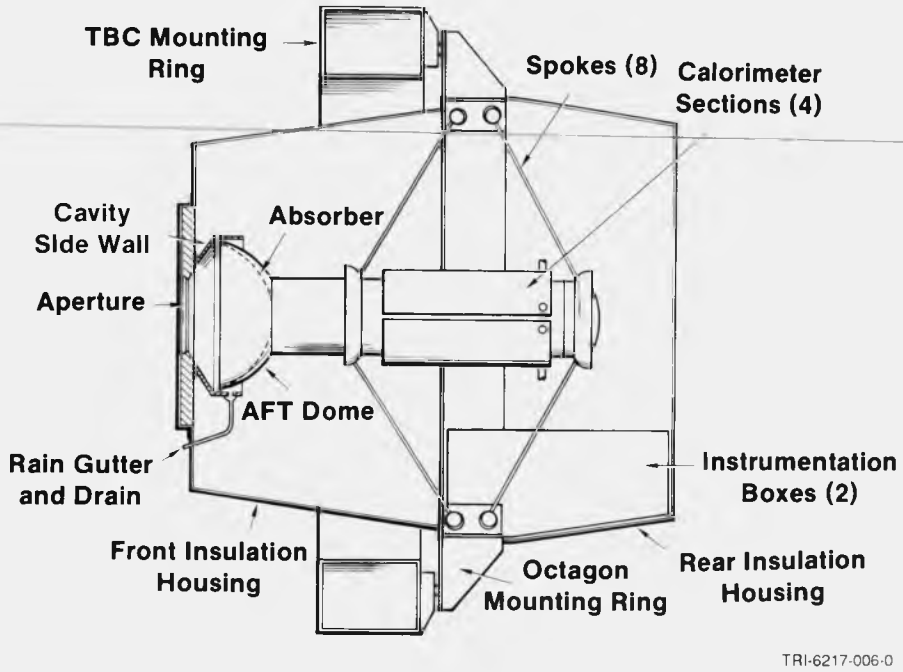

Figure B-2. Schematic of a coaxially mounted heat-pipe receiver in the support structure.

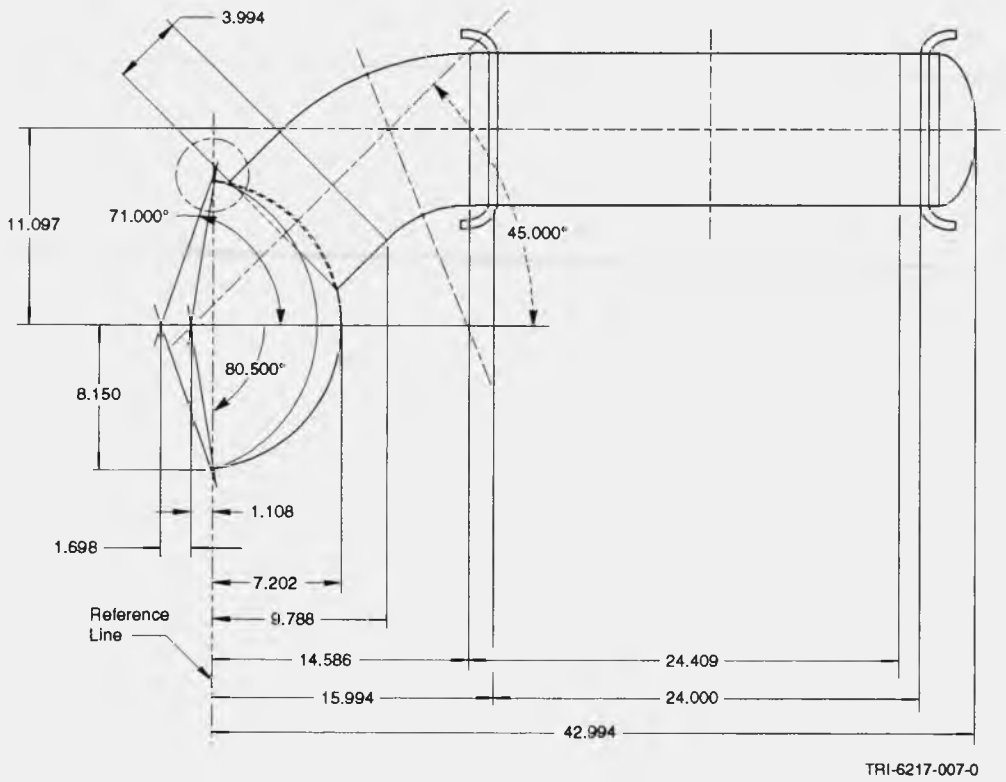

Figure B-3. Nominal dimensions of the pool-boiler receiver.

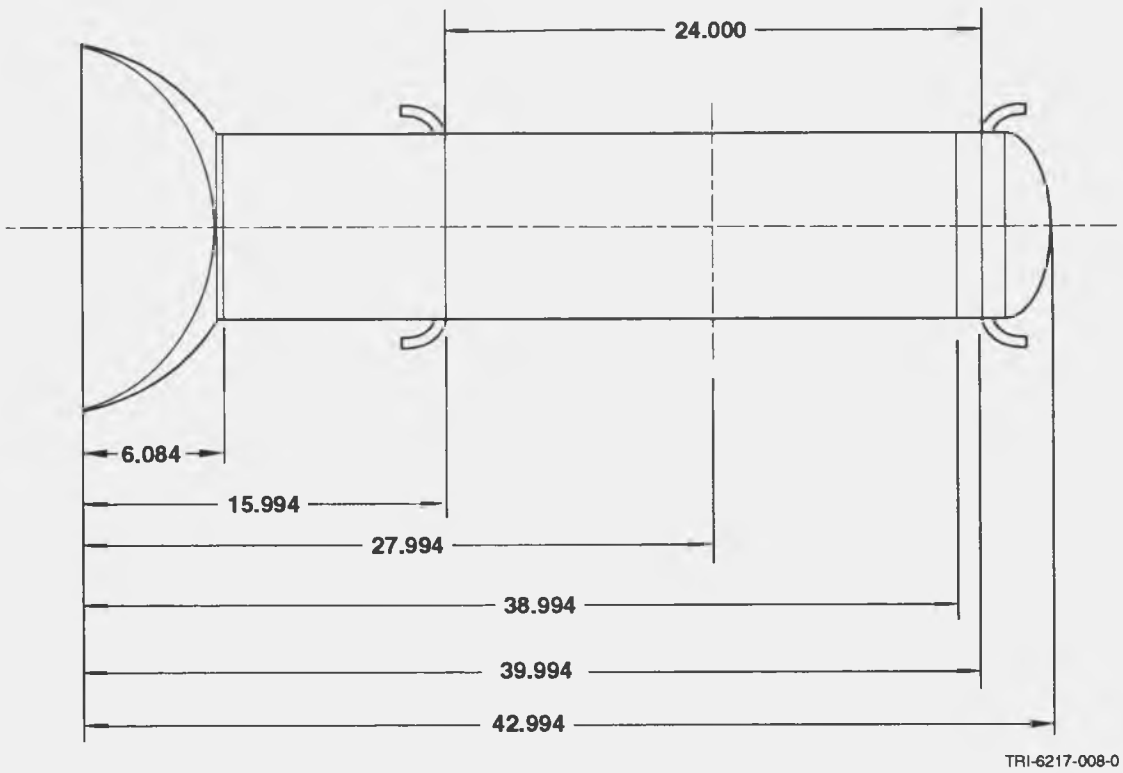

Figure B-4. Nominal dimensions of a heat-pipe receiver.

Figure B-5. Photograph of the pool-boiler receiver in the mounting ring.

Figure B-6. Photograph showing the spoke attachments to the pool-boiler hub assembly.

Figure B-7. Photograph of the pool-boiler receiver aperture. Front surface thermocouples brazed to the absorber can be seen through the aperture.

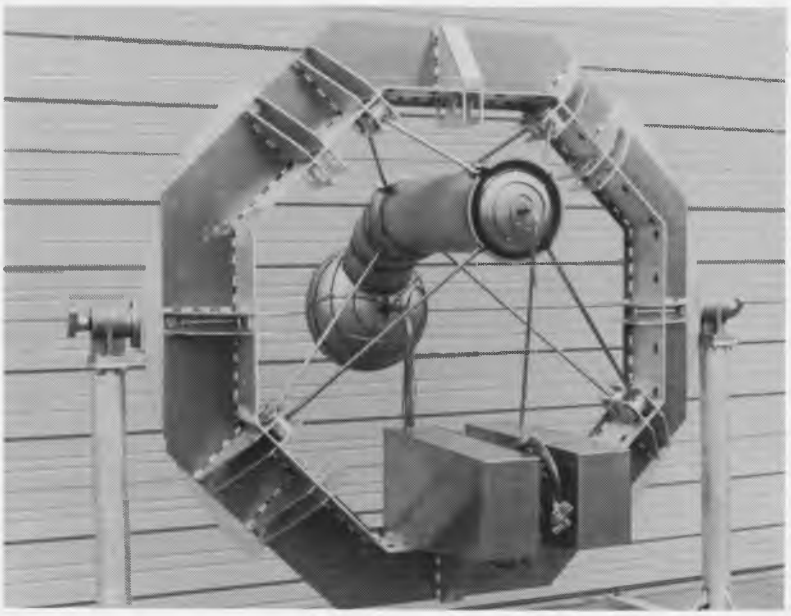

Figure B-8. Photograph showing a rear view of the pool-boiler receiver in the mounting ring.

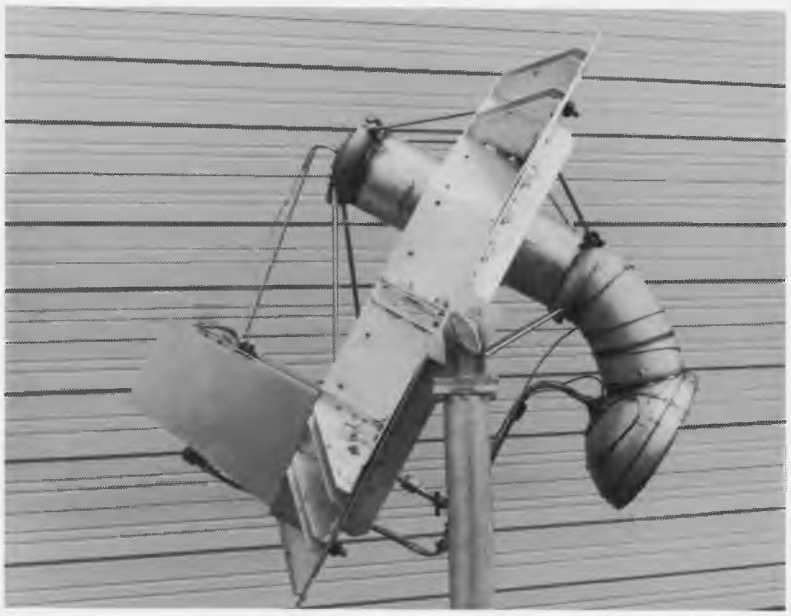

Figure B-9. Photograph showing a side view of the pool-boiler receiver in the mounting ring.

Figure B-10. Photograph of the pool-boiler receiver with the insulation housing.

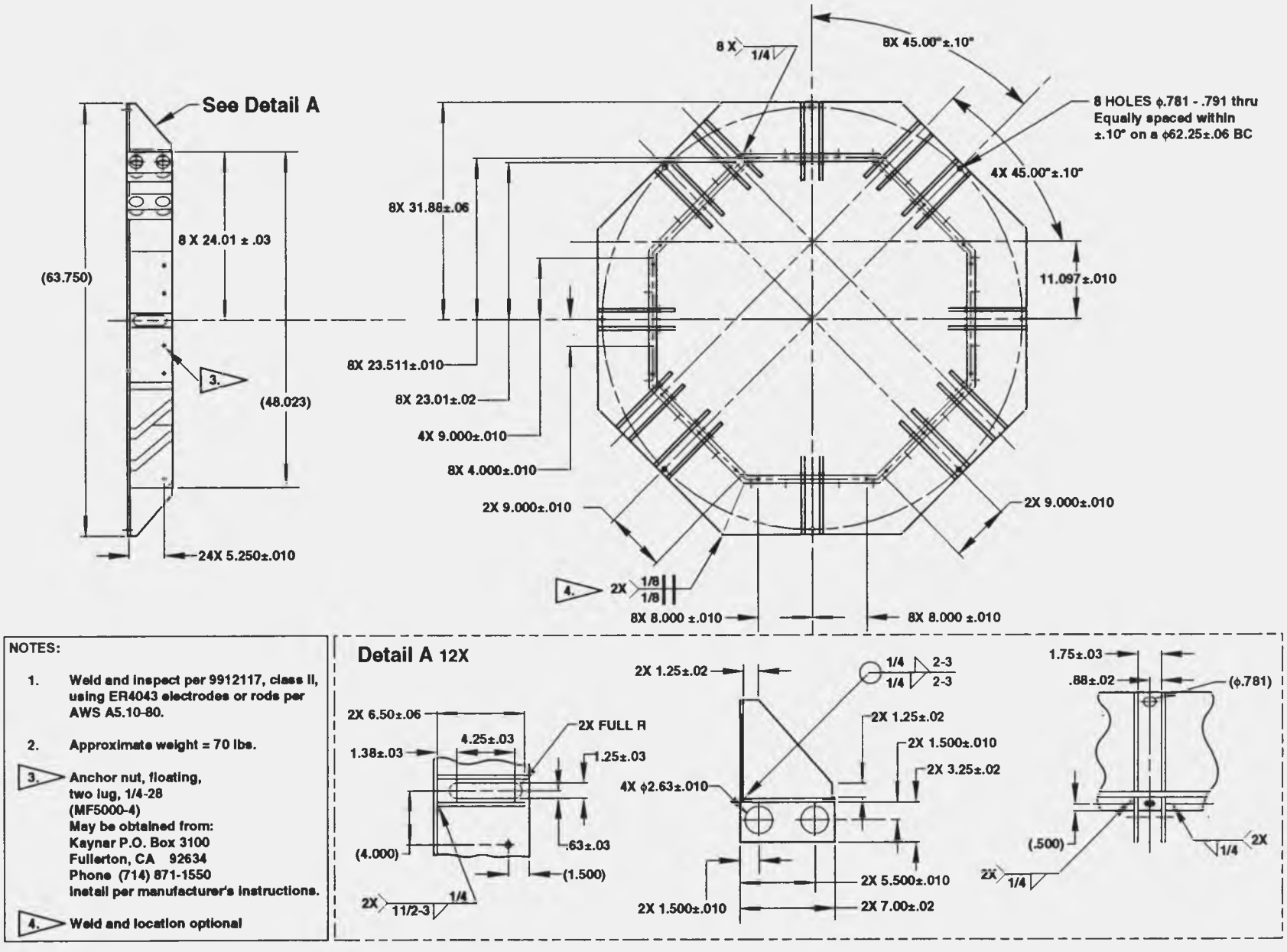

Figure B-11. Engineering drawing of the Sandia reflux receiver octagon support ring.

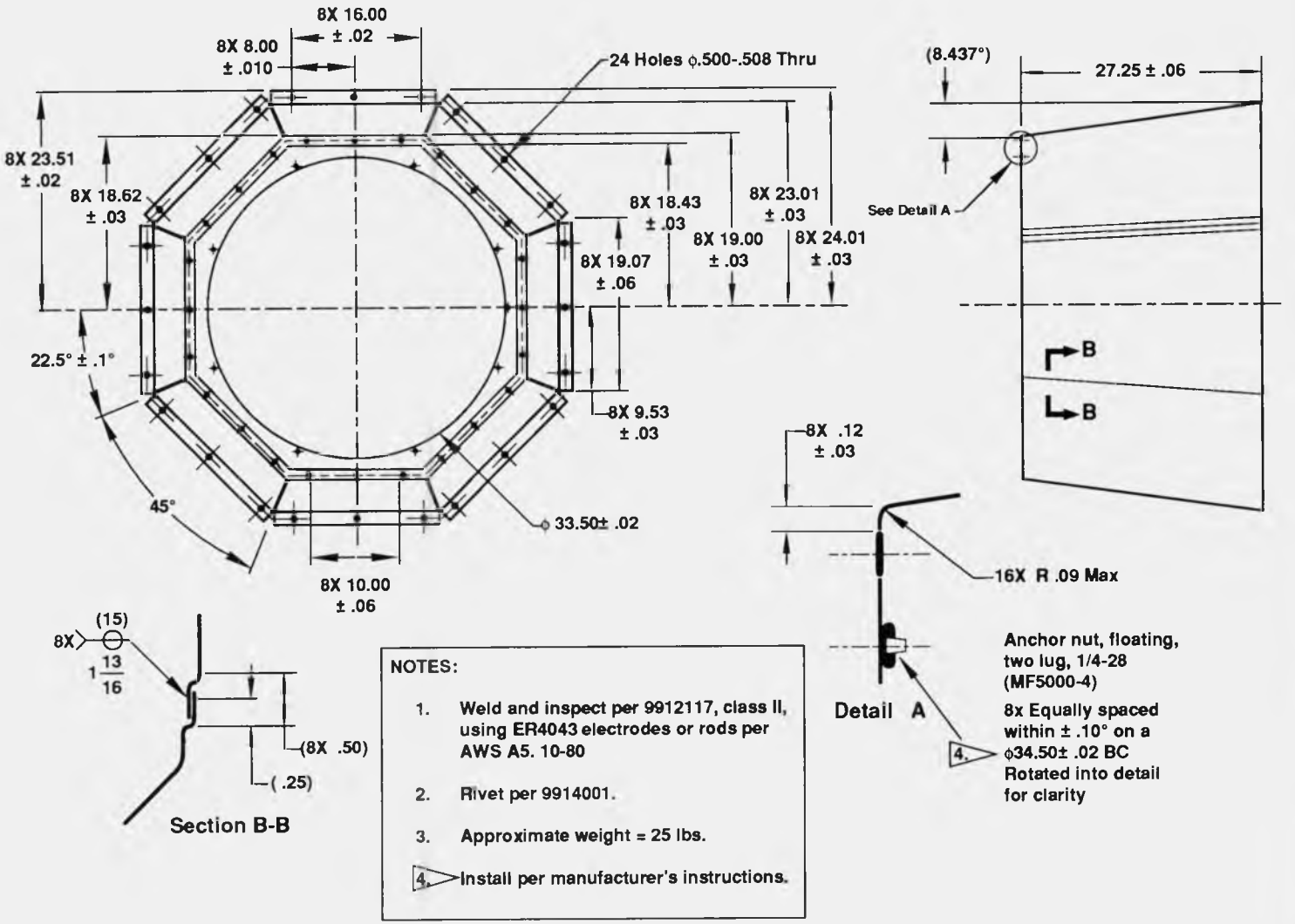

Figure B-12. Engineering drawing of the Sandia reflux receiver front insulation housing.

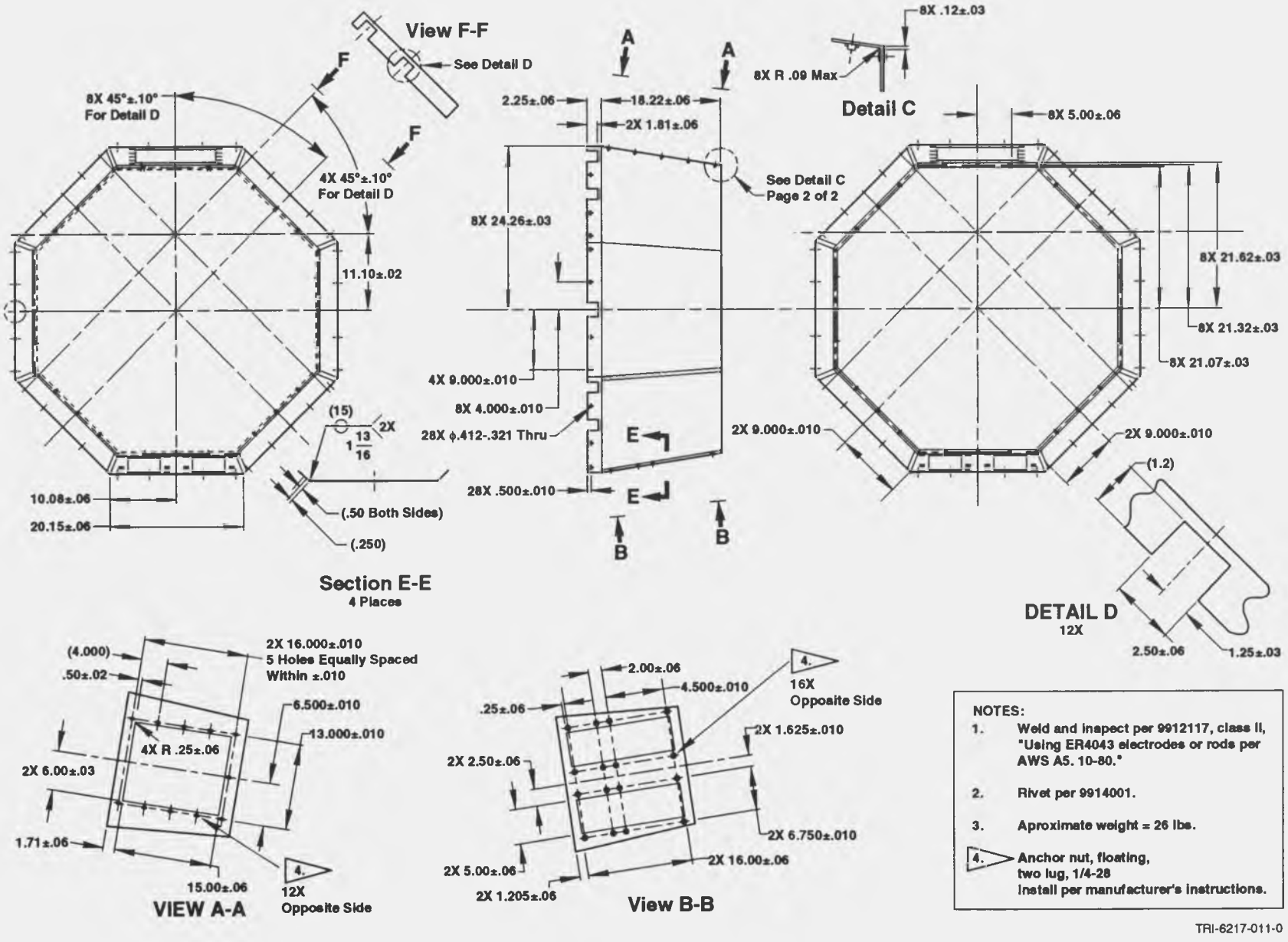

Figure B-13. Engineering drawing of the Sandia reflux receiver rear insulation housing.

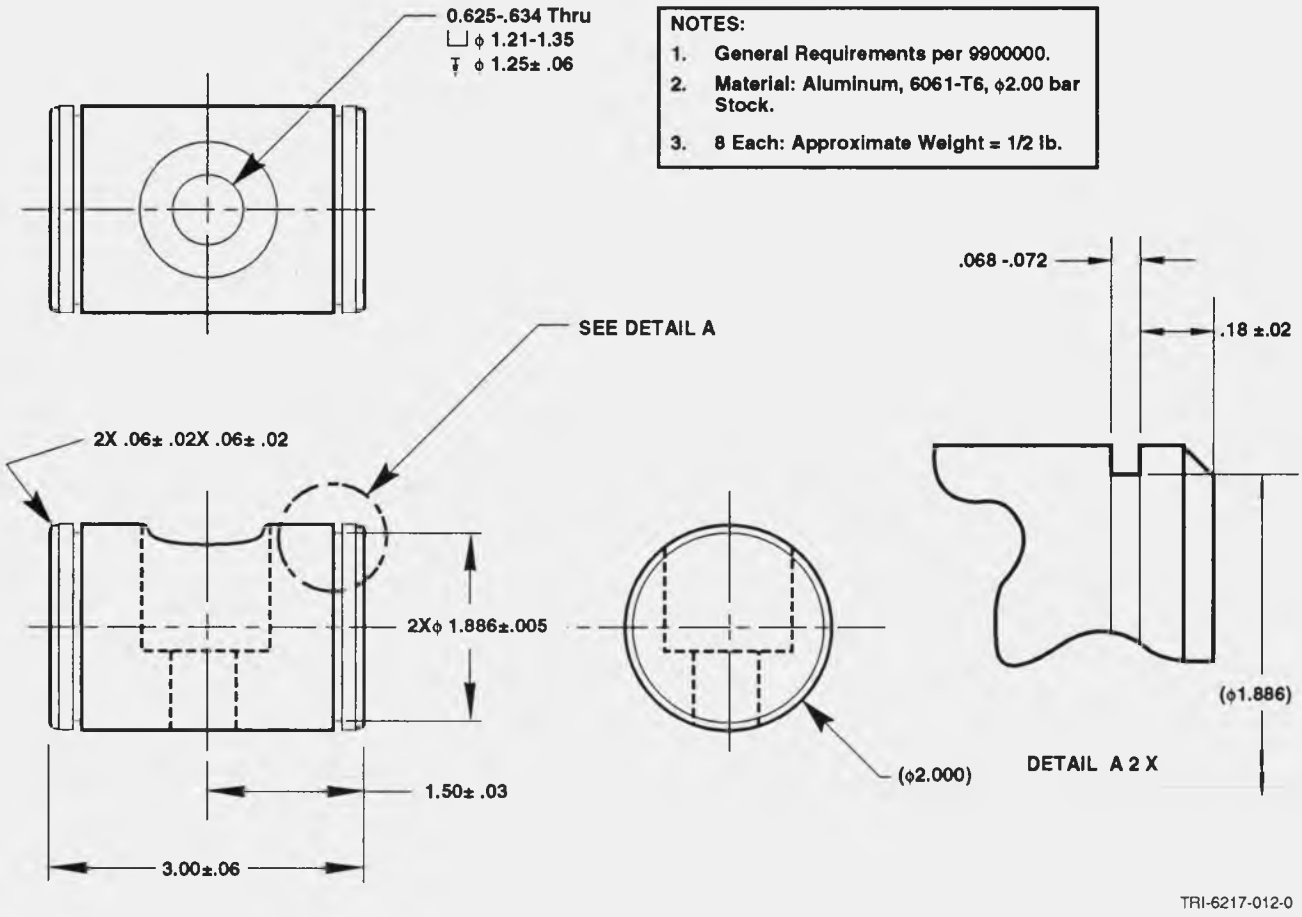

Figure B-14. Engineering drawing of a spoke pin used to attach the spokes to the octagon support ring.

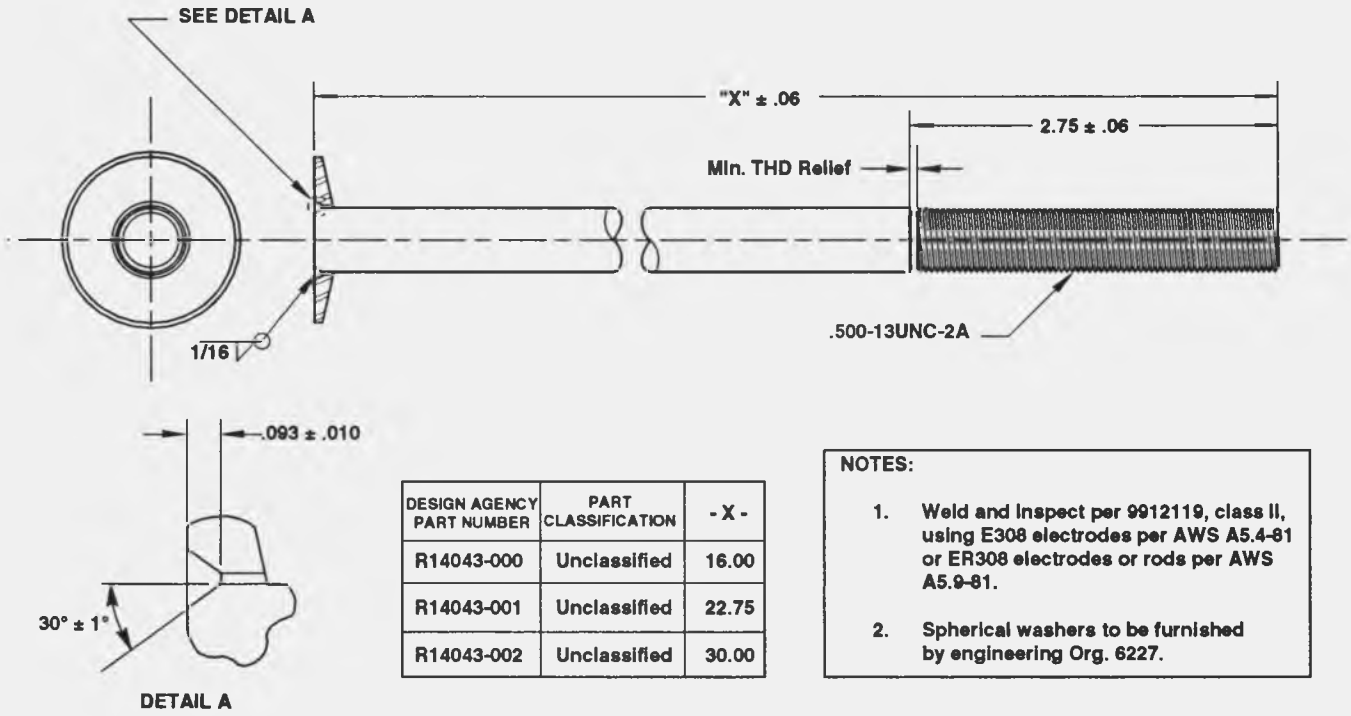

DESIGN AGENCY PART NUMBER	PART CLASSIFICATION	- X -
R14043-000	Unclassified	16.00
R14043-001	Unclassified	22.75
R14043-002	Unclassified	30.00

NOTES:

1. Weld and inspect per 9912119, class II, using E308 electrodes per AWS A5.4-81 or ER308 electrodes or rods per AWS A5.9-81.
2. Spherical washers to be furnished by engineering Org. 6227.

TRI-6217-013-0

Figure B-15. Engineering drawing of the spokes.

APPENDIX C

MATERIALS SELECTION FOR FIRST RECEIVER

APPENDIX C
MATERIALS SELECTION FOR FIRST RECEIVER

Materials selection for the first full-scale solar receiver was largely based on decisions made and lessons learned during the design, fabrication, and testing of its predecessor, the bench-scale liquid-metal reflux receiver (Moreno and Andraka, 1989). For the full-scale receiver, the selection process encompassed the following:

1. The absorber (front dome)
2. The aft dome
3. Balance of receiver vacuum envelope
4. Thermocouple sheaths
5. Thermocouple attachment braze filler metals
6. Heat transfer fluid (liquid metal)
7. Aperture
8. Optical cavity
9. Thermal insulation
10. Insulation housing and mounting ring
11. The water cooled gas-gap calorimeters

Front and Aft Domes

The front and aft domes of the receiver were hydroformed from type 316L stainless-steel sheet stock. This selection was based on the considerations summarized in Table C-1. A previous assessment (Lukens et al., 1988) had deemed 316L stainless steel to be adequate for short-term testing at 800°C, a good choice with respect to all of the cost and schedule items in Table C-1, and adequate regarding most of the damage resistance considerations. Also, this alloy is known to be sodium compatible (Foust, ed., 1979). The oxidation resistance and thermal stability were verified to be adequate by tensile-testing samples of the materials and weldments cut from a mockup of the receiver. Tensile strength and force-displacement curves were nominally the same from both as-prepared samples and samples that were air-baked for up to 1000 hours at 800°C. Also, absorber thickness measurements made before and after the receiver was tested indicate less than 0.001-inch (in.) thickness reduction. At 800°C, the yield strength of this material is only about 84.1 MPa (12,200 psi), or 40% of its room-temperature strength, its modulus of elasticity is about 138 GPa (20,000 ksi), or 70% of the value at room temperature, and its creep rupture time at 68.9 MPa (10,000 psi) is only 200 hours (hrs) (Aerospace Structural Materials, 1975). For the limited objectives of the first pool-boiler receiver design, stress analysis (Appendix H of this report) showed that these properties are acceptable.

Balance of Receiver Vacuum Envelope

Other components in the vacuum envelope included the 8-in. pipe parts, the vacuum and fill tube assemblies and valves, and the thermocouple feedthroughs. These were expected to experience less severe service conditions. The 8-in. pipe parts were chosen to be type 304L stainless steel, based on availability. The tube assemblies and valves were type 316L stainless steel, all welded. The thermocouple feedthroughs were also type 316L stainless steel.

After a mockup of the first receiver was constructed, concerns were raised about the thermal stability of the stainless steels and their weldments (Moreno and Andraka, 1989). To assure that no serious loss of strength or embrittlement would occur, tests of the actual materials were run. Samples were cut from the mockup front and back domes, and from its 8-in. pipe components. Samples were also cut from the dome rim weld, the 8-in. pipe weldments,

TABLE C-1. MATERIAL SELECTION CONCERNS FOR FIRST RECEIVER

DAMAGE RESISTANCE	COST AND SCHEDULE
Sodium compatibility	Availability
Oxidation resistance	Formability
Thermal stability	Machineability
High-temperature strength	Weldability
Creep characteristics	
Fatigue Life	

and the welds joining the fill and evacuation tube assemblies to the receiver. Tensile tests were performed on one set of parts as cut, on a second set that had been baked at 800°C for 100 hrs, and on a third set that had been baked for 1000 hrs. The resulting force-displacement curves showed a mild loss of strength and ductility in a few cases, but overall, indicated that thermal stability would not be a problem.

Thermocouple Sheaths and Attachment Braze Filler Metals

Sheath material for thermocouples used on the outside of the receiver was chosen to be IN600 based on its good oxidation resistance. Type 316L stainless steel was chosen for internal thermocouple sheaths because of its good thermal expansion match to the feedthroughs during brazing. The braze filler alloy used to attach the thermocouples to the feedthroughs and the inner surfaces of the receiver was BNi-3. This selection was based on a Sandia evaluation (Hosking, 1985) of various braze filler candidates for service in high-temperature sodium. Incuro 60 was the braze filler alloy used to attach thermocouples to the air side of the absorber. Previous experience (Moreno and Andraka, 1989) had shown that this alloy would be suitable for air-side service and would permit the internal and external thermocouples to be brazed on in separate operations.

Heat-Transfer Fluid

Sodium was chosen as the heat-transfer fluid, in order to maintain continuity with the earlier bench-scale tests. The decision to use Na in the bench-scale tests was based on sodium's relatively low vapor pressure at 800°C, and on the extent of its boiling-behavior documentation in the literature. Sodium's primary disadvantage is that it is solid at room temperature. Sodium, potassium, and alloys thereof are the only heat transfer materials available for two-phase operation in the 700° to 800°C range.

Aperture and Optical Cavity

The aperture was machined from a 2-in. thick Fiberfrax 3000 insulation board (70% alumina and 26% silica, typical). This material was selected based on ready availability and previous use in this application. A small sample of a similar board has been documented to survive without melting when subjected to solar fluxes of up to 100 watts/square centimeter (W/cm^2) in air, and in full-scale application is estimated to be able to survive up to 80 W/cm^2 (Holmes et al., 1985). The aperture diameter, 8.66 in., is large enough so that this condition is met by the positioning used with the Test Bed Concentrator #1 (TBC-1).

The optical cavity was made from 3/16-in. thick type 316L stainless-steel sheet stock. Because the cavity was not subjected to direct solar flux, it was expected to operate at approximately the same temperature as the absorber. Therefore the choice of material was based on the same reasons as for the absorber itself.

Thermal Insulation

Cerablanket mineral-wool batting and vermiculite were the materials used to thermally insulate the receiver. The batting was used mainly to form a high-temperature seal between the receiver and the aluminum weather housing. Vermiculite comprised the bulk of the insulation package that was poured into the space between the receiver and its sheet-metal insulation housing. Vermiculite was easy to apply. It was also easily removed using a shop vacuum cleaner. A minor inconvenience was that it would settle with time, requiring an occasional "topping off."

Insulation Housing and Mounting Ring

The insulation housing and mounting ring were made from aluminum sheet and plate, respectively. Aluminum's advantages are that it is lightweight, easily formed, and only moderately expensive.

Gas-gap Calorimeters

The watercooled gas-gap calorimeters were made from type 304L stainless-steel sheet stock. Internal baffles were furnace-brazed in place. The external envelope was welded. Each of the four calorimeter quadrants has one surface that must be an accurately formed cylindrical segment, because it defines one side of the very-narrow gas gap between the calorimeter and the receiver. Corrections to welding-induced distortion were made by arc-spraying a copper coating on this surface, and then milling the surface true. Copper was chosen because it introduces very little additional thermal impedance.

References

Aerospace Structural Materials Handbook, 1975. Code 1307, 9, Belfour Stulen, Inc.

Foust, O. J., ed. 1979. *Sodium NaK Engineering Handbook*, Vol. V. Gordon and Breach, Science Publisher, Inc.

Holmes, J. T., R. M. Edgar, and P. F. Gerrish. 1985. "Screening Ceramic Materials for Intense Radiant Heat Applications." Presented at *The American Ceramic Society Conference on Composites and Advanced Ceramic Materials, Cocoa Beach, FL, January 20-24, 1985*. SAND84-1648C. Albuquerque, NM: Sandia National Laboratories.

Hosking, F. M. 1985. "Sodium Compatibility of Refractory Metal Alloy-Type 304L Stainless Steel Joints." *Welding Research Supplement to The Welding Journal* July 1985, pp 181-190-s.

Lukens, L. L., C. E. Andraka, and J. B. Moreno. 1988. *Liquid Metal Thermal Electric Converter.* SAND88-0458. Albuquerque, NM: Sandia National Laboratories.

Moreno, J. B., and C. E. Andraka. 1989. *Test Results from Bench-Scale Sodium-Pool-Boiler Solar Receiver.* SAND89-0899. Albuquerque, NM: Sandia National Laboratories.

APPENDIX D

MATERIALS AND METHODS FOR NEXT-GENERATION RECEIVER

APPENDIX D
MATERIALS AND METHODS FOR NEXT-GENERATION RECEIVER

Approximately two months after testing began on the first pool-boiler receiver, an effort was begun to address lifetime and commercialization issues for the next-generation receiver. The issues that have been considered include: (1) materials for improved lifetime of the receiver envelope, (2) improving the manufacturability and inspectability of the front-to-aft-dome rim weld, (3) use of NaK-78 as the heat-transfer fluid to eliminate the need for trace heaters, (4) alternatives to electric-discharge-machined cavities for boiling stabilization, (5) receiver-envelope-material creep/fatigue characterizations, (6) stress analyses and creep/fatigue analyses leading to lifetime predictions, and (7) receiver hybridization (solar and fossil-fuel dual use). The results of these efforts are summarized in this Appendix.

Materials for Improved Lifetime of the Receiver Envelope

A meeting of Sandia National Laboratories (Sandia) solar engineers and material specialists was held on November 6, 1989 to discuss the issue of materials for improved lifetime. A prioritized list of selection criteria was provided to the materials specialists, and appears in their response (memo dated December 12, 1989 included in this appendix). Their recommendation was to use Haynes Alloy 230. As noted or implied at the time of their response, some information about this alloy was still incomplete, specifically: (1) emissivity after oxidation, (2) brazing behavior and sintering properties, (3) welding behavior, (4) sodium and NaK (sodium-potassium) compatibility, and (5) creep/fatigue properties. Subsequently, steps were planned to remedy the situation. Most of the steps have since been completed. The steps, and their status are listed below:

1. Measurement of Haynes Alloy 230 optical properties: the focus was shifted from infrared emissivity to solar absorptivity, because the latter property is more important in determining receiver performance, and because emissivity should not vary greatly among potential candidates. Measurements were performed by A. R. Mahoney at Sandia. The solar-averaged absorptivity of an as-delivered sample of Haynes Alloy 230 sheet stock was approximately 0.5. After an air bake at 850°C for 2 hours (hrs), the value rose to 0.87. After 280 hrs at 850°C, the value had reached 0.91, with some spalling of the oxide coating observable as microscopic bright areas. In comparison, the solar-averaged absorptivity of oxidized IN625 is typically 0.85, and IN617 is expected to be similar, according to Mahoney. Mahoney estimates that the emissivity of oxidized Haynes Alloy 230 would be about 0.8 at elevated temperature.

2. Brazing behavior and sintering properties: some brazing tests and extensive sintering tests have been carried out. Although brazed joints are not anticipated in a commercial receiver, there is continuing interest, during the evaluation stage, in attaching thermocouples to the external surface of the absorber using the braze-filler alloy Incuro 60. In a feasibility test, an IN600 rod was joined to a Haynes Alloy 230 sheet-stock sample using Incuro 60. No problems with Haynes 230 wettability or Incuro 60 flow were discovered, and the resultant joint looked identical to those previously made on the 316L stainless steel absorber.

   Sintering is of interest because of the possibility of stabilizing boiling with sintered powder-metal coatings instead of with artificial cavities. Work done by Thermacore, Inc. has demonstrated stabilization using a coating made from type 304L stainless steel powder applied to an IN625 heated wall (Anderson, 1990). At Sandia, testing of this concept is planned, using quartz-lamp-heated bench-scale pool boilers. IN600 powder has been chosen in order to closely match the thermal-expansion characteristics of Haynes 230. Type 304L stainless steel powder has also been included in the test matrix, and will be tested if IN600 is not satisfactory. Bonding strength requirements have been established from thermal stress estimates at the coating/substrate interface: 1000 psi for IN600 and 3700 psi for 304L stainless steel. Pore dimensional requirements have been established based on a very conservative application of the method of Shai and Rohsenow (1969): at least one pore that is 0.005 inches (in.) in diameter and 0.018 in. deep is needed within a 1/4-in.-diameter disc of coating. The two memos from Moss, dated June 28, 1990 and October 8, 1990, summarize the development effort and its various results that culminated in nominal satisfaction of these requirements.

3. Welding behavior: manual tungsten-arc welding tests were sucessfully done on some joints typical of the first receiver. These were (1) butt welds between Haynes Alloy 230 and type 316L stainless steel tubing, (2) corner groove welds between Haynes Alloy 230 plates and tubes, and (3) standing edge welds between IN600 tubes and Haynes Alloy 230 plates. The details are summarized in the memos to Moss dated February 9, 1990, April 12, 1990, and July 2, 1990, included in this Appendix.

4. Sodium and NaK compatibility: there is little concern for short-term testing (memo dated December 12, 1989 included in this Appendix). The long-life issue will be addressed by a planned long-term test of a bench-scale pool boiler expected to begin in late 1991.

5. Creep/Fatigue properties: a program to characterize the creep/fatigue of Haynes Alloy 230 at high temperature was initiated at Sandia. Experimental evaluation of the alloy has been completed, but at the time of this writing, the results and analysis are not yet available.

Manufacturability and Inspectability of the Front-to-Aft-Dome Rim Weld

At a December 21, 1989 meeting on materials and methods for improved lifetime, the front-to-aft-dome rim weld in the first receiver was identified as difficult to inspect. This and other concerns were summarized and addressed in the memo to Distribution, dated February 8, 1990, included in this Appendix. As shown in the memo, a slight redesign of the weld configuration should make it inspectable. Subsequent consultations with J. H. Gieske, R. W. Munford, G. A. Knorovsky, and R. K. Sager, Jr. (all at Sandia), and with Ultimate Hydroforming and Saffron Engineering (Sterling Heights, Michigan) have confirmed this redesign for the next-generation receiver.

Use of NaK-78 as the Heat-Transfer Fluid

Because the melting point of sodium is 97.82°C (Foust, ed., 1979), a receiver that uses sodium will require trace heaters. These heaters must be arranged and controlled so that cumulative damage associated with repeated phase changes does not occur. Because NaK-78 melts at -12.6°C (Foust, ed., 1979), substituting it for sodium can eliminate the heaters and heater controls expense. The liabilities associated with NaK are (1) it is more expensive than sodium, (2) it is more hazardous than sodium, mainly because it is liquid at room temperature, and (3) its boiling behavior and materials compatibilities aren't as well studied as those of sodium. Each of these concerns is addressed below.

In Appendix E of this report, the cost of commercial-grade NaK-78 in a pool-boiler receiver is estimated at $70.11 (about 3.5% of the total receiver cost); the estimate is doubled for high-purity NaK-78. This expense should easily be recouped by elimination of the heaters and heater controllers.

NaK-78 hazards have been discussed with private utilities, and have not been identified as a major concern according to D. Menicucci of Sandia.

Some work has already been done by Thermacore, Inc., on the question of NaK-78 boiling behavior and material compatibility (Anderson, 1990). No short-term problems have been encountered. Bench-scale tests at Sandia are planned to further address short-term as well as long-term questions.

Alternatives to Electric-Discharge-Machined Cavities

Several cost-effective (Appendix E) alternatives to electric-discharge-machined cavities have been identified. The development of one alternative, sintered powder metal coatings, has been discussed above in the section "Materials for improved lifetime of the receiver envelope." The development of another alternative, laser-drilled cavities, is summarized in the memo to Moss, dated September 19, 1990, included in this Appendix.

Stress and Creep/Fatigue Analyses

A summary of the stress analyses performed to date can be found in Appendix H of this report. As of this writing, an analysis to estimate the effects of creep and fatigue on the lifetime of the next-generation Haynes Alloy 230 receiver has just begun.

Receiver Hybridization

Hybridization efforts are just beginning. The National Renewable Energy Laboratory (NREL) (formerly the Solar Energy Research Institute [SERI]) in Boulder, Colorado, has prepared a solicitation package for a Hybrid Receiver subcontract. The package includes a Statement of Work for design, fabrication, and testing of a 10-kW_t heat-pipe or pool-boiler receiver capable of operating on solar energy or natural gas combustion.

References

Anderson, J. 1990. "Subscale Boiler Experiments - Review and Status." *Solar Stirling Heat Transport System Workshop, Lancaster, PA, November 13-14, 1990.*

Foust, O. J., ed. 1979. *Sodium NaK Engineering Handbook*, Vol. I. Gordon and Breach, Science Publisher, Inc.

Shai, I., and W. M. Rohsenow. 1969. "The Mechanism and Stability Criterion for Nucleate Boiling of Sodium." *Trans. ASME, Series C, Journal of Heat Transfer*. 91: 315.

Sandia National Laboratories

Albuquerque, New Mexico 87185

date: December 12, 1989

to: J. B. Moreno - 2542

from: J. A. VanDenAvyle - 1832, J. W. Munford - 1832, and J. J. Stephens - 1831

subject: Alloy Selection for a Solar Pool Boiler

Summary

This memo reports on an evaluation of alloys to replace 316 stainless steel for construction of a solar heated molten sodium boiler for extented operation at 800°C. The recommended alloy is Haynes Alloy 230, which has superior oxidation resistance, metallurgical stability, and elevated temperature mechanical properties. Staff who contributed to this selection include Jon Munford, 1832, John Stephens, 1831, Maury Karnowsky, 1831, and Mike Cieslak, 1833.

Evaluation

The primary design requirements of the boiler include 60,000 hr. life at an average operating temperature of 800°C with exposure to air, liquid Na or NaK, and possibly flue gas. The specified worst case design stress is 10 ksi. These requirements, combined with the expected fluctuating temperature profile, impose substantial requirements for the selected structural alloy. Fabrication of the structure is by hydroforming to a hemispherical dome shape with both autogenous and filler metal welds. Small diameter tubular product is also used; the tubes are welded to the main boiler structure.

Several alloys were investigated and rated using the prioritized attributes you listed in a memo to us dated 11/6/89. Three alloys were selected as the best of their representative class and rated relative to 316L stainless steel (Table 1). Inconel 600 is a simple solid solution strengthened alloy with better oxidation resistance and thermal stability than 316L, but still with relatively poor creep and fatigue properties. Inconel 617 has better oxidation resistance, high temperature stability, and creep resistance, but its large grain size makes it more susceptible to fatigue cracking. In 617 is also difficult to cold form due to its very high work hardening rate.

Haynes Alloy 230 is the alloy we recommend for this application. It is a relatively new alloy which was developed for extended air exposure up to 1150°C. According to Bob Herchenroeder, the Haynes representative we met with, this alloy is readily available in standard sheet thicknesses. A reference

price is $17/lb in quantities over 1000 lb.; cost per pound could double for small purchases.

The rankings in Table 1 show Haynes 230 has the best thermal stability, oxidation resistance, and mechanical properties at high temperature. It has an extremely stable microstructure which is solid solution strengthened, with a relatively small grain size that is stabilized by carbides (small grains are favorable for fatigue). Haynes 230 has short time stress rupture properties at 816 °C which are similar to several other Ni-based superalloys (Figure 1). Extrapolated rupture times for creep tests at 10 ksi and 760°C are in excess of 200,000 hr. The alloy contains a small amount of Al (0.3%) which is incorporated into a very protective oxide layer which forms during high temperature exposure. This stable oxide would likely make sintering more difficult if it is not properly removed, although we have no specific data on this. **We suggest a few simple vacuum furnace experiments to evaluate sintering properties (as well as brazing behavior).**

The thermal conductivity of Haynes 230 is 24.4 W/m-°C, which is average for high temperature alloys. It has a relatively low coefficient of thermal expansion -- 15.2 μm/m-°C over the range 25-800°C; this should improve thermal fatigue resistance since smaller strains would be generated by thermal fluctuations. Emissivity of the alloy has not been determined, and we recently supplied you with a sample for measurements.

Fabrication of the boiler will require more care using Haynes 230 compared to 316L stainless steel. **The alloy should hydroform like 316L.** Weldability should not be a problem for fabrication of the thin wall boiler structure, but specified welding procedures must be followed; these are routine for most high temperature superalloys. Weld hot cracking can be a problem in section thicknesses greater than 0.5 in. Low boron filler wire is recommended to minimize this concern. Overall the welding will require more process specification and control.

Tube product availability for Haynes 230 is currently limited to only 0.5 in. diameter. If smaller sizes are required, we suggest substituting Haynes Alloy 214 tubing which is available in Schedule 40 sizes ranging from 0.25 - 4.0 in. This alloy also has excellent high temperature properties up to 800 °C and is weldable to Haynes 230 using 230 filler wire.

We have been unable to find specific data covering these alloys in Na or NaK for temperatures around 800°C. This included a rather extensive computerized literature search. Embrittlement of these types of alloys by molten Na has not been observed, and the major problem seen in circulating Na systems has been dissolution and transport of alloying elements from hot to cold regions. Binary phase diagrams for the alloys' major alloying constituents in Na at 800°C show limited solubilities in cases where data are available. The current design of your boiler should minimize dissolution and transport of alloying elements: the pool temperature is relatively uniform, and liquid Na does not circulate from hot to cool regions as in heat pipes or Na-cooled reactors, so once the concentrations of alloying elements reach equilbrium values in the Na, dissolution should cease. **Coupon testing of candidate alloys in 800°C molten Na should be conducted** to confirm this opinion.

Comments:

Among a large number of alloys investigated, the recommended alloy Haynes 230 has the greatest probability to withstand your demanding service conditions. Some information is still incomplete, particularly emissivity values and long term compatibility with molten sodium, but we do not have strong concerns about these. Fabrication of the boiler will not be as easy or as cheap as with 316L stainless steel but still should fall within your cost goals.

copy to:

1800 - R. J. Eagan
1830 - M. J. Davis
1831 - A. D. Romig
1831 - M. M. Karnowsky
1831 - J. J. Stephens
1832 - W. B. Jones
1832 - J. W. Munford
1832 - J. A. VanDenAvyle
1833 - J. L. Jellison
1833 - M. J. Cieslak
1832 - File

Table 1. Alloy Rankings for Extended Service at 800°C

	Alloy			
Material Attributes	In 600[a]	In 617[a]	Haynes 230	316L
1.Thermal stability	3	2	1	4
2.Air-side corrosion	3	2	1	4
3.Na and NaK compatible	All probably ok, but unable to rank.			
4.Sintering compatibility	3	3	4	3
5.Emissivity, oxidized	?	?	(b)	1
6.Weldability	3	3	4	1
7.Formability	1	4	2	1
8.Fatigue life	4	3	1	4
9.Creep life	4	1	1	4
10.Cost	2	3	4	1
11.Flue-gas compatibility	3	2	1	4

1 = Best; 4 = Worst
(a) - solutionized, large grain condition for optimum creep and stress rupture resistance
(b) - currently being measured

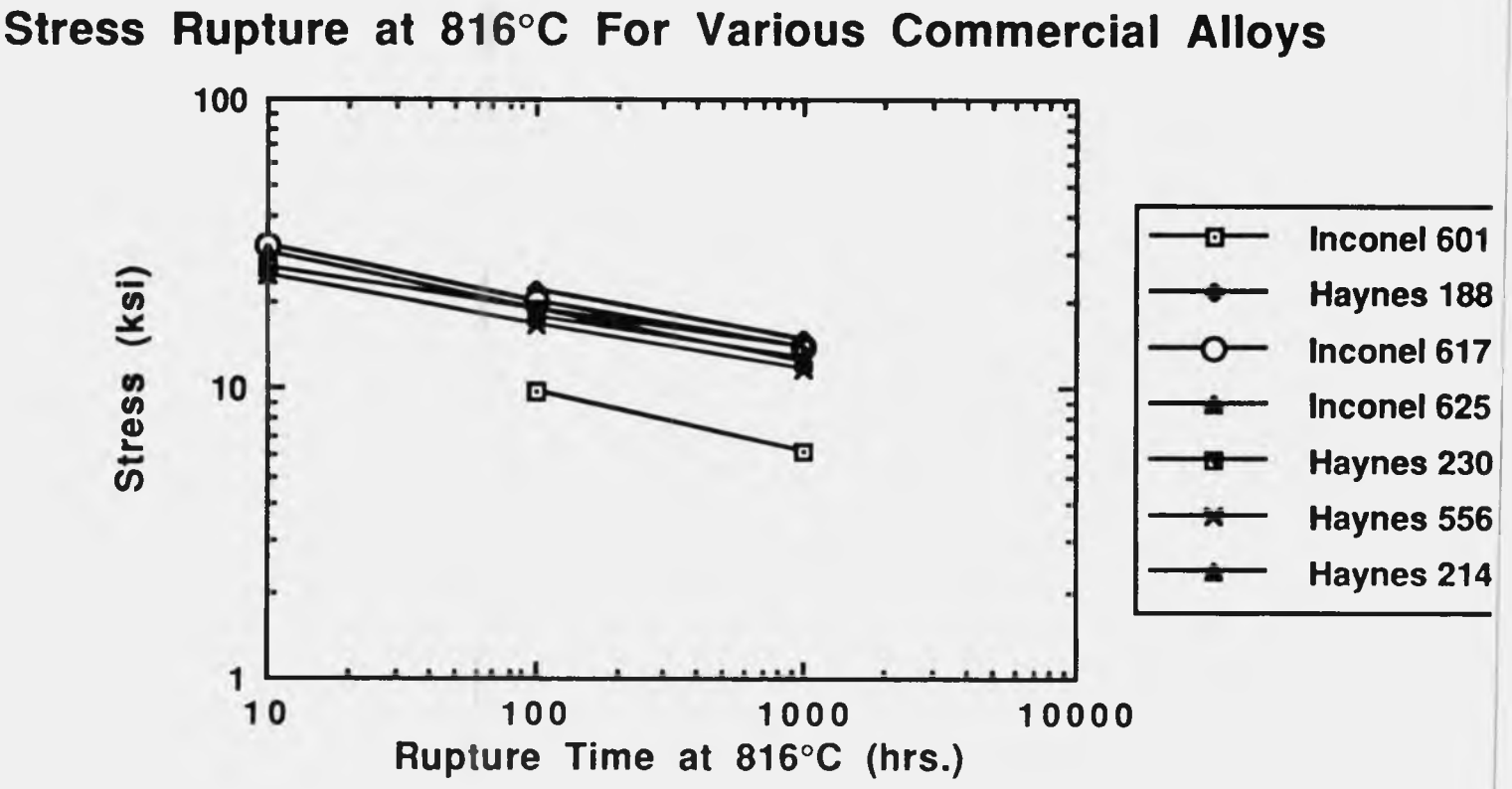

Figure 1. Short time stress rupture properties at 816°C for several commercial alloys

Sandia National Laboratories

date: June 28, 1990

Albuquerque, New Mexico 87185

to: Distribution

Timothy A. Moss

from: T.A. Moss, 6217

subject: Sintering tests of In 600 powder on Haynes-230 alloy

Haynes 230 was selected as the material of choice for long term testing of a sodium, or NaK, pool boiler at 800°C (memo written by J.A. VanDenAvyle et. al. on Dec. 12, 1989). Na and NaK, however, have unstable boiling characteristics. One potential method to stabilize the boiling, identified by Thermacore, is to add a layer of sintered powder metal on the inside surface of the receiver. To be assured that the sintered powder will remain intact and on the surface during use the minimum bond strength needed was determined to be 1,000 PSI. This was based on the differences of thermal coefficient of expansion and the pressures the sintered particles experience from the expanding bubbles during boiling.

Tests were conducted to determine the bonding strength of Inconel 600 powder (-100, +140 mesh) sintered to 0.047" thick sheet of Haynes 230. No plating or brazing were used in these tests. Dots of In 600 powder, 15/16" diameter and 0.027" to 0.033" thick, were sandwiched between two pieces of Haynes 230. Using Incuro 600, an organic cement, as a binder to hold the powder together, varying weights were placed on the sandwiches and then sintered. The sintering was done in a hydrogen furnace at 1150°C for 2 hours.

The table below lists the various weights used and the force needed to pull apart the two plates held together by the sintered powder. The test with 13 lbs. of weight exceeded the limit of the load cell of 500 kg. Using the lower limit of 1,000 PSI, the minimum acceptable force to pull the two plates apart is 314 kg. As the table shows, 9 lbs. is the minimum weight that can be used to meet the required adhesion.

Weight placed on top (lbs.)	Force needed to pull plates apart (kg)
5	252
9	375, 315
13	> 500
19	455

One test with a 19 lb. weight was run using the vacuum furnace, instead of the hydrogen furnace, with all the other parameters remaining the same. The plates pulled apart at a force of 295 kg, just below the minimum of 314 kg.

Sectioning indicated that adding weights does affect the porosity of the sintered powder but should not affect its ability to stabilize boiling. Increasing the weight, however, increased the number of smaller sized pores and decreased the number of larger sized pores. It is believed that the larger size pores provide the necessary boiling sites to stabilize boiling. Suitable pore sizes should be about 0.004" in diameter and 0.015" deep. In theory, only one boiling site is needed to stabilize boiling and even the test with the highest weight had suitable pore sizes.

Distribution:

1513 D.R. Adkins
2542 J.B. Moreno
6217 C.E. Andraka
6217 R.B. Diver
6217 P.C. Klimas
6217 T.A. Moss
7471 E. Roherty-Osmun

Sandia National Laboratories

date: October 8, 1990

Albuquerque, New Mexico 87185

to: Distribution

T. A. Moss

from: T.A. Moss, 6217

subject: Sintering Tests of 304L Stainless Steel Powder On Haynes 230 Alloy

Haynes 230 was selected as the material of choice for long-term operation of a sodium, or NaK, pool boiler between 700 to 800°C (memo written by J.A. VanDenAvyle et. al. on Dec. 12, 1989). Na and NaK, however, have unstable boiling characteristics. One method to stabilize boiling, identified by Thermacore, is to sinter a layer of powdered metal on the wetted heated surface of the receiver. To assure that the sintered powder will remain intact and attached to the surface during use, the minimum bond strength was determined to be 3,700 PSI. This was based on the estimated stresses caused by the differences in the thermal expansion coefficient between the powdered metal and the substrate.

Tests were conducted to determine the bonding strength of 304L SS powder (-100, +140 mesh) sintered to 0.047" thick sheets of Haynes 230. The 304L SS will not sinter to the Haynes 230 unless a thin layer of Ni, 0.0004" thick, is electroless plated onto the Haynes 230. The plating solution contained Boron at 1% or less, by weight. Dots of 304L SS powder, 1/4" and 1/2" diameter, and 0.027" to 0.033" thick, were sandwiched between two pieces of electroless Ni plated Haynes 230. Using Incuro 600, an organic cement, as a binder to hold the powder together, various weights were put on the sandwiches and then sintered in a hydrogen furnace at 1150°C for 2 hours.

The attached plot shows the relationship between the sintering forces and the pull forces used to separate the two plates. Using the lower limit of 3,700 PSI, the minimum acceptable sintering force is 25 PSI, or a 1.4 lb. weight on a 1/4" diameter dot.

Sectioning indicated that adding weight decreases the porosity of the sintered powder, but this should not affect its ability to stabilize boiling. Increasing the weight increased the number of smaller sized pores and decreased the number of larger sized pores. The larger size pores are about 0.004" wide and about 0.015" deep. It is believed that these pore sizes will provide the necessary boiling sites to stabilize boiling. In theory, only one boiling site is needed to stabilize boiling and even the test with the highest weight had pore sizes in the range of 0.004" wide and 0.015"deep.

Distribution:

1513 D.R. Adkins
2542 J.B. Moreno
6217 C.E. Andraka
6217 R.B. Diver
6217 P.C. Klimas
7471-2 C.A. Walker

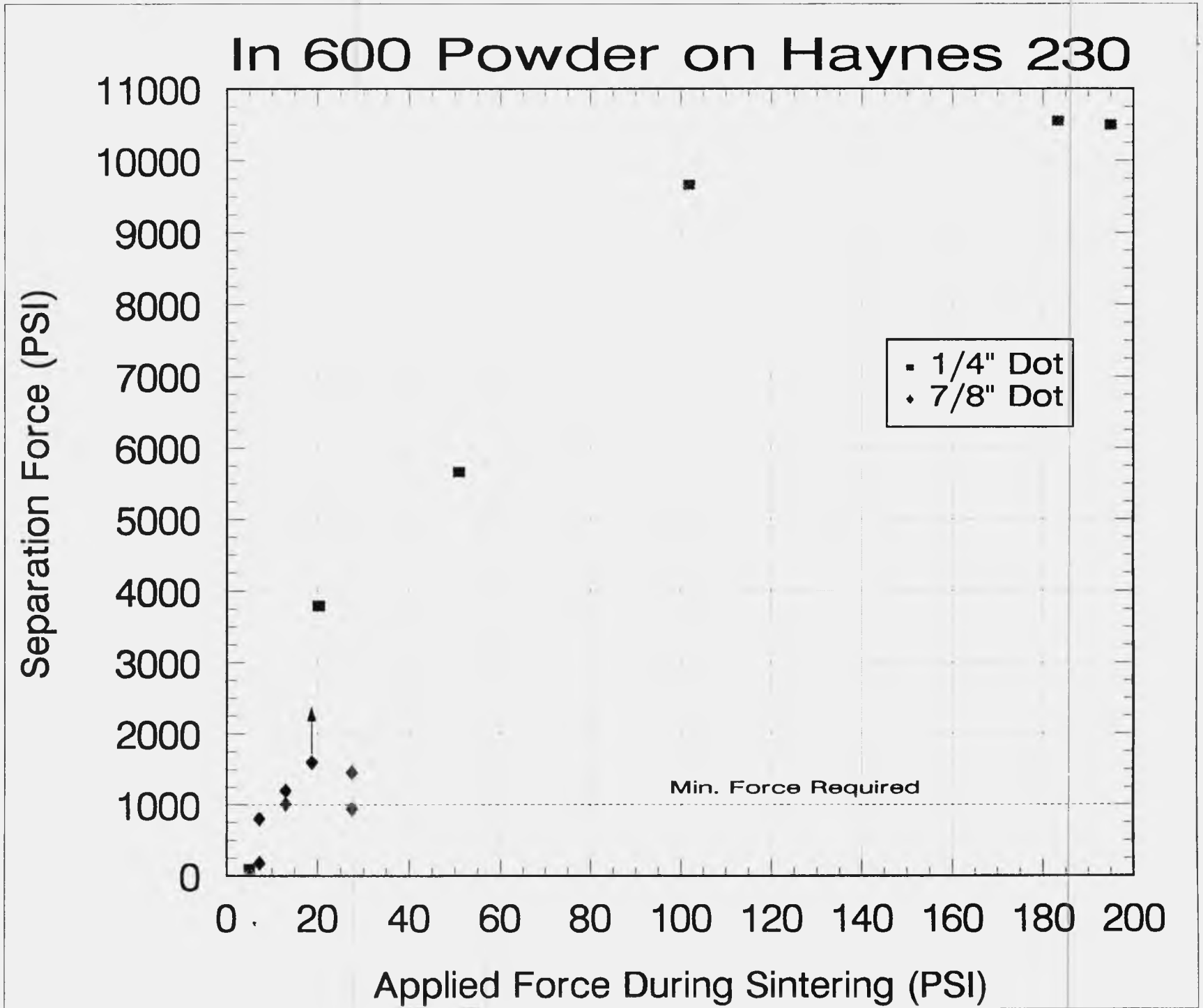
In 600 Powder on Haynes 230
Separation Force (PSI)
11000
10000
9000
8000
7000
6000
5000
4000
3000
2000
1000
0
0
20
40
60
80
100
120
140
160
180
200
Applied Force During Sintering (PSI)
1/4" Dot
7/8" Dot
Min. Force Required

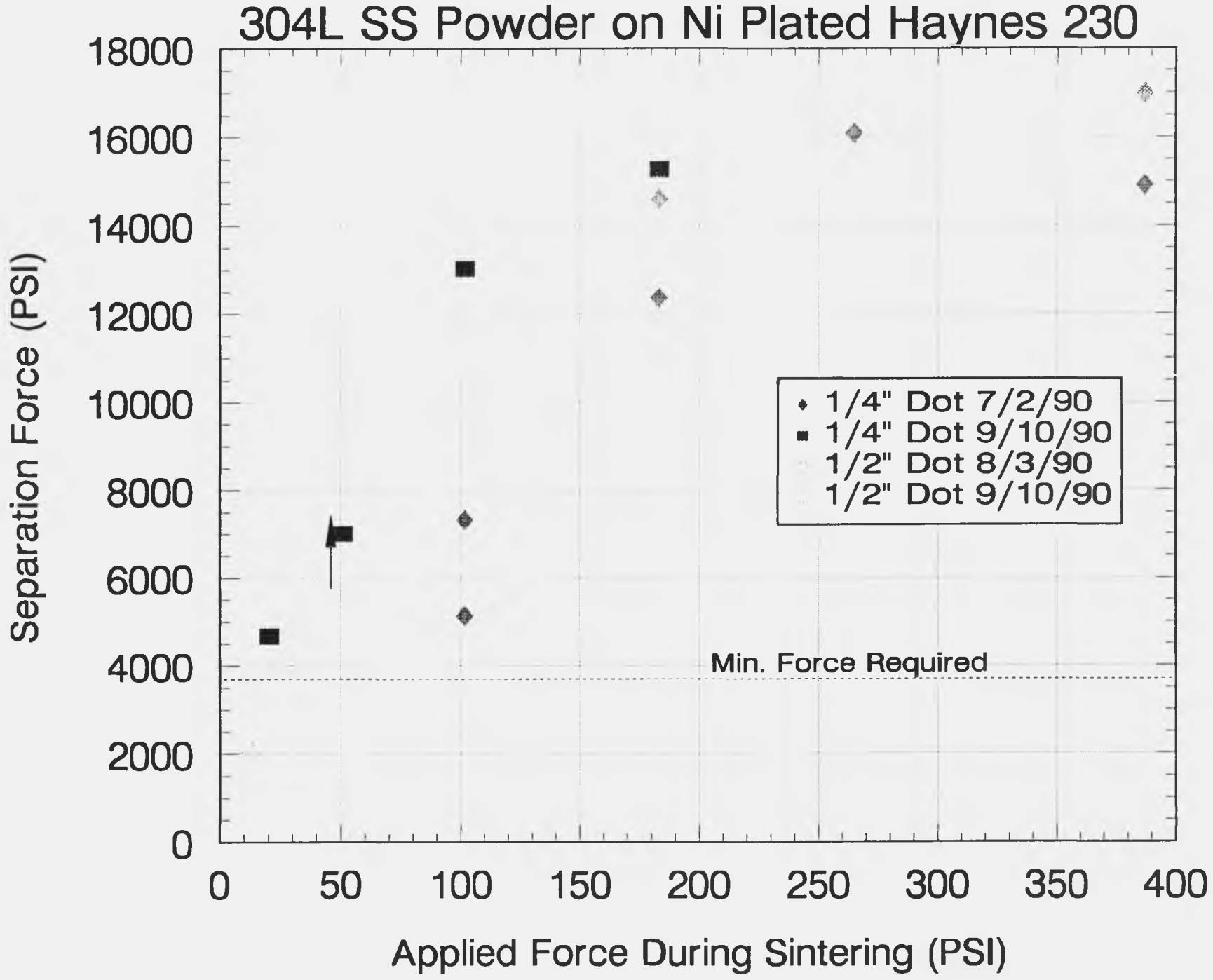
304L SS Powder on Ni Plated Haynes 230
Separation Force (PSI)
18000
16000
14000
12000
10000
8000
6000
4000
2000
0
0
50
100
150
200
250
300
350
400
Applied Force During Sintering (PSI)
1/4" Dot 7/2/90
1/4" Dot 9/10/90
1/2" Dot 8/3/90
1/2" Dot 9/10/90
Min. Force Required

Sandia National Laboratories
Albuquerque, New Mexico 87185

date: 9 February 1990

to: Tim Moss - 6217

Mike Cieslak

from: M. J. Cieslak - 1833

subject: Haynes 230/316 Stainless Steel Welds

Executive Summary: *Manual gas tungsten arc welds made between tubing of Haynes Alloy 230 and 316 stainless steel were crack free. I do not anticipate encountering problems welding this combination in real hardware. This work was done in support of the Heat Pipe Development Program for Tim Moss, Org. 6217, on case 2216.320.*

I recently examined manual gas tungsten arc (GTA) welds made between Haynes Alloy 230 and 316 stainless steel tubings in support of the Heat Pipe Development program. Representative sections are shown in Figs. 1 and 2. (Metallography was performed by A. C. Kilgo - 1822) No cracks were observed in any of the sections which I examined, indicating a relatively low restraint joint configuration. Some porosity was occasionally found. In addition, full penetration was not achieved along the entire circumference of the welds. As these welds were only practice to indicate proof of concept, the lack of full penetration should not be a concern. I fully anticipate that real hardware can be joined using the GTA process without requiring the use of filler metal. I would only suggest that an inert gas be used to backshield the weld and that some form of fixturing be used to align the parts during welding. I do not recommend that hand welding be performed.

copy to:

1800 - R. J. Eagan
1820 - J. B. Woodard
1822 - M. J. Carr
1822 - A. C. Kilgo
1830 - M. J. Davis
1833 - J. L. Jellison
1833 - M. J. Cieslak
1833 - File

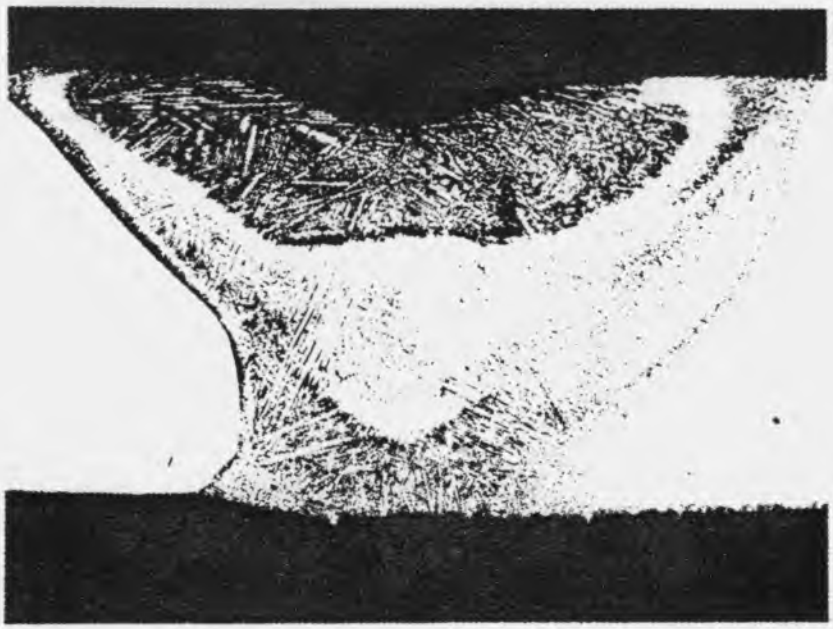

Fig. 1 Full Penetration Haynes 230/316 GTA weld. 40x magnification.

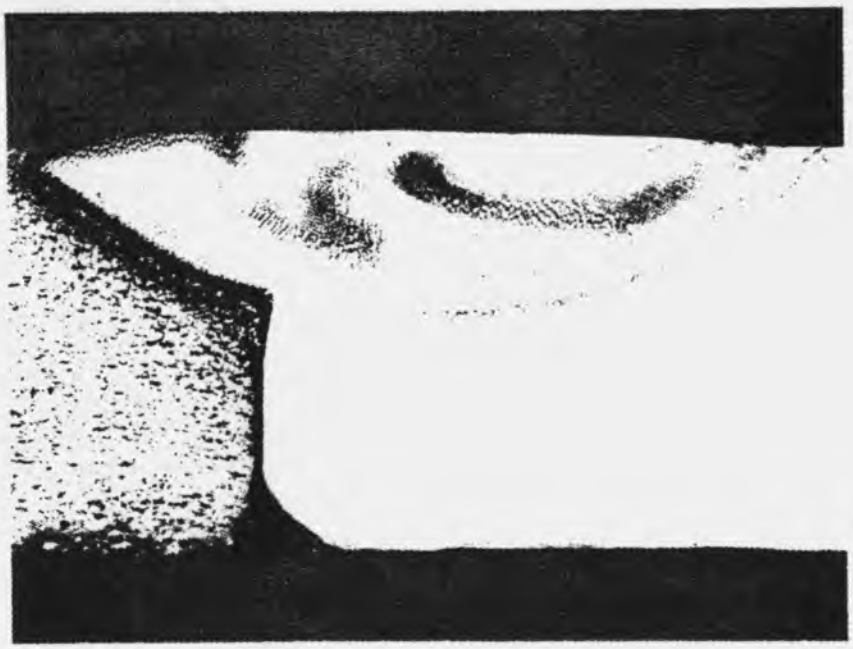

Fig. 2 Partial penetration Haynes 230/316 GTA weld. 40x magnification.

Sandia National Laboratories
Albuquerque, New Mexico 87185

date: April 12, 1990

to: Tim Moss, 6217

from: M. C. Maguire and M J. Cieslak, 1833

subject: Haynes 230/Inconel 600 Welds

Executive Summary: *Manual gas tungsten arc welds on Haynes Alloy 230 and Inconel 600 in a standing edge joint configuration were crack free. There were significant differences in penetration along the length of the weld due to difficulties in controlling heat input with manual welding. Although not a factor in the integrity of the joint, some regions of the weld overhang into a tube opening which could negatively influence the performance of the heat tube. This work was done for Tim Moss, Org. 6217, on case 2216.230.*

Several manual gas tungsen arc (GTA) welds were recently submitted for metallographic evaluation. The weld consisted of a standing edge joint between an Inconel 600 tube and a Haynes Alloy 230 disc. Representative cross sections of the weld joints are shown in Figs. 1 and 2 (metallography was performed by A.C. Kilgo, Org. 1822). The welds were found to be crack free with only minor observations of porosity. The depth of penetration varied somewhat along the length of the weld which would be expected with a manual GTA weld. In one case, shown in Fig. 3, the heat input was sufficient to cause the weld bead to partially collapse into the tupe opening. Depending on design intent, this additional constriction to the tube opening may be unacceptable. Since controlled heat input is difficult to regulate in a manual GTA weld, I would recommend that automatic GTA welding be used to remedy this problem. I would not recommend manual welding, even with an attempt at lower heat input. Automatic welding would eliminate the large variations in melting along the length of the circumferential weld, and eliminate the need for any post-weld machining.

copy to:

2542 - J. B. Moreno
1800 - R. J. Eagan
1820 - J. B. Woodard
1822 - A. C. Kilgo
1822 - M. J. Carr
1830 - M. J. Davis
1833 - J. L. Jellison
1833 - M. J. Cieslak
1833 - M. C. Maguire
1833 - File

Figure 1. Cross section of Haynes 230/Inconel 600 weld in standing edge configuration. 100X magnification.

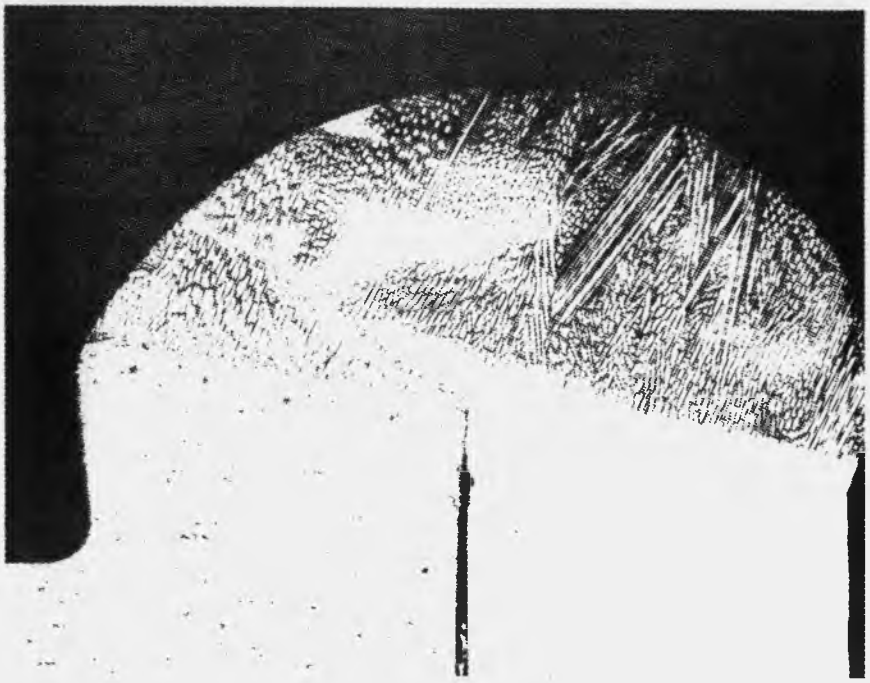

Figure 2. Cross section of Haynes 230/Inconel 600 weld in standing edge configuration. 100X magnification.

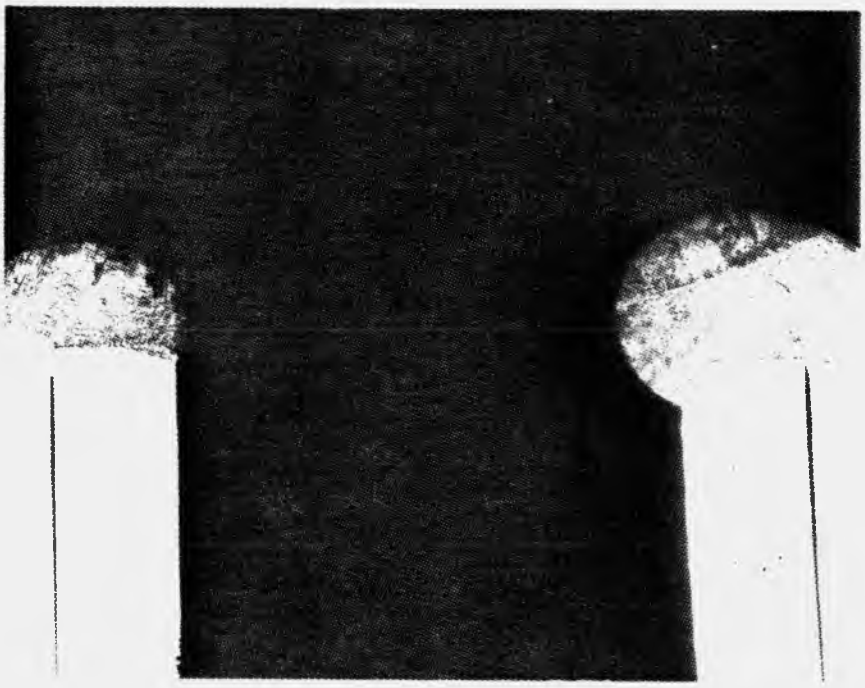

Figure 3. Cross section of Haynes Alloy 230/Inconel 625 weld showing collapse of weld into tube entry. 30X magnification.

Sandia National Laboratories
Albuquerque, New Mexico 87185

date: July 2, 1990

to: Tim Moss, 6217

from: M. C. Maguire, 1833

subject: Haynes 230 Welds

Executive Summary: *Manual gas tungsten arc welds on Haynes Alloy 230 with and without filler metal were crack free. Penetration varied from 0.018 to 0.025 in. along the length of the weld due to difficulties in controlling heat input with manual welding. This work was done for Tim Moss, Org. 6217, on case 2216.230.*

Several manual gas tungsen arc (GTA) welds were submitted for metallographic evaluation. Welds were made with a square corner groove configuration on Haynes Alloy 230. Welds with and without filler metal were evaluated. Representative cross sections of the weld joints are shown in Figs. 1 and 2 (metallography was performed by A.C. Kilgo, Org. 1822). The welds were found to be crack free with no indication of porosity. The depth of penetration varied somewhat along the length of the weld which would be expected with a manual GTA weld. Weld penetration varied from 0.018 to 0.025 in. and was not dependent on the addition of filler metal for the given welding parameters. If design constraints are satisfied for the minimum weld penetration observed, then this procedure should be satisfactory.

copy to:

2542 - J. B. Moreno
1800 - R. J. Eagan
1820 - J. B. Woodard
1822 - A. C. Kilgo
1822 - M. J. Carr
1830 - A. D. Romig, Jr.
1833 - J. L. Jellison
1833 - M. C. Maguire
1833 - File

Figure 1. Cross section of autogenous Haynes 230 corner groove weld (no filler metal). 32X magnification.

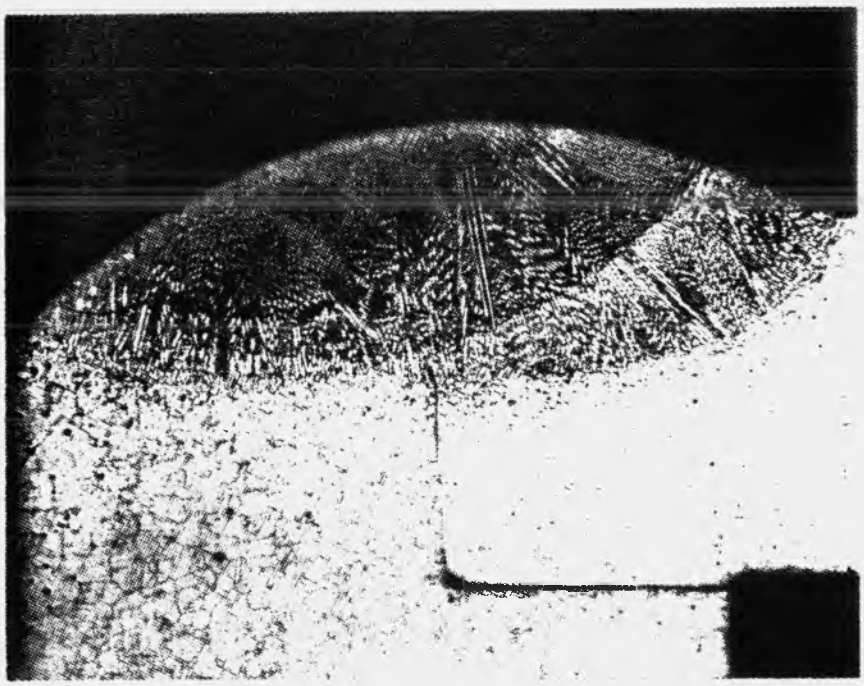

Figure 2. Cross section of Haynes 230 corner groove weld with filler metal. 32X magnification.

Sandia National Laboratories

Albuquerque, New Mexico 87185

date: February 8, 1990

to: DISTRIBUTION

from: J. B. Moreno, 2542, and C. E. Andraka, 6217

subject: Review of Sodium Pool Boiler Rim Design

Ref: Memo, J. T. Holmes, 6215, to J. B. Moreno, 2542, Dated 01/12/90, Subject: Sodium Component Design - A Rule of Thumb

At our 12/21/89 meeting on lifetime issues for the pool boiler receiver, we discussed what particular issues we should focus on. One issue identified was the current rim design. Particular concerns about the rim design were summarized in the reference memo and are re-capped here:

1. That corrosion and caustic cracking will be accelerated in the crevice because it traps impurities.

2. That the crevice would be difficult or impossible to clean in the event of a repair, aggravating the corrosion and cracking problem.

3. That the design is not amenable to non-destructive testing.

4. That the crevice is a stress riser.

Since the meeting, we have been trying to determine what is actually known in each of these areas.

In brief, we have found that:

1. Corrosion and cracking are probably avoidable if we continue to follow our current procedures.

2. Re-using parts with crevices that have seen sodium service is not recommended, and indeed we do not. Nor do we anticipate that this would be necessary with the present design.

3. The rim weld cannot be ultrasonically or radiographically inspected for ligament length. However, this may not be a requirement. Also, with a minor design change, either inspection could be done.

4. The crevice is not a stress riser in the present design; analysis has shown this to be one of the lowest-stress designs considered by us or the Advanced Stirling Conversion System contractors.

The rationale for each of these findings is presented in the attached appendix.

APPENDIX

Concerns 1 and 2

For the corrosion and cracking concerns, we enlisted the help of John Holmes to see if he could turn up any information in the literature or from his former associates in this area. He responded in the referenced memo which we summarize here:

1. No written reports on the subject were found.

2. John contacted Harvey Olson at Argonne West (Idaho Falls, ID), who has about 30 years experience with sodium component design. Harvey confirmed that crevices can be a source of problems.

John put us in touch with Harvey, who added the following information:

1. Harvey had two stories of crevice-associated problems. In the first, a pump-shaft housing removed from the French nuclear reactor Phoenix was steam cleaned. One bolted flange on the housing was not disassembled. This left sodium hydroxide trapped in the crevice between the mating flanges. The housing was put back in service. On the next disassembly, caustic stress corrosion cracking was found at the flange bolt holes. The second story involved a sodium storage tank associated with an American reactor. A piece of angle stock was welded to the inside surface. Again, cracking was found, but Harvey thought that the cause in this case was not clear, and could have been chloride stress corrosion cracking.

2. Although Harvey prefers butt welds to socket welds, sometimes the latter are unavoidable and he does use them in sodium service. A major advantage of butt welds is easier inspection. However, he said that he knew of no cases of socket weld failures.

3. Harvey felt that we could work around our design. We must recognize however that there may be some added risk. With crevices, attention must be paid to cleanliness. He recommended a vacuum bakeout after assembly, and to not attempt to clean and re-use parts containing crevices.

This information, while cautionary, does not rule out the current rim design. All of Harvey's recommendations regarding cleanliness are already part of our practices. We have included them in our manufacturing analysis as well.

With regard to repairs, we expect that repairs, if any, would involve draining the receiver and cutting off and discarding the absorber dome. This would eliminate the crevice and permit cleaning and repairing the rest of the unit.

The reference memo makes another point worth considering both for the receiver and the STM heat pipes: oxides and hydrides migrate to the coldest part of a system if their concentration is high enough. This can lead to local corrosion. In the case of the receiver, oxides and hydrides will be cold trapped by the pinched-off fill tube, and can be hot trapped by getters. Both are proven techniques that should keep these impurity levels low in the sodium pool and prevent concentration at vulnerable points such as the rim.

One last point with regard to concerns 1 and 2: it should be kept in mind that our long-term tests are being designed precisely for situations such as this, where definitive answers are not available. Finally, we want to thank John Holmes for his interest in our project and for his help with this section.

Concern # 3

The concern here is that there might not be a practical way to adequately inspect the rim weld. We have consulted with John Gieske (7552) and Dick Sager (7473) on this question. They confirmed that neither x-rays nor ultrasonics would be appropriate because of the geometry (assuming that the object of the inspection is to determine the weld ligament length). However, by sizing the absorber slightly smaller, the edge weld can be replaced by a fillet weld (Figure 1), which could then be inspected by either technique.

Dick also felt that 100% inspection might not be mandatory. The requirement will depend on many factors, including the insurance industry, site location, on-site personnel risk, design factor of safety, and other quality assurance that is done. Dick points out that common compressed-air tanks (ASME code vessels) made with a large circumferential weld are hydrostatically tested and receive only a visual inspection of the weld.

If we should decide to re-design the rim, Dick has many ideas on practical and economical alternatives, and should be consulted.

Concern # 4

The question here is whether the present design should be avoided because the crevice is a stress riser. It is true that crevices can be stress risers in typical tensile-load situations. However, the primary loading on the reflux receiver during steady-state operation is a result of the partial vacuum within, so that the rear dome and absorber dome are pressed together. This produces a shear stress at the rim. If the two domes are not hemispheres, the shear stress is accompanied by a slight bending moment.

Since the domes are axisymmetric, any bending caused by the shear stress is constrained by the hoop, and results in a compressive hoop stress at the joint. There is no tensile force applied across the weld and crevice.

A number of edge weld designs have been considered, both at Sandia during the design phase and again through the ASCS contracts [1,2,3]. Some designs that eliminated the crevice were investigated. Figure 2 shows why the bending moment caused by shear stress will increase when the current design is replaced by a typical convoluted design having butt welds. As the illustration suggests and our analysis confirms, the bending moment is orders of magnitude larger for the convoluted design, causing extremely high hoop and bending stresses in the rim region. For the designs that we have seen, these stresses proved to be higher than published creep limits in the analysis, and in some cases were higher than yield strength [4]. While there may be a design that eliminates the crevice and at the same time has acceptable stresses, we have not identified any stress-related issue that would compel us to continue to seek it out.

References:

1. STC draft final report.

2. "Pool Boiler Heat Transport System for Advanced Stirling Conversion System," Solar Stirling Heat Transport system Workshop, Lancaster Pa., September 27-28, 1989.

3. Discussions at Materials meeting, December 21,1989.

4. "Heat Pipe Heat Transport System for a 25 kW$_e$ Advanced Stirling Conversion System," Solar Stirling Heat Transport system Workshop, Lancaster Pa., September 27-28, 1989.

DISTRIBUTION:

1513 D. R. Adkins
1521 C. M. Stone
1832 W. B. Jones
1832 J. A. Van Den Avyle
1833 M. J. Cieslak
2542 S. B. Martin (Acting)
6210 B. W. Marshall
6215 J. T. Holmes
6215 K. S. Rawlinson
6217 C. E. Andraka
6217 R. B. Diver
6217 P. C. Klimas
6217 K. L. Linker
6217 T. A. Moss

Figure 1. Illustration of slight change needed to make the rim weld inspectable (compare with Figure 2 "Current Rim Design").

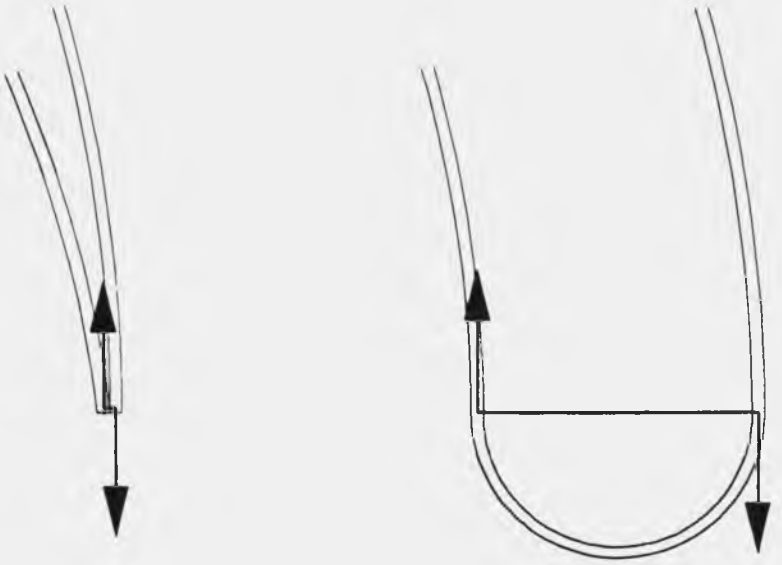

Current Rim Design Convoluted Edge Weld Design

Figure 2. Comparison of shear bending moments in several rim weld designs.

Sandia National Laboratories

Albuquerque, New Mexico 87185

date September 19, 1990

to T. A. Moss, 6217

from H. C. Peebles and N. A. Creager, 1831

subject Production of Vapor Generation Sites for the Bench Test Pool Boiler

Executive Summary

At the request of Org. 6217, methodology was developed for the formation of very small diameter blind holes in the interior wall of 1.75 inch diameter tubing using a pulsed Nd:YAG laser. This tubing will be used as a bench test pool boiler in the Solar Thermal Receiver Development Program. The purpose of the holes is to act as vapor generation sites to prevent superheating of the heat transfer fluid in the boiler. Org. 6217 requested that a single 0.005 ± 0.001 inch diameter hole, 0.018 ± 0.002 inches in depth, be place in a 3 foot section of Haynes 230 alloy tubing. We were able to deliver a conical shaped hole 0.017 inches deep with a throat diameter of 0.008 inches. The hole diameter is 0.002 inches larger than specifications. However, Org. 6217 found these results satisfactory for test purposes.

At the request of Org. 6217, we have developed methodology for the formation of very small diameter blind holes in the interior wall of 1.75 inch diameter Haynes 230 alloy tubing using a pulsed Nd:YAG laser. A 3 foot section of this tubing will be used as a bench test pool boiler in the Solar Thermal Receiver Development Program. The purpose of the holes is to act as vapor generation sites to prevent superheating of the heat transfer fluid in the boiler. Org. 6217 requested that a single 0.005 ± 0.001 inch diameter hole, 0.018 ± 0.002 inches in depth, be placed on the inside wall of the tubing. The wall thickness of the tubing is 0.050 inches. Holes of this dimension are extremely difficult and costly to produce in Haynes 230 alloy by mechanical methods. However, the holes can be economically produced using focused laser radiation. This memo presents details of the methodology used to place a single laser drilled hole in the bench test pool boiler provided by Org. 6217. The results of destructive and non-destructive characterization of test holes drilled in Haynes 230 alloy test coupons are also presented.

A schematic diagram of the laser optical system used for drilling operations on the Haynes 230 tubing is shown in figure 1. A 1.00 inch by 1.19 inch rectangular access hole was cut in the side of the tube by Org. 6217 to allow optical access to the inside wall of the tube. The laser beam was focused through the geometric center of the access hole onto the back wall of the tubing with the optical axis of the beam normal to the tube surface. The focusing lens was a 2 inch diameter fused silica lens with a focal length of 100 mm at 500 nm wavelength. The Nd:YAG laser was a Quanta-Ray Model DCR-2A with an output wavelength of 1.064 μm, a beam diameter of 7 mm ($1/e^2$) and a divergence of 0.5 mrad. A typical laser pulse profile is shown in figure 2. The profile is composed of a series of oscillator spikes nominally 800 nsec wide at full width half maximum intensity. The intensity of individual spikes in the pulse is highly variable from pulse to pulse, however, the overall temporial profile remains essentially the same. The total width of the pulse profile is nominally 160 μsec. The total pulse energy of the

laser has a shot to shot reproducibility of ± 0.7 %. A limiting aperture, centered on the optical axis of the laser beam, was placed in the Nd:YAG beam to reduce the beam diameter. This limiting aperture provided a small degree of independent control of hole diameter relative to hole depth. A small diameter (0.6 mm) He-Ne laser beam was passed through the back of the dichroic mirror shown in the figure and aligned coaxial with the Nd:YAG laser beam to aid in the positioning of the invisible Nd:YAG beam. Laser pulse energies were measured with a Scientech Model 380101 calorimeter (Boulder, Co.) and represent the actual laser energy incident on the metal surface.

For the hole geometry requirements stated above, the best conditions for reproducible hole formation corresponded to a single pulse of laser radiation in the range of 140 to 200 mJ. A limiting aperture diameter of 5.5 mm was employed. The focal position of the laser beam was placed as close as possible to the geometric plane defined by the surface of the tubing wall. This was accomplished by Q-switching the laser and centering the air breakdown spark formed at threshold pulse energy on the surface plane of the part. The tolerance in placement of the beam focal position using this method is roughly ± 0.2 mm. To a rough approximation, hole diameter and depth vary in direct proportion to the laser pulse energy. The selected drilling parameters yielded an aspect ratio for the hole (defined as depth/throat diameter) in the range of 2.2 to 2.7. An aspect ratio of 3.6, which corresponds to the requirements stated above, could not be achieved reproducibly using this laser system. Following consultations, Org. 6217 decided to accept a deviation in hole diameter provided the hole depth was within tolerance.

The holes produced by laser drilling were characterized by one of two methods. Most holes were cross sectioned with a diamond saw. The holes were lightly polished and examined with either a light microscope or scanning electron microscope. Results for a typical hole formed with a 200 mJ laser pulse are shown in figure 3. The hole profile is conical in shape with a depth of 0.0145 inches and a throat diameter of 0.0058 inches. Ejection of the laser melted material from this hole is very good. In some cases, melt metal may collect at the throat of the hole resulting in partial or complete blockage of the hole. An example is shown in figure 4. Incomplete clearing of melt metal from the hole is a phenomena whose frequency has a strong dependence on laser pulse energy and beam diameter. Using the conditions chosen for drilling in the bench test pool boiler, partial blockage was rarely observed, and complete blockage was never observed.

Whenever the optical system in figure 1 was broken down and subsequently reconstructed, the resulting hole diameters and depths as a function of laser pulse energy and limiting aperture diameter could vary by as much as 50 % in extreme cases. The reason for this variance is not well understood. It appears to be related to the positioning of the lens in the optical system as opposed to differences in target material properties or laser performance. As a result of this variance, every set-up of the optical system required detailed calibration of drilling parameters to obtain the desired hole geometry. However, for a given set-up the reproducibility of the drilling process is very good. An example is shown in table 1 for a series of 6 laser shots formed with a pulse energy of 153 mJ. The average hole depth for this series of test holes is 0.018 inches with an uncertainty of ± 0.001 inches. The average hole diameter is 0.0073 inches with an uncertainty of ± 0.0004 inches.

A non-destructive technique was developed by S. G. Giron, 7485, to characterize the depth of the hole drilled in the bench test pool boiler. In this technique, the depth of the hole is measured by alternately focusing an optical microscope at the bottom of the hole and at the surface of the part at high magnification. The difference in vertical position of the microscope objective, as measured by a micrometer on the vertical stage of the microscope, gives the depth of the hole. The accuracy of this optical technique relative to cross sectional measurements for the series of holes is shown in table 2. The results are in agreement to within ± 0.002 inches

The hole in the bench test pool boiler was drilled using a laser pulse energy of 139 mJ and a limiting aperture diameter of 5.5 mm. Using the optical microscope, the hole depth was measured to be 0.017 inches and the diameter at the throat of the hole was estimated to be 0.008 inches based on a top view of the hole. The hole depth is within the original specifications (0.018 ± 0.002 inches). The hole diameter exceeds the specified tolerance (0.005 ± 0.001 inches) by 0.002 inches.

HCP:1831:hcp

copy to:

1800	R. J. Eagan
1830	A. D. Romig, Jr.
1831	M. J. Cieslak
2542	J. B. Moreno
6217	P. C. Kimas
6217	C. E. Andraka
6217	R. B. Diver
7485-3	S. G. Giron
1831	File

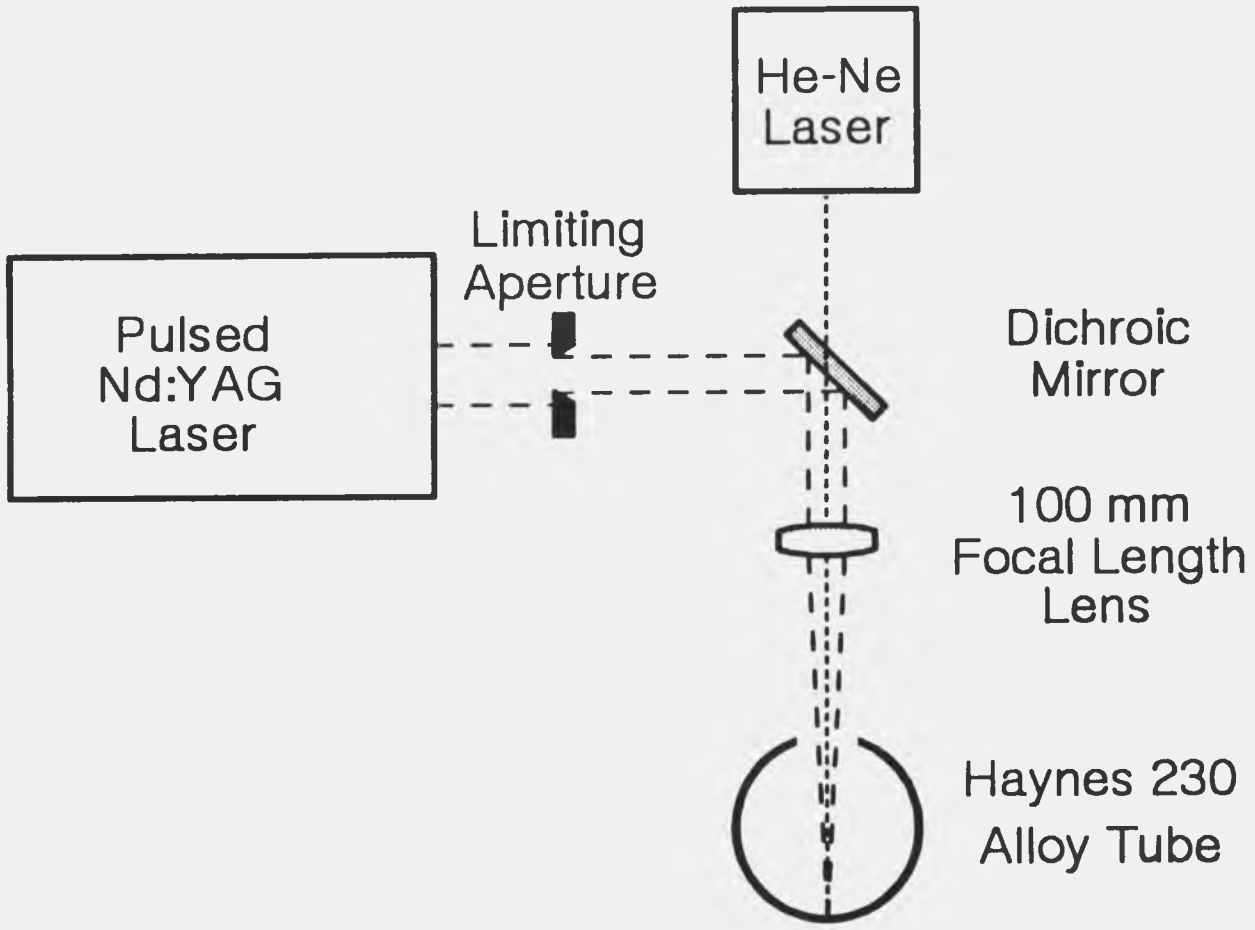

Figure 1: Schematic diagram of laser optical system used for drilling operations on the bench test pool boiler.

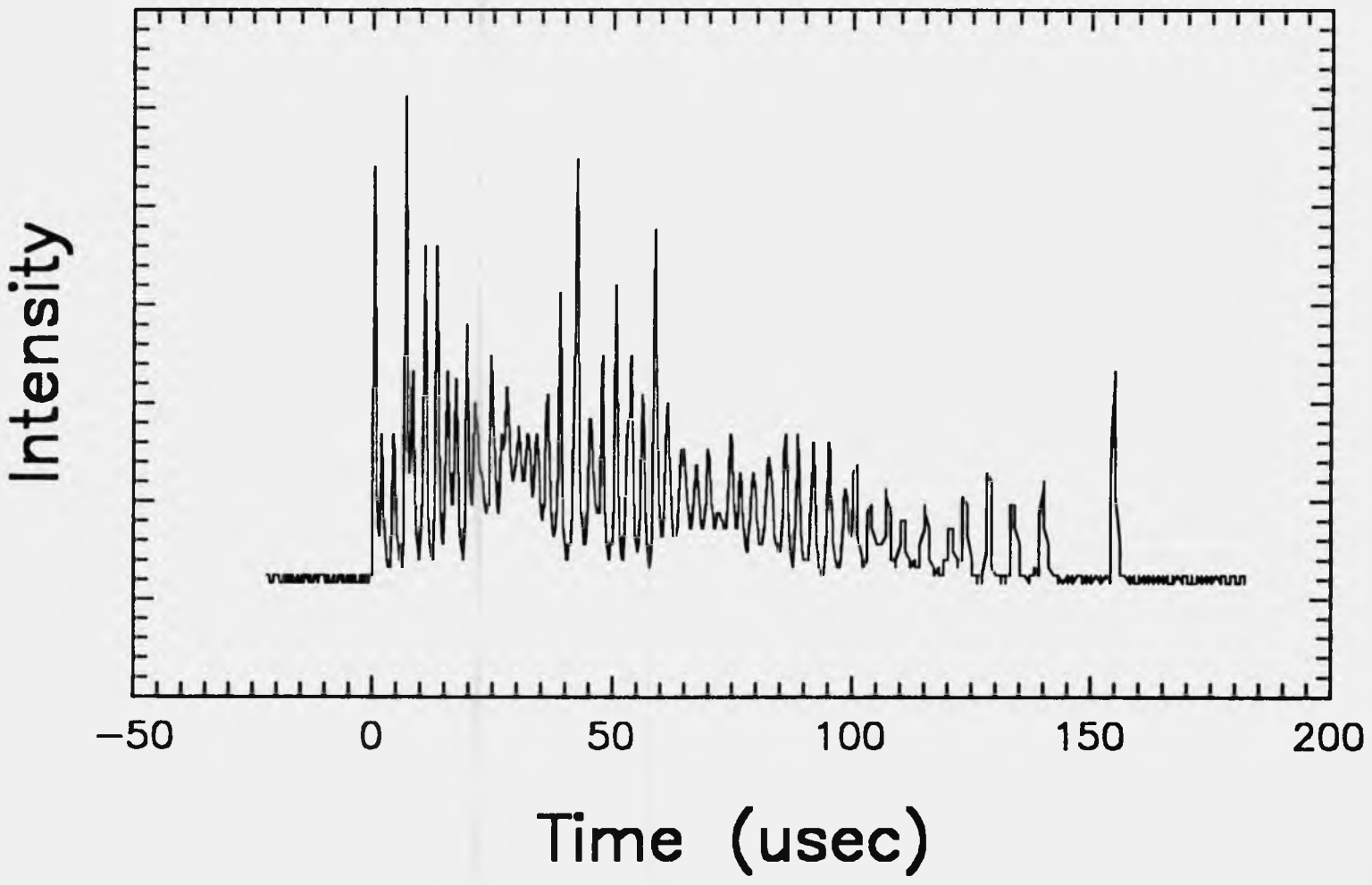

Figure 2. **Nd:YAG laser pulse profile for a 120 mJ pulse.**

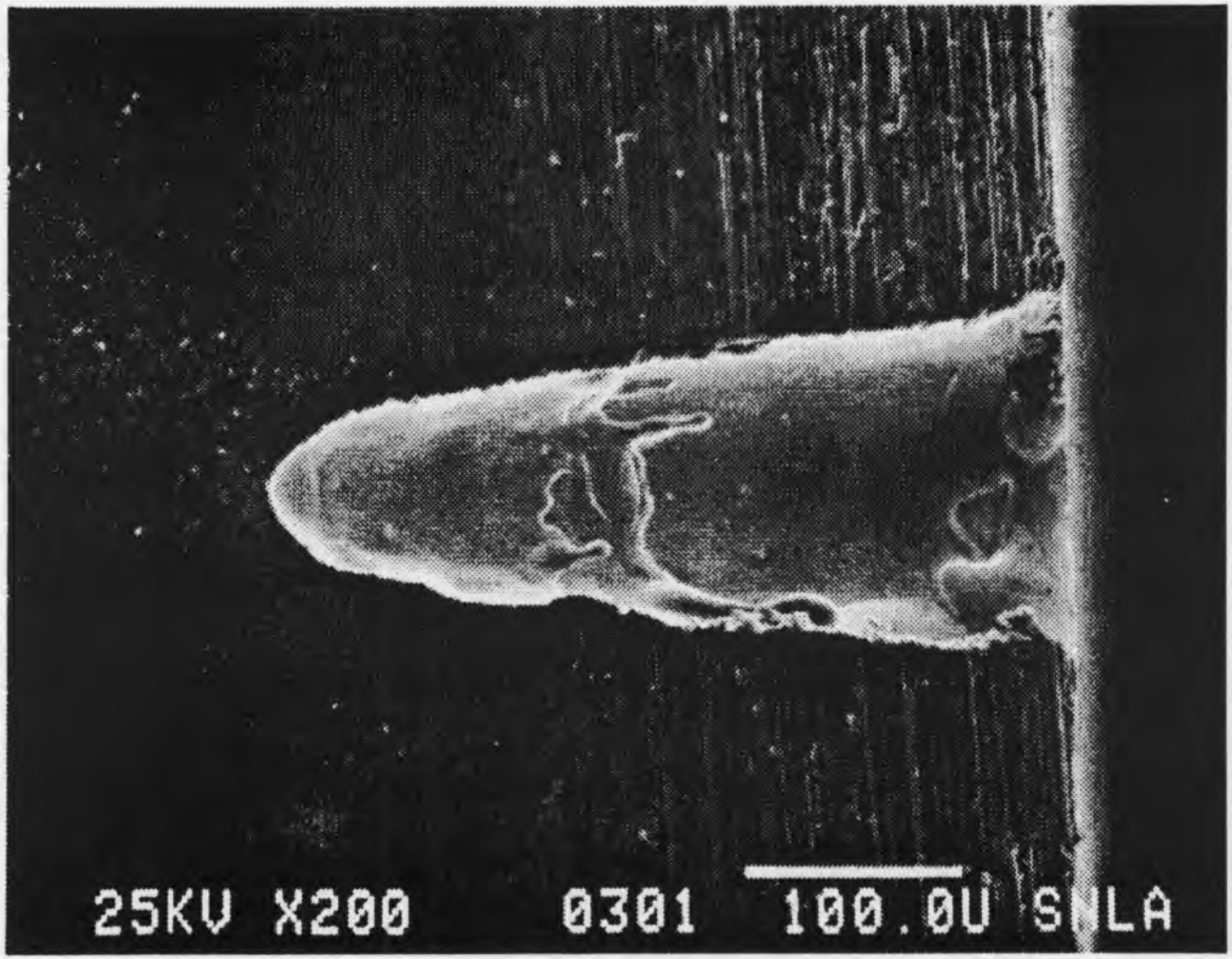

Figure 3. Electron Micrograph of a typical hole cross section. The hole was formed with a single 200 mJ laser pulse.

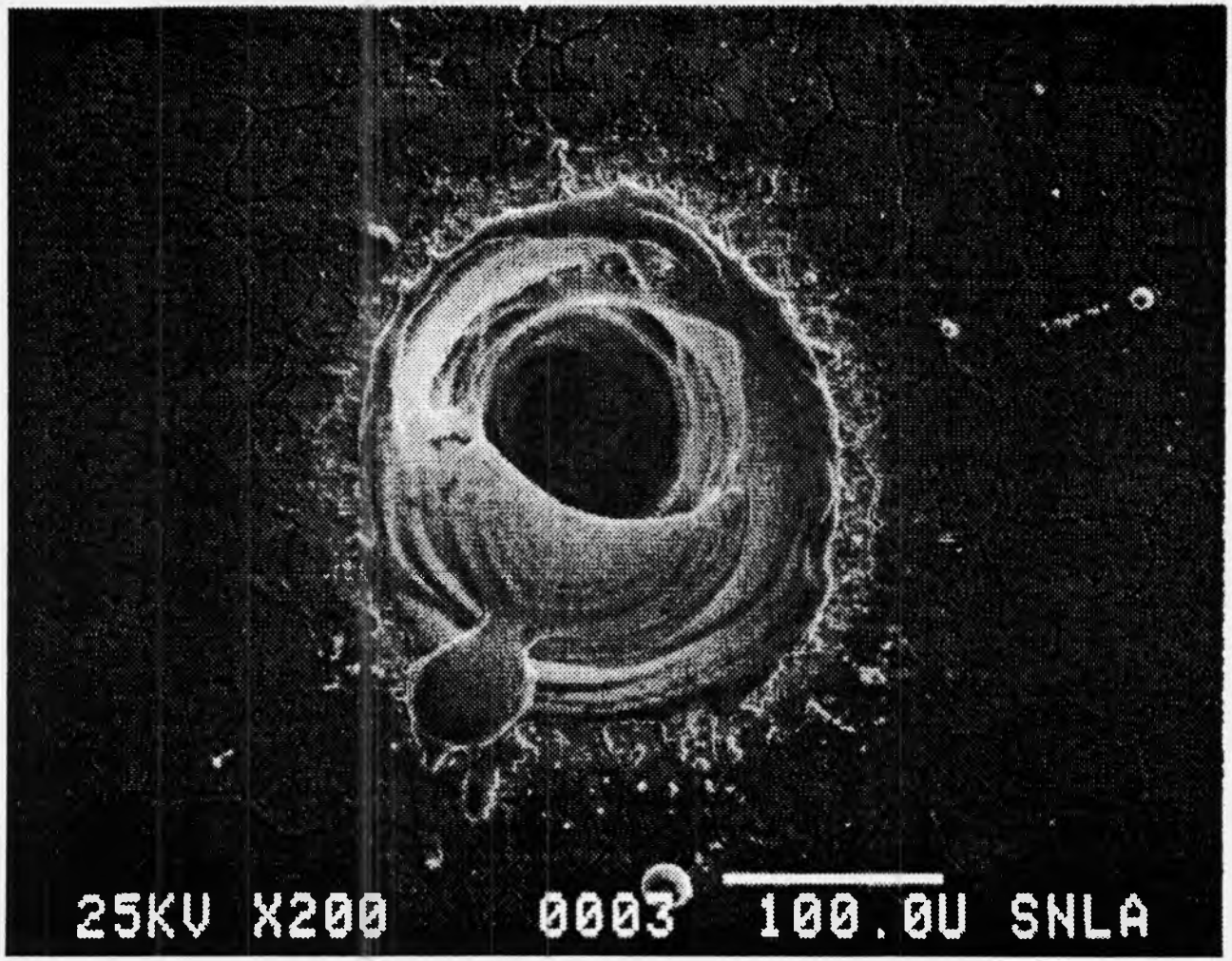

Figure 4. Top view of a laser drilled hole partially blocked by melt metal at the throat of the hole.

Table 1

Variability in Hole Geometry For a Laser Pulse Energy of 153 mJ

Hole Number	Hole Depth (inches)	Hole Diameter (inches)
1	0.0165	0.0076
2	0.0177	0.0069
3	0.0170	0.0075
4	0.0181	0.0076
5	0.0182	0.0074
6	0.0185	0.0069

Table 2

Comparison of Optical Depth Measurements With Cross Sectional Measurements.

Laser Pulse Energy (mJ)	Optical Measurement (inches)	Cross Sectional Measurement (inches)	Deviation (inches)
200	0.020	0.0190	0.001
200	0.020	0.0207	-0.001
160	0.018	0.0164	0.002
160	0.018	0.0163	0.002
100	0.013	0.0138	-0.001
100	0.009	0.0107	-0.002

APPENDIX E

COST ANALYSIS

APPENDIX E
COST ANALYSIS

Rough cost estimates have been made for producing 10,000 units per year of both pool-boiler and heat-pipe reflux receivers. The details are presented in the two memos included in this Appendix. The estimates are one element in developing evaluation criteria for dish-Stirling receivers that can be used to (1) compare reflux receiver and other receiver concepts, (2) help make design decisions, and (3) guide the use of resources for research and development.

The production-cost estimates considered (1) the receiver vacuum envelope (including vacuum bakeout and charging with liquid metal and inert gas), (2) the mounting hardware, and (3) the receiver housing (including the optical cavity, the aperture, and the insulation). The interface between the receiver and the engine was left unspecified and was not included in the estimates.

The design that was considered had the same dimensions as the first pool-boiler receiver (the subject of this report). It differed in the following details: (1) the receiver envelope and the optical cavity were considered to be made from Haynes Alloy 230 instead of stainless steel, (2) four thermowells were included in the design, instead of the dozens of brazed-on and welded-on thermocouples used in the first receiver, (3) artificial cavities to stabilize boiling were considered to be formed by laser drilling rather than by electric-discharge machining, (4) a sintered powder-metal-coating alternative to artificial cavities was considered, and (5) the heat-transfer fluid was NaK-78 instead of sodium. For the heat-pipe design, the boiling stabilizers were replaced by a sintered screen wick and the quantity of NaK was reduced.

The first memo, from Moreno and Adkins, presents details of the cost estimates for (1) the receiver with laser-drilled holes, (2) the receiver with a sintered powder-metal-coating alternative to laser-drilled holes, (3) the receiver with a sintered screen wick, and (4) the receiver mount and housing. The memo also compares the cost estimate for the heat-pipe receiver with a cost estimate made by Thermacore, Inc., and reconciles the differences.

The second memo from Moreno summmarizes a partial critique of the methodology used in the first memo and compares the receiver cost estimates of the first memo with estimates made by Pioneer Co., reconciling the differences.

In summary:

1. The rough cost estimate for a Haynes 230 pool-boiler receiver with laser-drilled artificial cavities is $1964.97.

2. The rough cost estimate for a Haynes 230 pool-boiler receiver with a sintered-powder-metal coating is $2056.61.

3. The rough cost estimate for a Haynes 230 heat-pipe receiver with a sintered-screen wick is $2485.65.

4. The corrected rough cost estimate for a receiver housing is $2091.56.

5. Our cost estimates are higher than those of Thermacore, Inc. and Pioneer Co. primarily because of our use of more-expensive materials, and secondarily because of our higher overhead estimates.

Sandia National Laboratories

Albuquerque, New Mexico 87185

date: March 2, 1990

to: DISTRIBUTION

from: J. B. Moreno, 2542, and D. R. Adkins, 1513

subject: Reflux Receiver Cost Estimates

We have completed zeroth-order estimates of the cost of a heat-pipe reflux receiver (DRA) and of two pool-boiler reflux receivers and a receiver housing (JBM). The starting point for the designs that we considered was the existing full-scale hardware. For the heat pipe receiver, the latest wick design was used. The engine end of the receiver shell was left unspecified. We included the new materials recommendations and assumed that NaK can be used. We did not attempt to optimize the designs for cost. The results are:

1. $1964.97 - pool boiler with laser-drilled holes.

2. $2056.61 - pool boiler with sintered-powder coating.

3. $2485.65 - heat pipe receiver with screens.

4. $1474.37 - mount and housing.

We have also reconciled the heat-pipe receiver estimate with Thermacore's presentation made at the ASCS Preliminary Design Review Meeting, November 8-9, 1989. The $1456.20 difference is primarily attributable to our use of more-expensive materials in the receiver envelope and our larger overhead estimate.

Details are presented in Appendices A-E (attached).

To complete this brief study, one of us (JBM) has asked Gary Randall (2542) to critique the methodology that we used. Gary has just arrived at Sandia from AT&T Indianapolis, and has experience in manufacturing engineering. We hope to have his input by mid-April.

DISTRIBUTION:

1513 D. R. Adkins
1513 R. E. Hogan
2542 W. T. Aldrich
2542 S. B. Martin (Acting)
2542 J. B. Moreno
2542 G. T. Randall
6215 K. S. Rawlinson
6217 C. E. Andraka
6217 R. B. Diver
6217 T. A. Moss
6217 P. C. Klimas
6217 K. L. Linker

APPENDIX A

POOL-BOILER COST ESTIMATE (LASER-DRILLED CAVITIES)

Item	Description	Category		Qty	Unit	Cost basis ($/unit)	Total ($)
1.	Front dome sheet (0.032")	material		7.5	SF	29.73	222.98
2.	Rear dome sheet (0.125")	material		7.5	SF	95.73	717.98
3.	Scrap sheet credit (0.032")	material		5.3	SF	14.86	-78.76
4.	Scrap sheet credit (0.125")	material		4.5	SF	47.86	-191.44
5.	Transition pipe (8" SCH10)	material		1.0	FT	257.00	257.00
6.	Thermowell tubing (.5x.083")	material		4.0	FT	12.00	80.00
7.	Thermowell caps (.35" round)	material		1.0	IN	1.00	1.00
8.	Thermowell wick	material		1.0	SF	12.00	20.00
9.	Vac/fill tube (.75x.083")	material		2.0	FT	25.00	50.00
10.	VCR gland (3/4")	material		1	EA	22.10	22.10
11.	VCR gasket (3/4")	material		1	EA	1.60	1.60
12.	NaK-78	material	*	11.4	LB	6.15	70.11
13.	Cut sheet for front dome	labor		0.01	HR	12.00	0.12
14.	Cut sheet for rear dome	labor		0.01	HR	12.00	0.12
15.	Cut transition pipe	labor		0.10	HR	12.00	1.20
16.	Cut 4 thermowell tubes	labor		0.02	HR	12.00	0.24
17.	Cut vac/fill tube	labor		0.01	HR	12.00	0.12
18.	Cut 4 thermowell caps	labor		0.02	HR	12.00	0.24
19.	Clean front dome sheet	labor	*	0.04	HR	12.00	0.48
20.	Laser-drill front dome holes	labor	*	0.20	HR	12.00	2.40
21.	Hydroform front dome	buy		1	EA	70.00	70.00
22.	Hydroform rear dome	buy		1	EA	70.00	70.00
23.	Clean front dome	labor		0.04	HR	12.00	0.48
24.	Drill rear dome for th'wells	labor		0.04	HR	12.00	0.48
25.	Drill rear dome for vac port	labor		0.02	HR	12.00	0.24
26.	Clean rear dome	labor		0.04	HR	12.00	0.48
27.	Drill 8" pipe for th'wells	labor		0.04	HR	12.00	0.48
28.	Clean 8" pipe	labor		0.04	HR	12.00	0.48
29.	Weld rear dome to 8" pipe	labor		0.25	HR	12.00	3.00
30.	Leak check pipe to dome weld	labor		0.25	HR	12.00	3.00
31.	Cut hole in rear dome	labor		0.50	HR	12.00	6.00
32.	Clean dome/pipe ass'y	labor		0.10	HR	12.00	1.20
33.	Bend vac/fill tube	labor		0.01	HR	12.00	0.12
34.	Clean vac/fill tube	labor		0.01	HR	12.00	0.12
35.	Weld vac/fill tube to fitt'g	labor		0.02	HR	12.00	0.24
36.	Leak check fill-tube ass'y	labor		0.12	HR	12.00	1.44
37.	Clean th'well tubes and caps	labor		0.04	HR	12.00	0.48
38.	Weld 4 th'well tubes to caps	labor		0.08	HR	12.00	0.96
39.	Leak check 4 tube cap welds	labor		0.50	HR	12.00	6.00
40.	Weld 2 th'wells to rear dome	labor		0.04	HR	12.00	0.48
41.	Leak check t'well-dome welds	labor		0.25	HR	12.00	3.00
42.	Weld fill assy to dome	labor		0.02	HR	12.00	0.24
43.	Leak check f-assy/dome weld	labor		0.25	HR	12.00	3.00
44.	Weld 2 th'wells to 8" pipe	labor		0.04	HR	12.00	0.48
45.	Leak check t'well-pipe welds	labor		0.25	HR	12.00	3.00
46.	Weld 8" pipe to engine	labor		0.25	HR	12.00	3.00
47.	Leak check pipe-engine weld	labor		0.50	HR	12.00	6.00
48.	Final cleaning - ass'y	labor		0.25	HR	12.00	3.00

Item	Description	Category		Qty	Unit	Cost basis ($/unit)	Total ($)
49.	Weld dome rims together	labor		0.50	HR	12.00	6.00
50.	Leak check dome rim weld	labor		0.50	HR	12.00	6.00
51.	Connect to vacuum fill ass'y	labor		0.25	HR	12.00	3.00
52.	Attach temporary TC's	labor		0.50	HR	12.00	6.00
53.	Attach temporary heaters	labor		0.50	HR	12.00	6.00
54.	Apply temporary insulation	labor		0.50	HR	12.00	6.00
55.	Vacuum bake 24 hours	labor		0.50	HR	12.00	6.00
56.	Transfer NaK-78	labor		0.25	HR	12.00	3.00
57.	Transfer xenon	labor	*	0.25	HR	12.00	3.00
58.	Transfer xenon	material	*	.004	LITER	12.00	0.08
59.	Pinch/weld closure	labor		0.10	HR	12.00	1.20
60.	Remove temporary insulation	labor		0.25	HR	12.00	3.00
61.	Remove temporary heaters	labor		0.20	HR	12.00	2.40
62.	Remove temporary TC's	labor		0.20	HR	12.00	2.40
63.	Restore vac. system to ready	labor		0.20	HR	12.00	2.40
	TOTAL						1421.37
	MATERIAL						1172.65
	BOUGHT SERVICES						140.00
	LABOR						108.72
	OVERHEAD						543.60
	TOTAL POOL-BOILER RECEIVER (MAT'L. PARTS. LABOR AND OV'HD)						1964.97
	POOL-BOILER-SPECIFIC MATERIAL (MARKED WITH * ABOVE)						70.19
	POOL-BOILER-SPECIFIC LABOR (MARKED WITH * ABOVE)						5.88
	POOL-BOILER-SPECIFIC OVERHEAD						29.40
	TOTAL POOL-BOILER SPECIFICS						105.47
	TOTAL RECEIVER LESS POOL-BOILER SPECIFICS						1859.50

Explanatory notes (pool-boiler receiver):

1. Sheet metal: use $17.00/lb; actual large-quantity estimate obtained via Reliance Metals was close to this for both gauges. Scrap credit at half new cost is my guess.

2. Pipe: also based on $17.00/lb.

3. Tube: based on roughly 2/3 small-quantity costs.

4. NaK-78: quote from John Madaus, MSA, for commercial-grade NaK in 750-lb $1000 deposit containers, minimum order of 13 containers. High-purity NaK in 30-gallon $1500 deposit containers, 800 lbs and up, would cost $21/lb.

5. Hydroforming: per Matthew Graham, Ultimate Hydroforming, based on 10,000 units per year, and including a final anneal.

6. Manufacturing operations: assume $12.00/hour labor costs and 500% overhead per Paul Richart's 11/89 presentation. An earlier, more-complicated method resulted in a total cost of $1846.59, only 6% less than the current estimate. The more complicated method made detailed estimates of machine capital costs and lifetimes, floor-space costs, engineering support, etc., but omitted many of the miscellaneous overhead items included by Richart, such as utilities, insurance, and plant maintenance.

7. Other: costs not documented are my estimates.

Not included (partial list):

1. Getters for metal purification.
2. Receiver instrumentation: thermocouples, pyrometer, etc.
3. Pressure-relief device
4. Transportation

APPENDIX B

POOL-BOILER RECEIVER COST ESTIMATE (SINTERED POWDER METAL COATING)

Item	Description	Category	Qty	Unit	Cost basis ($/unit)	Total ($)
1.	Stainless steel powder	material	3.7	LB	11.08	41.00
2.	NaK-78	material	11.4	LB	6.15	70.11
3.	Apply slurry	labor	0.5	HR	12.00	6.00
4.	Furnace run	buy	1	EA	50.00	50.00
	TOTAL					167.11
	MATERIAL					111.11
	BOUGHT SERVICES					50.00
	LABOR					6.00
	OVERHEAD					30.00
	TOTAL SINTERING AND NaK COST					197.11
	TOTAL RECEIVER LESS POOL-BOILER SPECIFICS					1859.50
	TOTAL RECEIVER WITH SINTERED SURFACE COST					2056.61

Explanatory notes (sintered-surface pool-boiler receiver):

1. Oven costs provided to DRA by Michigan Dynamics.
2. Labor and overhead rates same as for laser-hole pool boiler.
3. Assumed 40-mil powder coating over entire surface; did not account for porosity in estimating weight.
4. Used Thermacore's nickel powder cost for stainless steel powder.
5. Assumed xenon addition will not be needed.

Not included (partial list):

1. Getters for metal purification.
2. Receiver instrumentation: thermocouples, pyrometer, etc.
3. Pressure-relief device.
4. Transportation.

APPENDIX C

HEAT-PIPE RECEIVER COST ESTIMATE

Item	Description	Category	Qty	Unit	Cost basis ($/unit)	Total ($)
1.	Surf. wick, 8x2'x2' 325 mesh	material	32.0	SF	7.00	224.00
2.	Rad. arteries, 12x.5'x2' 325	material	12.0	SF	7.00	84.00
3.	Rad. arteries, 12x.5'x2' 55	material	12.0	SF	3.00	36.00
4.	Cir. arteries, 2x.5'x5' 325	material	5.0	SF	7.00	35.00
5.	Cir. arteries, 2x.5'x5' 55	material	5.0	SF	3.00	15.00
6.	NaK-78	material	1.0	LB	6.15	6.15
7.	Fixture surface screens	labor	0.25	HR	12.00	3.00
8.	Fold and clamp arteries	labor	1.00	HR	12.00	12.00
9.	Mount arteries on dome	labor	0.50	HR	12.00	6.00
10.	Oven sintering runs	buy	2	EA	50.00	100.00
	TOTAL					521.15
	MATERIAL					400.15
	BOUGHT SERVICES					100.00
	LABOR					21.00
	OVERHEAD					105.00
	TOTAL HEAT-PIPE SPECIFICS					626.15
	TOTAL RECEIVER LESS POOL-BOILER SPECIFICS					1859.50
	TOTAL HEAT PIPE COSTS					2485.65

Explanatory notes (heat-pipe receiver):

1. Oven costs provided by Michigan Dynamics.
2. Labor and overhead rates same as for pool boiler.
3. Screen costs from Tylinter Inc..

Not included (partial list):

1. Getters for metal purification.
2. Receiver instrumentation: thermocouples, pyrometer, etc.
3. Pressure-relief device.
4. Transportation.

APPENDIX D

MOUNT AND HOUSING COST ESTIMATE

Item	Description	Category	Qty	Unit	Cost basis ($/unit)	Total ($)
1.	Octagon ring (.25" Al plate)	material	62.0	LB	2.25	139.50
2.	Covers (0.050" Al sheet)	material	46.1	LB	2.25	103.73
3.	Support bushings (2" Al rod)	material	6.8	LB	2.25	15.30
4.	Cavity (0.032" HA 230)	material	7.1	SF	29.73	211.08
5.	Drain tube (.375x.035 HA230)	material	1.0	FT	15.00	15.00
6.	Support rods (.5" IN600 rod)	material	11.4	LB	4.00	45.60
7.	Rod ends (1" IN600 rod)	material	0.94	LB	4.00	3.76
8.	Rod anchors (.25" IN600 plt)	material	14.4	LB	4.00	57.60
9.	Aperture board (2'x2'x2")	material	4.0	SF	2.40	9.60
10.	Mineral bat (2" thick)	material	20.0	SF	1.60	32.00
11.	Vermiculite	material	44.0	CF	0.50	22.00
12.	Machine screws for covers	material	56	EA	0.05	2.80
13.	Self tap screws (sml covers)	material	40	EA	0.01	0.40
14.	Bolts/anchors (front assy)	material	16	EA	0.20	3.20
15.	Snap rings (2")	material	16	EA	0.10	1.60
16.	Belville washers	material	16	EA	0.10	1.60
17.	Nuts for rod ends	material	8	EA	0.10	0.80
18.	Lay out 1/4" Al plate	labor	0.50	HR	12.00	10.00
19.	Shear 1/4" Al plate (68 ops)	labor	0.19	EA	12.00	3.80
20.	Saw 1/4" Al plate (160")	labor	0.09	HR	12.00	1.80
21.	Drill 1/4" Al (109 small)	labor	0.30	HR	12.00	6.00
22.	Tap 1/4" plate (56 ops)	labor	0.08	HR	12.00	1.60
23.	Drill 1/4" Al (20 large)	labor	0.50	HR	12.00	10.00
24.	Weld 1/4" Al (48' skip)	labor	1.00	HR	12.00	12.00
25.	Lay out 0.032" Al sheet	labor	0.25	HR	12.00	5.00
26.	Shear 0.032" Al (63 ops)	labor	0.15	HR	12.00	3.00
27.	Saw 0.032" Al (755")	labor	0.23	HR	12.00	4.60
28.	Drill 0.032" Al (115 ops)	labor	0.30	HR	12.00	6.00
29.	Bend 0.032" Al (80 ops)	labor	0.22	HR	12.00	4.40
30.	Spot weld Al sheet (720 ops)	labor	0.40	HR	12.00	8.00
31.	Caulk cover-seams	labor	0.40	HR	12.00	4.80
32.	Apply weather stripping	labor	0.20	HR	12.00	2.40
33.	Weld Al aperture assy (150")	labor	0.10	HR	12.00	2.00
34.	Lay out 0.032" HA230 cavity	labor	0.05	HR	12.00	1.00
35.	Shear 0.032" HA230 (7 ops)	labor	0.02	HR	12.00	0.40
36.	Drill 0.032" HA230 (18 ops)	labor	0.10	HR	12.00	2.00
37.	Saw 0.032" HA230 (114")	labor	0.32	HR	12.00	6.40
38.	Weld cavity assy (89")	labor	0.25	HR	12.00	5.00
39.	Cut 1/2" rods (8 cuts)	labor	0.03	HR	12.00	0.60
40.	Thread 1/2" rods (8 cuts)	labor	0.03	HR	12.00	0.60
41.	Cut 1" rods into disks (8)	labor	0.03	HR	12.00	0.60
42.	Weld disks to rods (8)	labor	0.03	HR	12.00	0.60
43.	Turn disk profile (8)	labor	0.13	HR	12.00	2.60
44.	Lay out 1/4" IN600 plate	labor	0.02	HR	12.00	0.40
45.	Shear 1/4" IN600 (40 ops)	labor	0.11	HR	12.00	2.20
46.	Drill/mill 1/4" IN60 (8 ops)	labor	0.07	HR	12.00	1.40
47.	Bend IN600 (8 ops)	labor	0.02	HR	12.00	0.40
48.	Weld IN600 to rcvr (96")	labor	0.27	HR	12.00	5.40
49.	Cut 2" Al rod (8 ops)	labor	0.03	HR	12.00	0.60
50.	Turn 2" Al rod (16 ops)	labor	0.13	HR	12.00	2.60
51.	Drill 2" Al rod (8 ops)	labor	0.04	HR	12.00	0.80
52.	Saw aperture board (50")	labor	0.02	HR	12.00	0.40

Item	Description	Category	Qty	Unit	Cost basis ($/unit)	Total ($)
53.	Turn aperture ID	labor	0.04	HR	12.00	0.80
54.	Mount cavity, recvr, align	labor	0.50	HR	12.00	10.00
55.	Apply bat insulation	labor	0.08	HR	12.00	1.60
56.	Mount covers	labor	0.13	HR	12.00	2.60
57.	Pour vermiculite and close	labor	0.02	HR	12.00	.40
	TOTAL					800.37
	MATERIALS					665.57
	LABOR					134.80
	OVERHEAD					674.00
	HOUSING TOTAL					1474.37

Explanatory notes (mount and housing):

1. Aluminum cost for 10^6 lbs/yr supplied by Maury Karnowski.
2. Haynes 230 cost basis is same as used for receiver.
3. Mineral wool batting is assumed to be Kaowool, 8 lb. Price obtained (12/85) for 1" thickness was doubled for present 2" thickness, divided by 3 for wholesale.
4. For 2" insulating board, assumed 1.5 times batting cost.
5. Vermiculite at Solico sells for $1.50/CF; divide by 3 for wholesale.
6. Labor and overhead rates are the same as used for the receiver.
7. Items not justified are my estimates.

Not included:

1. Transportation.

APPENDIX E

COMPARISON OF SANDIA AND THERMACORE HEAT-PIPE RECEIVER COST ESTIMATES

	Sandia estimate (dollars)	Thermacore estimate (dollars)
1. Formed envelope material	1242.46	321.44
2. Wick material	394.00	243.47
3. Furnace runs	100.00	125.00
4. Labor	123.84	200.00
5. Liquid metal	6.15	27.62
6. Overhead*	619.20	111.92
TOTAL ESTIMATE	2485.65	1029.45

* Thermacore does not call this item "overhead": they include in this figure "procurement/handling" and "shipping/receiving". Our (Richart's) overhead includes many other items, but does not include transportation, as shown on the next page.

1.0.1.

LABOR RELATED MANUFACTURING EXPENSE

BURDEN RATE DISTRIBUTION - BASE LABOR RATE $12/HR.

STERLING (25)KW ALTERNATOR

10000 UNITS ANNUAL VOLUME

CATAGORY	FIXED % 260% BASE	VARIABLE % 240% BASE
EXEMPT WAGES	0.1106	
SET UP		0.0373
DIRECT WAGES		0.1251
MAINT. SUPPLIES		0.0072
OPERATING SUPPLIES		0.0311
TOOLS & EQUIP.		0.0512
SCRAP		0.0425
APPROPREATED EXPENSES	0.0002	0.0004
OVERTIME PREMIUM.		0.1016
FRINGES	0.0267	0.2417
DEPRECIATION	0.2419	
INSURANCE	0.0119	
TAXES	0.0670	
UTILITIES	0.0144	0.0373
AREA MAINTENANCE	0.0896	0.0405
MAINTENANCE OPERATIONS	0.0361	0.1258
IND/MFG.ENGINEERING	0.1672	0.0009
TOOL ENGINEERING	0.0331	0.0603
FACILITIES ENGINEERING	0.1157	
QUALITY	0.0580	0.0923

Overhead breakdown presented by Paul Richart at the ASCS Preliminary Design Review Meeting, November 8-9, 1989.

Sandia National Laboratories
Albuquerque, New Mexico 87185

date: June 12, 1991

to: DISTRIBUTION

from: J. B. Moreno, 6217

subject: Reflux-Receiver Cost-Estimate Activities

The purpose of this memo is to report on follow-up activities suggested both in Ref. [1] and in our receiver group meetings.

In Ref. [1], cost estimates were presented for two pool-boiler receivers, a heat-pipe receiver, and a mount/housing; the heat-pipe estimate was compared with one given in Ref. [2] by Thermacore. The followup activities are:

1. Critique of Ref. [1] methodology by Gary Randall (2541).

2. Comparison of Ref. [1] results with those of Refs. [3] and [4].

The results are:

1. For the pool boilers, Gary's estimates are within 4% of Ref. [1]. For the mount/housing, his estimate is $2091.56 versus $1474.37 in Ref. [1]. The differences are in his materials quantities, which are more accurately calculated, and in his more-realistic estimate of scrap quantities. He did not attempt to refine Ref. [1] labor-cost estimates and considered only the pool boilers and the mount/housing. He recommends vendor quotes if further refinement is desired.

2. Ref. [3] estimates $140.89 for a pool boiler and Ref. [4] estimates $659.59 for a powdered-metal-wick heat pipe receiver, in 1986 dollars, before "Pareto's extension @ 125% on cost." The estimates in Ref. [1] are much higher, but include "extras" such as more-expensive materials, thermowells, a vacuum/fill port, leak checks, bakeout, and fill and pinchoff processes. Comparing only those components and operations that are common to both (see attachment), the major difference is materials costs. Smaller but significant labor and burden differences also exist; on these we need a third opinion.

DISTRIBUTION (with attachment):

1513 D. R. Adkins
2541 G. T. Randall
6215 K. S. Rawlinson
6217 C. E. Andraka
6217 R. B. Diver
6217 T. A. Moss
6217 P. C. Klimas

Comparison of Pool-Boiler Receiver Cost Estimates

Item	Pioneer estimate ($) Mat'l	Pioneer estimate ($) Labor & burden	Sandia estimate ($) Mat'l	Sandia estimate ($) Labor & burden
1. Absorber: blank, form	31.70	2.04	144.22	70.00
2. Aft dome: " "	55.17	2.07	526.54	70.00
3. Support tube: " "	21.80	5.09	257.00	7.20
4. Weld, finish details	.07	7.21		62.64
TOTALS	108.74	16.41	927.76	209.84
GRAND TOTALS	125.15		1137.60	

Comparison of Heat-Pipe Receiver Cost Estimates

Item	Pioneer estimate ($) Mat'l	Pioneer estimate ($) Labor & burden	Sandia estimate ($) Mat'l	Sandia estimate ($) Labor & burden
1. Absorber: blank, form	242.09	2.42	144.22	70.00
2. Rear shell or aft dome and tube: blank, form	230.39	11.28	783.54	77.20
3. Wick + arteries: form	126.10	47.31	394.00	226.00
TOTALS	598.58	61.01	1321.76	373.20
GRAND TOTALS	659.59		1694.96	

Notes:

1. Envelope material was Haynes 230 in Sandia study, 316 Stainless Steel in Pioneer pool boiler study, IN 800 in Pioneer heat pipe study.

2. No cost of welding envelope was found in Pioneer wicked heat pipe study, so this is omitted in the comparison of heat pipe costs above.

REFERENCES

1. Memo from Moreno and Adkins to DISTRIBUTION, titled "Reflux Receiver Cost Estimates", 3/2/90.

2. Presentation by Thermacore at the ASCS Preliminary Design Review Meeting, November 8-9, 1989.

3. "Final Report Cost Analysis for Stirling Technology 25 kW Solar Drive Electrical Generator as Forecast Utilizing Pareto's Law," October 1987, prepared by Pioneer Engineering and Manufacturing Company.

4. "Final Report Cost Analysis for Mechanical Technology 25 kW Solar Drive Electrical Generator as Forecast Utilizing Pareto's Law," October 1987, prepared by Pioneer Engineering and Manufacturing Company.

APPENDIX F

CALORIMETER

APPENDIX F
CALORIMETER

Design

This section presents the mechanical design of the water-cooled gas-gap calorimeter. A discussion of the instrumentation used for the gas and water flows can be found in Appendix I of this report. A discussion of materials selections can be found in Appendix C of this report. The purpose of the calorimeter is to (1) provide a thermal load for the receiver, (2) enable the extracted power to be measured, and (3) enable the receiver temperature to be controlled. The water-cooled gas-gap calorimeter accomplishes these objectives using a water jacket that is closely fitted to the condenser (Figure F-1). Thermal energy is transported across the narrow gap between the condenser and the water jacket by radiation and conduction. A controlled mixture of helium and argon in the gas gap determines the conductive component of the heat extraction (and hence the receiver temperature). The extracted power can be accurately determined by measuring the flow rate and the temperature change of the water. A much-simpler way to thermally load the receiver would be to allow the condenser to be passively cooled by radiation and natural convection. However, with passive cooling it would be very difficult to determine the extracted power, and the receiver temperature would vary with the input power in an uncontrolled manner.

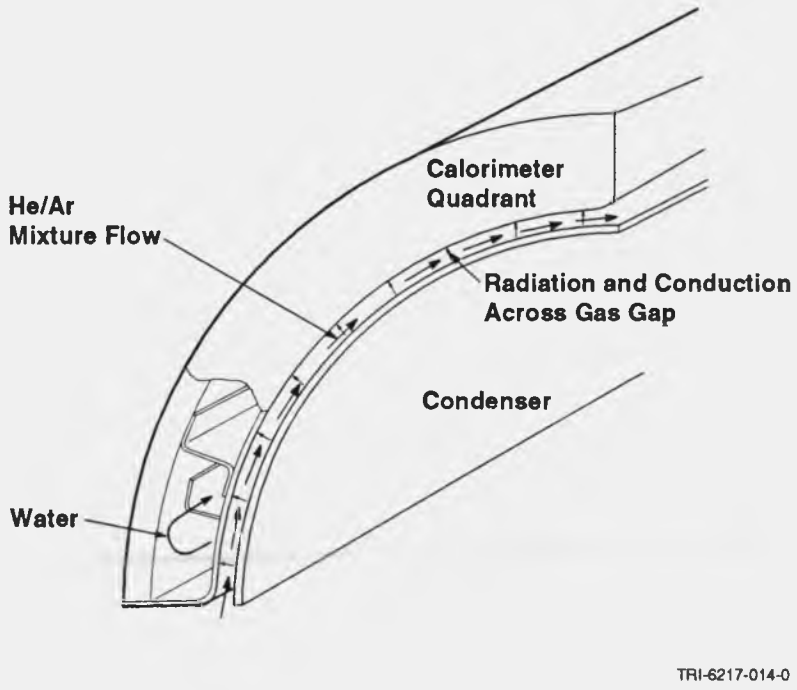

Figure F-1. Schematic of water-cooled gas-gap calorimeter (one quadrant shown) mounted on the pool-boiler receiver's condenser section.

The calorimeter was designed by J. F. Muir and W. C. Ginn of Sandia, and was built in four quadrants to facilitate both handling and accurate fit to the condenser section. The narrow gap (approximately 0.04 inches [in.]) between the condenser and the quadrants was maintained by spring-loading each quadrant against longitudinal spacer wires welded to the condenser. To distribute the helium-argon gas mixture uniformly over the gas gap, a circumferential plenum was built into one end of each calorimeter quadrant. Once the calorimeter was spring-loaded onto the condenser, the spaces between the quadrants and between the gas plenum and the condenser were sealed with mineral-wool insulation backed by stainless-steel foil. Two quadrants were connected in series for each half section of calorimeter, and the halves were connected in parallel to achieve the required water flow rates. Baffles within each quadrant were arranged to ensure high flow velocities and to prevent stagnation regions, so that boiling would not occur (Figure F-2). Two metal-sheathed thermocouples were brazed into one of the quadrants to sense temperatures on the wet side of the heated surface, near the water inlet and outlet ports. By monitoring these temperatures over time, it was hoped that potentially-damaging mineral scaling of the surfaces could be detected. Photographic views of the quadrants are shown in Figures F-3, F-4, and F-5.

Figure F-2. Photograph of the inner and outer shell of one calorimeter quadrant, with the inner shell slid back to reveal the water-flow baffles.

Figure F-3. Photograph of four calorimeter quadrants showing inside and outside surfaces. The quadrant second from the right has two thermocouples brazed in place to sense the heated-surface temperature near the water inlet and outlet. A square shim-stock protector is spot-welded over the area where the thermocouples pass through the outer (unheated) surface.

Figure F-4. Photograph of the four calorimeter quadrants grouped as installed on the pool-boiler receiver. The large and small fittings at the bottom are the water and gas ports, respectively.

Figure F-5. Photograph of the four calorimeter quadrants installed on the pool-boiler receiver with one water connection between quadrants completed.

A computer model developed by Muir that accounts for (1) conduction and radiation across the gas gap, (2) convective heat transfer and temperature rise in the water channel, and (3) thermal expansion of the condenser was used as the basis for the selection of dimensions. The model features include (1) cylindrical condenser, (2) axisymmetric approximation to the calorimeter, (3) temperature-dependent condenser material properties, (4) composition and temperature-dependence of gas properties, (5) diffuse-gray condenser and calorimeter, and (6) turbulent convective-heat-transfer correlation in the water. The model requires the user to specify the dimensions, the diffuse-gray emissivities, the receiver operating temperature, and the water-temperature change in order to calculate (1) the extracted power, (2) the required water flow rate, (2) the gas mixture, (3) the fraction of heat transport by conduction across the gas gap, (4) the temperature profile from inside the condenser to the bulk water, and (5) the gas-gap dimension at operating temperature. The least-certain of the independent variables are the emissivities. Figure F-6 shows calculated calorimeter performance for a fixed gas gap of 0.04 in. and for various values of the radiation parameter, K. This parameter is defined as $(\varepsilon_1^{-1} + \varepsilon_2^{-1}-1)^{-1}$, where ε_1 and ε_2 are the emissivities of the condenser and calorimeter. Also shown are data taken during the first three days of testing, corresponding to operation at nominally 1/2, 3/4, and full power, at 800°C. The data are well fit by the calculations when K = 0.7. Using this value of the radiation parameter, calorimeter performance was calculated for temperatures between 700° and 800°C. The results (Figure F-7) show that the receiver temperature should be controllable between 700° and 800°C for power levels between about 26 and 65 kW_t.

During the design process, the effects of a possible loss of coolant accident (LOCA) were considered. A stress analysis was performed to determine the maximum pressure that the calorimeter could tolerate without damage. A memo summarizing these calculations is included at the end of this Appendix. Hydraulic calculations were made to determine the maximum pressure that would occur within the calorimeter if coolant flow was interrupted. The hydraulic calculations assumed that steam would be produced at a rate consistent with the heat-transfer capacity of the gas gap, and that rising pressure would drive the steam flow through the discharge pipe attached to the outlet side of the calorimeter. The calculations showed that the discharge pipe was too long to safely vent steam during a LOCA. As a result of these analyses, a 50-psi burst disc was installed in the discharge line just downstream of the calorimeter.

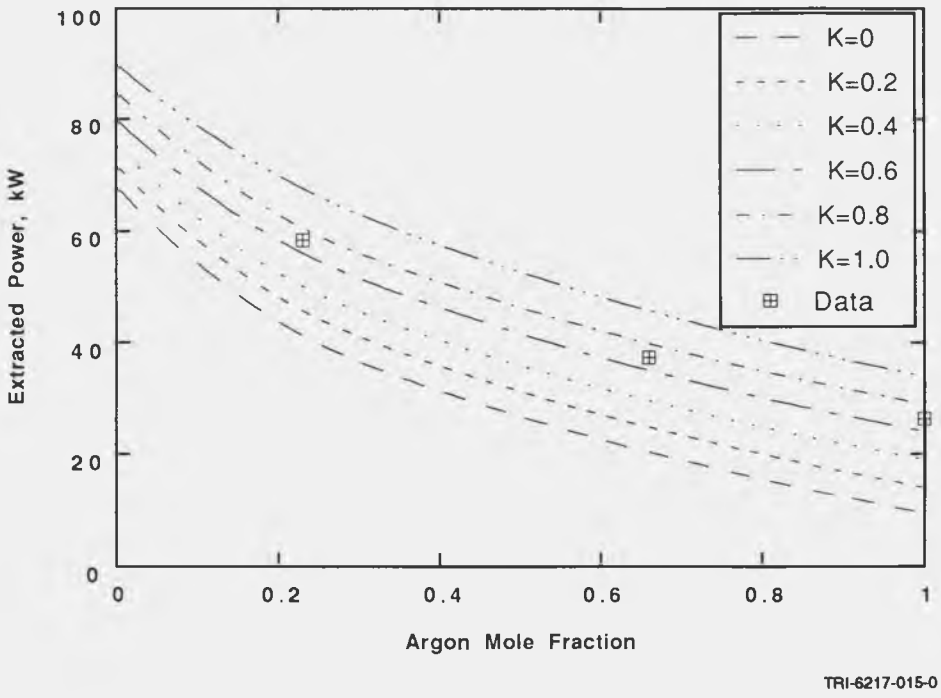

Figure F-6. Calculated and actual calorimeter performance for a pool-boiler receiver operating at 800°C with a gas gap of 0.04 in.; K is the radiation parameter $(\varepsilon_1^{-1} + \varepsilon_2^{-1}-1)^{-1}$, where ε_1 and ε_2 are the emissivities of the condenser and calorimeter.

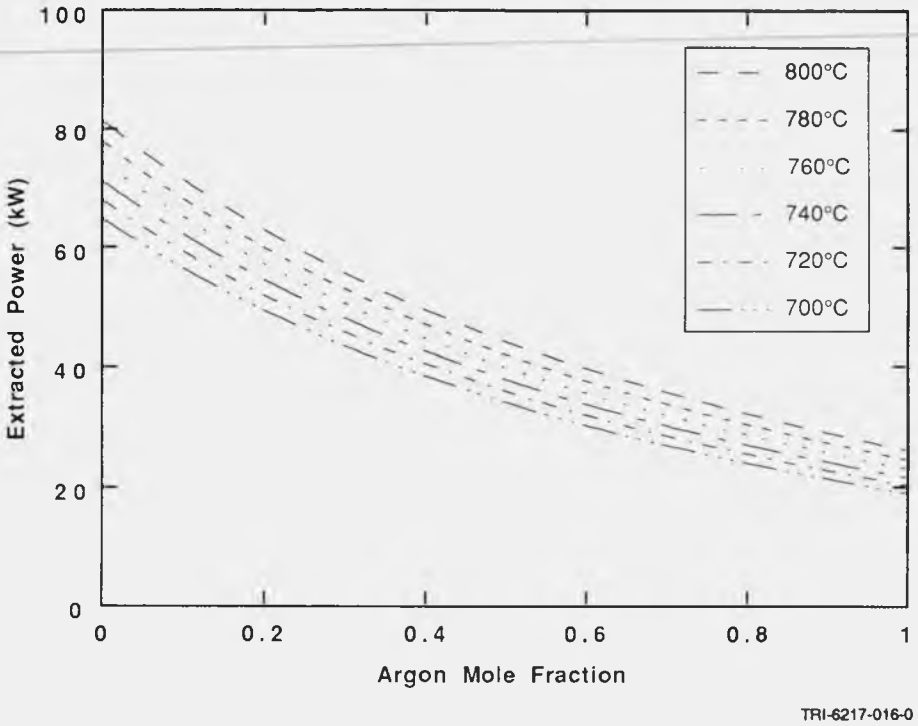

Figure F-7. Calculated calorimeter performance for various pool-boiler receiver temperatures, with a gas gap of 0.04 in. and a radiation parameter K = 0.7.

Implementation Difficulties

Two problems were encountered during the calorimeter assembly. The first was difficulty in brazing the water baffles to the cylindrical inner and outer shells, because of less than perfect mating of the parts. This problem was eventually solved by tack welding every joint to force a good fit. A more serious problem was encountered when the longitudinal seams between the inner and outer shells were welded shut. The resulting distortion caused the gas gap to vary by several tenths of an inch along the length of the calorimeter creating a clearly unacceptable situation. An accurate cylindrical profile was obtained by arc-spraying each quadrant with a heavy coating of copper, which was then machined to the desired shape.

Two other difficulties were encountered while implementing the calorimeter. The first involved a moderate deviation of the calorimeter performance from model predictions (Figure F-8). Results from Figure F-7 have been cross-plotted at 61.7 kW_t for comparison with data taken on October 12, 1991. This comparison shows that somewhat less control is possible than the model predicts. The model indicates that the temperature should be controllable down to about 680°C at 61.7 kW_t, while in reality the temperature could only be forced down to 710°C. Inaccurate estimates of emissive properties and gap dimensions may affect the results. The second difficulty involved rapid corrosion of the aluminum burst disc in the calorimeter water discharge line. This was a result of galvanic action between the disc and its steel holder. The problem was solved by using teflon-coated aluminum discs.

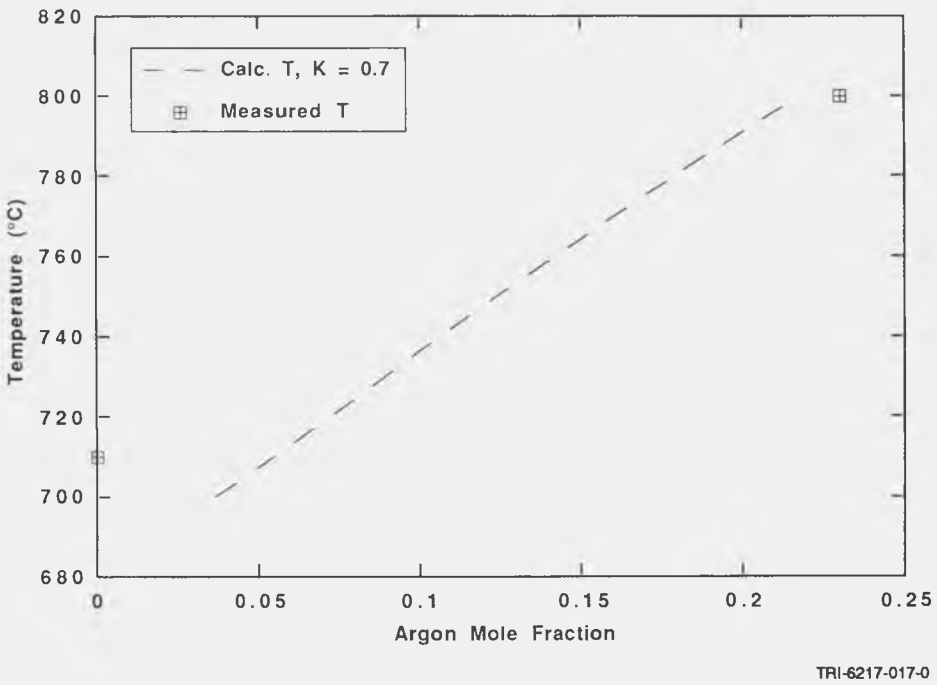

Figure F-8. Calculated and actual calorimeter performance when the extracted power is 61.7 kW, for various pool-boiler receiver temperatures, with a gas gap of 0.04 in. and a radiation parameter, K = 0.7.

Sandia National Laboratories

Albuquerque, New Mexico 87185

date November 2, 1988

to: J. F. Muir, 6227

from: M. K. Neilsen, 1521

subject: Structural Analysis of a Gas Gap Calorimeter Subjected to an Accident Environment

INTRODUCTION

A new gas gap calorimeter is being developed by researchers in Divisions 2541 and 6227 for use in an upcoming receiver experiment. Specifically, it will be used to measure the energy generated by a sodium pool boiler heat pipe receiver. A cross-section of the gas gap calorimeter is shown in Figure 1. The calorimeter has a length of 20.5 inches and has cover plates on each end. During normal operation, water flows through the channels that are formed by the cover and support plates. In this mode, the cover and support plates are subjected to very small loads. However, if water flow to the calorimeter is lost during operation, water in the calorimeter will begin to boil and pressures of up to 250 psi will be generated in the calorimeter. If this internal pressure causes the gas gap between the calorimeter and the heat pipe to close significantly then the calorimeter temperature and internal pressure will significantly increase which will in turn lead to further gap closure and an unstable situation. As requested, a series of analyses was completed to characterize the effects of internal pressure on the calorimeter. Results from these analyses were presented at a working group meeting. The purpose of this memo is to document these analytic results.

EFFECTS OF INTERNAL PRESSURE ON THE CALORIMETER

Effects of internal pressure were initially investigated using closed-form solutions for the response of a linear elastic plate. Consider a section of the cover as shown in Figure 2a. If the edges of each plate section do not rotate or translate (i.e. are fixed) then the maximum deflection at the center of the section, Δ, will be given by

$$\Delta = \frac{p\ell^4}{384D} \qquad D = \frac{Et^3}{12(1-\nu^2)} \qquad (1)$$

where p is the applied pressure, ℓ is the unsupported length in inches, D is the flexural rigidity of the plate, E is the elastic modulus for the plate material in psi, ν is Poisson's ratio, and t is the thickness of the plate in inches. This linear elastic plate equation indicated that a pressure of 509 psi would generate a maximum gas gap closure displacement of 1.0 mil. A gas gap closure of 1 mil was considered a safe displacement. The maximum stress in the plate, σ, will occur near the fixed edge and is given by the following equation

$$\sigma = \frac{p\ell^2}{2t^2} \qquad (2)$$

This equation indicated that an applied pressure of 349 psi would generate a maximum stress of 35,000 psi in the plate. Since annealed 304 Stainless Steel has a yield strength of 35,000 psi, an applied pressure of 349 psi will initiate plastic deformation of the plate. Once plastic deformation is initiated the linear elastic equations given above are no longer applicable. Thus, an applied pressure in excess of 349 psi will generate more displacement than was predicted by Equation 1.

Next, the support plate response was computed using linear elastic equations. Consider a unit width section of a typical support plate as shown in Figure 2b. Each support plate will be required to carry a tensile load of F lbs./in. where

$$F = \ell * p \qquad (3)$$

and p is the applied pressure in psi. This load will generate an average tensile stress, σ_t psi, in each support of

$$\sigma_t = F/t = 14.2 * p \qquad (4)$$

where t is the thickness of each support. This equation indicated that an applied pressure of 500 psi would generate a tensile stress of only 7080 psi in the support plate and across the braze joint. Also, each support plate will be stretched by the mechanical load a distance d in. where

$$d = F*L / A*E = 2.64 \times 10^{-7} * p \qquad (5)$$

where L is the length of each support as shown in Figure 2b. This equation indicated that an applied pressure of 500 psi would stretch the support plates 0.13 mils which is small compared with the displacement generated by cover plate bending.

FINITE ELEMENT ANALYSES

Next, two-dimensional plane strain finite element analyses were completed to investigate the effects of using three different support plate cross sections. These analyses were completed using JAC [2] and the finite element models shown in Figure 3. Due to the symmetry present in the calorimeter, only a representative section of the calorimeter was modeled. The support plates used in these models had L-, Z- and I-shaped cross sections. In these analyses, internal pressure was increased from an initial value of 0 psi to a final value of 1000 psi.

Results from these analyses indicated that acceptable amounts of displacement would be generated when the calorimeter was subjected to internal pressures of 800 psi or less (Figure 4). The displacement predicted by the linear elastic solution (Equation 1) is included in this figure for comparison with the finite element solutions. The finite element solutions indicated that the gap closure displacement would increase at a much faster rate for pressures in excess of 800 psi. Plots of interfacial stress across the braze joint at an applied pressure of 500 psi indicate that normal tensile stress across the braze joint is not uniform and tends to be much higher near the edges than at the center of the joint (Figure 5). Note that in Figure 5 the x-component of the stress tensor has been plotted and not the stress component oriented in a direction normal to the local interface; however, the x-component of the stress tensor will have nearly the same magnitude as the normal interfacial stress component. Interfacial stress was significantly reduced on the flange side when a z-shaped support was used in place of the L-shaped support. The third analysis indicated that use of an I-shaped support would significantly reduce interfacial stress across the braze joint.

A final finite element analysis was completed assuming that one braze joint had failed. The linear elastic solution (Equation 1) indicated that cover displacement would increase by a factor of 16 when the unsupported length was increased by a factor of 2. Results from the finite element analysis indicated that the calorimeter cover would displace towards the heat pipe 60 mils and contact the heat pipe when a pressure of only 415 psi was generated (Figure 6). Also, the interfacial stress in the nearby support plate joints significantly increased from 12,000 psi to 24,000 psi when one joint failed. These results indicated that one joint failure may lead to multiple joint failures.

CONCLUSIONS

The following conclusions were generated based on results from the above analyses:

1. Acceptable cover plate displacements will be generated by pressures of 500 psi or less.

2. Large braze joint stresses will be generated with the original L-shaped support plate design.

3. Braze joint stresses can be significantly reduced by using I-shaped support plates in place of the L- or Z-shaped support plates.

4. If one joint fails, additional joint failures are likely to follow.

At this point, I have some concern about the blind braze joints that will be made between the cover and support plates when the cover is brazed in place. I understand that proof testing will be completed to determine if the calorimeter can survive an internal pressure of 200 psi. The proof tests should generate no permanent deformation in good units. If braze joint failures are a problem with the original design they could probably be eliminated by using an I-shaped support plate. Another option that you may want to consider is to avoid making a blind structural braze joint by using square tube sections in place of the support plates that could be brazed together and leak checked prior to brazing on the cover plate. With this design the cover plate would no longer be a structural member and the blind braze joint between the cover plate and the structural tubing would not be critical.

REFERENCES

1. American Society for Metals, "Metals Handbook", Metals Park, Ohio, 1984.

Table 1. Material Properties for 304 Stainless Steel [1]

Young's Modulus psi	Poisson's Ratio	Yield Strength psi	Hardening Modulus psi	Thermal Expansion /°C
28.0E+06	0.30	35,000	2.80E+05	17.8E-06

MKN:1521:tbh

Copy to:
1510 J. W. Nunziato
1520 L. W. Davison
1521 R. D. Krieg
1522 R. C. Reuter
1523 J. H. Biffle
1524 A. K. Miller
1530 D. B. Hayes
1550 C. W. Peterson
2541 J. P. Abbin
2541 C. E. Andraka
2541 J. B. Moreno
6226 J. T. Holmes
6227 D. R. Adkins
6227 R. B. Diver
6227 C. Ginn
6227 P. C. Klimas
1521 M. K. Neilsen

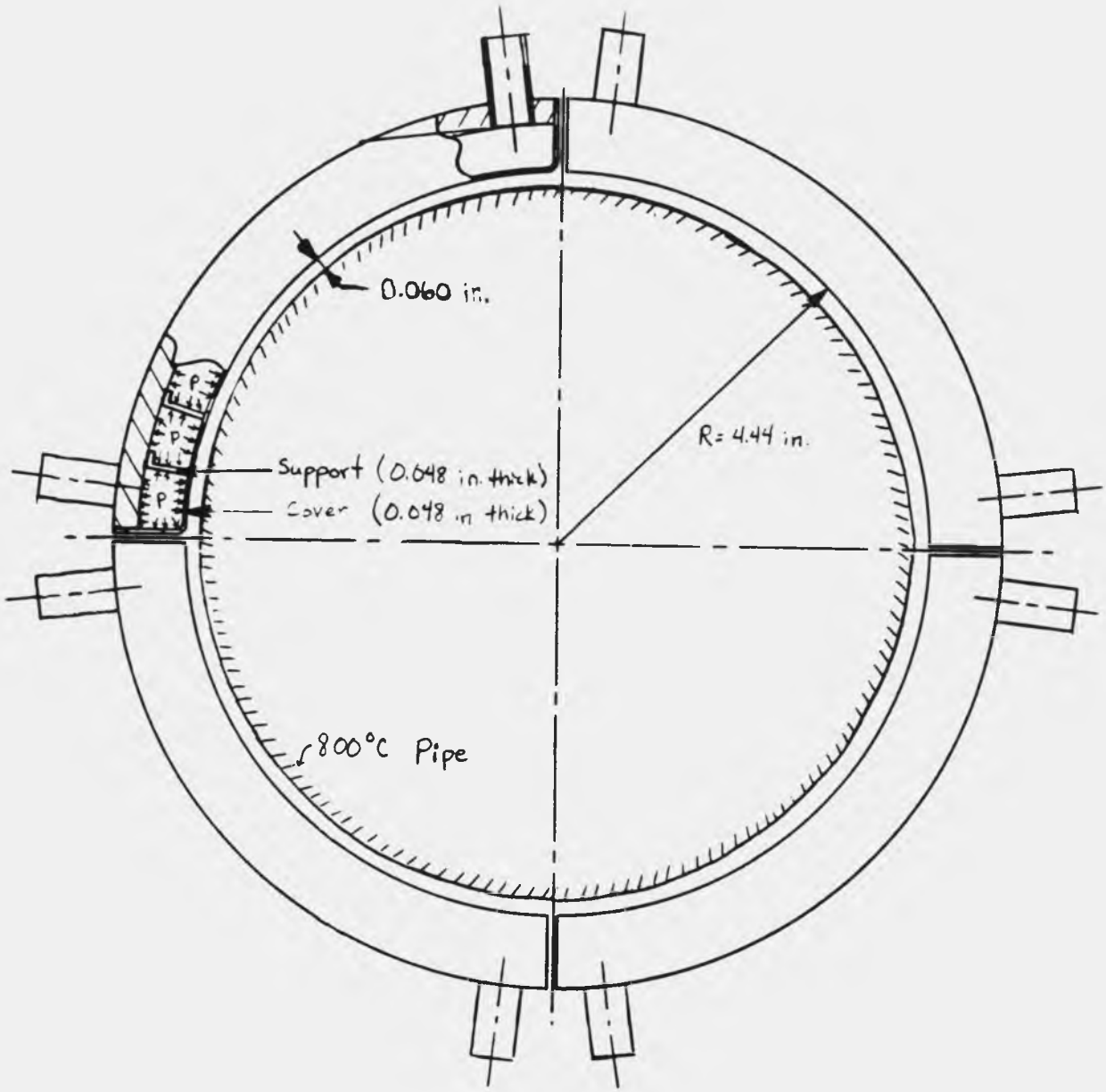

FIGURE 1. Gas gap calorimeter cross-section.

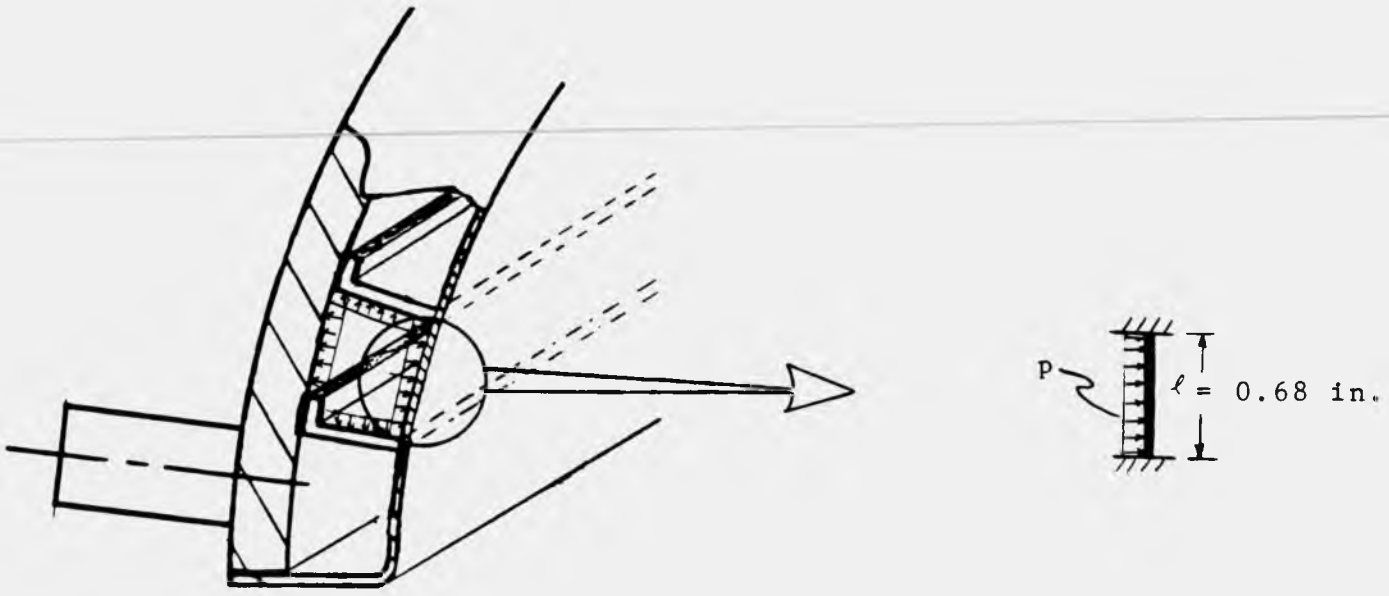

FIGURE 2a. Typical cover plate section.

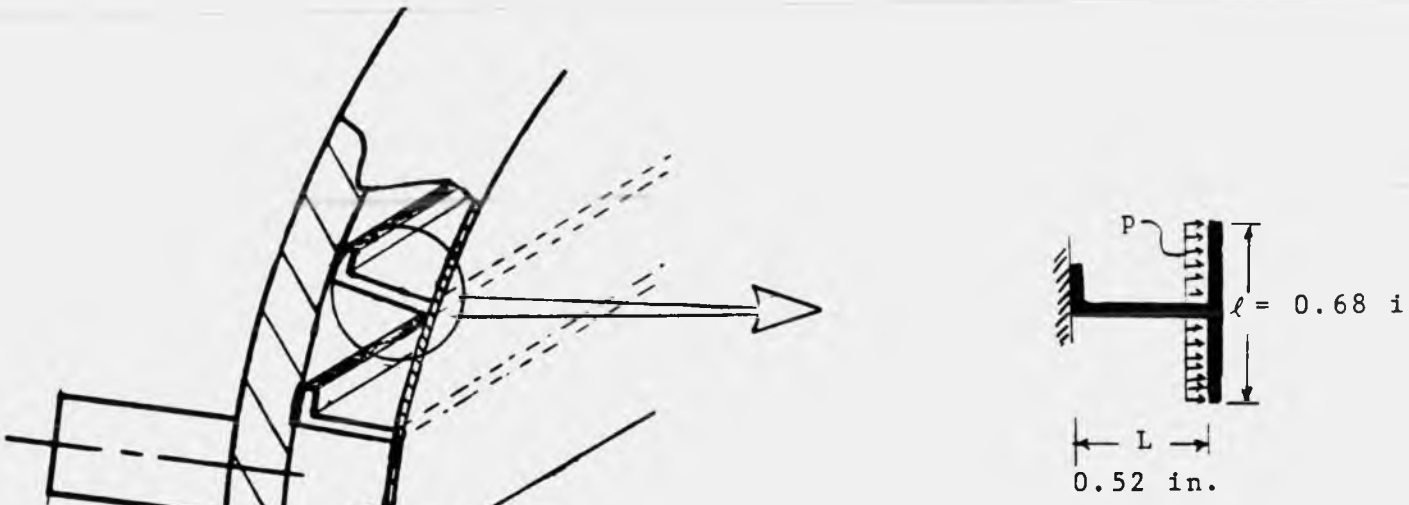

FIGURE 2b. Typical support plate section.

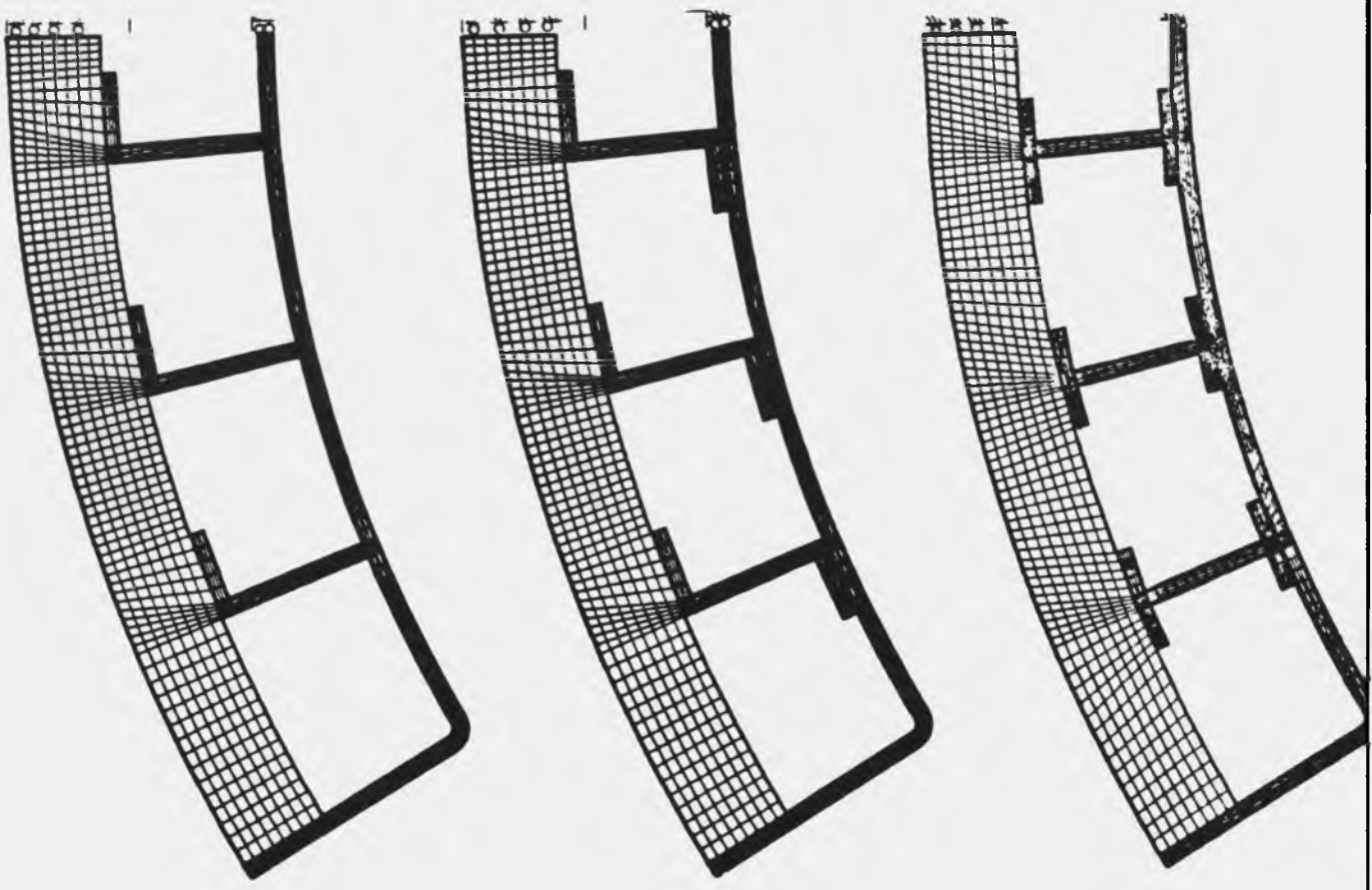

Model A (L-support)

Model B (S-support)

Model C (I-support)

FIGURE 3. Two-dimensional, plane strain finite element models.

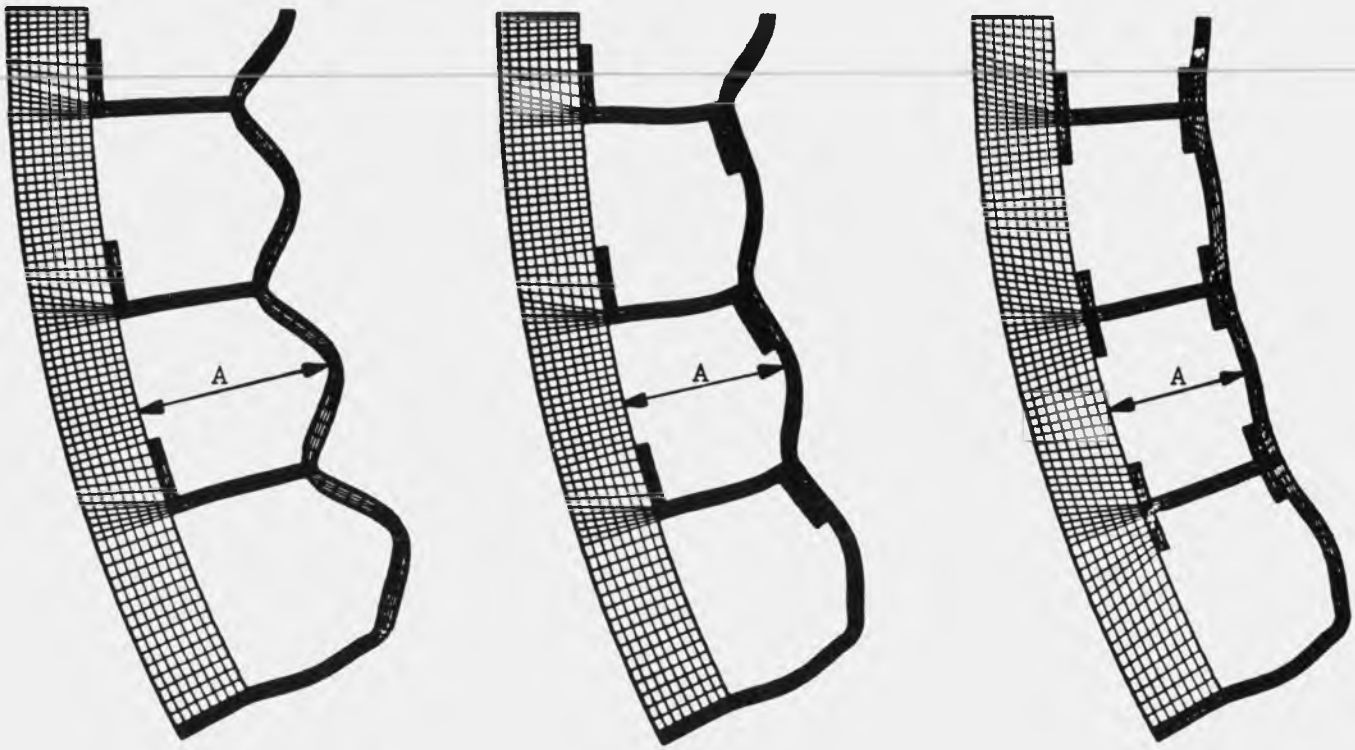

a) Deformed finite element models, displacements magnified X 50, p=1000 psi.

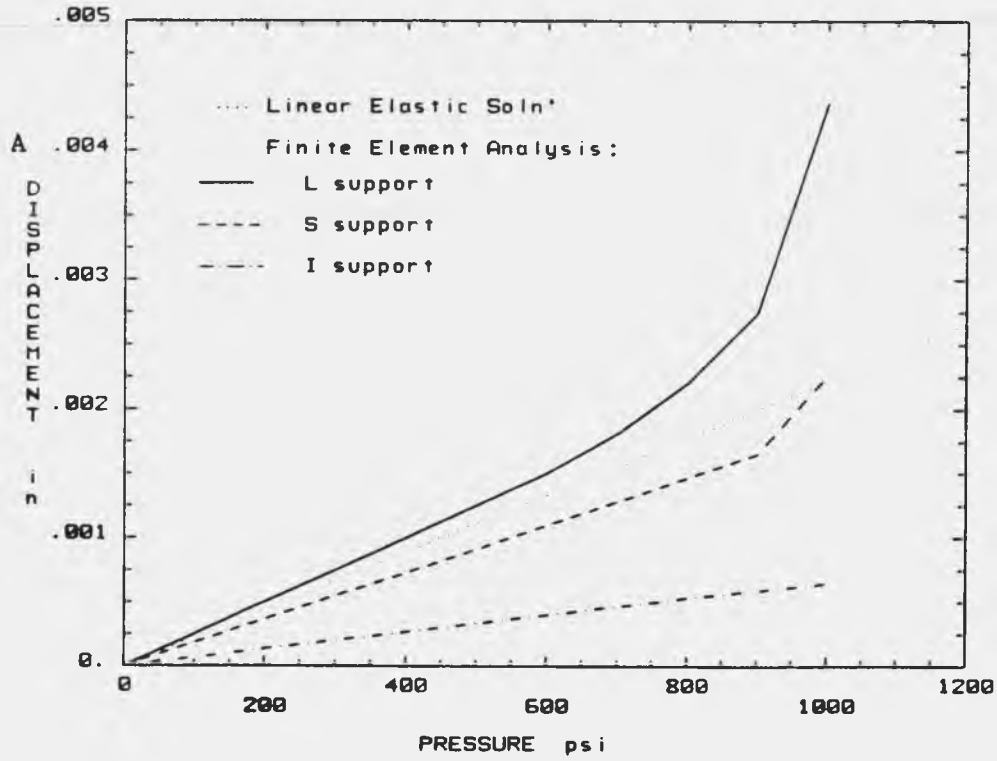

b) Displacement A plotted as a function of applied pressure.

FIGURE 4. Results from finite element analysis.

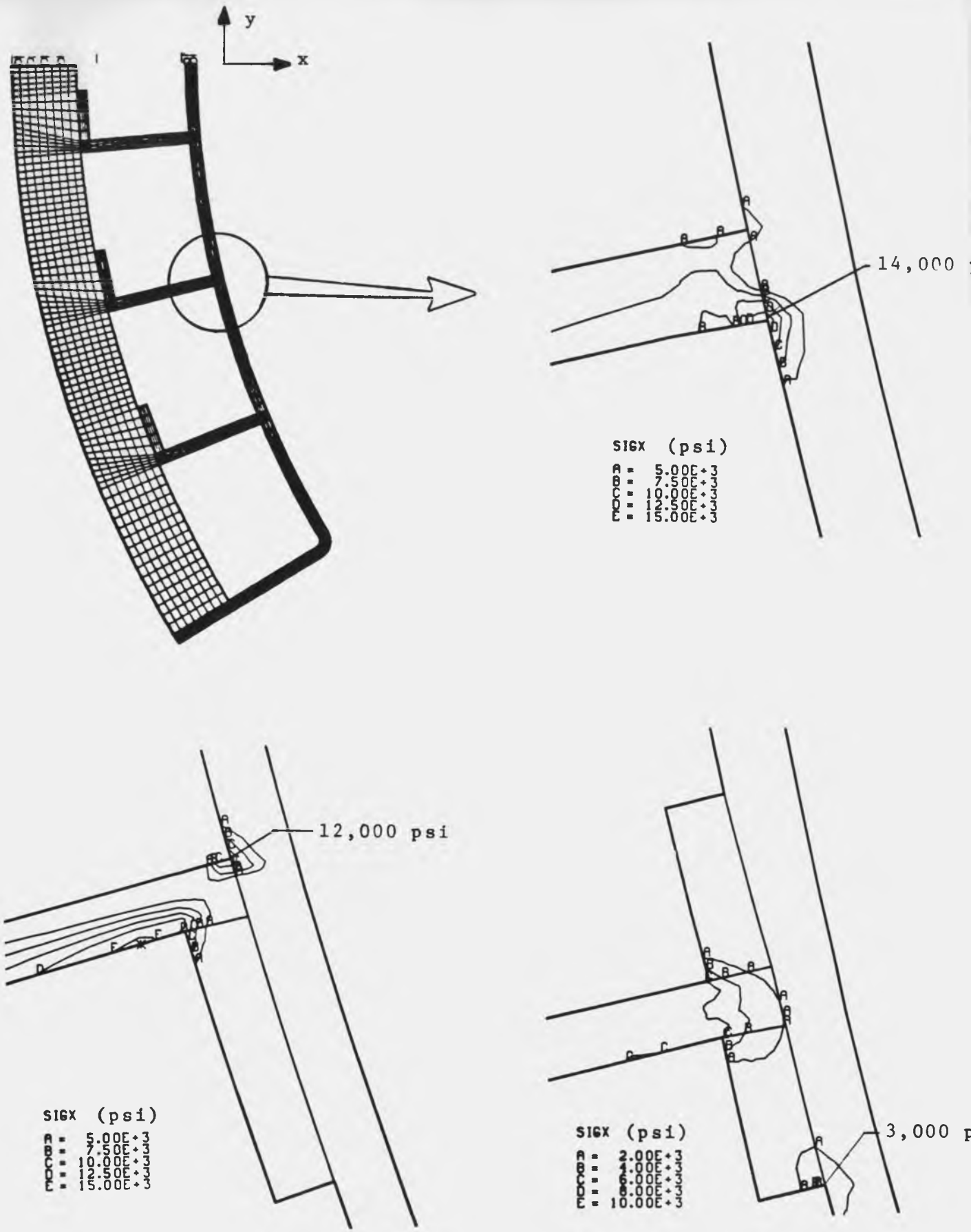

FIGURE 5. Interfacial stress across the braze joint generated by an applied pressure of 500 psi.

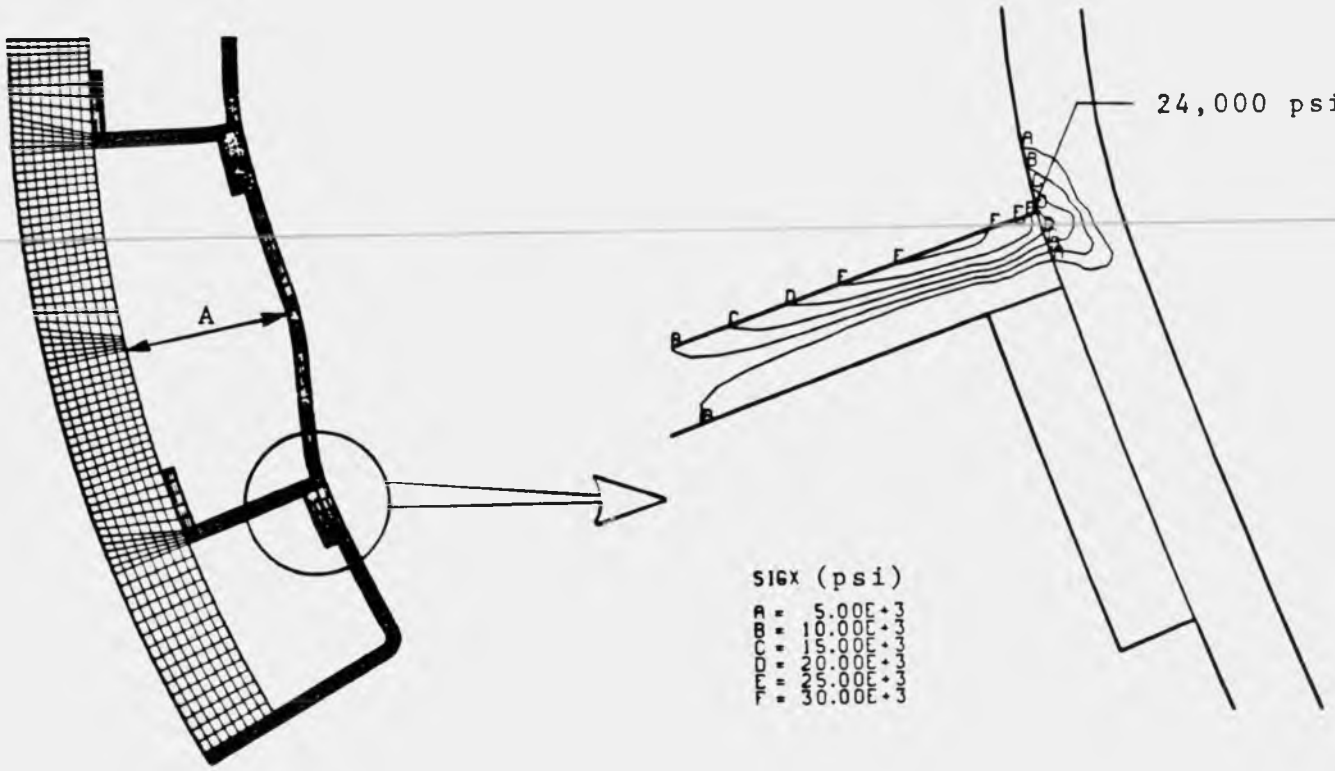

a) Deformed finite element model actual displacements, p=500 psi.

b) Interfacial stress across braze joint generated by an applied pressure of 500 psi.

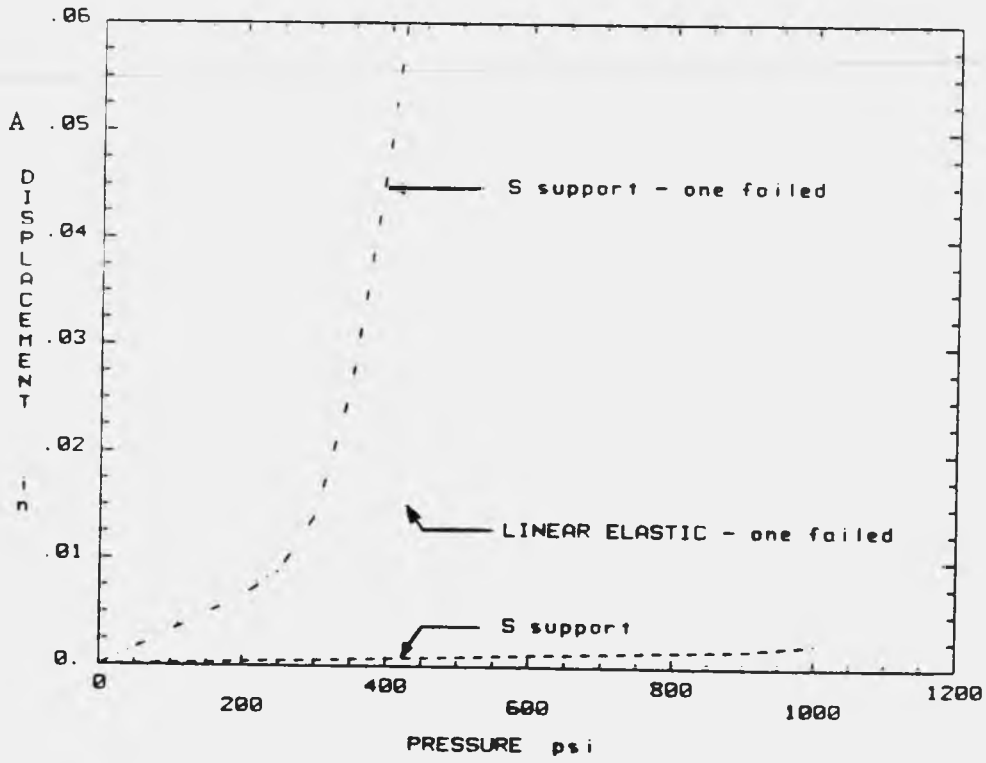

c) Displacement A plotted as a function of applied pressure.

FIGURE 6. Results from finite element analysis with one section failed.

APPENDIX G

OPTICAL ANALYSIS

APPENDIX G
OPTICAL ANALYSIS

The spherical absorber's shape utilized in the Sandia pool-boiler receiver was selected primarily for structural reasons (see Appendix A of this report). The absorber's size and cavity geometry, however, were based, to a large extent, on peak flux considerations. A design objective was to operate at relatively high-peak flux intensities, approximately 70 watts per square centimeter (W/cm^2), as previously demonstrated in bench-scale tests (Moreno and Andraka, 1989). For comparison, the Stirling Technology Co. conceptual design for a 75-kW_t pool-boiler receiver with a similar geometry specifies an absorber diameter of 0.508 m (20 inches [in.]) and is designed to operate at peak flux intensities of approximately 46 W/cm^2 (Stirling Technology Co., 1988).

Figure G-1 shows the receiver cavity design schematic. This design utilizes a 0.414-m (16.3-in.) diameter spherical absorber with a 0.219-m (8.62-in.) radius of curvature. The sphere half angle is therefore about 71 degrees. The cavity design utilizes a 0.22-m (8.66-in.) diameter aperture. Because the Test Bed Concentrators (TBC) have a rim angle of approximately 45 degrees, the rim of the absorber is placed 0.097 m (3.8 in.) behind the aperture/focal plane to match the cavity side-wall angle with the concentrator rim angle and avoid directly illuminating the uncooled cavity side wall.

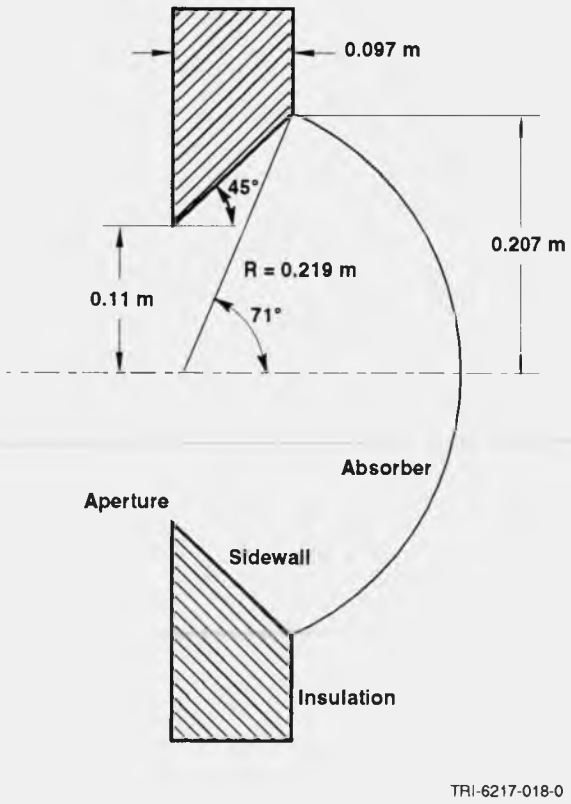

Figure G-1. Schematic showing the Sandia reflux receiver cavity design. The height of the cavity side wall was reduced from 0.097 to 0.077 m (3.8 to 3.0 in.) for the receiver tested to protect the rim weld from possible overheating.

Figure G-2 is the CIRCE2-predicted incident solar flux distribution for the design configuration. CIRCE2 is an improved version of CIRCE (Ratzel and Boughton, 1987) and accounts for (1) dish and facet geometry, (2) facet curvature, (3) facet alignment, (4) facet shading and blockage, and (5) receiver geometry. Table G-1 lists the CIRCE2 sun shape, slope error, and facet parameters which characterize Sandia's TBC-1 used in these tests, and solar conditions used in these analyses. Figure G-1 shows the receiver geometry assumed for the prediction. The peak incident flux is 73 W/cm^2 for the design condition with 75-kW_t incident power.

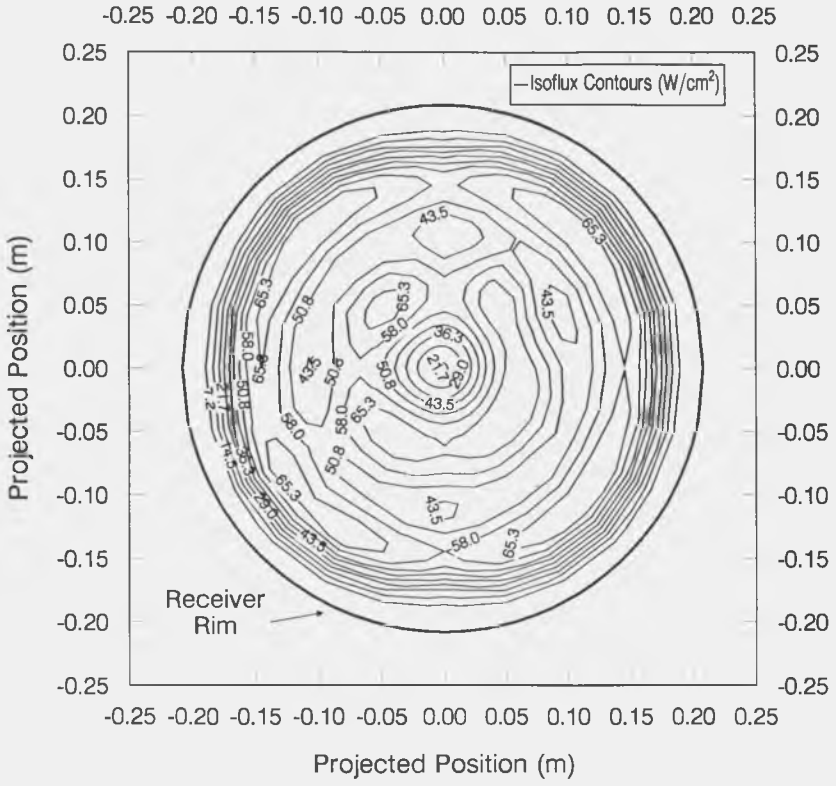

Figure G-2. CIRCE2-predicted incident solar flux for the design condition. The integrated solar power is 74.6 kW. The image is reversed left-to-right (like a mirror image) from what an observer, standing at the concentrator looking at the receiver, sees. The reversed image is presented to facilitate comparison with the infrared camera images presented in Appendix P of this report, which are reversed by a mirror in the camera system. The peak flux intensity is 73 W/cm².

A concern with this design was the possibility of overheating the absorber-to-aft-dome weld. The nested dome arrangement results in a narrow gap between the two domes near the weld. In fact, the outside 1.3 cm (0.5 in.) of the absorber, next to the rim, has virtually no gap. To assess the potential for weld overheating, finite element thermal analyses of the weld with various boundary condition assumptions were conducted (see attached memorandum). Although these analyses indicated that weld overheating is not a significant concern, the potential for concentrator mistrack, especially with enlarged apertures, suggested moving the absorber nearer to the aperture. At the same time, the power delivered by TBC-1 (normalized to 1000-W/m² direct normal solar insolation) was measured to be about 65 kW_t. Given the degraded TBC-1 performance (and therefore peak flux) and in the interest of conservatism, the absorber was moved 2 cm (0.79 in.) closer to the aperture. As a result of the competing effects, the CIRCE2 predicted peak flux (normalized) for the tested configuration remained essentially unchanged. Figure G-3 shows the predicted incident solar flux distribution for the configuration tested with no concentrator mistrack. For this CIRCE2 analysis the absorber was moved 2 cm (0.79 in.) closer to the aperture and the concentrator reflectivity was decreased to 0.762.

TABLE G-1. CIRCE2 INPUT DATA FOR THE SANDIA POOL-BOILER RECEIVER

Sun-on Axis With Concentrator (no mistrack)
1000-W/m² Direct Normal Insolation

Standard Tabular Sunshape for High Insolation

Radians	Intensity (arbitrary units)
0.0	202.40
2.2×10^{-4}	202.40
6.5×10^{-4}	202.40
1.09×10^{-3}	200.28
1.53×10^{-3}	197.10
1.96×10^{-3}	192.86
2.40×10^{-3}	188.63
2.84×10^{-3}	182.27
3.27×10^{-3}	172.73
3.71×10^{-3}	155.78
4.15×10^{-3}	105.97
5.02×10^{-3}	7.50
5.45×10^{-3}	2.83×10^{-1}
5.89×10^{-3}	1.76×10^{-1}
6.33×10^{-3}	8.80×10^{-2}
6.76×10^{-3}	7.40×10^{-2}
7.20×10^{-3}	5.60×10^{-2}

One Milliradian Circular Normal Concentrator Slope Error

	X(m)	Y(m)	Z(m)
Aperture Center	0.0	0.0	6.385
Aperture Edges	-.11	0.0	6.385
	0.0	-.11	6.385
	-.11	0.0	6.385
	0.0	-.11	6.385

Aim Point	X(m)	Y(m)	Z(m)
1	0.0	0.0	6.417
2	0.0	0.0	6.385
3	0.0	0.0	6.385

Rectangular Spherical Curvature Facets
Facet Reflectivity = 0.875
Facet Dimensions (M) X = 0.7049, Y = 0.6033

TABLE G-1. CIRCE2 INPUT DATA FOR THE SANDIA POOL-BOILER RECEIVER (continued)

TBC-1 FACET DATA BASED ON OCTOBER 1988 SURVEY

FACET	X(m)	Y(m)	Z(m)	RADIUS (m) of curv.	BLOCK	AIM POINT
1	-1.8009	5.1816	1.2668	15.9004	0	3
2	-1.082	5.1816	1.1883	15.6718	0.01	3
3	1.082	5.1816	1.1883	15.6972	0	3
4	1.8009	5.1816	1.2668	16.002	0.01	3
5	-3.2207	4.5974	1.3205	16.3068	0	3
6	-2.5146	4.5974	1.3205	16.002	0.02	2
7	-1.8009	4.5974	1.0504	15.6464	0	2
8	-1.082	4.5974	0.9719	15.4432	0	2
9	-0.3607	4.5974	0.9325	15.8242	0.12	2
10	0.3607	4.5974	0.9325	15.621	0.11	2
11	1.082	4.5974	0.9719	15.6718	0.0	2
12	1.8009	4.5974	1.0504	15.6718	0.0	2
13	2.5146	5974	1.1671	15.7988	0.0	2
14	3.2207	4.5974	1.3205	16.3576	0.0	3
15	-3.9192	4.003	1.3158	16.002	0.0	3
16	-3.2207	4.003	1.1269	15.9258	0	2
17	-2.5146	4.003	0.9735	15.748	0	2
18	-1.8009	4.003	0.8568	15.9004	0.01	2
19	-1.082	4.003	0.7783	15.9004	0	2
20	-0.3607	4.003	0.7389	15.8242	0.11	2
21	0.3607	4.003	0.7389	15.748	0.11	2
22	1.082	4.003	0.7783	15.5956	0	2
23	1.8009	4.003	0.8568	15.5956	0	2
24	2.5146	4.003	0.9735	15.621	0	2
25	3.2207	4.003	1.1269	15.621	0	2
26	3.9192	4.003	1.3158	16.1544	0	3
27	-3.9192	3.4011	1.147	15.9004	0	2
28	-3.2207	3.4011	0.9581	15.8496	0	2
29	-2.5146	3.4011	0.8047	15.7226	0	2
30	-1.8009	3.4011	0.688	15.6972	0	2
31	-1.082	3.4011	0.6095	15.6972	0	2
32	-0.3607	3.4011	0.5701	15.748	0.11	2
33	0.3607	3.4011	0.5701	15.3416	0.12	2
34	1.082	3.4011	0.6095	15.3924	0	2
35	1.8009	3.4011	0.688	15.5956	0	2
36	2.5146	3.4011	0.8047	15.621	0.02	2
37	2207	3.4011	0.9581	15.621	0	2
38	3.9192	3.4011	1.147	15.8496	0	2
39	-4.6076	2.7915	1.2263	16.2052	0	3
40	-3.9192	2.7915	1.004	15.7734	0	2
41	-3.2207	2.7915	0.8151	15.7734	0	2
42	-2.5146	2.7915	0.6617	15.7734	0	2
43	-1.8009	2.7915	0.545	15.6718	0	2
44	-1.082	2.7915	0.4665	13.462	0	1
45	-0.3607	2.7915	0.4271	13.3096	0.12	1
46	0.3607	2.7915	0.4271	13.7668	0.12	1
47	1.082	2.7915	0.4665	13.5636	0	1

TABLE G-1. CIRCE2 INPUT DATA FOR THE SANDIA POOL-BOILER RECEIVER
(continued)

TBC-1 FACET DATA BASED ON OCTOBER 1988 SURVEY

FACET	X(m)	Y(m)	Z(m)	RADIUS (m) of curv.	BLOCK	AIM POINT
48	1.8009	2.7915	0.545	12.827	0	2
49	2.5146	2.7915	0.6617	15.5702	0	2
50	3.2207	2.7915	0.8151	15.5448	0.01	2
51	3.9192	2.7915	1.004	15.748	0	2
52	4.6076	2.7915	1.2263	16.1036	0	3
53	-4.6076	2.1768	1.1106	15.6464	0	2
54	-3.9192	2.1768	0.8883	15.6718	0	2
55	-3.2207	2.1768	0.6994	15.5194	0	2
56	-2.5146	2.1768	0.546	15.5194	0	2
57	-1.8009	2.1768	0.4293	13.1318	0	1
58	-1.082	2.1768	0.3508	13.0302	0	1
59	-0.3607	2.1768	0.3114	12.9794	0.11	1
60	0.3607	2.1768	0.3114	13.3858	0.11	1
61	1.082	2.1768	0.3508	13.1826	0	1
62	1.8009	2.1768	0.4293	13.1826	0	1
63	2.5146	2.1768	0.546	15.24	0	2
64	3.2207	2.1768	0.6994	13.0302	0	2
65	3.9192	2.1768	0.8883	13.081	0	2
66	4.6076	2.1768	1.1106	15.494	0	2
67	-5.2832	1.5596	1.2764	16.0528	0.01	3
68	-4.6076	1.5596	1.0233	16.0274	0	2
69	-3.9192	1.5596	0.8009	15.6972	0	2
70	-3.2207	1.5596	0.612	15.5448	0	2
71	-2.5146	1.5596	0.4586	13.208	0	1
72	-1.8009	1.5596	0.342	13.3858	0	1
73	-1.082	1.5596	0.2635	13.0556	0	1
74	-0.3607	1.5596	0.2241	13.0048	0.11	1
75	0.3607	1.5596	0.2241	13.1826	0.12	1
76	1.082	1.5596	0.2635	13.2588	0	1
77	1.8009	1.5596	0.342	13.3858	0	1
78	2.5146	1.5596	0.4586	13.335	0	1
79	3.2207	1.5596	0.612	15.4686	0	2
80	3.9192	1.5596	0.8009	15.5194	0	2
81	4.6076	1.5596	1.0233	15.7988	0	2
82	5.2832	1.5596	1.2764	16.0274	0.01	3
83	-5.2832	0.9373	1.2175	16.256	0.02	3
84	-4.6076	0.9373	0.9644	15.6972	02	2
85	-3.9192	0.9373	0.7421	15.621	0	2
86	-3.2207	0.9373	0.5532	15.4432	0	2
87	-2.5146	0.9373	0.3998	13.3604	0	1
88	-1.8009	0.9373	0.2831	13.081	0	1
89	-1.082	0.9373	0.2046	13.0302	0.01	1
90	-0.3607	0.9373	0.1652	13.0048	0.32	1
91	0.3607	0.9373	0.1652	13.0302	0.32	1
92	1.082	0.9373	0.2046	13.208	0.01	1
93	1.8009	0.9373	0.3998	13.5382	0	1
94	1.8009	0.9373	0.3998	13.5382	0	1

TABLE G-1. CIRCE2 INPUT DATA FOR THE SANDIA POOL-BOILER RECEIVER
(continued)

TBC-1 FACET DATA BASED ON OCTOBER 1988 SURVEY

FACET	X(m)	Y(m)	Z(m)	RADIUS (m) of curv.	BLOCK	AIM POINT
95	3.2207	0.9373	0.5532	15.7988	0	2
96	3.9192	0.9373	0.7421	15.7988	0	2
97	4.6076	0.9373	0.9644	15.7988	0	2
98	5.2832	0.9373	1.2175	16.0782	0.01	3
99	-4.6076	0.3124	0.9348	15.7226	0.05	2
100	-3.9192	0.3124	0.7125	15.5194	0.04	2
101	-3.2207	0.3124	0.5236	15.4178	0.04	2
102	-2.5146	0.3124	0.3702	13.0556	0.04	1
103	-1.8009	0.3124	0.2535	13.2334	0.04	1
104	-1.082	0.3124	0.175	13.3604	0.15	1
105	1.082	0.3124	0.175	13.0302	0.44	1
106	1.8009	0.3124	0.2535	13.208	0.44	1
107	2.5146	0.3124	0.3702	13.462	0.04	1
108	3.2207	0.3124	0.5236	15.4432	0.04	2
109	3.9192	0.3124	0.7125	15.5448	0.04	2
110	4.6076	0.3124	0.9348	15.5702	0.04	2
111	-4.6076	-0.3124	0.9348	15.9004	0.04	2
112	-3.9192	-0.3124	0.7125	15.8242	0.04	2
113	-3.2207	-0.3124	0.5236	15.6718	0.04	2
114	-2.5146	-0.3124	0.3702	13.7414	0.04	1
115	-1.8009	-0.3124	0.2535	13.1826	0.06	1
116	-1.082	-0.3124	0.175	13.1064	0.15	1
117	1.082	-0.3124	0.175	13.1826	0.44	1
118	1.8009	-0.3124	0.2535	13.2842	0.44	1
119	2.5146	-0.3124	0.3702	13.2334	0.04	1
120	3.2207	-0.3124	0.5236	15.5448	0.04	2
121	3.9192	-0.3124	0.7125	15.8242	0.04	2
122	4.6076	-0.3124	0.9348	15.9004	0.04	2
123	-5.2832	-0.9373	1.2175	15.6718	0	3
124	-4.6076	-0.9373	0.9644	15.9512	0	2
125	-3.9192	-0.9373	0.7421	15.9258	0	2
126	-3.2207	-0.9373	0.5532	15.748	0	2
127	-2.5146	-0.9373	0.3998	15.494	0	1
128	-1.8009	-0.9373	0.2831	13.2588	0	1
129	-1.082	-0.9373	0.2046	13.208	0.02	1
130	-0.3607	-0.9373	0.1652	12.954	0.3	1
131	0.3607	-0.9373	0.1652	13.335	0.3	1
132	1.082	-0.9373	0.2046	13.6144	0.01	1
133	1.8009	-0.9373	0.2831	13.081	0	1
134	2.5146	-0.9373	0.3998	13.0556	0	1
135	3.2207	-0.9373	0.5532	15.8496	0	2
136	3.9192	-0.9373	0.7421	15.8242	0	2
137	4.6076	-0.9373	0.9644	15.9766	0	2
138	5.2832	-0.9373	1.2175	15.6718	0	3
139	-5.2832	-1.5596	1.2764	15.5956	0	3
140	-4.6076	-1.5596	1.0233	15.9004	0	2
141	-3.9192	-1.5596	0.8009	15.5448	0	2

TABLE G-1. CIRCE2 INPUT DATA FOR THE SANDIA POOL-BOILER RECEIVER (continued)

TBC-1 FACET DATA BASED ON OCTOBER 1988 SURVEY

FACET	X(m)	Y(m)	Z(m)	RADIUS (m) of curv.	BLOCK	AIM POINT
142	-3.2207	-1.5596	0.612	15.6972	0	2
143	-2.5146	-1.5596	0.4586	15.9004	0	1
144	-1.8009	-1.5596	0.342	13.3604	0	1
145	-1.082	-1.5596	0.2635	13.462	0	1
146	-0.3607	-1.5596	0.2241	13.2334	0.38	1
147	0.3607	-1.5596	0.2241	13.0048	0.38	1
148	1.082	-1.5596	0.2635	13.2334	0.01	1
149	1.8009	-1.5596	0.342	13.3858	0	1
150	2.5146	-1.5596	0.4586	13.208	0	1
151	3.2207	-1.5596	0.612	15.5956	0	2
152	3.9192	-1.5596	0.8009	15.748	0	2
153	4.6076	-1.5596	1.0233	15.875	0.01	2
154	5.2832	-1.5596	1.2764	16.0274	0	3
155	-4.6076	-2.1768	1.1106	15.9766	0	2
156	-3.9192	-2.1768	0.8883	15.9512	0.01	2
157	-3.2207	-2.1768	0.6994	15.748	0	2
158	-2.5146	-2.1768	0.546	15.875	0.04	2
159	-1.8009	-2.1768	0.4293	13.462	0	1
160	-1.082	-2.1768	0.3508	13.1572	0	1
161	-0.3607	-2.1768	0.3114	13.1318	0.38	1
162	0.3607	-2.1768	0.3114	13.0048	0.38	1
163	1.082	-2.1768	0.3508	13.1572	0	1
164	1.8009	-2.1768	0.4293	13.208	0	1
165	2.5146	-2.1768	0.546	15.7226	0	2
166	3.2207	-2.1768	0.6994	15.748	0	2
167	3.9192	-2.1768	0.8883	15.9766	0	2
168	4.6076	-2.1768	1.1106	15.8496	0	2
169	-4.6076	-2.7915	1.2263	16.0782	0	3
170	-3.9192	-2.7915	1.004	15.748	0	2
171	-3.2207	-2.7915	0.8151	15.9766	0.01	2
172	-2.5146	-2.7915	0.6617	15.621	0	2
173	-1.8009	-2.7915	0.545	15.5194	0	2
174	-1.082	-2.7915	0.4665	13.5128	0	1
175	-0.3607	-2.7915	0.4271	15.3162	0.2	1
176	0.3607	-2.7915	0.4271	13.0048	0.21	1
177	1.082	-2.7915	0.4665	13.0048	0	1
178	1.8009	-2.7915	0.545	15.5448	0	2
179	2.5146	-2.7915	0.6617	15.6718	0	2
180	3.2207	-2.7915	0.8151	15.748	0	2
181	3.9192	-2.7915	1.004	15.9512	0	2
182	4.6076	-2.7915	1.2263	16.1036	0.02	3
183	-3.9192	-3.4011	1.147	15.6718	0	2
184	-3.2207	-3.4011	0.9581	15.9004	0	2
185	-2.5146	-3.4011	0.8047	15.621	0.01	2
186	-1.8009	-3.4011	0.688	15.6464	0	2
187	-1.082	-3.4011	0.6095	15.5448	0	2
188	-0.3607	-3.4011	0.5701	15.6464	0.2	2

TABLE G-1. CIRCE2 INPUT DATA FOR THE SANDIA POOL-BOILER RECEIVER (continued)

TBC-1 FACET DATA BASED ON OCTOBER 1988 SURVEY

FACET	X(m)	Y(m)	Z(m)	RADIUS (m) of curv.	BLOCK	AIM POINT
189	0.3607	-3.4011	0.5701	15.4432	0.2	2
190	1.082	-3.4011	0.6095	15.6972	0	2
191	1.8009	-3.4011	0.688	15.8496	0	2
192	2.5146	-3.4011	0.8047	15.9004	0	2
193	3.2207	-3.4011	0.9581	15.4178	0	2
194	3.9192	-3.4011	1.147	15.621	0	2
195	-3.9192	-4.003	1.3158	16.0782	0	3
196	-3.2207	-4.003	1.1269	15.5702	0	2
197	-2.5146	-4.003	0.9735	15.8496	0	2
198	-1.8009	-4.003	0.8568	15.9258	0	2
199	-1.082	-4.003	0.7783	15.621	0	2
200	-0.3607	-4.003	0.7389	15.7226	0.2	2
201	0.3607	-4.003	0.7389	15.6972	0.2	2
202	1.082	-4.003	0.7783	15.4686	0	2
203	1.8009	-4.003	0.8568	15.7988	0	2
204	2.5146	-4.003	0.9735	15.3416	0	2
205	3.2207	-4.003	1.1269	15.748	0	2
206	3.9192	-4.003	1.3158	16.002	0	3
207	-3.2207	-4.5974	1.3205	16.5354	0	3
208	-2.5146	-4.5974	1.3205	15.6972	0	2
209	-1.8009	-4.5974	1.0504	15.5956	0	2
210	-1.082	-4.5974	0.9719	15.5702	0	2
211	-0.3607	-4.5974	0.9325	15.6718	0.21	2
212	0.3607	-4.5974	0.9325	15.6464	0.2	2
213	1.082	-4.5974	0.9719	15.5702	0	2
214	1.8009	-4.5974	1.0504	15.5956	0	2
215	2.5146	-4.5974	1.1671	15.9258	0	2
216	3.2207	-4.5974	1.3205	16.4084	0	3
217	-1.8009	-5.1816	1.2668	15.875	0	3
218	-1.082	-5.1816	1.1883	15.748	0	3
219	1.082	-5.1816	1.1883	15.748	0	3
220	1.8009	-5.1816	1.2668	16.6116	0.01	3

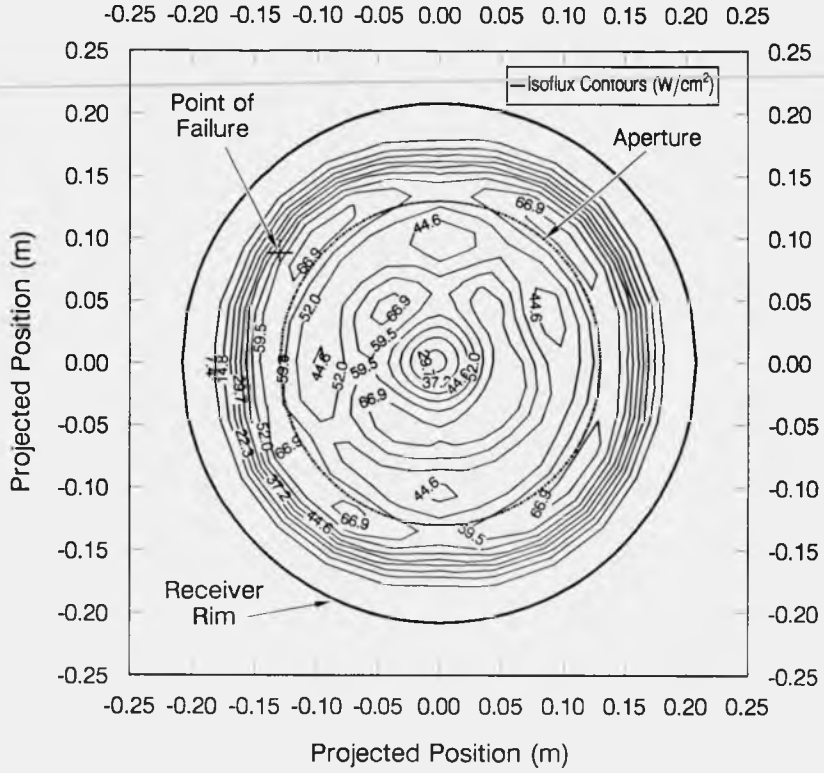

Figure G-3. CIRCE2-predicted incident solar flux for the tested receiver. The integrated solar power of 65.3 kW is approximately equal to calorimeter measurements. Perfect tracking of TBC-1 was assumed. The image is reversed left-to-right (like a mirror image) of what an observer, standing at the concentrator looking at the receiver, sees. The peak flux intensity is 75 W/cm².

Based on infrared thermography results, the concentrator may have been mistracked during the last weeks of testing. In these tests, the receiver aperture diameter was expanded from 22 to 26 cm (8.7 to 10.2 in.). The TBC nominal focus diameter is about 18 cm (7.1 in.). Figure G-4 is a CIRCE2 prediction of the incident solar flux distribution with a 3-milliradian (mrd) azimuth mistrack. This predicted flux distribution appears to match the infrared camera startup temperature distribution (see Figure P-3 in Appendix P of this report) and places a flux "hot spot" in the vicinity of the failure.

To assess the actual flux intensity, a flux gage was positioned at the point of failure, and the TBC-1 tracking was adjusted while looking for a local "hot spot." Within the uncertainty of the measurements, the magnitude of the peak flux and the presence of a localized area of high flux was substantiated. However, because tracking offsets are determined visually (using light scattered from the edge of the aperture as a reference) and are input to the automatic tracking system at the beginning of each test, it is impossible to substantiate whether the same tracking error occurred at the time of the failure.

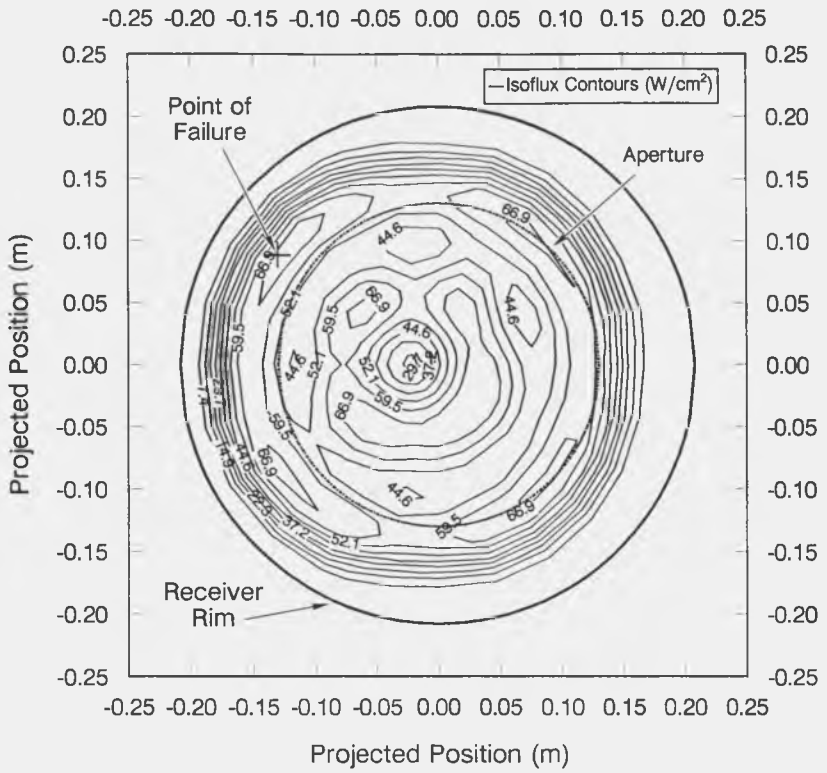

Figure G-4. CIRCE2-predicted incident solar flux for the tested receiver assuming a 3-mrd concentrator mistrack—consistent with observation with the infrared camera. The integrated solar power is 65.0 kW. The image is reversed left-to-right (like a mirror image) of what an observer, standing at the concentrator looking at the receiver, sees. The peak flux intensity is 74 W/cm².

References

Moreno, J. B., and C. E. Andraka. 1989. *Test Results from Bench-Scale Sodium-Pool-Boiler Solar Receiver.* SAND89-0899. Albuquerque, NM: Sandia National Laboratories.

Ratzel, A. C., and B. D. Boughton. 1987. *CIRCE.001: A Computer Code for Analysis of Point Focus Concentrators with Flat Targets.* SAND86-1866. Albuquerque, NM: Sandia National Laboratories.

Stirling Technology Company. 1988. *25-kWe Solar Thermal Stirling Hydraulic Engine System, Final Conceptual Design Report.* DOE/NASA/0371-1, NASA CR- 180889. National Aeronautics and Space Administration, Lewis Research Center, Cleveland, OH.

Sandia National Laboratories
Albuquerque, New Mexico 87185

date: February 14, 1990

to: R. B. Diver, 6217

from: R. E. Hogan, 1513

subject: Evaluation of Potential Weld Overheating in Reflux Pool-Boiler Receivers

SUMMARY

Possible overheating of the weld between the absorber and the aft-dome in reflux pool-boiler receivers is a concern because overheating could result in catastrophic weld failure. Overheating conditions could occur if there is insufficient convective cooling of the absorber by the sodium pool. In general, weld integrity begins to be considered as a potential problem at a temperature of about 900°C and as a definite problem when greater than 1000°C. The severity of this threat was assessed using a numerical model developed for these receivers. For design operating conditions and with minimum cooling (insulated on the sodium-side of absorber and no convective air-side cooling) of the absorber near the weld, the maximum predicted weld temperature was 923°C. The maximum weld temperature for this limiting case is slightly into the temperature range that could represent a threat. For more likely boundary conditions, the case with stationary sodium near the weld region, the maximum weld temperature was 895°C. For normal operating conditions, the maximum computed weld temperature is 805°C. Based on this analysis, weld overheating does not represent a significant concern. This memo documents the analysis to determine the maximum weld temperatures.

INTRODUCTION

Possible overheating of the weld between the front absorber and the aft-dome in reflux pool-boiler receivers has been identified as a potential threat to these receivers. Overheating could occur due to inadequate convective cooling of the absorber in this region. The convective cooling of the sodium could be reduced in this area because the distances between the absorber and the aft-dome are small near the weld. Weld overheating begins to become a concern when the weld temperature reaches the 900-950°C range. Temperatures above 1000°C are a serious threat to the weld and are unacceptable.

Figure 1 shows a diagram of the reflux pool-boiler receiver. The aperture is 22 cm in diameter and the absorber is a 71°, 21.9 cm spherical section of 0.032 inch (32 mil) 316L stainless steel. This receiver is designed for operation on the Test Bed Concentrators.

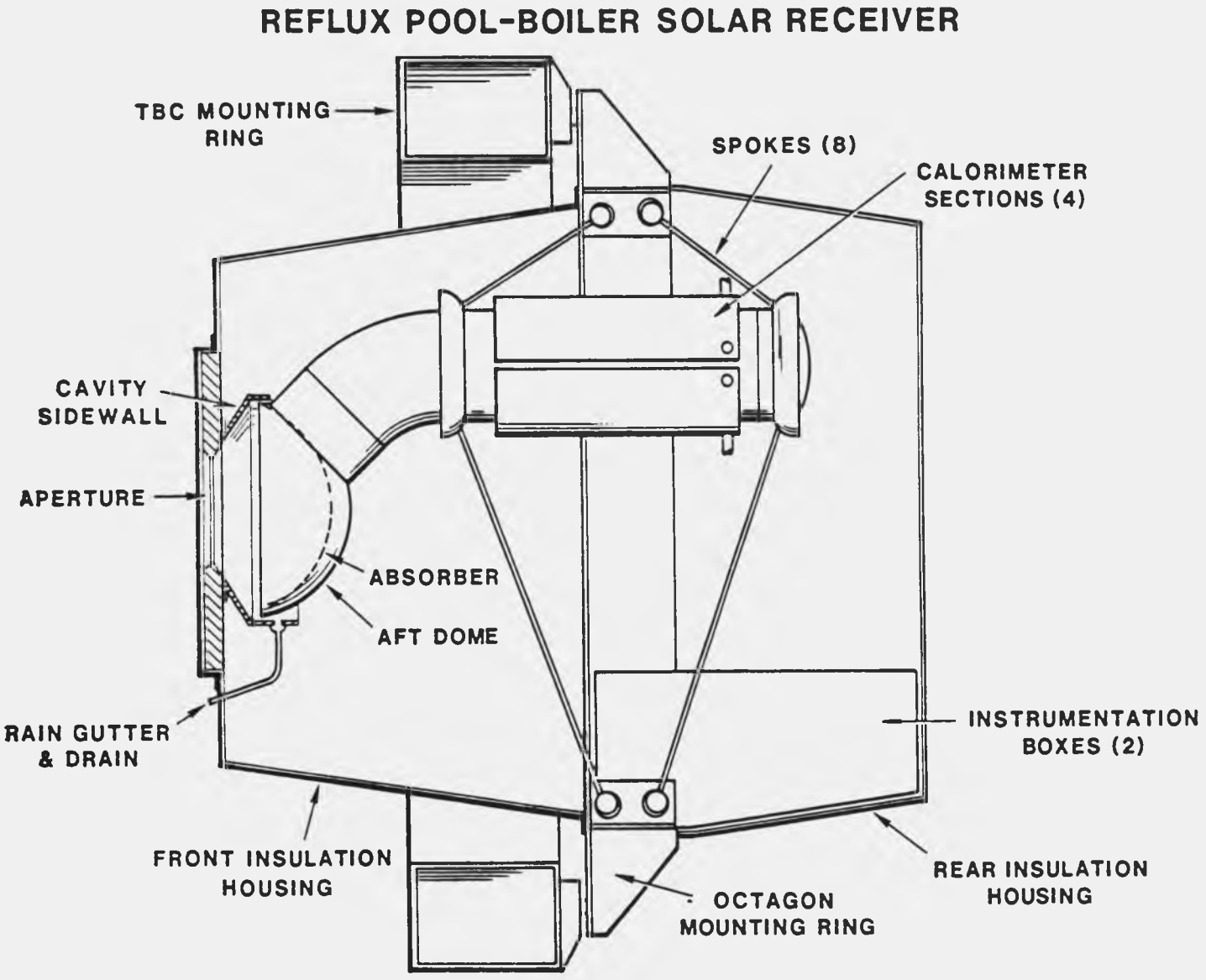

Figure 1. Diagram of the reflux pool-boiler receiver.

Figure 2 shows the numerical model of the receiver. The model considers the absorber-dome, aft-dome, sidewall, aperture board, aluminum housing, and insulation near the front of the receiver. The numerical model includes both the infrared and solar radiative heat transfer in the cavity, the conductive heat transfer within the receiver, and the convective heat transfer from both the cavity and the exterior surfaces of the receiver to the surroundings. The problem is assumed axisymmetric and steady-state solutions with minimum cooling in the weld region have been computed to assess the severity of the possible overheating of the weld between the absorber and the aft-dome. The numerical model is formulated using the Finite Control Volume Method [1]. This memo documents the analysis and the results of the investigation.

NUMERICAL MODEL

Operating and Boundary Conditions

To assess the significance of this potential problem, the temperature distribution was predicted for the maximum design operation conditions with minimal cooling near the weld. The maximum design operating conditions are a total solar input power of 75 kW and a sodium pool temperature of 800°C. The incident solar flux distribution on the absorber was calculated using the CIRCE2 computer code. Figure 3 shows the incident solar flux as a function of angle, ϕ, from the receiver axis of symmetry (see Figure 2). Table 1 shows the material properties used in the numerical model.

Table 1. Material properties used in the numerical model.

Material	k (W/mK)	ϵ	α_{solar}	Reference
316L stainless steel	12.46	0.85*	0.87*	2
Alumina insulating board	0.053 (@533°C) - 0.235 (@1644°C)	0.80*	0.15*	3
Alumina bulk insulation	0.0622 (@480°C) - 0.242 (@1256°C)	- -	- -	4
Sodium	80.3 (@477°C) - 59.7 (@977°C)	- -	- -	5
*A. Rod Mahoney, Division 6224				

The absorbed energy is lost through the cavity aperture and conducted through the absorber to the sodium pool. The receiver cavity (absorber/sidewall) loses energy by solar reflection, infrared radiation, and convective cooling to the surroundings. The sodium-side of the absorber is convectively cooled by the sodium. In addition, the exterior of the receiver housing loses energy to the surroundings by both convection and radiation.

In normal operation, the convective cooling of the sodium-side of the absorber would provide a near isothermal boundary at the sodium temperature. For this case, the temperature is specified at 800°C over the entire sodium-side of the absorber ($0° < \phi < 68.5°$). The weld is approximately 3/8 inch long and extends between $68.5° < \phi < 71.0°$.

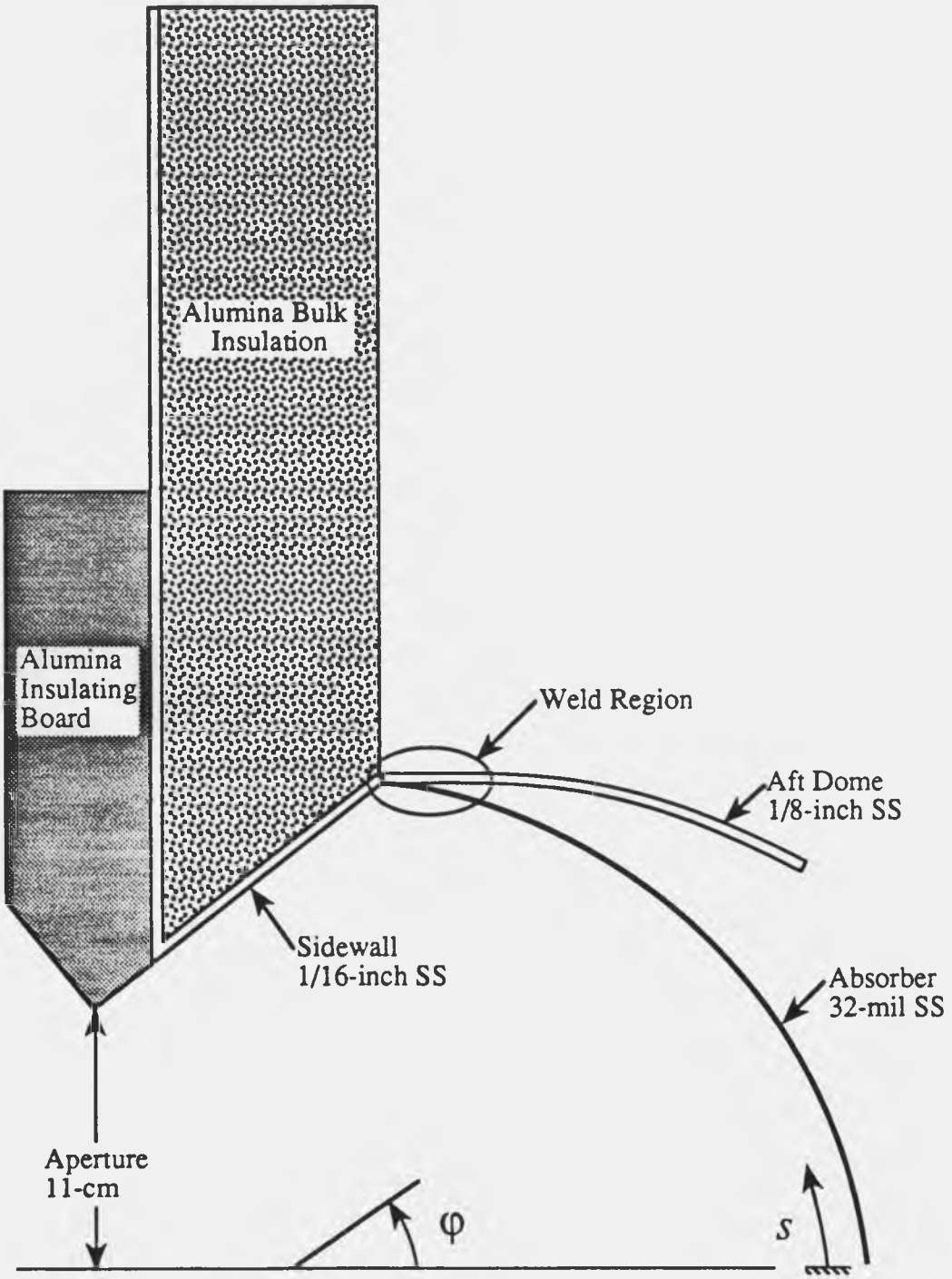

Figure 2. Numerical model of the axisymmetric pool-boiler reflux receiver.

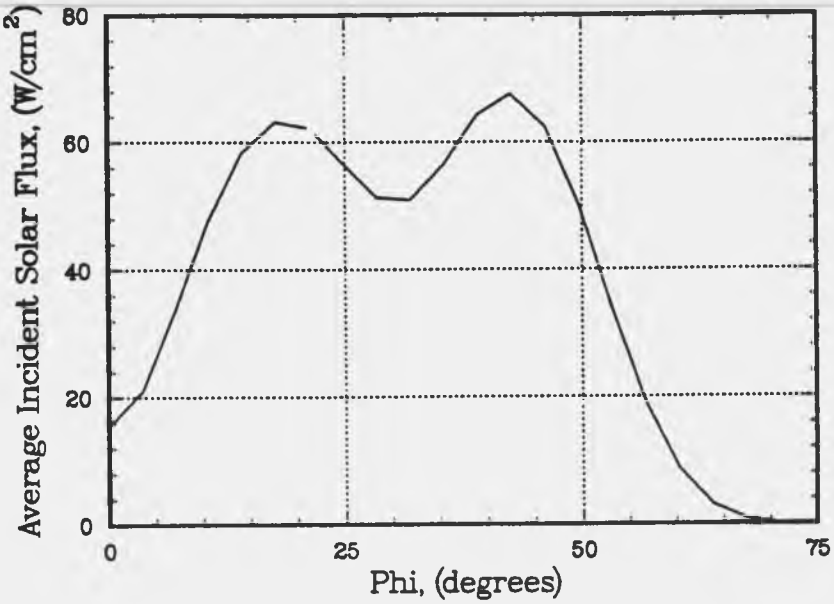

Figure 3. Incident solar flux distribution on the absorber as calculated by CIRCE2.

To compute the maximum weld temperature, calculations were made with minimal cooling near the weld. On the air-side of the absorber, the convective cooling of the air was neglected. On the sodium-side of the absorber, the boundary was divided into a specified temperature region and an insulated region. For the center region of the absorber ($0° < \phi < 59.2°$), which is 72% of the absorber surface area, the sodium-side absorber temperature was specified at 800°C. Over the rest of the absorber to the weld ($59.2° < \phi < 68.5°$), which is 22% of the absorber surface area, the sodium-side of the absorber was assumed insulated. Although the insulated boundary condition will provide minimum cooling and result in maximum weld temperatures, this condition is not the most likely situation.

Since the narrow region between the absorber and the aft-dome will not actually be void of sodium, but will more likely be filled with stationary sodium, this represents a more realistic situation for potential weld overheating. For this case, the model includes elements representing the stationary sodium within the region between the absorber and the aft-dome ($59.2° < \phi < 68.5°$). Due to the large thermal conductivity of the sodium, these boundary conditions are less threatening to the weld than the insulated boundary conditions.

Results

Figure 4 shows the temperature distribution (symbols denote nodes) along both the absorber and the sidewall with and without convective cooling along the air-side of the

absorber. The incident and net solar flux distributions (averaged for each element) are also shown. The distance, s, in these figures is the distance from the centerline along the absorber and then along the sidewall. Since the absorber temperature is dominated by the sodium temperature, there is little difference between the computed absorber temperatures with and without air-side convection. Increasing the convective coefficient, increases the energy loss from the receiver, but has an insignificant effect on the absorber temperature. The small increase in the absorber temperature near where the sidewalls and the absorber meet is due to the increased radiation from the hotter sidewalls. Since the sidewalls are insulated, the sidewall temperatures are significantly affected by the convection coefficient. Without convection, most of the solar and infrared radiation absorbed by the sidewall must be reradiated. For a convective coefficient of 5 W/m^{2}K, the sidewall temperatures decrease 45-50°C relative to the convectionless case.

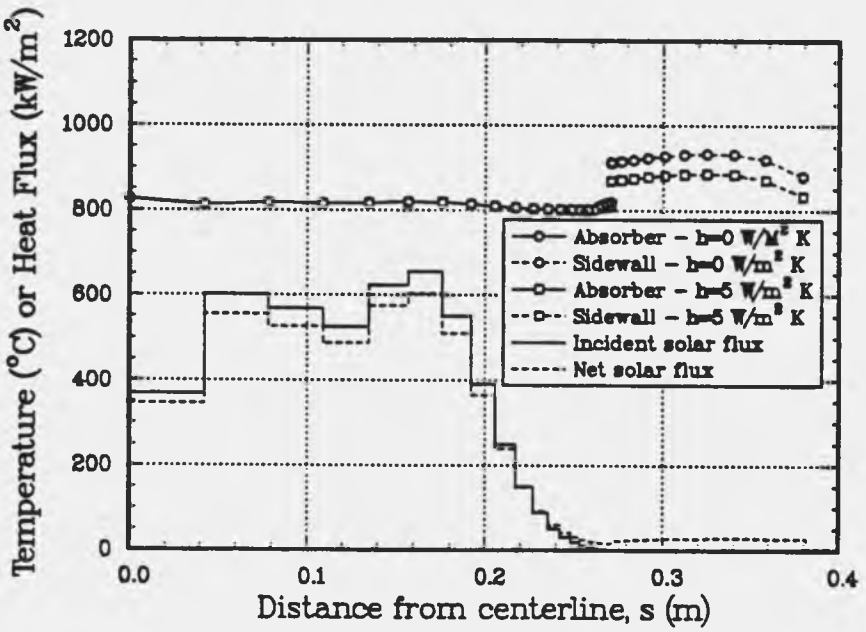

Figure 4. Air-side absorber temperature distribution with (5 W/m^{2}K) and without air-side convection.

Figure 5 shows both the effect of increasing the number of nodes in the absorber and the aft-dome and the effect of varying the distribution of nodes near the weld on the air-side absorber surface temperature for an insulated boundary ($59.2° < \phi < 68.5°$) on the sodium-side of the absorber. Table 2 gives the number of nodes within the absorber and the aft-dome for three different grids considered. As the number of nodes in the insulated region ($59.2° < \phi < 68.5°$) increases, the temperature distribution in this region is better resolved. The temperature distributions along the sidewall are identical for grids 5 and 5A. These operating and boundary conditions represent the worst case conditions with respect to the potential for weld overheating. For grid 5A, the maximum absorber

temperature occurs on the air-side and is 1059°C, and the average weld temperature is 923°C. This weld temperature is sufficiently high to cause concern of possible weld overheating. However, since this boundary condition represents a limiting condition, the threat to the weld is regarded as neither likely nor critical.

Although the insulated boundary on the sodium-side of the absorber is the worst case condition, it is not the most likely. If there is insufficient sodium motion in the region near the absorber and aft-dome weld, then the most likely situation is to have stationary sodium in this region. Figure 6 shows the air-side absorber surface temperature distribution for the specified temperature boundary, the stationary sodium boundary, and the insulated boundary conditions. For the stationary sodium (the most likely condition), the maximum absorber temperature occurs on the air-side and is 899°C and the average weld temperature is 895°C. This temperature is less than the insulated boundary (worst case) but greater than the specified temperature boundary (normal case).

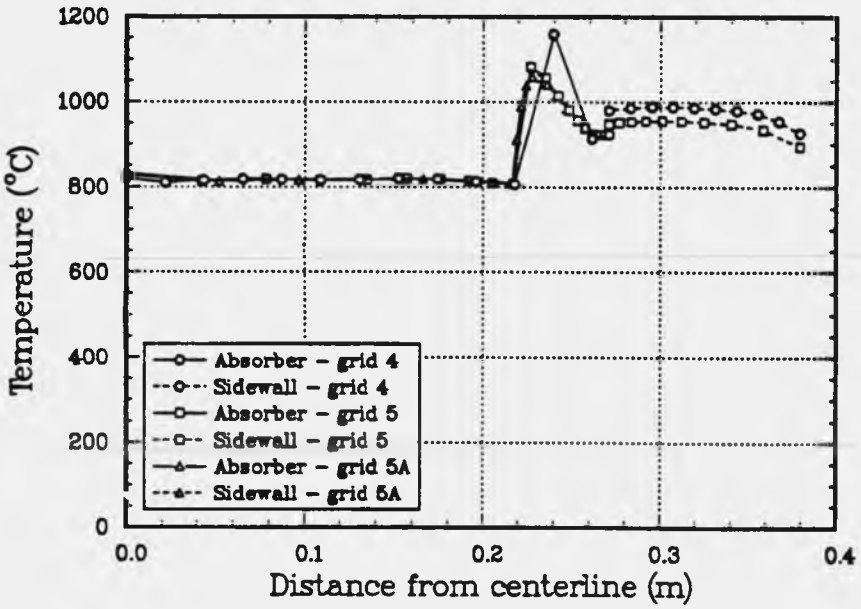

Figure 5. Air-side absorber temperature distribution for computational grids 4, 5, and 5A.

Table 2. Number of nodes in absorber and aft-dome for the insulated boundary condition ($59.2° < \phi < 68.5°$)

	Grid		
	4	5	5A
Weld $68.5° < \phi < 71.0°$	10	45	45
Insulated $59.2° < \phi < 68.5°$	10	63	90
Fixed Temperature $0° < \phi < 59.2°$	50	81	54
Absorber $0° < \phi < 71.0°$	75	189	189
Aft-Dome	40	91	91
Aft-Dome and Absorber	115	280	280
Total Model	395	562	562

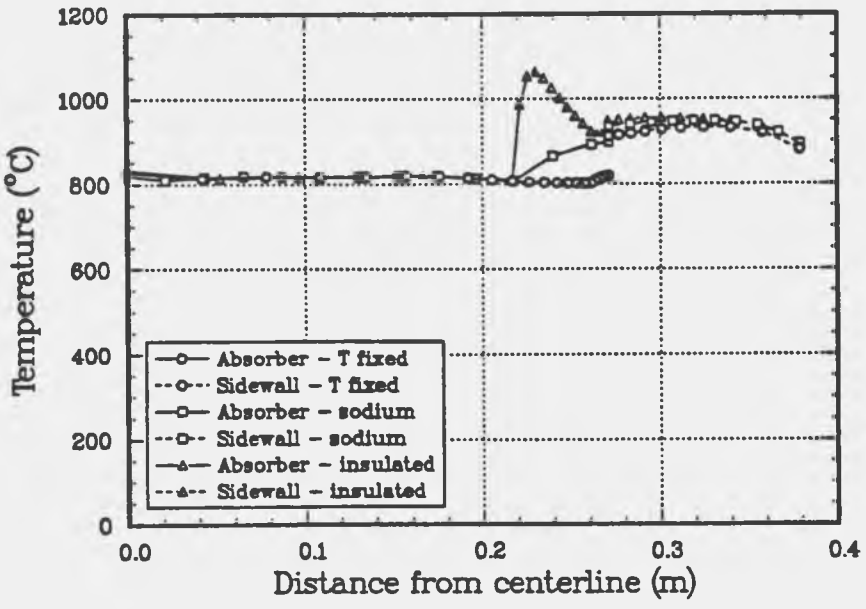

Figure 6. Air-side absorber temperature distribution for the specified temperature, the stationary sodium, and the insulated sodium-side boundary conditions near the weld ($59.2° < \phi < 68.5°$).

CONCLUSIONS

The maximum temperature of the weld between the absorber-dome and the aft-dome has been computed for no air-side convective cooling and the sodium-side of the absorber insulated over $59.2° < \phi < 68.5°$. For these conditions, the maximum weld temperature was 923°C, high enough to be of some concern, but well below the 1000°C limit. For the situation where the stationary sodium covers the absorber between $59.2° < \phi < 68.5°$, the maximum computed weld temperature was 895°C, which represents a small overheating threat to the weld. For normal operating conditions, an air-side convection coefficient of 5 W/m^2k and a specified sodium-side boundary temperature of 800°C, the average weld temperature was 805°C. Based on this analysis, overheating of the weld between the absorber and the aft-dome weld does not appear to be a significant threat.

References

1. Hogan, R. E., Diver, R. B., and Stine, W. B., Comparison of a Cavity Solar Receiver Numerical Model and Experimental Data, Eleventh Annual ASME Solar Energy Conference, San Diego, CA, April 2-5, 1989.

2. Myers, G. E., *Analytical Methods in Conduction Heat Transfer*, McGraw-Hill, New York, pg. 492, 1971.

3. Carborundum Resistant Materials Company, "Fiberfrax Duraboard 3000," Technical Note C-739H, 1982.

4. Carborundum Resistant Materials Company, "Fiberfrax Most-Pack D," Technical Note C734-G, 1981.

5. Holman, J. P., *Heat Transfer*, 4th edition, McGraw-Hill, New York, pg. 506, 1976.

REH:1513:tgr

Copy to:
1510 J. W. Nunziato
1511 D. K. Gartling
1512 J. C. Cummings
1513 D. W. Larson
1513 D. R. Adkins
1513 R. E. Hogan
1520 L. W. Davison
1521 C. M. Stone
1530 J. R. Asay
1550 C. W. Peterson
2542 J. B. Moreno
6210 B. W. Marshall
6215 J. T. Holmes
6216 C. E. Tyner
6217 P. C. Klimas
6217 C. E. Andraka
6217 T. A. Moss
6217 File 5.3.2
1513 Day File

Sandia National Laboratories
Albuquerque, New Mexico 87185

date: February 14, 1990

to: R. B. Diver, 6217

from: R. E. Hogan, 1513

subject: Evaluation of Potential Weld Overheating in Reflux Pool-Boiler Receivers

SUMMARY

Possible overheating of the weld between the absorber and the aft-dome in reflux pool-boiler receivers is a concern because overheating could result in catastrophic weld failure. Overheating conditions could occur if there is insufficient convective cooling of the absorber by the sodium pool. In general, weld integrity begins to be considered as a potential problem at a temperature of about 900°C and as a definite problem when greater than 1000°C. The severity of this threat was assessed using a numerical model developed for these receivers. For design operating conditions and with minimum cooling (insulated on the sodium-side of absorber and no convective air-side cooling) of the absorber near the weld, the maximum predicted weld temperature was 923°C. The maximum weld temperature for this limiting case is slightly into the temperature range that could represent a threat. For more likely boundary conditions, the case with stationary sodium near the weld region, the maximum weld temperature was 895°C. For normal operating conditions, the maximum computed weld temperature is 805°C. Based on this analysis, weld overheating does not represent a significant concern. This memo documents the analysis to determine the maximum weld temperatures.

INTRODUCTION

Possible overheating of the weld between the front absorber and the aft-dome in reflux pool-boiler receivers has been identified as a potential threat to these receivers. Overheating could occur due to inadequate convective cooling of the absorber in this region. The convective cooling of the sodium could be reduced in this area because the distances between the absorber and the aft-dome are small near the weld. Weld overheating begins to become a concern when the weld temperature reaches the 900-950°C range. Temperatures above 1000°C are a serious threat to the weld and are unacceptable.

Figure 1 shows a diagram of the reflux pool-boiler receiver. The aperture is 22 cm in diameter and the absorber is a 71°, 21.9 cm spherical section of 0.032 inch (32 mil) 316L stainless steel. This receiver is designed for operation on the Test Bed Concentrators.

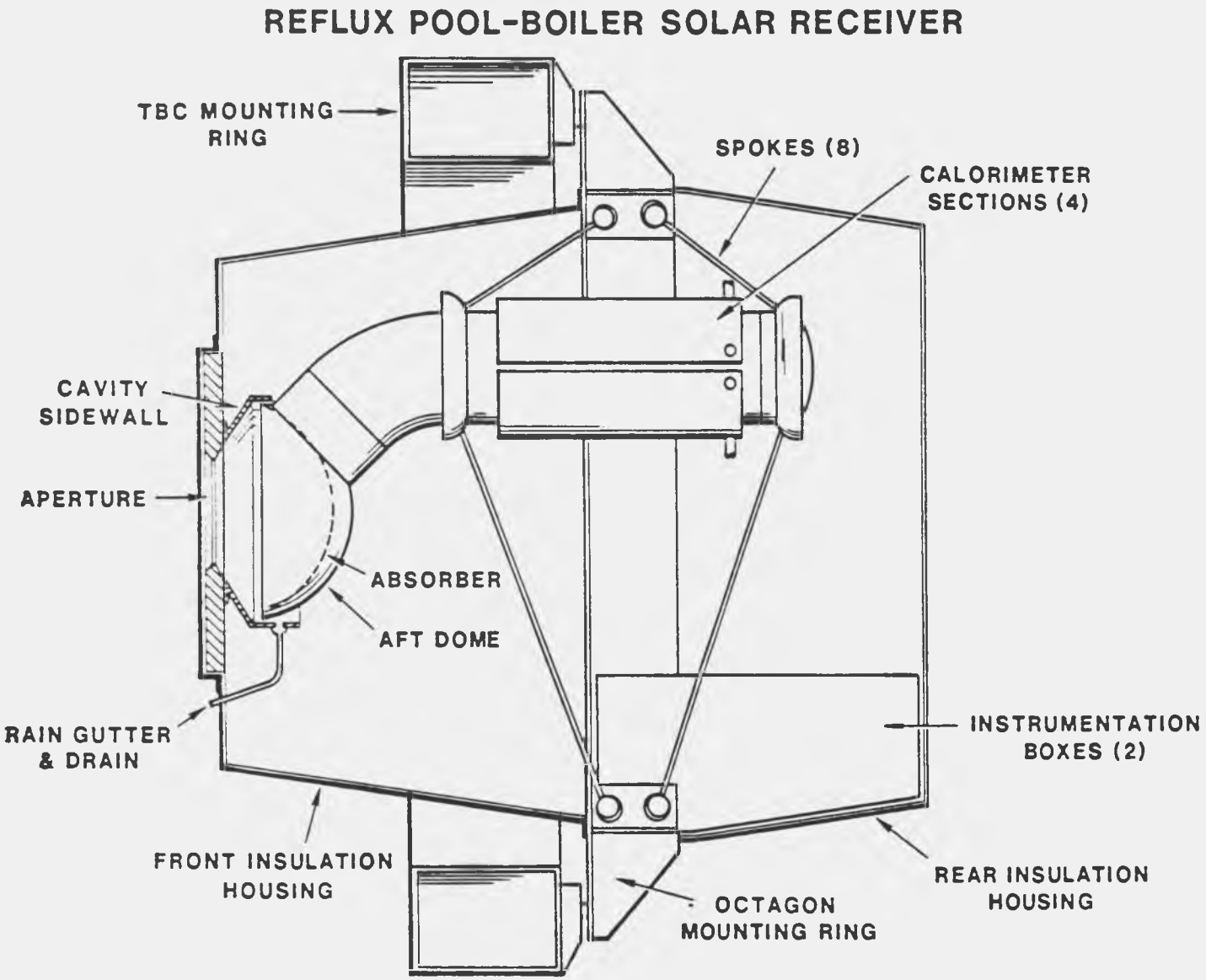

Figure 1. Diagram of the reflux pool-boiler receiver.

Figure 2 shows the numerical model of the receiver. The model considers the absorber-dome, aft-dome, sidewall, aperture board, aluminum housing, and insulation near the front of the receiver. The numerical model includes both the infrared and solar radiative heat transfer in the cavity, the conductive heat transfer within the receiver, and the convective heat transfer from both the cavity and the exterior surfaces of the receiver to the surroundings. The problem is assumed axisymmetric and steady-state solutions with minimum cooling in the weld region have been computed to assess the severity of the possible overheating of the weld between the absorber and the aft-dome. The numerical model is formulated using the Finite Control Volume Method [1]. This memo documents the analysis and the results of the investigation.

NUMERICAL MODEL

Operating and Boundary Conditions

To assess the significance of this potential problem, the temperature distribution was predicted for the maximum design operation conditions with minimal cooling near the weld. The maximum design operating conditions are a total solar input power of 75 kW and a sodium pool temperature of 800°C. The incident solar flux distribution on the absorber was calculated using the CIRCE2 computer code. Figure 3 shows the incident solar flux as a function of angle, ϕ, from the receiver axis of symmetry (see Figure 2). Table 1 shows the material properties used in the numerical model.

Table 1. Material properties used in the numerical model.

Material	k (W/mK)	ϵ	α_{solar}	Reference
316L stainless steel	12.46	0.85*	0.87*	2
Alumina insulating board	0.053 (@533°C) - 0.235 (@1644°C)	0.80*	0.15*	3
Alumina bulk insulation	0.0622 (@480°C) - 0.242 (@1256°C)	- -	- -	4
Sodium	80.3 (@477°C) - 59.7 (@977°C)	- -	- -	5
*A. Rod Mahoney, Division 6224				

The absorbed energy is lost through the cavity aperture and conducted through the absorber to the sodium pool. The receiver cavity (absorber/sidewall) loses energy by solar reflection, infrared radiation, and convective cooling to the surroundings. The sodium-side of the absorber is convectively cooled by the sodium. In addition, the exterior of the receiver housing loses energy to the surroundings by both convection and radiation.

In normal operation, the convective cooling of the sodium-side of the absorber would provide a near isothermal boundary at the sodium temperature. For this case, the temperature is specified at 800°C over the entire sodium-side of the absorber ($0° < \phi < 68.5°$). The weld is approximately 3/8 inch long and extends between $68.5° < \phi < 71.0°$.

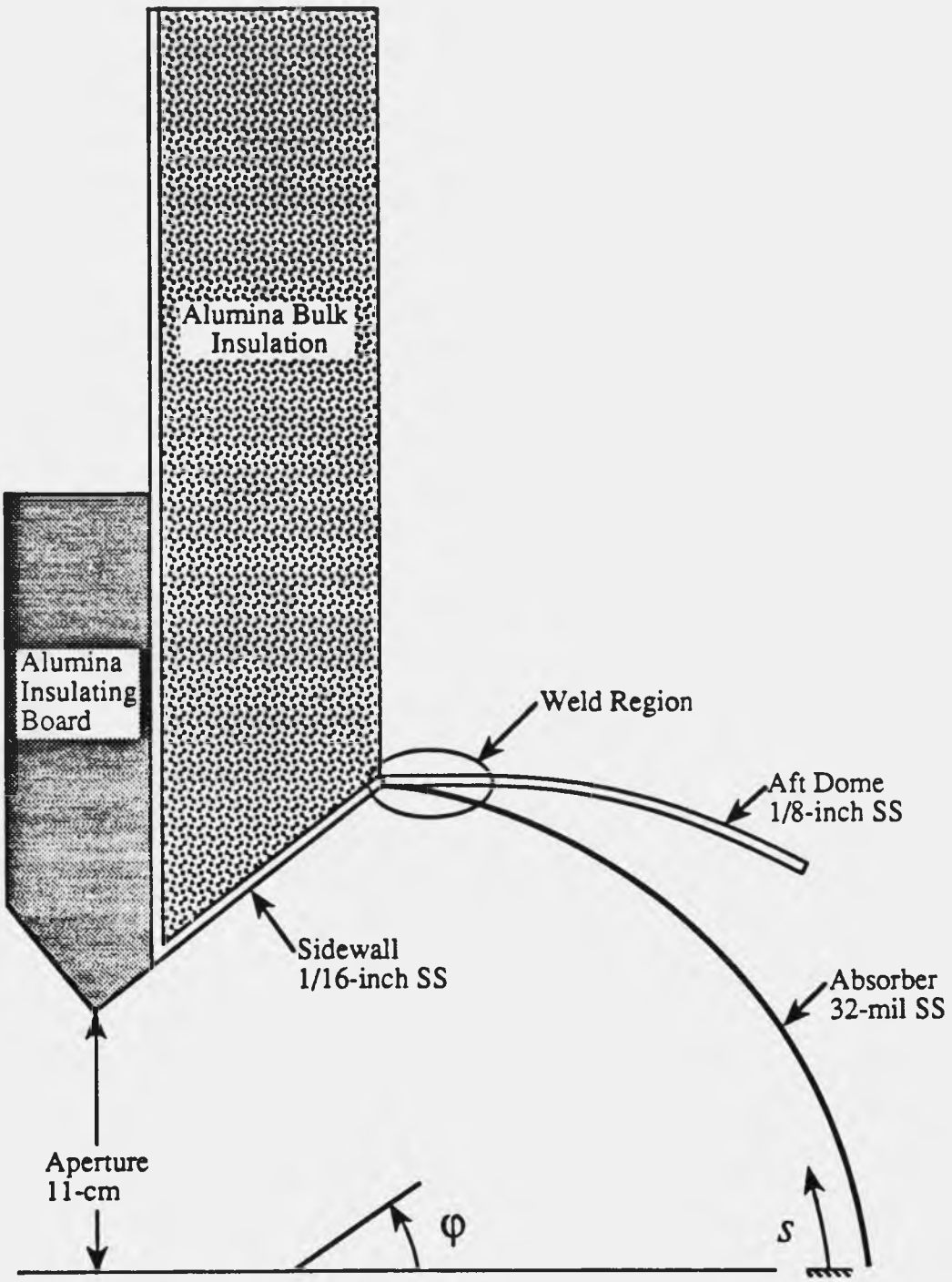

Figure 2. Numerical model of the axisymmetric pool-boiler reflux receiver.

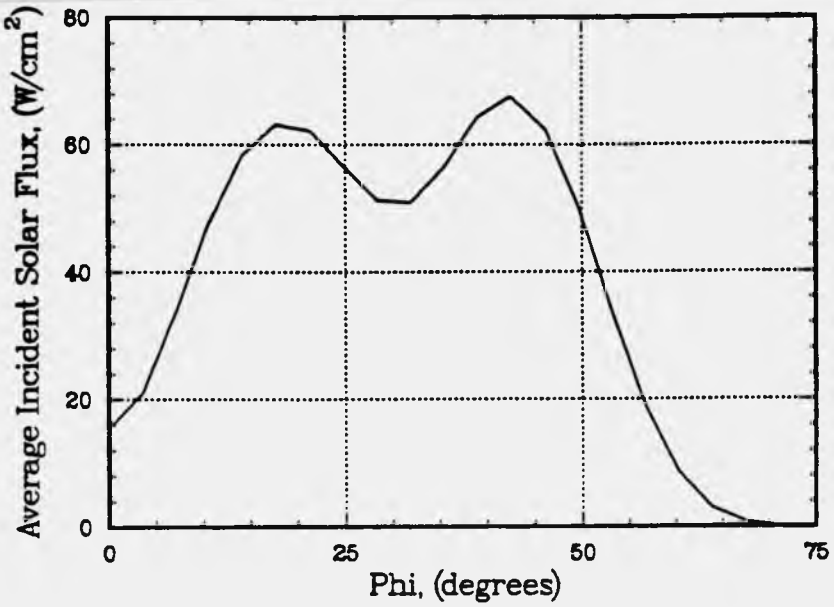

Figure 3. Incident solar flux distribution on the absorber as calculated by CIRCE2.

To compute the maximum weld temperature, calculations were made with minimal cooling near the weld. On the air-side of the absorber, the convective cooling of the air was neglected. On the sodium-side of the absorber, the boundary was divided into a specified temperature region and an insulated region. For the center region of the absorber ($0° < \phi < 59.2°$), which is 72% of the absorber surface area, the sodium-side absorber temperature was specified at 800°C. Over the rest of the absorber to the weld ($59.2° < \phi < 68.5°$), which is 22% of the absorber surface area, the sodium-side of the absorber was assumed insulated. Although the insulated boundary condition will provide minimum cooling and result in maximum weld temperatures, this condition is not the most likely situation.

Since the narrow region between the absorber and the aft-dome will not actually be void of sodium, but will more likely be filled with stationary sodium, this represents a more realistic situation for potential weld overheating. For this case, the model includes elements representing the stationary sodium within the region between the absorber and the aft-dome ($59.2° < \phi < 68.5°$). Due to the large thermal conductivity of the sodium, these boundary conditions are less threatening to the weld than the insulated boundary conditions.

Results

Figure 4 shows the temperature distribution (symbols denote nodes) along both the absorber and the sidewall with and without convective cooling along the air-side of the

absorber. The incident and net solar flux distributions (averaged for each element) are also shown. The distance, s, in these figures is the distance from the centerline along the absorber and then along the sidewall. Since the absorber temperature is dominated by the sodium temperature, there is little difference between the computed absorber temperatures with and without air-side convection. Increasing the convective coefficient, increases the energy loss from the receiver, but has an insignificant effect on the absorber temperature. The small increase in the absorber temperature near where the sidewalls and the absorber meet is due to the increased radiation from the hotter sidewalls. Since the sidewalls are insulated, the sidewall temperatures are significantly affected by the convection coefficient. Without convection, most of the solar and infrared radiation absorbed by the sidewall must be reradiated. For a convective coefficient of 5 W/m^{2}K, the sidewall temperatures decrease 45-50°C relative to the convectionless case.

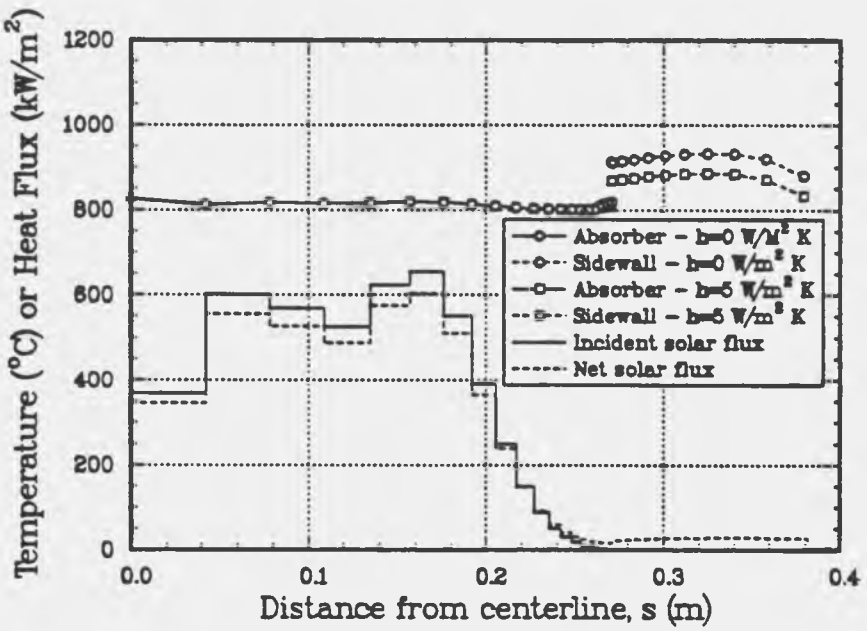

Figure 4. Air-side absorber temperature distribution with (5 W/m^{2}K) and without air-side convection.

Figure 5 shows both the effect of increasing the number of nodes in the absorber and the aft-dome and the effect of varying the distribution of nodes near the weld on the air-side absorber surface temperature for an insulated boundary ($59.2° < \phi < 68.5°$) on the sodium-side of the absorber. Table 2 gives the number of nodes within the absorber and the aft-dome for three different grids considered. As the number of nodes in the insulated region ($59.2° < \phi < 68.5°$) increases, the temperature distribution in this region is better resolved. The temperature distributions along the sidewall are identical for grids 5 and 5A. These operating and boundary conditions represent the worst case conditions with respect to the potential for weld overheating. For grid 5A, the maximum absorber

temperature occurs on the air-side and is 1059°C, and the average weld temperature is 923°C. This weld temperature is sufficiently high to cause concern of possible weld overheating. However, since this boundary condition represents a limiting condition, the threat to the weld is regarded as neither likely nor critical.

Although the insulated boundary on the sodium-side of the absorber is the worst case condition, it is not the most likely. If there is insufficient sodium motion in the region near the absorber and aft-dome weld, then the most likely situation is to have stationary sodium in this region. Figure 6 shows the air-side absorber surface temperature distribution for the specified temperature boundary, the stationary sodium boundary, and the insulated boundary conditions. For the stationary sodium (the most likely condition), the maximum absorber temperature occurs on the air-side and is 899°C and the average weld temperature is 895°C. This temperature is less than the insulated boundary (worst case) but greater than the specified temperature boundary (normal case).

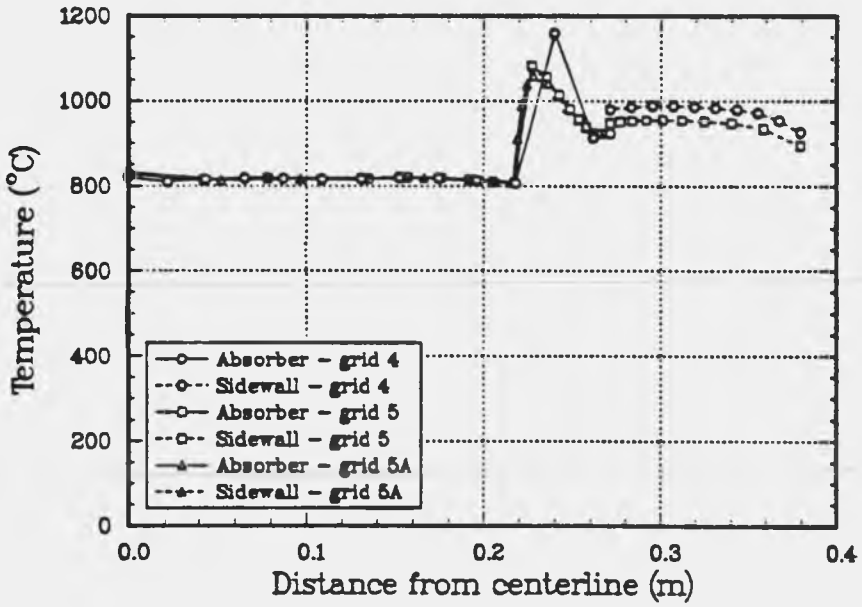

Figure 5. Air-side absorber temperature distribution for computational grids 4, 5, and 5A.

Table 2. Number of nodes in absorber and aft-dome for the insulated boundary condition ($59.2° < \phi < 68.5°$)

	Grid		
	4	5	5A
Weld $68.5° < \phi < 71.0°$	10	45	45
Insulated $59.2° < \phi < 68.5°$	10	63	90
Fixed Temperature $0° < \phi < 59.2°$	50	81	54
Absorber $0° < \phi < 71.0°$	75	189	189
Aft-Dome	40	91	91
Aft-Dome and Absorber	115	280	280
Total Model	395	562	562

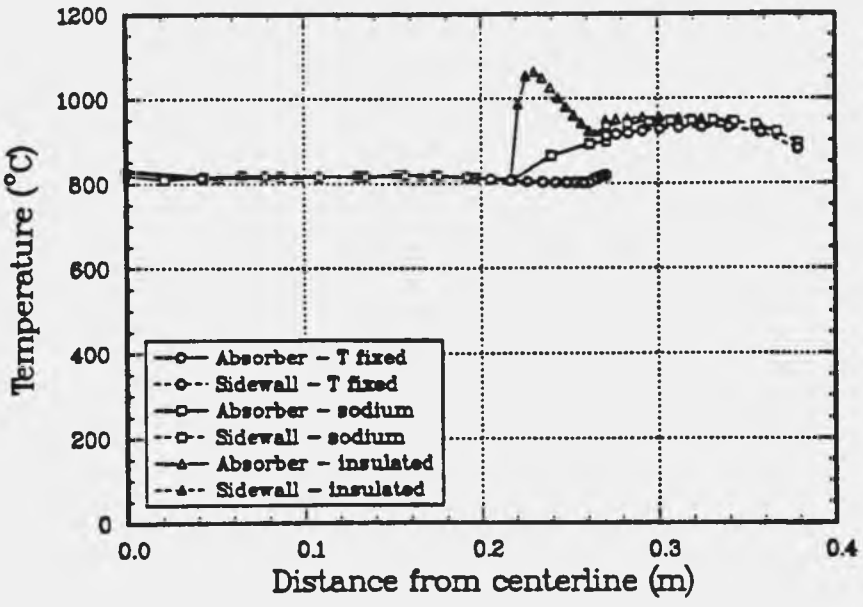

Figure 6. Air-side absorber temperature distribution for the specified temperature, the stationary sodium, and the insulated sodium-side boundary conditions near the weld ($59.2° < \phi < 68.5°$).

CONCLUSIONS

The maximum temperature of the weld between the absorber-dome and the aft-dome has been computed for no air-side convective cooling and the sodium-side of the absorber insulated over $59.2° < \phi < 68.5°$. For these conditions, the maximum weld temperature was 923°C, high enough to be of some concern, but well below the 1000°C limit. For the situation where the stationary sodium covers the absorber between $59.2° < \phi < 68.5°$, the maximum computed weld temperature was 895°C, which represents a small overheating threat to the weld. For normal operating conditions, an air-side convection coefficient of 5 W/m^2k and a specified sodium-side boundary temperature of 800°C, the average weld temperature was 805°C. Based on this analysis, overheating of the weld between the absorber and the aft-dome weld does not appear to be a significant threat.

References

1. Hogan, R. E., Diver, R. B., and Stine, W. B., Comparison of a Cavity Solar Receiver Numerical Model and Experimental Data, Eleventh Annual ASME Solar Energy Conference, San Diego, CA, April 2-5, 1989.

2. Myers, G. E., *Analytical Methods in Conduction Heat Transfer*, McGraw-Hill, New York, pg. 492, 1971.

3. Carborundum Resistant Materials Company, "Fiberfrax Duraboard 3000," Technical Note C-739H, 1982.

4. Carborundum Resistant Materials Company, "Fiberfrax Most-Pack D," Technical Note C734-G, 1981.

5. Holman, J. P., *Heat Transfer*, 4th edition, McGraw-Hill, New York, pg. 506, 1976.

REH:1513:tgr

Copy to:
1510 J. W. Nunziato
1511 D. K. Gartling
1512 J. C. Cummings
1513 D. W. Larson
1513 D. R. Adkins
1513 R. E. Hogan
1520 L. W. Davison
1521 C. M. Stone
1530 J. R. Asay
1550 C. W. Peterson
2542 J. B. Moreno
6210 B. W. Marshall
6215 J. T. Holmes
6216 C. E. Tyner
6217 P. C. Klimas
6217 C. E. Andraka
6217 T. A. Moss
6217 File 5.3.2
1513 Day File

APPENDIX H

STRESS ANALYSIS

APPENDIX H
STRESS ANALYSIS

Stress analyses on the pool-boiler receiver have been performed to determine the net effect of the mechanical and thermally induced loads on the front dome. Analyses of increasing complexity were performed, and were detailed in four memos, one of which is included in this Appendix. Most of this work has been summarized in Hoffman and Stone (1991). A brief overview is outlined below.

Source of Stresses

The mechanical load is a result of the difference between atmospheric pressure acting on the outside of the receiver and the vapor pressure of the liquid metal acting on the inside of the receiver. This load is greatest during startup, when the metal vapor pressure is the lowest (sub-atmospheric).

The thermally induced loads are a result of temperature differences between different parts of the receiver. Several important temperature differences develop in the front dome. One of these occurs across the dome thickness as a result of the solar flux passing through it. A second temperature difference develops radially, especially during startup, as a result of the flux distribution.

Non-axisymmetric effects have not been taken into account. The assembly was approximated by a model that consists of two spherical shell segments joined at their rim. The analysis was rendered axisymmetric by omitting the hole leading to the condenser section and averaging out asymmetries in the applied solar flux and the receiver temperature distributions.

Artificial cavities drilled in the wetted surface of the absorber have been considered in the stress analyses. The influence of the artificial cavities on the stress field has been estimated in two different ways. The starting point for both estimates was the stress field calculated for a dome having no artificial cavities. The first estimate applied stress-multiplication factors of up to 3, found in the literature for a stressed membrane problem containing a hole. The second estimate (not documented elsewhere) used a finite element method to calulate the stress field around an artificial cavity, including the effect of the oscillating temperature associated (Moreno and Andraka, 1989) with the bubble cycle. The necessary boundary conditions distant from the cavity were obtained from the solution for a dome with no cavities. A description of the various analyses and their most important results follows.

Analysis Based on Estimated Radial Temperature Differences

The initial analysis (Neilson, 1989 - not included in this report) presented results for stress in the front dome under four conditions:

1. At ambient temperature with internal vacuum
2. At a particular instant during startup, with an assumed radial temperature distribution
3. At steady operation at 800°C
4. At ambient temperature after some yielding had occurred during operation

Simple estimates of the effect of the artificial cavities were also presented. The emphasis in these calculations was on the effect of the estimated radial temperature distribution during startup. The temperature gradient through the dome thickness was not taken into account. The results showed that the yield strength of the material could be exceeded during startup, if the actual radial temperature distributions were similar to the assumed distribution presented in the memo.

Analysis Based on Measured Temperature and Calculated Flux Distributions

The second memo (Stone and Hoffman, 1990 - not included in this report) presented front dome stress results under two conditions (1) at a particular instant during startup for which the stresses were determined to be maximized and (2) at steady operation at 800°C.

This work extended Neilson's results by (1) accounting for the temperature gradient through the dome thickness, (2) using measured rather than estimated radial temperature distributions, and (3) repeating the calculations for a long-life material candidate, Haynes Alloy 230.

The radial variation of temperature gradient through the dome thickness was estimated from the calculated incident solar flux distribution. The results for type 316L stainless steel showed that the highest stresses occur during startup, and that they are less than the yield stress. The Haynes Alloy 230 results showed that the stresses will be well below the yield stress except at the artificial cavities, but should still be acceptable.

Analysis Extended to Account for Temperature-Dependent Properties, Various Dome Thicknesses, and Artificial Cavities

The third memo is included in this Appendix. It is dated November 29, 1990 and was also written by E. L. Hoffman and C. M. Stone. It presents results for stress in the front and rear domes under the same conditions and using the same methodology as in their previous memo. This work extended the earlier work by (1) accounting for the temperature-dependence of material properties (elastic modulus, thermal conductivity, and coefficient of thermal expansion) and (2) determining the effect of using a thinner back dome in a receiver made from Haynes Alloy 230.

The results showed that using temperature-dependent material properties increases the predicted startup stresses by up to 10% for type 316L stainless steel and 20% for Haynes Alloy 230. The results at 800°C were unaffected. The effect of decreasing the back-dome thickness reduced front-dome stresses during startup but not during steady operation. The improvement was moderate at half-thickness, and only slightly more so at quarter-thickness. In all cases, the calculated stresses were less than the yield stress at the local, instantaneous temperature.

The finite element analysis of stress in the vicinity of an artificial cavity during 800°C operation of the first receiver (316L stainless steel) revealed an 8-MPa (1160-psi) peak-to-peak oscillating local stress associated with the bubble cycle superposed on a 70-MPa (10,155-psi) steady stress that includes the effect of stress concentration at the cavity. This analysis has not been documented, but the information was applied to the fatigue analysis presented in Figure S-1 of Appendix S of this report.

Fatigue-Crack Analysis of Pool-Boiler Seam Weld

The fourth memo (Hoffman, Stone, and Wellman, 1991 - not included in this report) presented more-detailed results for stress in the vicinity of the front-to-aft-dome seam weld. Using these results, a linear elastic fracture mechanics analysis was also carried out. This work was motivated by concerns that the built-in notch in the seam weld could lead to premature fatigue failure. The analysis shows that stress distribution in the neighborhood of the weld is strongly dependent on the pressure inside the receiver, and only weakly dependent on thermal loads. The analysis establishes that the stress field ahead of the seam-weld notch cycles in compression, and finally, that the fluctuation of the stress intensity factor is well below the fatigue threshold.

References

Hoffman, E. L., and C. M. Stone. 1991. "Structural Analysis of a Reflux Pool-Boiler Solar Receiver." Presented at *The ASME-JSES-KSES International Solar Energy Conference, Maui, HI, April 4-8, 1992.* SAND91-1321C. Albuquerque, NM: Sandia National Laboratories.

Hoffman, E. L., C. M. Stone, and G. W. Wellman. 1991. "Fatigue-Crack Analysis of Seam Weld in the Reflux Pool-Boiler Receiver," memorandum to J. B. Moreno (January 17). Albuquerque, NM: Sandia National Laboratories.

Moreno, J. B., and C. E. Andraka. 1989. *Test Results from Bench-Scale Sodium-Pool-Boiler Solar Receiver.* SAND89-0899. Albuquerque, NM: Sandia National Laboratories.

Neilson, M. K. 1989. "Solar Receiver Thermal Stress Analysis," memorandum to J. B. Moreno (September 18). Albuquerque, NM: Sandia National Laboratories.

Stone, C. M., and E. L. Hoffman. 1990. "Thermal Stress Analysis of a Sodium Reflux Pool-Boiler Solar Receiver," memorandum to J. B. Moreno (October 3). Albuquerque, NM: Sandia National Laboratories.

Sandia National Laboratories
Albuquerque, New Mexico 87185

date: November 29, 1990

to: J. B. Moreno, 2542

Edwood L Hoffman Charles M. Stone

from: E. L. Hoffman and C. M. Stone, 1514

subject: Thermal Stress Analysis of a Sodium Reflux Pool-Boiler Receiver Studying the Effects of Nonlinear Material Properties and Reduced Aft Dome Thickness

1 INTRODUCTION

A sodium reflux pool-boiler solar receiver is undergoing engineering development and prototype on-sun testing at Sandia National Laboratories in Albuquerque. In the reflux receiver concept a liquid metal, such as sodium, is evaporated at the solar absorber and condensed at heater tubes to drive a Stirling engine. During current on-sun testing, the Stirling engine has been replaced by a cold water calorimeter for heat extraction. A schematic of the Sandia reflux pool-boiler solar receiver is shown in Figure 1. The receiver must contain the liquid sodium which will burn when exposed to air. The operating environment of the receiver exposes the absorber to transient temperatures ranging from 150 °C to 830 °C during startup to a steady state operating temperature near 820 °C. The loading is cyclic with at least 10,000 startup/shutdown cycles expected during the design lifetime. The component consisting of the absorber and aft dome has been the subject of extensive stress analyses to determine its reaction to the applied thermal loads. The prototype on-sun receiver is constructed of 316L stainless steel, but plans call for the next generation receiver to be constructed of Haynes 230 steel which is more creep resistant than 316L. Detailed knowledge of the thermal stresses induced in the absorber is needed to design the receiver to operate for its 30-year lifetime. Initial structural analyses of the reflux pool-boiler receiver [1] studied thermally induced stresses with coupled thermal-displacement shell elements assuming constant temperature through the shell wall. A more recent analysis [2] considered thermal gradient effects through the shell wall by using coupled thermal-displacement elements with temperature computed at specified points through the thickness of the shell. The analysis was performed to compare 316L and Haynes 230 stainless steels.

The absorber dome is the critical component of the receiver because it must be thin to facili-

tate efficient heat transfer. The aft dome does not have the same thermal constraints and can be made much thicker. The current generation reflux pool-boiler receiver uses a 0.813 mm-thick absorber and a 3.18 mm-thick aft dome. The earlier analyses [1, 2] indicated that the thickness of the aft dome was sufficient for the given load conditions. However, optimizing the aft dome thickness could significantly reduce material costs. This study, which is an extension of the previous analyses, considers the effect of reducing aft dome thickness. In addition, temperature dependent material properties are used. In earlier analyses of the receiver [1, 2], constant material properties, evaluated near the steady state operating temperature, were considered. This approximation affected the analyses under the startup operating conditions. However, the highest stresses in the absorber were exhibited in the startup regime. In the present analyses, the temperature dependencies of the elastic modulus, coefficient of thermal expansion and thermal conductivity of the receiver material are investigated.

The new analyses presented here were performed with the same model used in [2]. For completeness, the model description is reviewed in the following section. The third section presents the results of the analyses. First, responses of the prototype 316L and next generation Haynes 230 stainless steel receivers with temperature dependent material properties are compared to those presented in [2] for constant material properties. Next, responses of the Haynes 230 receiver are presented for reduced aft dome thicknesses of 1.59 and 0.813 mm. The last section presents the conclusions of the study.

2 NUMERICAL MODEL

Figure 2 shows the idealized geometry and dimensions of the receiver used in the model. The model consists of the absorber, which is a spherical shell with a 219 mm radius and a 70.2 degree half angle, and the aft dome, which is another spherical shell with a 208 mm radius. The thickness of the absorber is 0.813 mm compared to 3.18 mm for the aft dome. The absorber is welded to the aft dome around its outer circumference. The temperature dependent material properties used for 316L and Haynes 230 are the elastic moduli presented in Table 1, the thermal conductivities in Table 2 and the coefficients of thermal expansion in Table 3. A constant Poisson's ratio of 0.3 was used for both steels and yield strengths of 103 and 275 MPa were assumed for 316L and Haynes 230, respectively.

Table 1. Temperature Dependent Elastic Moduli Used for the Pool-Boiler Receiver Analysis.

Temperature (°C)	316L Elastic Modulus ($\times 10^9$ MPa)	Haynes 230 Elastic Modulus ($\times 10^9$ MPa)
100	190.1	207
200	184.0	202
300	176.7	196
400	168.3	190
500	159.9	184
600	149.1	177
700	138.6	171
800	126.1	164

Table 2. Temperature Dependent Thermal Conductivities Used for the Pool-Boiler Receiver Analysis.

Temperature (°C)	316L Conductivity (W/m °K)	Haynes 230 Conductivity (W/m °K)
100	14.7	10.4
200	16.34	12.4
300	17.94	14.4
400	19.48	16.4
500	20.96	18.4
600	22.39	20.4
700	23.76	22.4
800	25.07	24.4

Table 3. Temperature Dependent Coefficients of Thermal Expansion Used for the Pool-Boiler Receiver Analysis.

Temperature (°C)	316L Coefficient of Thermal Expansion ($\times 10^{-6}$ °C $^{-1}$)	Haynes 230 Coefficient of Thermal Expansion ($\times 10^{-6}$ °C $^{-1}$)
100	15.8	12.7
200	16.7	13.0
300	17.2	13.3
400	17.8	13.7
500	18.3	14.0
600	18.6	14.4
700	18.9	14.8
800	19.2	15.2

The thermal stress analyses were performed using the general purpose finite element code ABAQUS [3]. The receiver geometry and loading allow the use of an axisymmetric model of the receiver. The model was constructed using 80 axisymmetric shell elements developed specifically for coupled temperature-displacement analysis. The three-noded elements use quadratic interpolation for the geometry and displacements while the temperatures are linearly interpolated from the end nodes and piecewise quadratically through the shell thickness. Five integration points through the shell thickness were specified. The specific finite element formulation used for this problem involves solution for the nodal displacements and temperatures simultaneously. The appropriate boundary conditions are defined below for both the mechanical and thermal loading.

2.1 Structural Boundary Conditions

The structural boundary conditions used in the analyses are shown schematically in Figure 3a. Radial displacements at the absorber and aft dome are specified to be zero at the axis of symmetry. The nodal point which connects the absorber and the aft dome at the outer radius is constrained to move only in the radial direction. This particular boundary condition is used to remove axial rigid body deformation from the problem. The surface coordinate, *s*, denoting position on the receiver and aft dome, is defined in Figure 3b.

To represent loading induced by the liquid sodium, a uniform pressure boundary condition was applied to the aft dome and absorber as shown in Figure 3. The external pressure, P_{amb}, represents the local ambient pressure (84.1 kPa in Albuquerque, NM), while P_{int} is the absolute pressure of the liquid sodium given by

$$\log P_{int} = 6.354 - \frac{5567}{T} - 0.5 \log T \qquad (1)$$

where T is the sodium temperature in K and P_{int} is in standard atmospheres. The internal pressure, P_{int}, is zero absolute at ambient temperature (300 K) and increases with increasing temperature. Consequently, the applied pressure (P_{amb}-P_{int}) is initially 84.1 kPa, and decreases during startup to a steady state value of 32.9 kPa.

2.2 Thermal Boundary Conditions

For the specification of the thermal boundary conditions, the convention in Figure 4 is used to denote the two sides of the aft dome and the absorber shells. The inner surfaces of the shells are in contact with the liquid sodium (internal to the sodium containment), while the outer surfaces are exposed to the atmosphere. This convention will also be used in describing the results of the analysis.

The thermal model of the receiver utilizes temperature data taken from thermocouples at discrete points on the outer surfaces of the absorber and aft dome as well as a computed incident solar flux distribution. The thermal boundary conditions are applied as shown in Figure 4 based on known temperature data for both the startup and steady state phases of operation. During startup (Figure 4a), temperatures are defined on the outer surface of the absorber where they were measured, and the solar flux is applied on the inner surface. Temperatures in the aft dome are assumed constant through the thickness of the shell. The measured temperatures vary temporally and spatially across the face of the absorber and aft dome as shown in Figure 5. The data are presented as a function of the surface distance coordinate s which is measured from Node 161 along the absorber surface to Node 81 and continues along the aft dome surface to Node 1 (see Figure 3b). The spatially varying flux distribution, shown in Figure 6, was calculated using CIRCE2 [5], a computer code for calculating incident solar flux distributions of point-focus concentrators. For each absorber element, the flux data was entered into the analysis as a function of the radial coordinate of the element. The sodium temperature used to calculate the internal pressure in Equation (1) was assumed to be the temperature at the aft dome axis of symmetry.

When steady state operating conditions are reached (Figure 4b), a constant temperature boundary condition of 811.5 °C is specified on the inner surface of the absorber, and the spatially varying flux distribution in Figure 6 is specified on the outer surface of the absorber. The temperature specification was moved to the inner surface because the sodium temperature was known during this phase of operation. The aft dome is subjected to a constant temperature boundary condition of 811.5 °C through the thickness of the shell.

2.3 Solution Steps

Each of the temperature distributions shown in Figure 5 is applied independently, and a corresponding steady state solution is obtained. For each solution, the thermal strains are calculated

from an initial (stress free) temperature of 20 °C. The steady state assumption is based on the thermal diffusivity of the material, the absorber wall thickness and the relatively long time scale of the startup process. The absorber wall is so thin that the temperature distribution through the wall will approach a steady state solution in a time frame much shorter than the 1 to 2 min sampling rate of the temperature data. The temperature distributions for Steps 1 through 6 in Figure 5 correspond to various steps in the startup phase of operation and Step 7 corresponds to the normal on-sun operating conditions.

3 ANALYSIS RESULTS

The analysis of the receiver shell model is presented for three aft dome thicknesses: full-thickness (3.18 mm), half-thickness (1.59 mm) and quarter-thickness (0.819 mm). Both the prototype 316L and next generation Haynes 230 stainless steel receivers are analyzed with the full-thickness aft dome. The 316L material properties are not considered for thinner aft dome models because only Haynes 230 is under consideration for a next generation solar receiver.

The results of the analyses are displayed for various locations through the shell thickness. Each nodal point has temperatures computed at five points through the shell. The temperatures at the inner and outer surfaces are presented for all seven time steps. In addition, stress output from the axisymmetric shell elements is presented in the form of meridional and circumferential stresses at the inner and outer surfaces. The stress components are presented for Steps 3 and 7 for each analysis. Step 3 corresponds to the temperature profile which generates the largest stresses during startup, and Step 7 gives the stress distribution during steady state operation.

3.1 Full-Thickness Aft Dome

The analyses presented in this section are the same as those in [2] with the addition of temperature dependent material properties. The analyses were performed to determine the effects, if any, of considering temperature dependencies.

3.1.1 316L Receiver

The nodal temperatures computed along the inner and outer surfaces of the receiver are shown in Figures 7 and 8, respectively. Curves 1 through 6 correspond to the startup thermal profiles and Curve 7 corresponds to the steady-state temperature distribution. These temperature profiles verify the temperature prescribed boundary conditions in Figure 4.

The meridional and circumferential stress distributions in the receiver are shown in Figure 9 and Figure 10 for Steps 3 and 7, respectively. The meridional and the circumferential stress profiles are very similar in shape and magnitude. The absorber shell is subjected to nearly pure bending with the inner surface of the shell in tension with values exceeding 100 MPa during startup and the outer surface in compression. Large stress gradients occur near the edge of the absorber due to the difference between the average temperatures of the absorber and aft dome. Membrane stresses in the receiver are characterized by an offset from zero in the average meridional and circumferential stress components. This membrane stress is tensile in the absorber and compressive in the aft dome. These stresses are very close to the 103 MPa yield strength of 316L. At steady state operating conditions, the inner surface remains in tension and the outer surface remains in compression with the maximum tensile and compressive stresses reduced to 42 MPa and -33 MPa, respectively. The stress near the absorber edge has dropped to 10 MPa from a startup value of 100 MPa, and is due primarily to the geometric discontinuity which exists at the absorber/aft dome interface. The stress profile is characterized by the distinctive double hump that is produced by the incident solar flux distribution shown in Figure 6.

Compared to previous analyses which assumed constant material properties [2], the analysis of the 316L receiver considering temperature dependent material properties resulted in a 10 percent increase in the maximum receiver stresses during the startup phase of operation. However, the maximum stress in the weld region remained the same. As expected, the steady state stresses were unaffected because prior analyses assumed constant material properties evaluated at the steady state operating temperature.

3.1.2 Haynes 230 Receiver

The temperatures generated on the inner and outer surfaces of the receiver using the Haynes 230 thermal properties are the same as those discussed for the 316L receiver. This is not surprising since the thermal conductivities of the two materials are almost the same. The comments made regarding the temperature distribution for the 316L receiver are still valid for this receiver material.

The meridional and circumferential stress profiles in the Haynes 230 receiver are shown in Figure 11 and Figure 12 for Steps 3 and 7, respectively. The stress gradients through the shells are caused by the thermal gradient and are characteristic of pure bending loads. The stresses are tensile on the inner surfaces and compressive on the outer surfaces. As in the 316L receiver,

large stress gradients occur near the edge of the absorber due to the difference between the average temperatures of the absorber and aft dome. During startup, the maximum tensile stress is near 100 MPa while the maximum compressive stress is -77 MPa. During steady-state operation, the inner surface values reach a maximum of 45 MPa, and the outer surface stresses reach a maximum near -35 MPa. The stress gradient near the absorber edge has reduced to 20 MPa from a startup value of 90 MPa because the surface temperature of the aft dome and absorber is uniform during steady state operation. The stress profile contains the double hump shape associated with the incident solar flux distribution shown in Figure 6. The maximum component is below the yield stress by a factor of 2.75, as compared to 1.0 for 316L.

Compared to the previous analyses which assumed constant material properties, the analysis of the Haynes 230 receiver considering temperature dependent material properties resulted in 10 to 20 percent increases in the maximum receiver stresses during the startup phase of operation. Again, the change in material properties did not affect the steady state stress profile.

3.2 Half-Thickness Aft Dome

The high stress gradients exhibited near the weld region of the receiver are due to (1) an uneven temperature distribution across the receiver surface, and (2) a geometric discontinuity at the absorber/aft dome interface. To determine the effect of reducing the aft dome thickness on the stress state in the receiver, the shell model of the receiver was analyzed for a reduced aft dome thickness of 1.59 mm. The meridional and circumferential stress profiles in the Haynes 230 receiver with a 1.59 mm aft dome are shown in Figure 13 and Figure 14 for Steps 3 and 7, respectively. Comparison of the startup stress profiles of the full-thickness (Figure 11) and half-thickness (Figure 13) receivers shows that the maximum stress at the inner surface of the absorber reduces from 100 MPa for the full-thickness aft dome to 75 MPa for the half-thickness aft dome. Similarly, the maximum stress at the outer surface of the absorber reduces from -75 MPa for the full-thickness aft dome to -52 MPa for the half-thickness aft dome. With the reduction in the aft dome thickness to 1.59 mm, the yield strength is 3.67 times the maximum stress component, compared to 2.75 for the 3.18 mm aft dome. The maximum stresses in the aft dome reduce from 25 MPa to 20 MPa for the half-thickness aft dome. These stress reductions are offset by a larger compressive membrane stress in the aft dome. Conversely, comparison of the steady state stress profiles of the full-thickness (Figure 12) and half-thickness (Figure 14) receivers shows that no significant changes occur.

3.3 Quarter-Thickness Aft Dome

The analysis presented in the previous section showed that the stress state in the Haynes 230 receiver was improved by reducing the aft dome thickness to 1.59 mm. To determine if further stress reductions could be achieved, the Haynes 230 shell model was analyzed for equal absorber and aft dome thicknesses (0.819 mm). The meridional and circumferential stress profiles in the Haynes 230 receiver with a quarter-thickness aft dome are shown in Figure 15 and Figure 16 for Steps 3 and 7, respectively. Comparison of the startup stress profiles for the quarter-thickness (Figure 15) and half-thickness (Figure 13) aft domes shows that the compressive membrane stress in the aft dome increases slightly and the maximum stress near the weld reduced to 45 MPa from 75 MPa for the 1.59 mm-thick aft dome. The startup stress profile is otherwise unaffected by the additional decrease in aft dome thickness. Similarly, the steady state stress profiles (Figure 14 and Figure 16) show little change with further reduced of aft dome thickness.

4 CONCLUSIONS

Coupled temperature-displacement analyses of the Sandia Pool-Boiler Solar Receiver have been performed to determine the effect of reducing the aft dome thickness on the receiver stress profile. The analyses were performed for startup and steady state operating conditions and for aft dome thicknesses of 3.18, 1.59 and 0.813 mm. The analyses consider temperature dependency of the elastic modulus, coefficient of thermal expansion and thermal conductivity of the receiver material. Both the prototype 316L and next generation Haynes 230 stainless steel receivers are analyzed with the full thickness aft dome (3.18 mm) because nonlinear properties were not considered in previous analyses [2]. The effect of reducing the aft dome thickness was studied only for Haynes 230 because it has been selected for next generation receiver development. Based on the analysis results, the following conclusions can be made:

- The maximum stresses in all models are generated during startup (Step 3) due to an uneven temperature distribution across the receiver surface and a geometric discontinuity at the absorber/aft dome interface.

- The consideration of temperature dependent material properties resulted in increased stress in the receiver during startup. The analyses of the full-thickness model resulted in stress increases of 10 to 20 percent when compared to similar analyses performed assuming temperature independent material properties [2].

- Reducing the aft dome thickness reduces the maximum absorber stresses during startup. A thickness change from 3.18 to 1.59 mm resulted in a 25 percent decrease in absorber stress during startup. Although subsequent reductions in the aft dome thickness can further decrease absorber stress, there are diminishing returns as the absorber wall thickness is approached. As expected, the compressive membrane stress in the aft dome increased with reductions in aft dome thickness.

- Reducing the aft dome thickness did not significantly affect the steady state stress profiles.

Although the 3.18 mm aft dome is satisfactory for the applied thermal loads, reducing the aft dome thickness significantly reduces the receiver stresses.

5 REFERENCES

1 M. K. Neilsen, *Solar Receiver Thermal Stress Analysis*, memo to J. B. Moreno, Sandia National Laboratories, September 18, 1989.

2 C. M. Stone and E. L. Hoffman, *Thermal Stress Analysis of a Sodium Reflux Pool-Boiler Receiver*, memo to J. B. Moreno, Sandia National Laboratories, October 3, 1990.

3 Karlsson and Sorensen, *ABAQUS User's Manual*, Version 4.8, 1989.

4 J. B. Moreno, C. E. Andraka, R. B. Diver, W. C. Ginn, V. Dudley and K. S. Rawlinson, *Test Results from a Full-Scale Sodium Reflux Pool-Boiler Solar Receiver*, ASME Solar Energy Division Conference, Miami, Florida, April, 1990.

5 A. C. Ratzel, B. D. Boughton, *Circe.001: A computer Code for Analysis of Point-Focus Concentrators with Flat Targets*, SAND86-1866, Sandia National Laboratories, 1986.

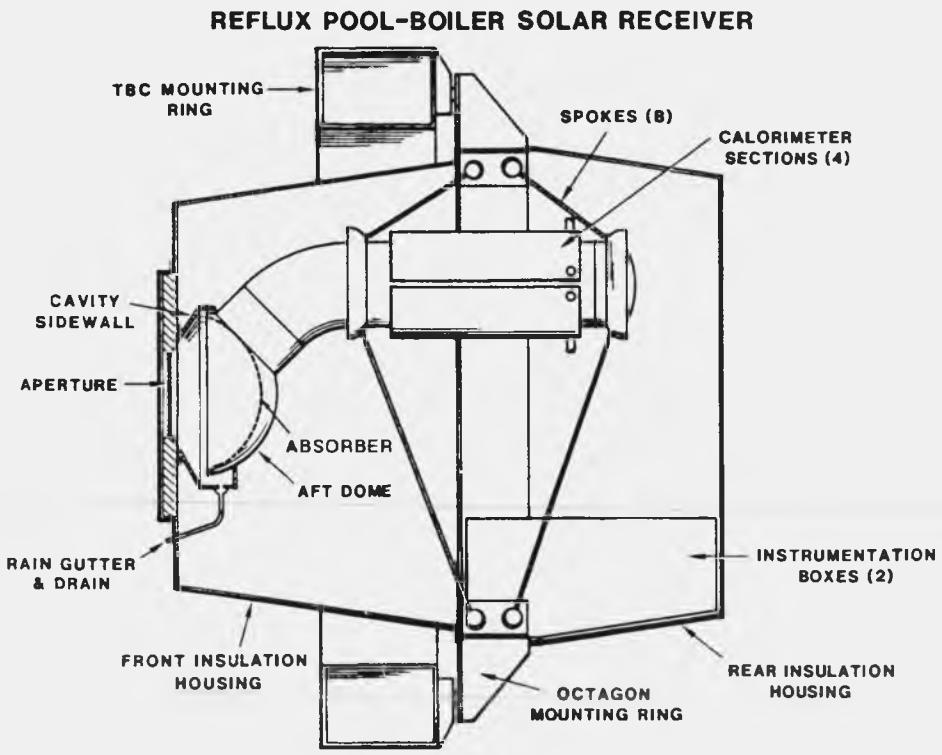

Figure 1. Schematic of the Sandia reflux pool-boiler receiver (taken from [4]).

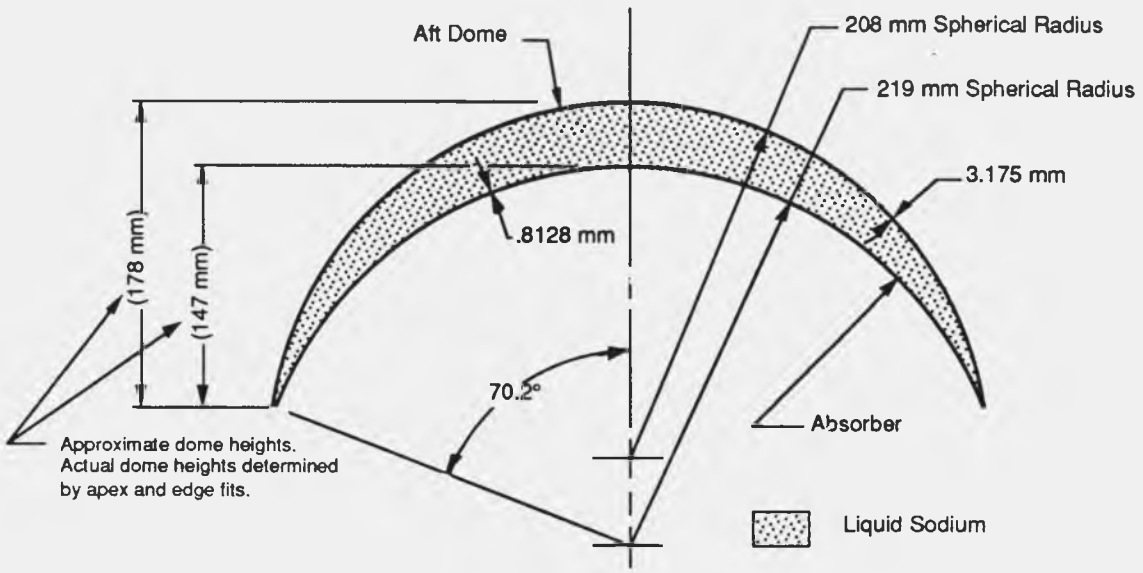

Figure 2. Geometry used in developing the finite element model of the reflux pool-boiler receiver.

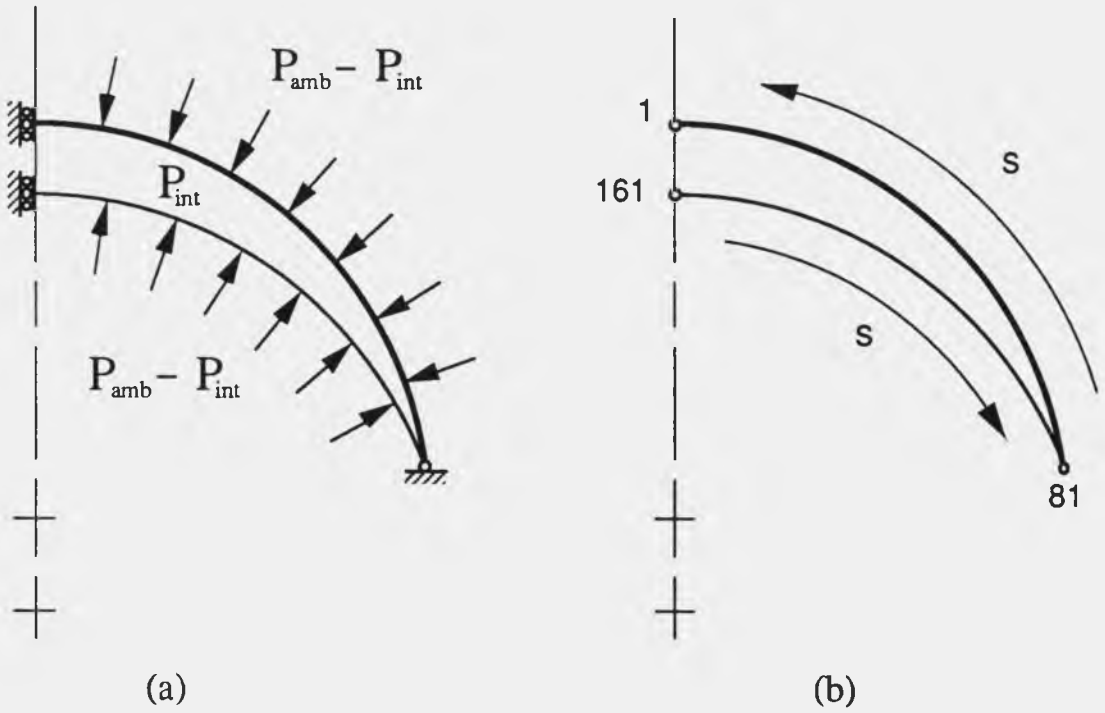

Figure 3. (a) Structural boundary conditions used for the reflux pool-boiler receiver analyses. (b) Definition of the surface position variable, *s*, used for the presentation of results.

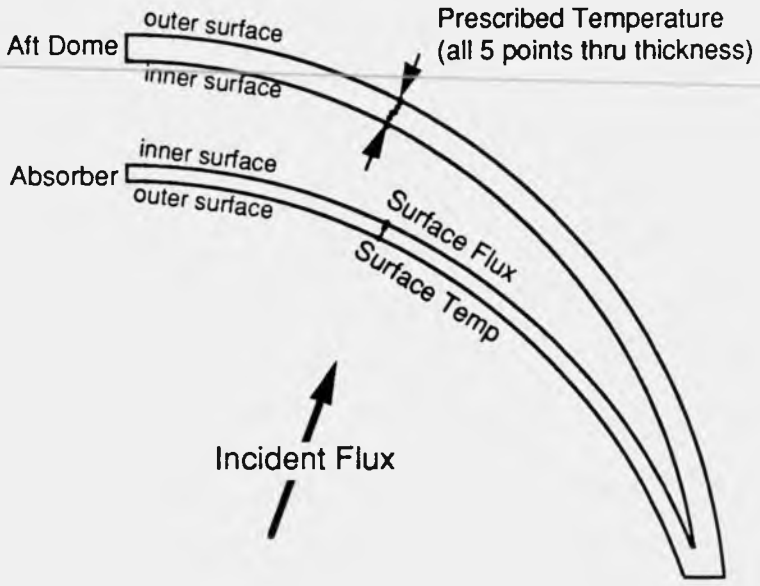

(a) Startup Phase

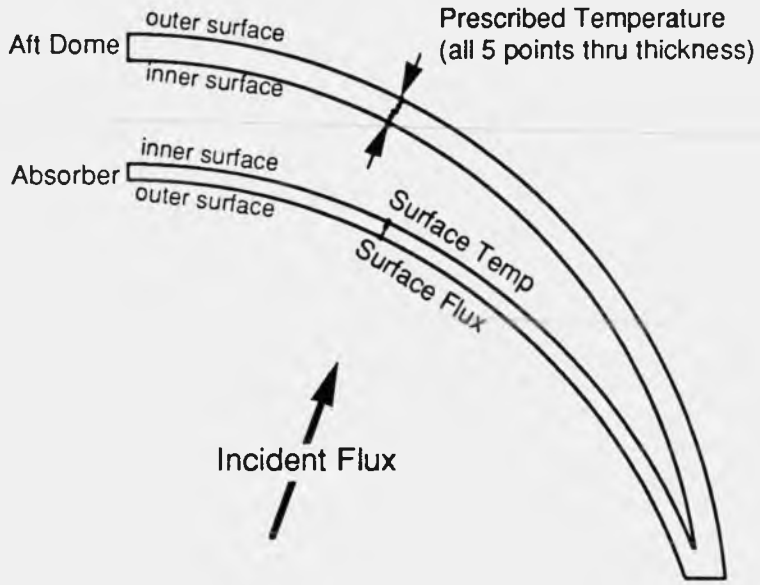

(b) Steady State Phase

Figure 4. Thermal boundary conditions used for the reflux pool-boiler receiver analysis.

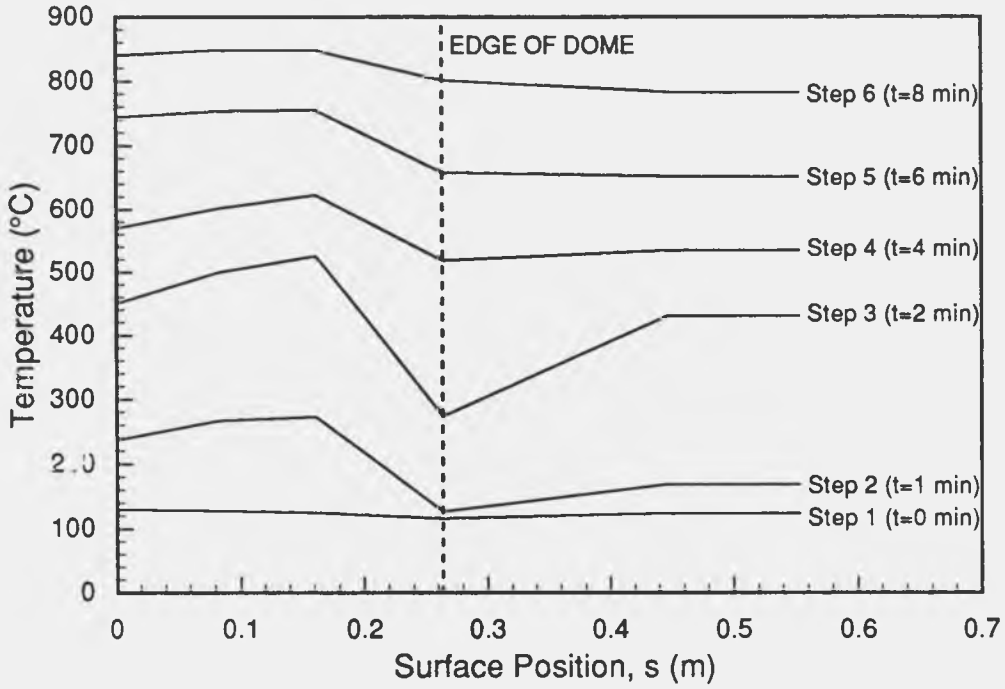

Figure 5. Temporal and spatial temperature distributions assumed for the startup and steady state operating conditions.

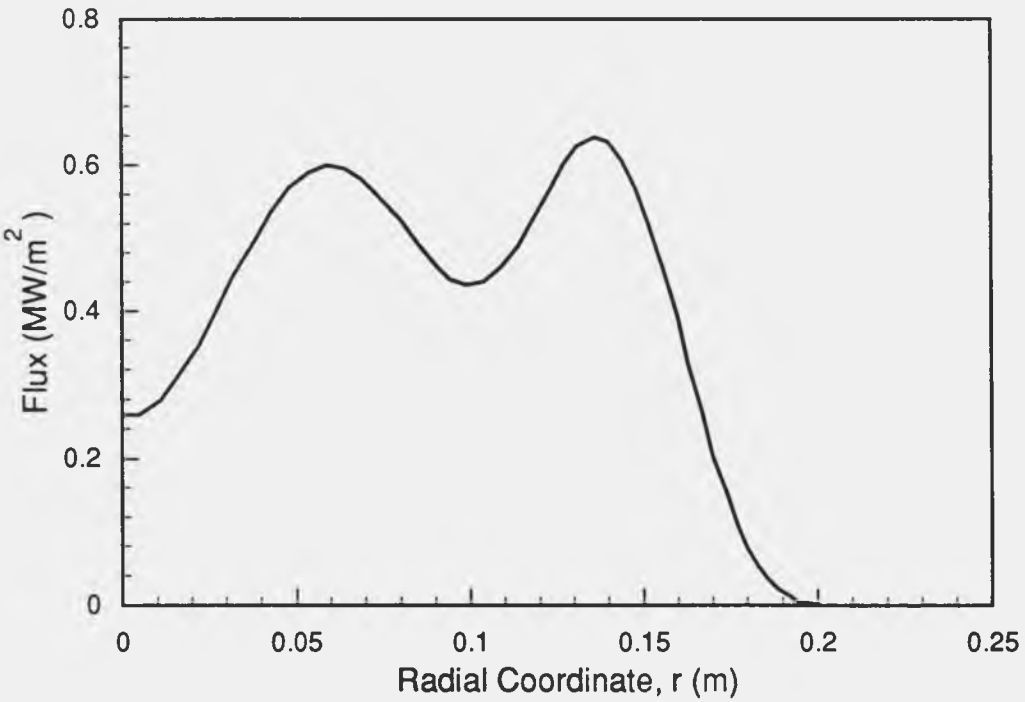

Figure 6. Computed incident solar flux distribution assumed for the startup and steady state operating conditions.

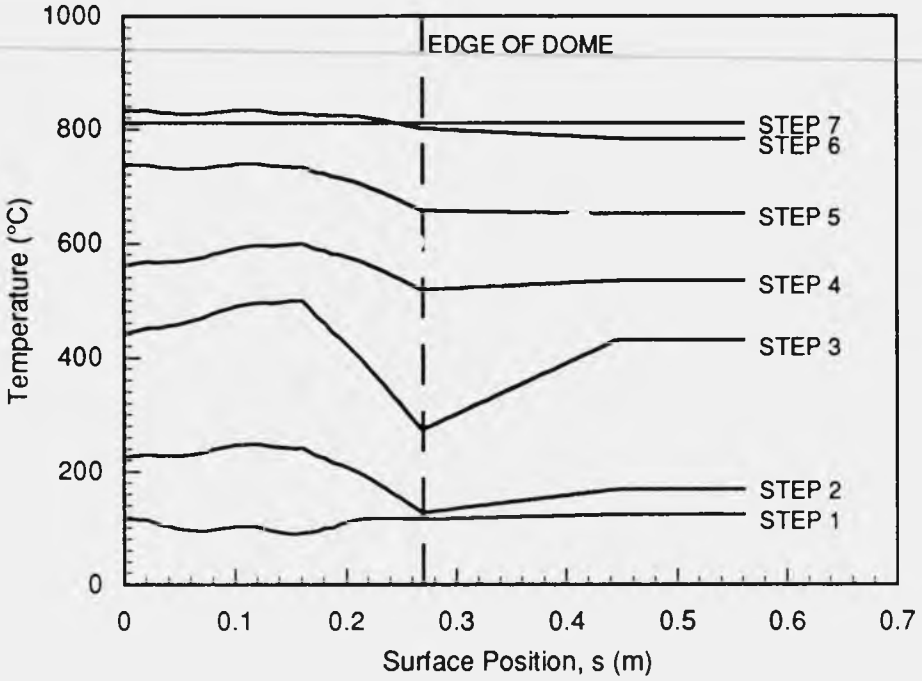

Figure 7. Absorber and aft dome inner surface temperature profiles for startup and steady state operating conditions.

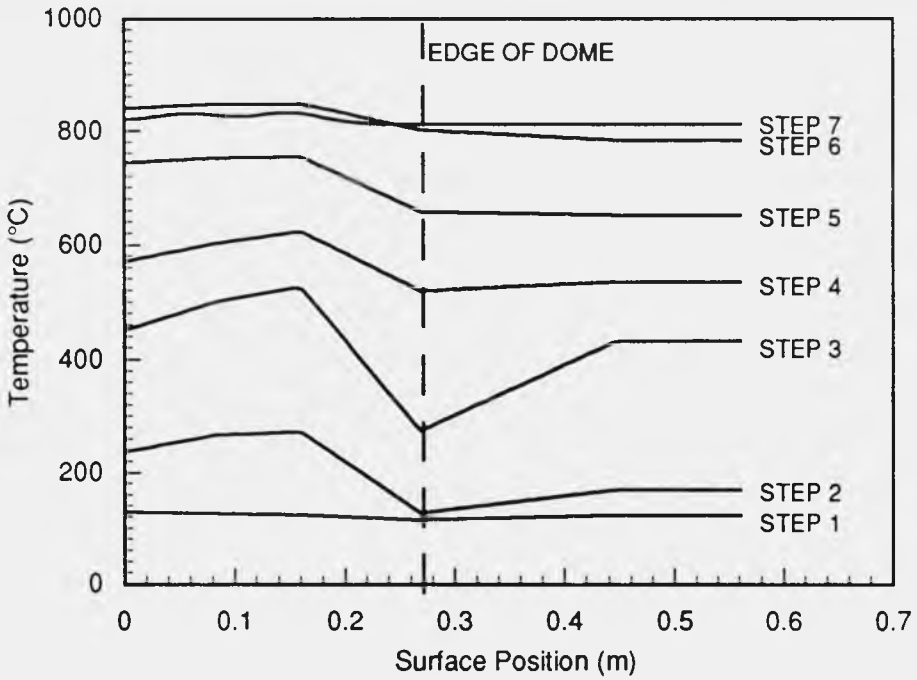

Figure 8. Absorber and aft dome outer surface temperature profiles for startup and steady state operating conditions.

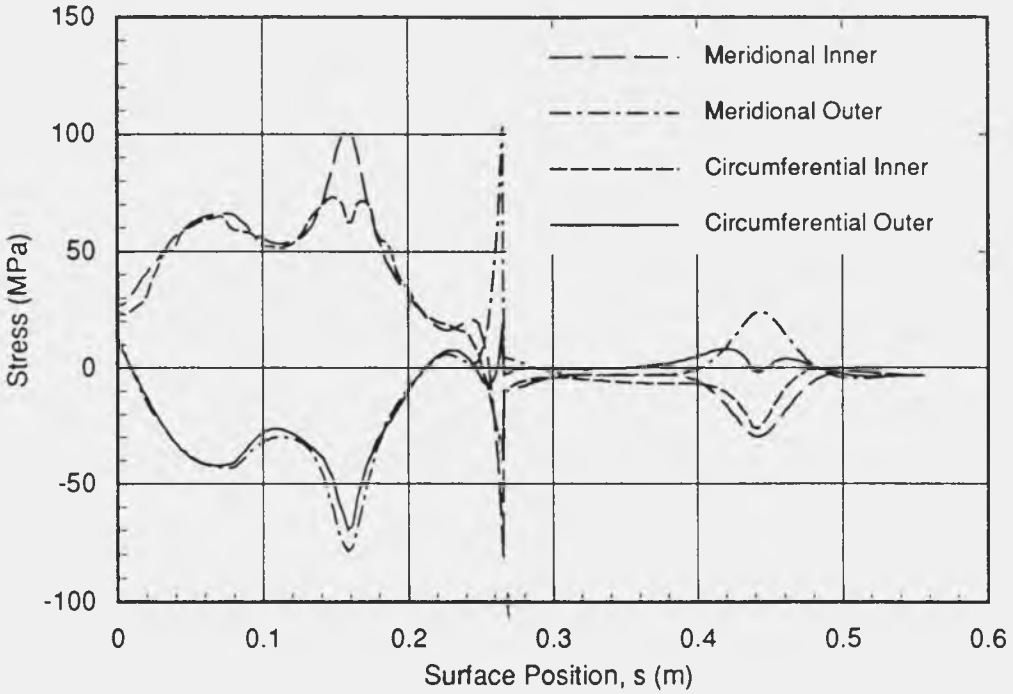

Figure 9. Receiver meridional and circumferential stress profiles during Step 3 of the receiver startup for 316L and a full-thickness (3.18) mm aft dome.

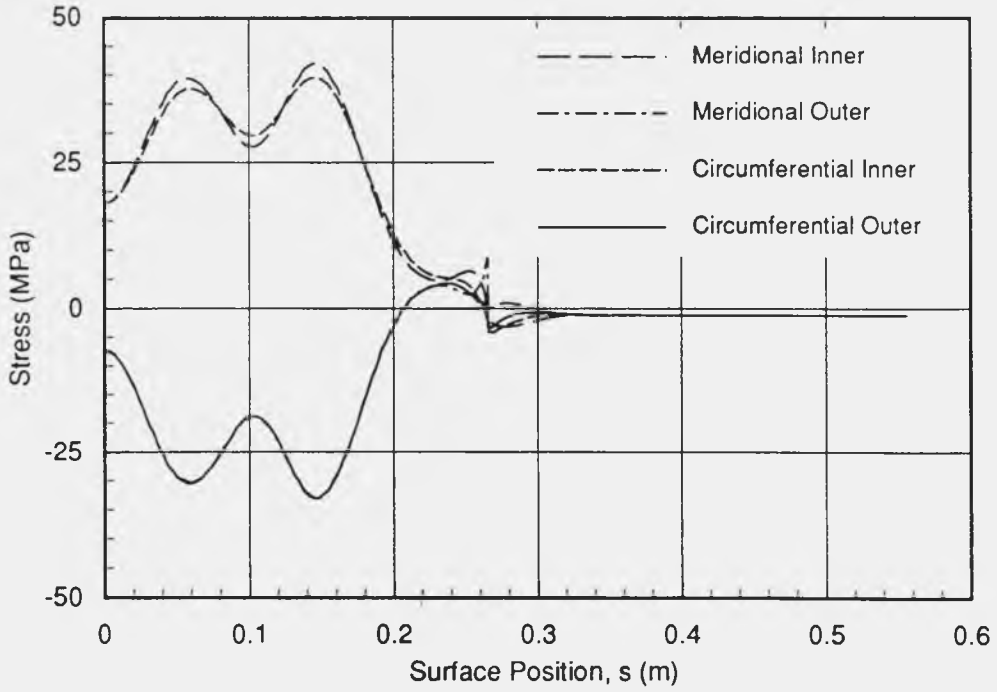

Figure 10. Receiver meridional and circumferential stress profiles during steady state operation for 316L and a full-thickness (3.18) mm aft dome.

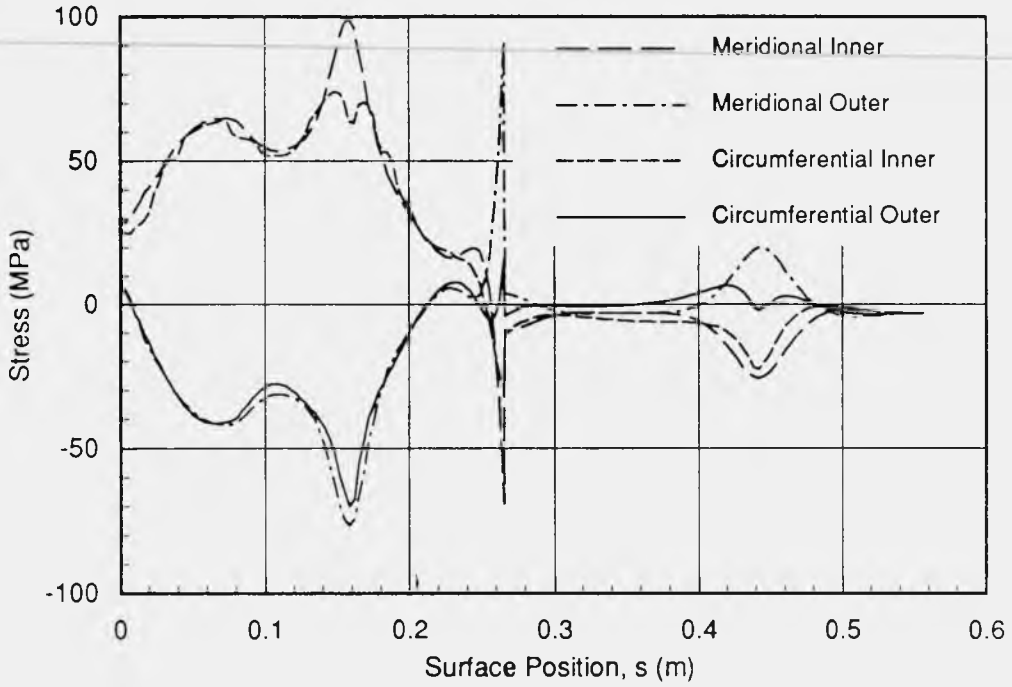

Figure 11. Receiver meridional and circumferential stress profiles during Step 3 of the receiver startup for Haynes 230 and a full-thickness (3.18 mm) aft dome.

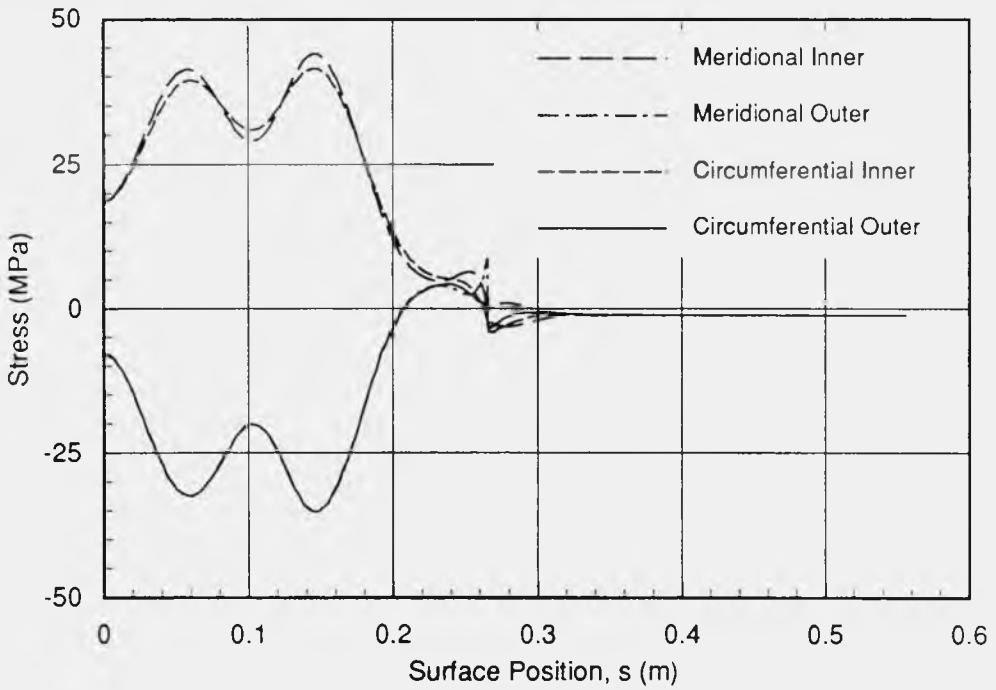

Figure 12. Receiver meridional and circumferential stress profiles during steady state operation for Haynes 230 and a full-thickness (3.18 mm) aft dome.

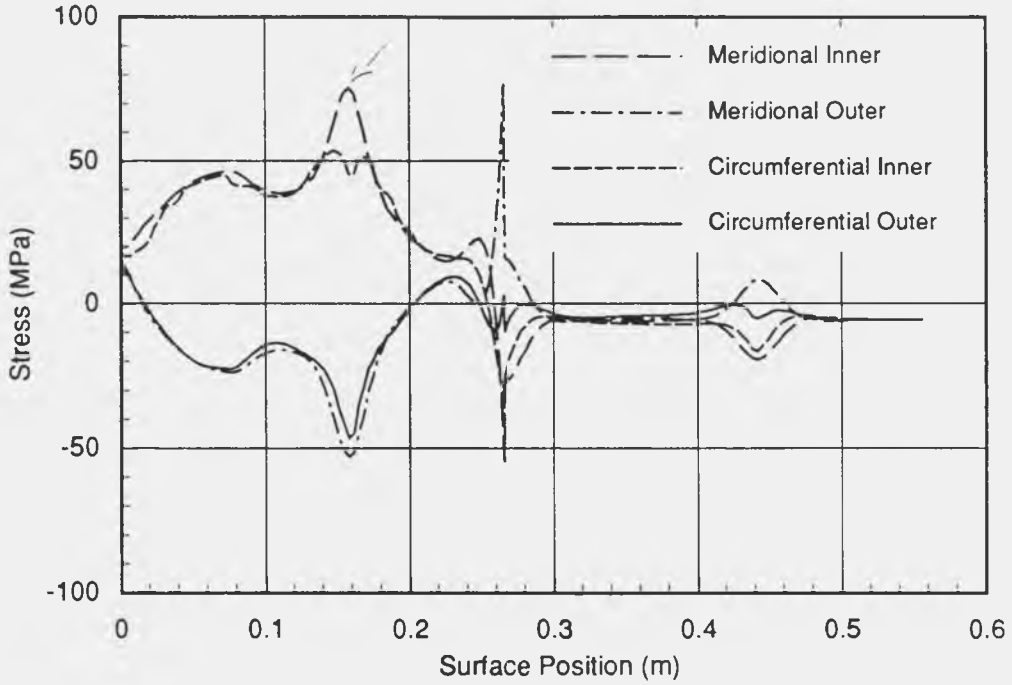

Figure 13. Receiver meridional and circumferential stress profiles during Step 3 of the receiver startup for Haynes 230 and a half-thickness (1.59 mm) aft dome.

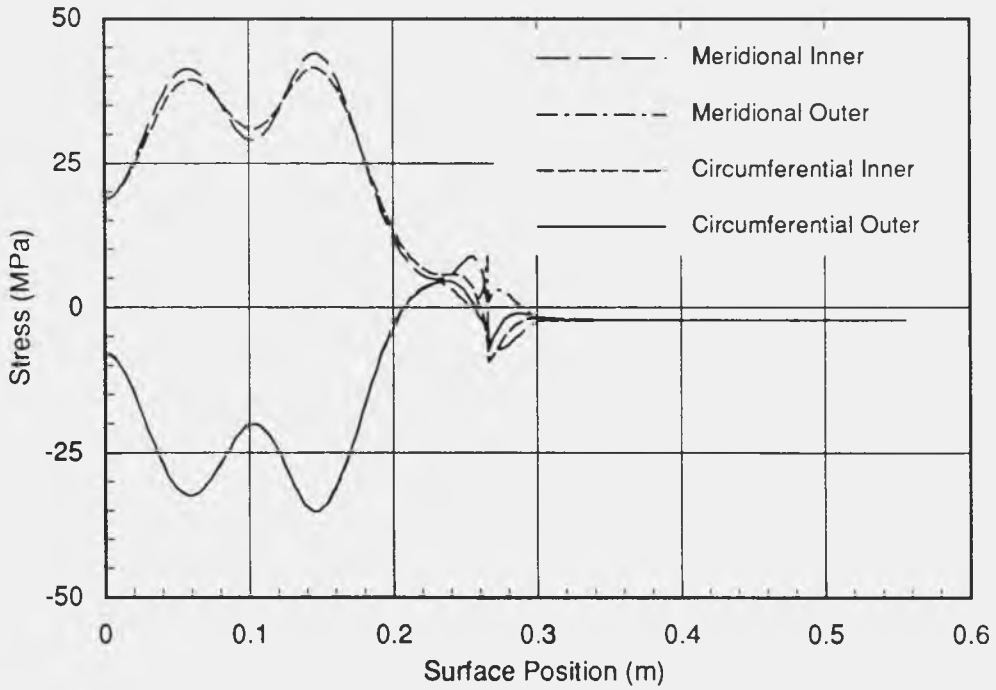

Figure 14. Receiver meridional and circumferential stress profiles during steady state operation for Haynes 230 and a half-thickness (1.59 mm) aft dome.

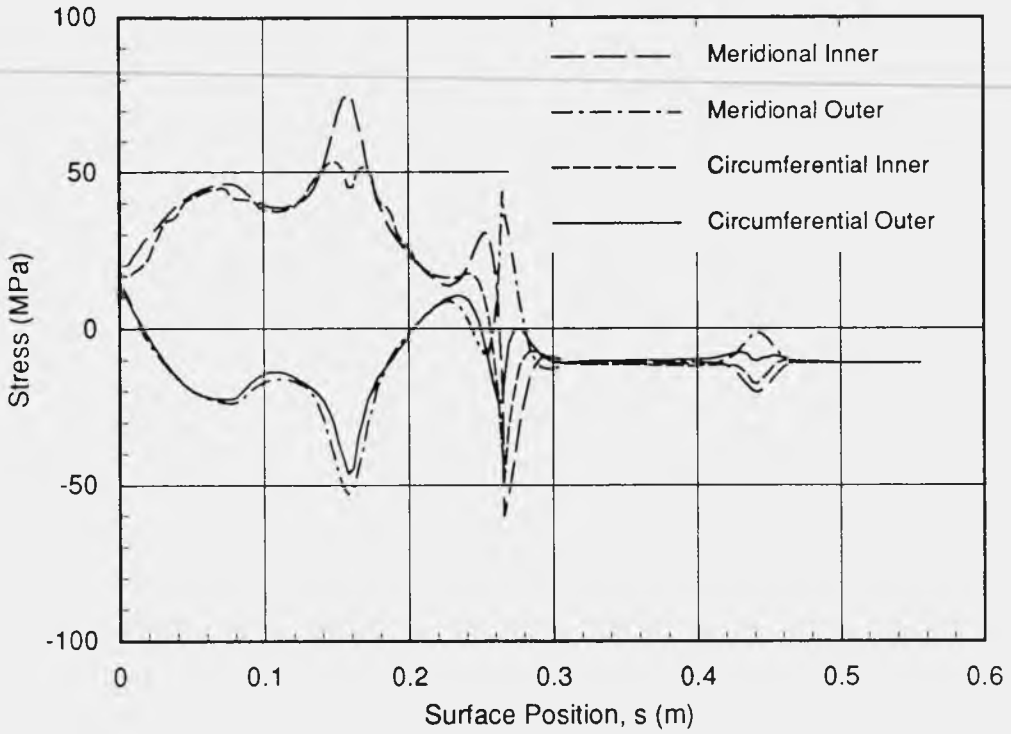

Figure 15. Receiver meridional and circumferential stress profiles during Step 3 of the receiver startup for Haynes 230 and a quarter-thickness (0.0813 mm) aft dome.

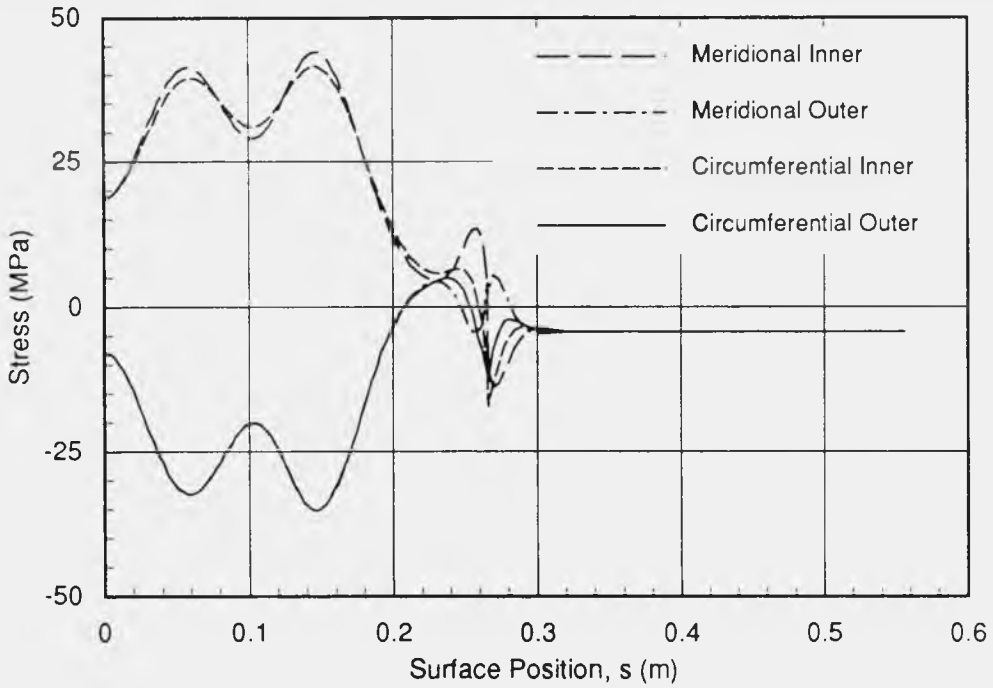

Figure 16. Receiver meridional and circumferential stress profiles during steady state operation for Haynes 230 and a quarter-thickness (0.0813 mm) aft dome.

Copy to:

1425 J. H. Biffle
1510 J. C. Cummings
1511 D. K. Gartling
1512 A. C. Ratzel
1513 D. W. Larson
1514 H. S. Morgan
1514 E. L. Hoffman
1514 M. K. Neilsen
1514 C. M. Stone
1500A L. W. Davison
1540 J. R. Asay
1544 R. C. Reuter
1545 D. R. Martinez
1550 C. W. Peterson
1832 J. A. Van Den Avyle
1833 G. A. Knorovsky
2542 J. B. Moreno
6217 C. E. Andraka
6217 R. B. Diver
6217 P. C. Klimas
6217 T. A. Moss

APPENDIX I

DATA ACQUISITION AND CONTROL

APPENDIX I
DATA ACQUISITION AND CONTROL

The reflux pool-boiler receiver was tested on the Test Bed Concentrator (TBC-1) at the National Solar Thermal Test Facility (NSTTF) located at Sandia National Laboratories in Albuquerque, New Mexico. The site data aquisition system, based on an HP-9845 computer and HP-3497 data system, was used to record the data generated during testing. In addition, a second HP-9845 and HP-3497 formed the heart of a safety/control system that monitored the operation of the test. This appendix describes the control system, data system channel allocation, and instrument selection and placement. An overview of the control and data system is shown in Figure 1 of the test procedure, included in the Operating Procedure section in Appendix K of this report. The figures in the test procedures will not be repeated here.

Fault Detection and Response

The primary function of the control system is to monitor the receiver system for faults and/or alarm conditions, and protect the receiver from damage in an emergency situation. If an abnormal condition is detected, a water-cooled shutter is closed over the aperture of the receiver, removing the concentrated solar flux. The shutter is air operated, and defaults to a closed position upon a loss of power. The shutter is part of the TBC system, and is cooled with a closed-loop water/glycol system. Emergency cooling was provided by a normally open valve connected to the city water supply.

The control system is based on an HP-9845 computer, which reads the selected data channels approximately every three seconds, and compares the readings against predetermined limits. In addition, a number of hardware display/controllers provide rapid response to some thermocouple channels and the pyrometer channel, as shown in the block diagram (Figure 2 of the test procedure, Appendix K). An alarm condition releases the controller output relay, breaking the relay chain, and causing the shutter to close. The particular channels to be monitored in hardware are determined by the project engineer, and are selected at the plugboard behind the computer.

A first-out failure indicator displays which instrument first sensed a failure in the case of multiple alarms. Figure 4 of the test plan (Appendix K) shows a schematic of the indicator. A red light indicates first failure. No light indicates subsequent failure. A green light indicates safe conditions for that instrument. Sixteen instruments may be monitored at once. Each instrument in the shutter relay chain contains an single-pole double-throw relay output. In the energized state, the relay completes the circuit, allowing the shutter relay to be energized. If a relay becomes de-energized, the shutter relay is also de-energized, and the five volts (V) is applied to one channel of both the inverting and noninverting buffers. A 1000-ohm resistor across the relay ensures that the 5V signal is available to other relays in the chain in the case of a multiple failure mode. The noninverting buffer has a latch that senses when the first input changes, and holds the condition until reset. This status is displayed with red light emitting diodes (LED). The inverting buffer controls the green LEDs, and shows the current condition of all channels. The control computer also monitors the buffer inputs and prints a time and cause message when a failure occurs.

An emergency stop (panic) button is included on the front panel. This button lights red when the control computer is active, all systems are ready, and the shutter circuit is energized. Actual shutter operation is manually controlled at the dish control panel, and is only enabled when the control system circuit is energized (uses "engine ready" input signal). A reset button is included to clear failure indications. A silence button will silence the alarm siren when the failure is acknowledged. The computer activates a time-delay relay each time through the program loop, providing a deadman stop in the case of a computer or program failure. The shutter activation relay is latching, providing protection (manual reset required) after momentary power interruptions.

Temperature Instrumentation

The primary measurable variable on the reflux receivers is temperature. The working fluid is in a two-phase system, so the internal pressure of the receiver can be directly determined from the bulk fluid or vapor temperature. Most of the temperatures are sensed by type K thermocouples (Chromel-Alumel) that are installed during fabrication.

The site wiring provides up to 48 channels of type-K thermocouples for TBC-1. Figures I-1 through I-5 show the locations of the 44 type-K thermocouples used during this test. Standard thermocouple locations are outlined in the test plan (Appendix J of this report). Up to six thermocouples can be monitored by the control system hardware displays for

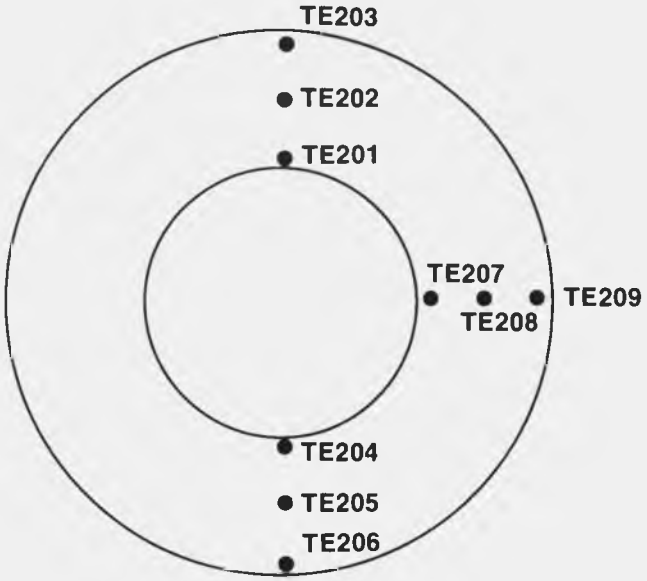

Figure I-1. Thermocouple placement on the conical stainless steel side wall looking toward the concentrator.

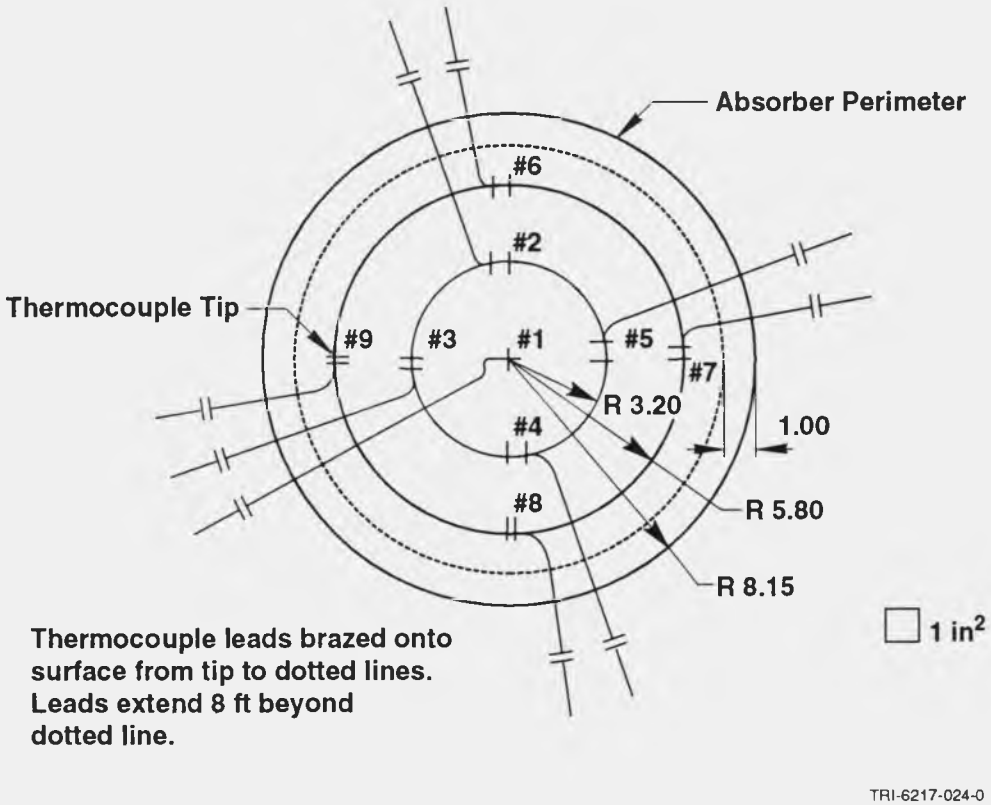

Figure I-2. Thermocouple placement on the air side of the absorber, as viewed from the concentrator. The thermocouples were brazed to the surface with Incuro-60 along their entire length to prevent overheating of the sheath.

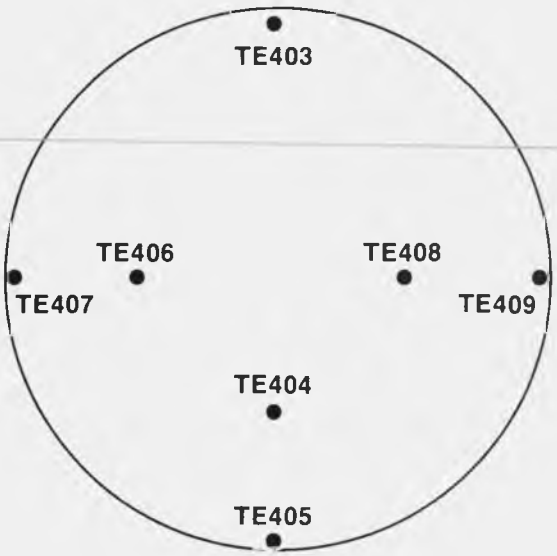

Figure I-3. Thermocouple placement on the aft dome as viewed from behind the receiver.

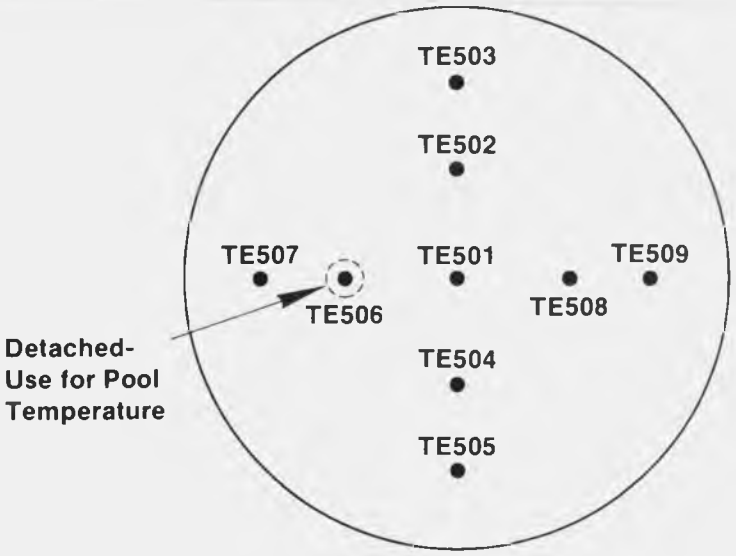

Figure I-4. Thermocouple placement on the sodium side of the absorber dome as viewed from inside the receiver.

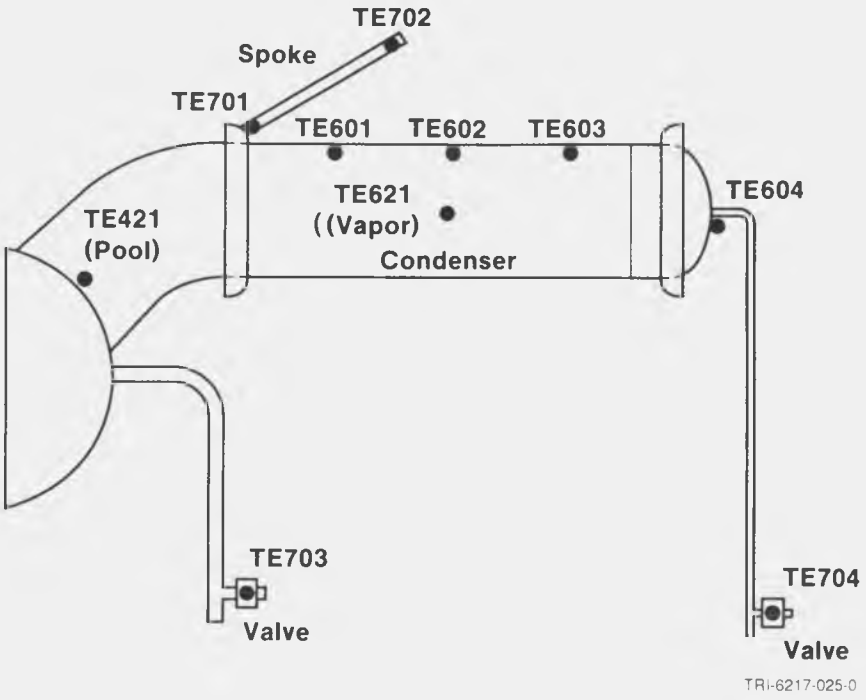

Figure I-5. Thermocouple placement on the remainder of the receiver.

almost instantaneous response. The recommended hardware-monitored thermocouples should include the pool temperature on a pool boiler, and several absorber thermocouples. Up to 12 additional thermocouples may be monitored by the HP-9845 computer. Table I-1 lists the initial selections for control monitoring of temperatures. All thermocouples are recorded by the test site data recording system. Table I-2 lists the initial data channels recorded. During the test, several thermocouples failed, including all of the internal absorber thermocouples and several front-face absorber thermocouples. During the x-ray tests, several new thermocouples were added to the receiver, and used these now-free channels for connection to the data acquisition and control system. Table I-3 lists the replacement thermocouple channel allocations. These replacements were made prior to the addition of xenon to the system.

A Mikron 8- to 14-micron (μm) pyrometer views the aborber surface through the aperture to supplement the absorber thermocouples. The pyrometer output consists of a 4-20 milliamp (mA) signal proportional to the average viewed temperature. The pyrometer output is monitored by a hardware display/shutdown device as well as the control computer. In the 8- to 14-μm infrared band seen by the pyrometer, very little reflected solar radiation is present, providing an accurate temperature response.

Preheat Control

The sodium working fluid used in the pool boiler receiver melts at about 98°C. Electrical preheating capability is provided to melt the sodium prior to on-sun operation. The preheat wiring is shown in Figure 5 of the test procedure (Appendix K). Three switches are provided on the front panel. The computer relay #5 provides 24V supply to the switches. These in turn pull down relays at the base of the dish, providing 120V power to the variacs. The variacs are set to provide uniform heating and prolonged heater life. The preheater circuits are also de-energized in an alarm situation.

Table I-1. CONTROL SYSTEM SIGNAL INPUTS

Symbol	Description	Software	Hardware
TE301	Absorber Center	X	X
TE302	Absorber Top Mid	X	X
TE303	Absorber Top Edge	X	X
TE304	Absorber Bot Mid	X	X
TE421	Pool	X	X
TE621	Vapor	X	X
TE601	Condenser Low	X	
TE602	Condenser Mid	X	
TE603	Condenser Top	X	
TE902	Cal Water Out	X	
FT103	Cal Water Flow	X	
TE310	Pyrometer	X	X
A3	Argon Bottle P		X
A4	Helium Bottle P		X
A5	Argon Reg P	X	X
A6	Helium Reg P	X	X

TABLE I-2. DATA SYSTEM CHANNEL ALLOCATIONS

Menu #	Channel #	Transdu	Description		(Units)
101		QTS	System number		(# 2)
102		Date	Date of test		(Menu updated - 16 Nov 89)
103		Clock	Mountain Standard Time		(HH:MM:SS)
104		Calc	Solar time		(HH:MM:SS)
105		Calc	Solar elevation		(Degrees above horizon)
106		Calc	Solar azimuth		(Degrees CW from North)
107	420	TH100	Ambient air temperature		(°C)
108	421	WS100	Wind speed		(m/s)
109	422	WD100	Wind direction		(Degrees CW from North)
110	423	NIP41	Direct normal insolation from site NIP		(W/m^2)
111	417	TE2385	K-Type #2 UTR plate temp, Box #1		(°C)
112	418	TE2383	K-Type #1 UTR plate temp, Box #1		(°C)
113	419	TE2382	T-Type #1 UTR plate temp, Box #1		(°C)
114		DT100	Calorimeter Delta-T output		
115	200	TC201	Receiver side wall, top-inner	temperature	(°C)
116	201	TC202	Receiver side wall, top-middle	temperature	(°C)
117	202	TC203	Receiver side wall, top-outer	temperature	(°C)
118	203	TC204	Receiver side wall, bot-inner	temperature	(°C)
119	204	TC205	Receiver side wall, bot-middle	temperature	(°C)
120	205	TC206	Receiver side wall, bot-outer	temperature	(°C)
121	206	TC207	Receiver side wall, side-inner	temperature	(°C)
122	207	TC208	Receiver side wall, side-middle	temperature	(°C)
123	208	TC209	Receiver side wall, side-outer	temperature	(°C)
124	209	TC301	Absorber air, center	temperature	(°C)
125	210	TC302	Absorber air, top-middle	temperature	(°C)
126	211	TC303	Absorber air, top-edge	temperature	(°C)
127	212	TC304	Absorber air, bottom-middle	temperature	(°C)
128	213	TC305	Absorber air, bottom-edge	temperature	(°C)
129	214	TC306	Absorber air, right-middle	temperature	(°C)
130	215	TC307	Absorber air, right-edge	temperature	(°C)
131	216	TC308	Absorber air, left-middle	temperature	(°C)
132	217	TC309	Absorber air, left-edge	temperature	(°C)
133	218	TC403	Aft dome, top	temperature	(°C)
134	219	TC404	Aft dome, bottom-middle	temperature	(°C)
135	220	TC405	Aft dome, bottom-edge	temperature	(°C)
136	221	TC406	Aft dome, right-middle	temperature	(°C)
137	222	TC407	Aft dome, right-edge	temperature	(°C)
138	223	TC408	Aft dome, left-middle	temperature	(°C)
139	224	TC409	Aft doem, left-edge	temperature	(°C)
140	225	TC421	Sodium pool, internal	temperature	(°C)
141	226	TC501	Absorber, internal, center	temperature	(°C)
142	227	TC502	Absorber, internal, top-middle	temperature	(°C)

TABLE I-2. DATA SYSTEM CHANNEL ALLOCATIONS (CONCLUDED)

Menu #	Channel #	Transdu	Description		(Units)
143	228	TC503	Absorber, internal, top-edge	temperature	(°C)
144	229	TC504	Absorber, internal, bottom-mid	temperature	(°C)
145	230	TC505	Absorber, internal, bot-edge	temperature	(°C)
146	231	TC506	Absorber, int, RT-middle (det)	temperature	(°C)
147	232	TC507	Absorber, internal, right-edge	temperature	(°C)
148	233	TC508	Absorber, internal, left-mid	temperature	(°C)
149	234	TC509	Absorber, internal, left-edge	temperature	(°C)
150	235	TC601	Condenser, internal, low	temperature	(°C)
151	236	TC602	Condenser, internal, middle	temperature	(°C)
152	237	TC603	Condenser, internal, high	temperature	(°C)
153	238	TC604	End cap, external	temperature	(°C)
154	239	TC621	Vapor, internal	temperature	(°C)
155	240	TC701	Hot spoke	temperature	(°C)
156	241	TC702	Cold spoke	temperature	(°C)
157	242	TC703	3/4-inch valve	temperature	(°C)
158	243	TC704	3/8-inch valve	temperature	(°C)
159	244	TC901	Calorimeter water input	temperature	(°C)
160	245	TC902	Calorimeter water output	temperature	(°C)
161	246	TC921	Calorimeter inlet surface	temperature	(°C)
162	247	TC922	Calorimeter outlet surface	temperature	(°C)
163	000	TC020	Aperture plate output	temperature	(°C)
164	001	TC022	Shutter plate output	temperature	(°C)
165	002	DT100	Calorimeter - input water ref.	temperature	(°C)
166	460	NIP41	Instantaneous solar power input	(kW)	
167	461	FT623	Aperture plate cooling water	flow	(L/min)
168	462	FT624	Shutter plate cooling water	flow	(L/min)
169	463	DT100	Calorimeter - cooling water delta-temp	(°C)	
170	464	FT201	Calorimeter - argon gas	flow	(scfh)
171	465	FT202	Calorimeter - helium gas	flow	(scfh)
172	466		Shutter plate position		(Open/Closed)
173	467	TE310	Pyrometer temperature		(°C)
174	468	FT103	Calorimeter - outlet water	flow	(L/min)
175	469	NIP05	Direct Insolation - TBC-1 boresight	(W/m^2)	
176	470	FT104	Calorimeter - inlet water	flow	(L/min)
177		Calc	Instantaneous receiver power output	(kW)	
178		Calc	Instantaneous receiver heat loss		(kW)
179		Calc	Instantaneous receiver efficiency	(%)	
180		Calc	Integrated solar power input		(kWh)
181		Calc	Integrated receiver power output	(kWh)	
182		Calc	Integrated receiver heat loss		(kWh)
183		Calc	Integrated receiver efficiency		(%)
184			Maximum - dish or site NIP		(W/m^2)

TABLE I-3. CHANGES TO THE DATA CHANNELS DURING AND AFTER THE ADDITION OF XENON TO THE RECEIVER

Failed TCs	Menu #	Failed TC Description	New TC Description
TE301	124	Abs, air, ctr	Aperture, E top
TE304	127	Abs, air, bot mid	Aperture, E ctr
TE308	131	Abs, air, lft mid	Aperture, E bot
TE501	141	Abs, int, ctr	Top, 3/8-in.tube
TE502	142	Abs, int, top mid	Mid, 3/8-in.tube
TE503	143	Abs, int, top edg	Bot, 3/8-in. tube
TE504	144	Abs, int, bot mid	Top, 3/4-in. tube
TE505	145	Abs, int, bot edg	Bot, cooling coil
TE506	146	Abs, int, rt mid det	Aperture, W top
TE507	147	Abs, int, rt edg	Aperture, W ctr
TE508	148	Abs, int, lft mid	X-ray head
TE509	149	Abs, int, lft edg	Aperture, W bot
TE603	152	Cond int, high	None

In addition, the following thermocouples were slightly moved:

Menu TCs	TC #	New TC Description	Description
TE703	157	3/4" valve	Top, cooling coil
TE704	158	3/8" valve	Air side of 3/8-in. valve

Calorimetry and Power Extraction

The control system also provides temperature control of the receiver working fluid. Temperature control is provided by varying the power extracted from the receiver by the cold water gas-gap calorimeter.

The gas-gap calorimeter (Figure 3 of the test procedure in Appendix K) draws heat out of the receiver into city water (Appendix F of this report). A mixture of helium and argon flows in the gap between the water jacket and receiver. The ratio of the gases in the mixture determines the thermal conductivity of the gap, and thus the power extracted. An LFE brand proportional integral differential (PID) controller monitors a condenser-section thermocouple and provides a 0-5 VDC signal to control the temperature. The output "heat" signal of the controller proportionally drives the argon mass flow control valve, while the signal is inverted to drive the helium mass flow control valve. Figure I-6 shows a detailed schematic of the gas-flow control circuit. Each flow control signal can be attenuated with a 10-turn pot to control the maximum gas flow rate. This rate determines the response time of the calorimeter to a changing heat load, and also determines the useful life of a gas bottle. The gas flows are monitored by the data computer at transducer

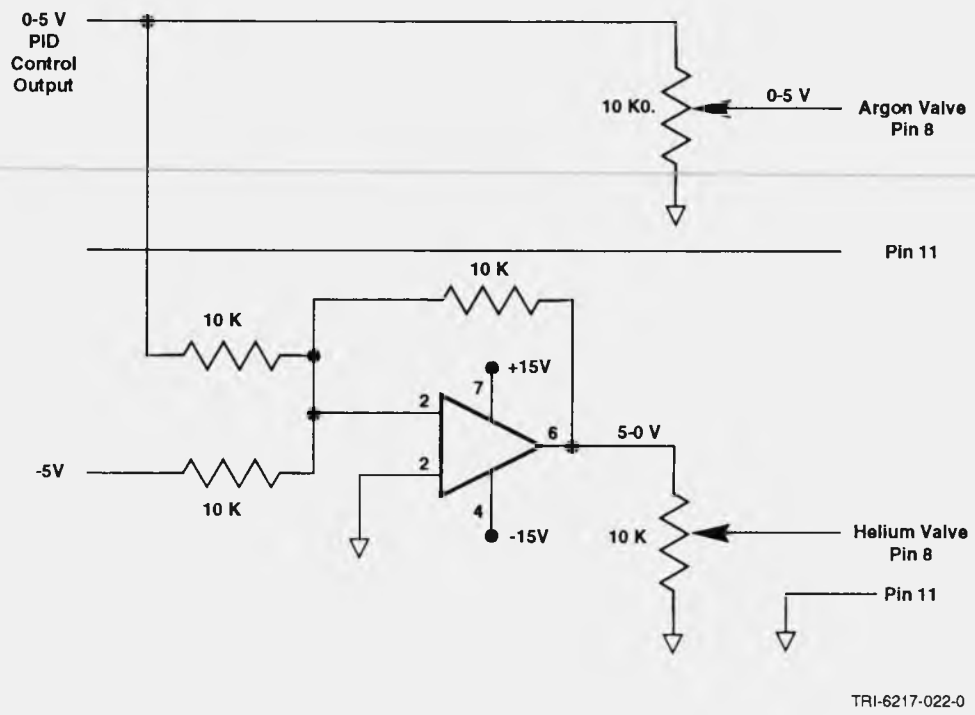

Figure I-6. Schematic of the calorimeter gas flow control circuit. The signal is inverted for the helium valve so that a constant total flow rate of the two gases is maintained.

outputs FT201 and FT202, which are 0-5 VDC signals. The 0-5 VDC corresponds to 0 to 5 l/min of nitrogen, which translates to 0 to 7 l/min of argon or helium. The gas flow had a reasonable response time when set to 5.0 on the 10-turn pot, which corresponds to 3.5 l/min of argon and helium flow. The gas flows may be manually turned off with the gas-off toggle switch, which grounds a shut-off signal pin on the gas control valves. The control computer also monitors pressure at the bottles with pressure switches PS201 and PS202, and sounds an alarm at 300-psi bottle pressure in order to prevent gas depletion. The regulated pressure is monitored by PT201 and PT202, which are 0-50 psig two-wire 4-20 mA pressure transducers. If the regulated pressure drops below 15 psi, the shutter is shut through the use of a pair of relay-output Action-Paks. The control computer also overrides the PID controller with relays 3 and 4 during any emergency shutdown. The relays demand full helium and no argon flow, providing the fastest possible cool-off. The water temperatures inside the calorimeter are also monitored and compared against limits to assure that boiling does not occur.

The calorimeter system is also used to determine the power extracted for performance evaluation. The water flow rate, temperature, and change in temperature are monitored. The water flow rate is measured with a Flowtech turbine flowmeter placed near the exit of the calorimeter. Because of the elevation of the dish, cavitation was occasionally experienced at the flowmeter. A valve at ground level on the exhaust line was slightly closed to provide a backpressure, preventing cavitation. Late in the testing, a second Flowtech turbine flowmeter was added to the inlet line at the calorimeter. The inlet and outlet water temperatures were monitored with type-T sheathed thermocouples to provide a rough temperature change measurement. A delta-T brand thermopile provided a more precise temperature change measurement. The flow rate and outlet temperature were monitored by the control computer, and could shut down the system if limits were exceeded. A 50-psi burst disk provides protection for the calorimeter in the case of flow failure and subsequent rapid boiling of the water. A normally open electric shutoff valve can be actuated manually from the control computer (relay 001) in the case of a sodium spill, but no software sequence would stop water flow. In most emergency scenarios, keeping the cooling water flowing was advantageous, unless both a water leak and a sodium leak occurred simultaneously. The calorimeter shell is stainless steel to minimize the possibility of sodium mixing with water. Several type-K sheathed thermocouples monitored the surface temperatures in the calorimeter in an attempt to verify that local boiling did not occur.

APPENDIX J

SANDIA REFLUX SOLAR RECEIVER STANDARD TEST AND INSTRUMENTATION PLAN

SANDIA REFLUX SOLAR RECEIVER
STANDARD TEST & INSTRUMENTATION PLAN

1. Introduction

The reflux solar receiver program involves the design, fabrication, and testing of prototype receivers. In Phase I of the program, receivers based on screen wick heat-pipe technology, reflux pool-boiler technology, and sintered powder wick and/or other wick technology, will be designed, fabricated, and tested in an effort to establish which approach has the most promise for long-lived, reliable, efficient, cost-effective operation. In Phase II, the most promising approach will be integrated with a fossil-fuel-fired heat-source and optimized for an advanced Stirling conversion system (ASCS).

All receiver testing will be conducted on the test bed concentrators (TBC) located at the U.S. Solar Thermal Test Facility operated by Sandia National Laboratories (SNL) in Albuquerque, NM. Since on-sun testing is a major factor in the selection of the preferred approach, all receiver prototypes will be subjected to similar test conditions and procedures.

A gas-gap, cold-water calorimeter will be used to absorb the receiver heat load and control receiver temperature. Control is obtained by varying the helium-argon ratio (and therefore the conductance) in a narrow gap (0.020"-0.050") between the condenser section of the receiver and a cold-water calorimeter. Water flow through the calorimeter is set to about 20 gpm (75 lit/min). Measurements are identical to those for the JPL cold-water calorimeter used to characterize the TBCs. Helium and argon flows are slow (one to ten standard cubic feet per hour) and are controlled remotely.

The overall objectives of testing are to, as efficiently as possible, establish the limitations of the specific hardware; and, assuming that the receiver is operationally capable of satisfying minimum requirements, to determine the performance characteristics of the hardware.

Receiver testing will, therefore, be conducted in two stages. In Stage I, hardware limitations will be established by subjecting the receivers to increasingly more severe test conditions. If the receiver survives the first stage of tests, additional tests will be conducted until receiver performance is fully characterized (Stage II). As much performance information as possible shall be collected during Stage I testing. Following the Stage I and II tests, additional testing may be conducted to subject the receiver to conditions that exceed the original design specifications, or to achieve a maximum amount of cycles and/or operating time.

The tests and procedures outlined in this document are intended to serve as common basis for all of the receivers tested in this program. It is expected that each receiver concept will call for additional instrumentation and/or tests, depending on the specific questions needed to be answered. Detailed instrumentation and test plans beyond those presented here can be included as an addendum to this standard test and instrumentation plan.

2. Pretest Procedures

Before each test, the receiver and Test Bed Concentrator will be inspected for safe operation. For all tests, including Stage I and II, and follow-on tests, the attached checklist will be completed and saved as part of the test documentation record.

3. Stage I Tests

The objective of Stage I tests will be to establish operating procedures, response characteristics, performance and hardware limitations. Receivers will be tested under increasingly severe conditions until all conditions that will be encountered under normal operation have been demonstrated. Stage I tests will be conducted at the design point temperature (condenser temperature equal to 800°C).

3.1 Low-Power, Steady-State Tests - The purpose of testing reflux receivers at low power is to demonstrate the operability of the receiver and calorimeter control system at reduced power (approximately 35 kW) under steady-state conditions. Methods of control during this test may include either manual or automatic operation. For the reflux pool-boiler receiver, this test should be conducted either early or late in the day to place the concentrator at minimum risk and, for the heat-pipe receivers, this test should be conducted towards solar noon so that capillary pumping requirements are minimum. Tests should only be conducted if long periods of cloudless weather are anticipated. Prior to on-sun operation, the receiver should be preheated sufficiently to insure that sodium does not solidify on the condenser and to avoid any stress or transient-related concerns. Figure 1 shows the mirrors on the TBC to be covered for these tests.

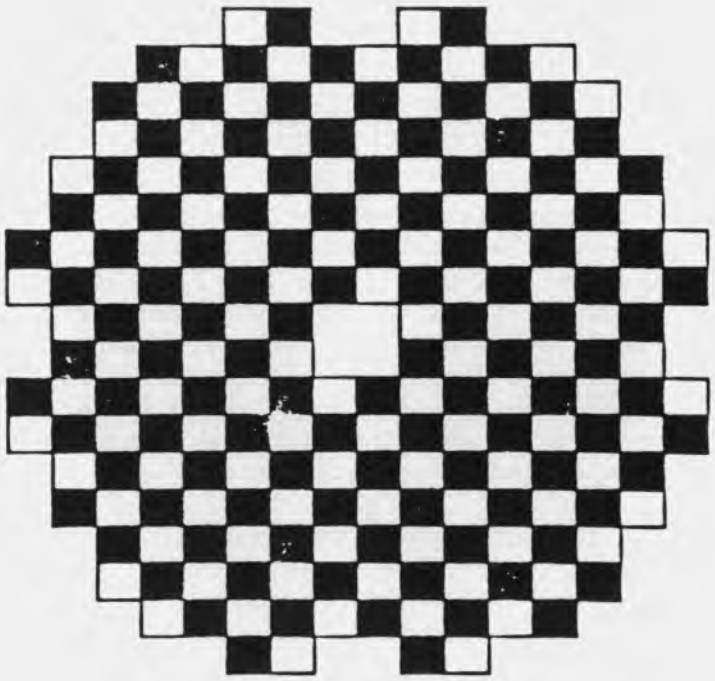

Figure 1. Low-power, steady-state tests. The darkened rectangles show the TBC facets to be covered as viewed from the receiver.

To demonstrate the operability of the emergency shutdown system, the ability of the system to close the shutter as a result of an overtemperature shall be verified.

The ability of the receiver to operate at low power in steady state at the design point temperature (±10°C) will be demonstrated for a period of at least 1 hour. Following the steady-state tests, the cool-down characteristics of the receiver will be recorded. Low-power steady-state tests should serve to debug system operation and data acquisition. Additional low-power steady-state tests are at the discretion of the project leader.

3.2 Intermediate-Power, Steady-State Tests - The purpose of testing reflux receivers at intermediate power is to demonstrate the operability and stability of the receiver at intermediate power (52 kW) in a steady-state condition. Methods of control during this test may be either manual or automatic. For the reflux pool-boiler receiver this test should be conducted either early or late in the day and, for the heat-pipe receivers, this test should be conducted towards solar noon. Tests should only be conducted if long periods of cloudless weather are anticipated. Prior to going on-sun, the receiver should be preheated sufficiently to insure that sodium does not solidify on the condenser. The amount of preheat (and therefore the transient shock) applied to the receiver is at the discretion of the project leader. Figure 2 shows the mirrors on the TBC to be covered for these tests.

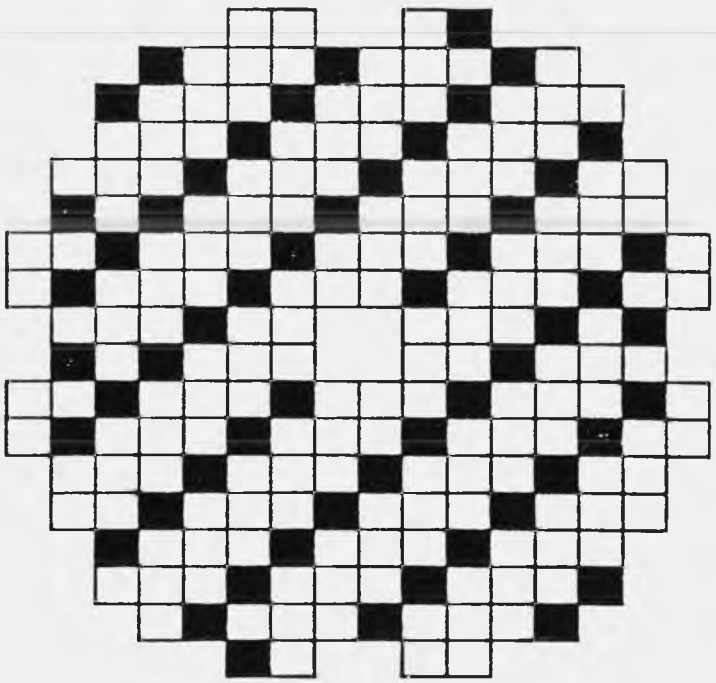

Figure 2. Intermediate-power, steady-state test. The darkened rectangles show the TBC facets to be covered as viewed from the receiver.

3.3 Full-Power, Steady-State Tests - The purpose of testing reflux receivers at full power is to demonstrate the operability and stability of the receiver at design power (≈70 kW) in a steady-state condition. Methods of control during this test may be either manual or automatic. For the reflux pool-boiler receiver this test should be conducted either early or late in the day and, for the heat-pipe receivers, this test should be conducted towards solar noon. Tests should only be conducted if long periods of cloudless weather are anticipated. Prior to going on-sun, the receiver should be preheated to insure that sodium does not solidify on the condenser. The number of full-power, steady-state tests and the amount of preheat is at the discretion of the project leader. All facets are uncovered for these tests.

3.4 Full-Power, All-Day Tests - The purpose of testing reflux receivers at full power throughout the day is to demonstrate the receiver's ability to respond to orientation variations under steady-state operation. These tests should be conducted only when long periods of cloudless weather are anticipated. Whether the receiver is allowed to operate during cloud transients during this test is at the discretion of the project leader.

3.5 Cloud Simulation Tests - The purpose of the cloud simulation tests is to demonstrate the receiver's ability to respond to cloud transients. These tests should be conducted during conditions of bright sunshine (>900 w/m^2 direct insolation). Actual cloud passages or the shutter can be used to create abrupt start and stop step changes. The receiver should demonstrate hot restart after it has been allowed to cool to approximately 700, 600, and 500°C (three tests minimum). At the project leader's discretion, these tests can be deferred until after the completion of Stage II testing.

3.6 Cold Start Tests - At some point during testing, the receiver should demonstrate the ability to start from a cold condition at full power. It is anticipated that during the course of steady-state testing, the degree of electrical preheat will be incrementally reduced. Whether the receiver is subjected to cold start transients and the degree of the transients is at the discretion of the project leader. Like the cloud simulation tests, the cold start tests can be deferred until after Stage II testing.

3.7 Additional Hardware Limitation Tests - Additional tests that the project leader feels are appropriate should be conducted. Tests such as operating at increased temperatures or frozen sodium starts should be deferred until after Stage I and II testing.

4. Stage II Tests

The objectives of Stage II tests are 1) to provide data for the verification of receiver performance models, 2) to provide data for the evaluation of convective heat loss from high-temperature dish receivers, and 3) to provide performance information to support system analysis and optimization studies.

Performance tests will be conducted like the full-power, all-day tests in Stage I. Performance parameters will be determined for the range of insolations, wind speeds and directions, receiver orientations, etc., available on the days of testing for a receiver operating temperature

of 800°C. It is anticipated that approximately 5 days of testing will be required. Test conditions which span a range of wind speeds and receiver orientations are desirable. Data taken during the Stage I tests can be used where appropriate.

4.1 Receiver Performance Model Verification - Receiver performance models under development simultaneously solve the steady-state radiative, conductive, and convective energy transfers in the receiver. Model results include surface temperature distributions, delivered power, and receiver efficiency. Receiver radiative properties (solar and infrared), convective and conductive heat loss coefficients, and the thermal properties and temperatures of materials are required as inputs to the thermal analysis models. Solar flux distributions and receiver geometry information are also required. Geometry, materials, thermal properties, and conduction are well understood. Relative to convection heat loss radiation is well understood, especially if the receiver surface radiative properties are well known. Because the radiation properties of materials can change with time, radiative properties will be measured after the optical coatings have cured and before initiating Phase II tests. Additional optical properties measurements should be taken as necessary. As tested receiver, geometry and location shall be measured.

4.2 Convective Heat Loss Measurements - Convective heat loss from dish cavity receivers is the largest uncertainty with respect to performance predictions. These tests represent a unique opportunity to determine the magnitude of convective loss and the effects of wind speed and direction and receiver orientation. Given that measurement of convective loss involves a great deal of uncertainty, a statistical approach will be attempted. Convective loss will be evaluated at many points, and an average convective coefficient determined and correlated with wind speed, orientation, and ambient temperature. The key to this approach is accurate measurements of available and delivered solar power and the maintenance of a stable operating temperature.

An objective will be to evaluate the daily average convective heat loss coefficient. More detailed convective loss information will be obtained if possible. After evaluation of the automatic control system (during Stage I tests) for stable operation, a decision will be made regarding the potential for making meaningful convective heat loss coefficient determinations.

4.3 Systems Analysis and Optimization - In order to predict annual efficiency and levelized energy costs, an understanding of performance in steady-state and transient operation is required. All-day tests provide a unique opportunity to directly measure the daily efficiency of receivers. In addition, transient tests can be used to measure thermal capacitance, for comparison to transient and systems analysis models.

5. Reflux Receiver Instrumentation Plan

Receiver instrumentation shall be standardized and designed to support the test plan objectives. Data from the receiver Stage I and II tests will be recorded on the DRTF HP 9845 data acquisition system. A separate computer will be used for control and emergency shutdown. The data acquisition system will be programmed to run at a high sampling range (scan every 10 sec) and be switchable to a low rate (scan every 60 sec).

Standardized receiver instrumentation will consist of Type K thermocouples and will include the following:

- o Pyrometer absorber temperature.
- o Front surface (absorber) temperatures (5 locations). See Figure 3.
- o Aft dome surface temperatures (7 locations) See Figure 4.
- o Condenser surface temperatures (4 locations), including one on the end-cap and the remainder evenly spaced along the top of the calorimeter section.
- o Receiver sidewall temperatures (9 locations). See Figure 5.
- o One thermocouple (penetration or thermowell) in the vapor space.
- o One thermocouple in the liquid metal pool (pool boiler only).

The receiver calorimeter flow rate and delta-T measurement should each have an accuracy of ±1% or better. Direct normal insolation and wind speed and direction in the vicinity of the TBCs will be recorded and shall be available to the DRTF data acquisition system for correlation with temperature and calorimeter measurements. Instrumentation and control measurements are summarized in Table 1.

A ±1% or better accuracy is desirable for the total power available to the receiver. This requires independent cold water calorimeter tests with the existing JPL cold water calorimeter with identical apertures. The TBC mirror facets should be washed as necessary for the Stage II tests. Facet reflectivity or cleanliness information as well as aim points, TBC number, and facet coverage information should be recorded with each test.

In addition, a microphone in the vicinity of the receiver transmitting to the control room shall be installed.

6. Safety Interlocks

Safety interlocks are needed to insure safe operation and to minimize the risk of damaging the receiver. For most situations, preventing overheat by measuring and checking the receiver's vapor temperature will trap the most serious preventable faults. At no time will a sodium reflux receiver ever be allowed to exceed 850°C. Additional checks (see Table 2) provide responses to specific problems. The receiver control system shall be capable of responding to the faults identified in Table 2. Tests should be performed as necessary to insure the system's ability to respond to foreseeable problems.

7. Test Documentation

For each test, a labeled file folder will be maintained at the DRTF containing the following:

- The completed Reflux Heat Pipe Receiver Checklist.
- Summary plot of solar insolation and instantaneous receiver efficiency versus solar time.
- Summary plot of solar insolation and receiver temperatures versus solar time. Receiver temperature thermocouple (or pyrometer) selected for display in figure should be noted on the plot.
- Labeled data diskettes with the test data.

Additional copies of the results should also be maintained by the project leader and those interested in the results.

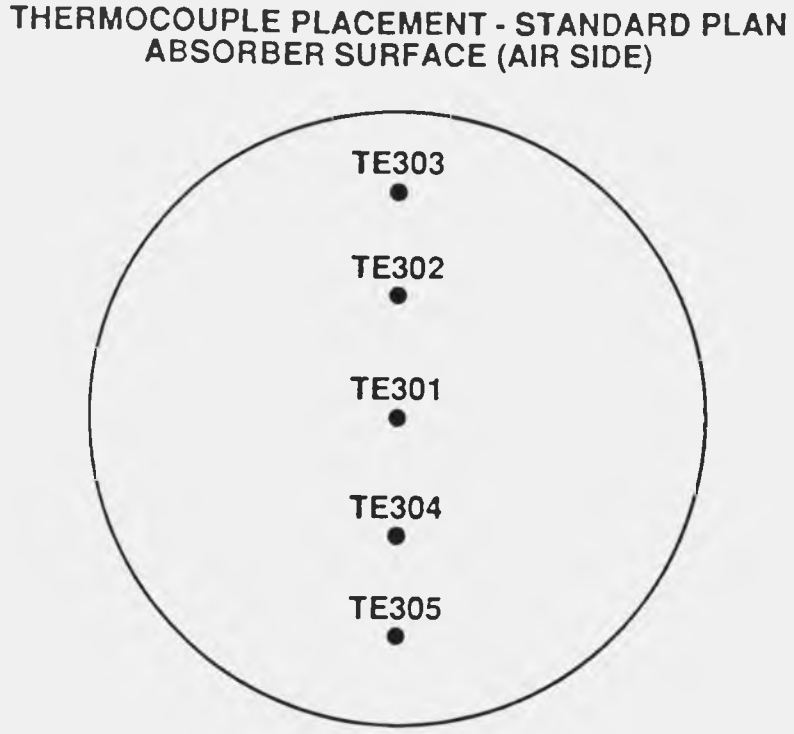

Figure 3. Thermocouple placements on the absorber surface as viewed from the concentrator.

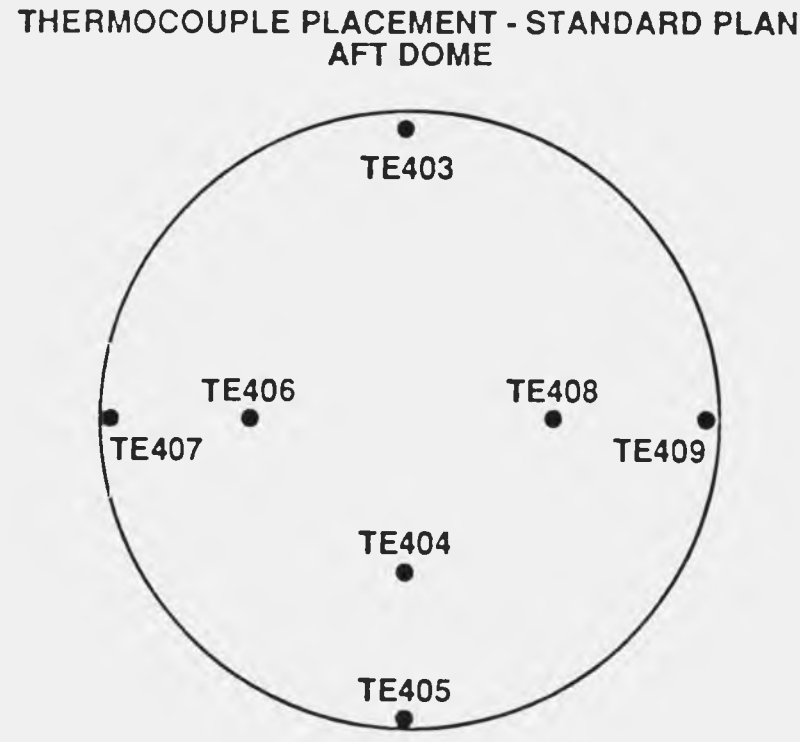

Figure 4. Thermocouple placements on the aft dome as viewed from the back of the receiver looking towards the concentrator.

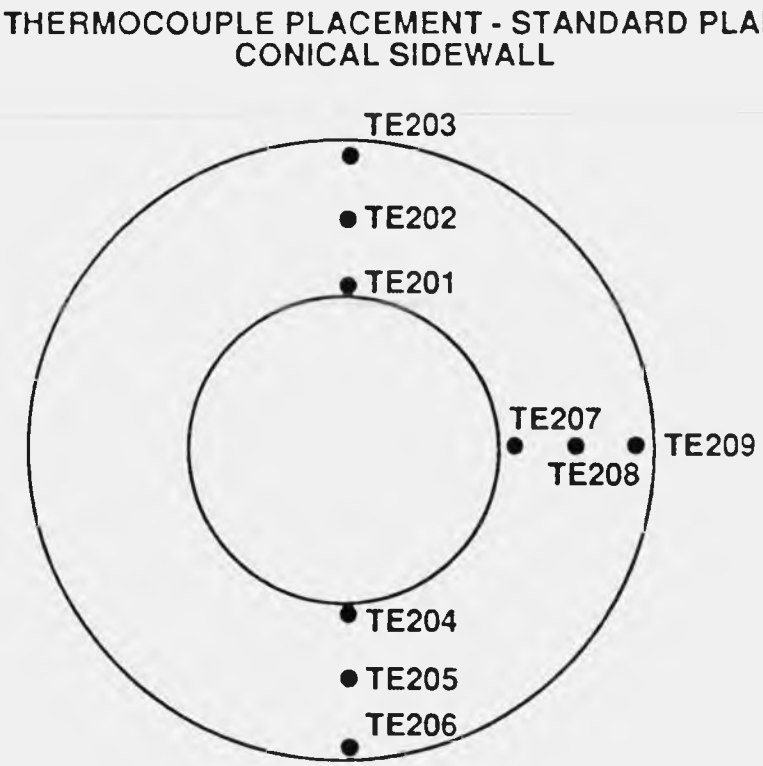

Figure 5. Thermocouple placements on the receiver sidewall as viewed from the receiver looking towards the concentrator.

Table 1

DATA MENU FOR STANDARD REFLUX-RECEIVER TESTS

Menu #	Chan #	S/C	Transdu	Description		(Units)
601				System number		(# 2)
602				Date of test		(YYMMDD)
603				Mountain Standard Time		(HH:MM:SS)
604				Solar time		(HH:MM:SS)
605				Solar elevation	(degrees	above horizon)
606				Solar azimuth	(Degrees	CW from North)
607	420	S20C00	TH100	Ambient air temperature		(Deg C)
608	421	S20C01	WS100	Wind speed		(m/s)
609	422	S20C02	WD100	Wind direction	(degrees	CW from North)
610	423	S20C03	NIP41	Direct normal insolation from site NIP		(W/m^2)
611	417	S29C17	TE2385	K-Type #2 UTR plate temp, Box #1		(Deg C)
612	418	S29C18	TE2383	K-Type #1 UTR plate temp, Box #1		(Deg C)
613	419	S29C19	TE2382	T-Type #1 UTR plate temp, Box #1		(Deg C)
614				Spare		
615	200	S10C00	TE201	Receiver sidewall, top-inner	temp	(Deg C)
616	201	S10C01	TE202	Receiver sidewall, top-middle	temp	(Deg C)
617	202	S10C02	TE203	Receiver sidewall, top-outer	temp	(Deg C)
618	203	S10C03	TE204	Receiver sidewall, bot-inner	temp	(Deg C)
619	204	S10C04	TE205	Receiver sidewall, bot-middle	temp	(Deg C)
620	205	S10C05	TE206	Receiver sidewall, bot-outer	temp	(Deg C)
621	206	S10C06	TE207	Receiver sidewall, side-inner	temp	(Deg C)
622	207	S10C07	TE208	Receiver sidewall, side-middle	temp	(Deg C)
623	208	S10C08	TE209	Receiver sidewall, side-outer	temp	(Deg C)
624	209	S10C09	TE301	Absorber air, center	temp	(Deg C)
625	210	S10C10	TE302	Absorber air, top-middle	temp	(Deg C)
626	211	S10C11	TE303	Absorber air, top-edge	temp	(Deg C)
627	212	S10C12	TE304	Absorber air, bottom-middle	temp	(Deg C)
628	213	S10C13	TE305	Absorber air, bottom-edge	temp	(Deg C)
629	214	S10C14	TExxx	Spare TC	temp	(Deg C)
630	215	S10C15	TExxx	Spare TC	temp	(Deg C)
631	216	S10C16	TExxx	Spare TC	temp	(Deg C)
632	217	S10C17	TExxx	Spare TC	temp	(Deg C)
633	218	S10C18	TE403	Aft dome, top-edge	temp	(Deg C)
634	219	S10C19	TE404	Aft dome, bottom-middle	temp	(Deg C)
635	220	S11C00	TE405	Aft dome, bottom-edge	temp	(Deg C)
636	221	S11C01	TE406	Aft dome, right-middle	temp	(Deg C)
637	222	S11C02	TE407	Aft dome, right-edge	temp	(Deg C)
638	223	S11C03	TE408	Aft dome, left-middle	temp	(Deg C)
639	224	S11C04	TE409	Aft dome, Left-edge	temp	(Deg C)
640	225	S11C05	TE421	Sodium pool (Pool-boiler only)	temp	(Deg C)
641	226	S11C06	TExxx	Spare TC	temp	(Deg C)
642	227	S11C07	TExxx	Spare TC	temp	(Deg C)
643	228	S11C08	TExxx	Spare TC	temp	(Deg C)
644	229	S11C09	TExxx	Spare TC	temp	(Deg C)
645	230	S11C10	TExxx	Spare TC	temp	(Deg C)
646	231	S11C11	TExxx	Spare TC	temp	(Deg C)
647	232	S11C12	TExxx	Spare TC	temp	(Deg C)
648	233	S11C13	TExxx	Spare TC	temp	(Deg C)
649	234	S11C14	TExxx	Spare TC	temp	(Deg C)
650	235	S11C15	TE601	Condenser, internal, low	temp	(Deg C)
651	236	S11C16	TE602	Condenser, internal, middle	temp	(Deg C)
652	237	S11C17	TE603	Condenser, internal, High	temp	(Deg C)
653	238	S11C18	TE604	End Cap, external	temp	(Deg C)
654	239	S11C19	TE621	Vapor, internal	temp	(Deg C)
655	240	S12C00	TExxx	Spare TC	temp	(Deg C)
656	241	S12C01	TExxx	Spare TC	temp	(Deg C)
657	242	S12C02	TExxx	Spare TC	temp	(Deg C)
658	243	S12C03	TExxx	Spare TC	temp	(Deg C)
659	244	S12C04	TE901	Calorimeter water input	temp	(Deg C)
660	245	S12C05	TE902	Calorimeter water output	temp	(Deg C)

Table 1 (cont.)

Menu #	Chan _#	S/C	Transdu	Description		(Units)
661	246	S12C06	TE921	Calorimeter inlet surface	temp	(Deg C)
662	247	S12C07	TE922	Calorimeter outlet surface	temp	(Deg C)
663	000	S00C00	TE020	Aperture plate output	temp	(Deg C)
664	001	S00C01	TE022	Shutter plate output	temp	(Deg C)
665	002	S00C02	DT100	Calorimeter - Input water ref.	temp	(Deg C)
666	460	S22C00	NIP41	Instantaneous solar power input		(kW)
667	461	S22C01	FT623	Aperture plate cooling water	flow	(L/min)
668	462	S22C02	FT624	Shutter plate cooling water	flow	(L/min)
669	463	S22C03	DT100	Calorimeter - Cooling water	delta-temp	(Deg C)
670	464	S22C04	FT201	Calorimeter - Argon gas	flow	(scfh)
671	465	S22C05	FT202	Calorimeter - Helium gas	flow	(scfh)
672	466	S22C06		Shutter plate position		(Open/Closed)
673	467	S22C07	TE310	Pyrometer temperature		(Deg C)
674	468	S22C08	FT103	Calorimeter - Cooling water	flow	(L/min)
675	469	S22C09	NIP05	Direct Insolation - TBC-1 Boresight		(W/m^2)
676	470	S22C10		Spare		
677				Instantaneous receiver power output		(kW)
678				Instantaneous receiver heat loss		(kW)
679				Instantaneous receiver efficiency		(%)
680				Integrated solar power input		(kWh)
681				Integrated receiver power output		(kWh)
682				Integrated receiver heat loss		(kWh)
683				Integrated receiver efficiency		(%)
684				Maximum - Dish or Site NIP		(W/m^2)

Table 2

Reflux Solar Receiver Faults and Response Analysis

Fault	Instrumentation	Indications	Action
Noncondensible gas in receiver	Vapor Temp TCs Condenser TCs	Large temperature difference, >100° C between vapor TC and some condenser TCs sharp gradient in condenser	Continue operation, but do not allow receiver to overheat
Superheat (pool boiler) only	Bulk Liq. TCs Condenser TCs	Large temperature difference between vapor TCs and all condenser TCs (ΔT >50°C)	Shut down and attempt restart, reevaluate concept
Wick dryout (H.P.) Film boiling (P.B.)	Pyrometer Absorber TCs and Vapor TCs	Large temperature difference between absorber TCs and vapor TCs	Fast Shut down, prime wick, restart, reevaluate design
Breach in receiver	Pyrometer, Absorber TCs Aft dome TCs Condenser TCs	White smoke from receiver, large temperature differences, >100° C throughout	Shut down, Notify all site personnel & direct to up-wind of dish.
Breach resulting in fire	Above; observer	Above; flames observed	Turn off bldg ventilation-9981, 82, 84. Report fire (117). Pull alarm. Do not fight fire. Read SOP.
Frozen sodium	Absorber TCs Aft dome TCs	Front or aft dome TCs less than 100°C	Check electric heaters, heat until all TCs indicate melt
Insufficient cooling load	Absorber TCs Aft dome TCs Condenser TCs	Inability to lower receiver temperatures with He/Ar controls and stable water flow	Shut down, check calorimeter and He/Ar controls
Calorimeter malfunctions			
- water leak	Condenser TCs Water ΔT Water flow rate	Excessive low or erratic flow ΔT	Shut down, inspect calorimeter
- boiling water in calorimeter	Water ΔT Water flow rate	Excessive surges in flow ΔT, unsteady	Shut down, inspect calorimeter and flow meter
- Loss of He/Ar	Helium/Argon mass	Inability to control	Shut down, replace

Reflux Receiver Checklist

Test Description _____

Test Data File Name _____ Date _____

Checklist is to be completed by trained and approved personnel familiar with the location and operation of the equipment. See attached map for locations corresponding to the numbers below.

Dish Checkout:

- Wind less than 30 MPH _____
- Turn on water systems: ❶
    1. Large ball and gate valves for raw water _____
    2. Power for Glycol loop _____
    3. Remove Glycol tank lid _____
    4. Small ball valve for emergency cooling _____
- Turn on Ar & He bottles, minimum 500psi: ❷ _____
- Turn on electric power at base of dish: ❸ _____
- Uncap pyrometer and verify aim _____
- Aim Normal Insolation Pyrheliometer (NIP): ❹ _____
- Turn on air compressor: ❺ _____
- Open air valves (2): ❻ _____
- Manlifts south of dish plane _____
- Barriers in place: ❼ _____
- Water cleared from base of dish _____
- Stow pin removed and placed in carrier: ❽ _____

Control Room Checkout:

- 12V and 24V power supplies on (rack) _____
- Start Data program (data computer) _____
    1. Interval 60 secs _____
    2. Site interval 300 secs unless windy _____
- Start control program (control computer) _____
    1. Hold "reset" and turn "on" experiment _____
- Start logbook program (log computer) _____
- Verify times on all programs (on computers) _____
- Turn on microphone system (top of rack) _____
- Safety equipment in place _____
    1. PVC protective gloves (N end control room desk)
    2. Fire retardant coveralls (same desk)
    3. Hard hats and full face shields (same desk)
    4. MET-L-X fire extinguishers: ⊖
    5. Dry MET-L-X and shovels: ⊖
- Check argon & helium flows
    1. Gas switch to "on" (control panel) _____
    2. Manual gas control, 0% output, 8scfh He (data) _____
    3. 100% output, 8scfh Ar (data computer) _____
    4. Auto gas control, setpoint set (control panel) _____
- Preheat on (control panel) _____
    1. Aft dome & elbow to 95°C
    2. Elbow only to 99°C
    3. Aft dome & elbow above 99°C

DRTF Checkout:

- Download memtrack information (data computer to dish controller) _____
- Shutter and aperture flows set (dish panel) _____
- Shutter operational (dish control) _____
- Emergency slew operational (dish control) _____
- TBC # and alignment (#1 east, #2 west) _____
- Mirror reflectivity (dish efficiency) (guess) _____

Final Checkout:

- "Test in Progress" lights on (rack) _____
- Communications established with observer _____
- Nontest personnel cleared from exclusion and control areas _____
- Site announcement ch's 4, 3, 1 (on radio) _____
- Stripchart recorders on, dated, time-stamped (rack) _____
- Command to bring TBC to standby position shall be given only after above checklist is completed and initialed by the Test/Safety engineer (dish control panel) _____
- Data interval 10 or 15 seconds (data computer) _____
- Turn off preheaters when shutter opened (control panel) _____

Comments:

Reflux Receiver Shutdown Checklist

Test Description _____

Date _____

- Bring TBC off-su: and to stow position (dish controller) ____
- Turn off "Test in Progress" light (rack) ____
- Turn off stripchart recorders (rack) ____
- Stop data program unless cooldown data desired (data computer) ____
- Verify preheat turned off (control panel) ____
- Turn off microphone system (rack) ____

After receiver is below 250°C:

- Stop control program and press "Silence" (control computer) ____
- Gas switch to "off" (control panel) ____
- Stow pin inserted in dish and chained in place: ❽ ____
- Close dish air valves(2): ❻ ____
- Turn off air compressor: ❺ ____
- Cap pyrometer ____
- Turn off electric power at base of dish: ❸ ____
- Turn off water: ❶

    1. Small ball valve for emergency cooling ____
    2. Power for Glycol loop ____
    3. Replace Glycol tank lid ____
    4. Large ball valve for raw water ____

- Turn off Ar & He bottles: ❷ ____

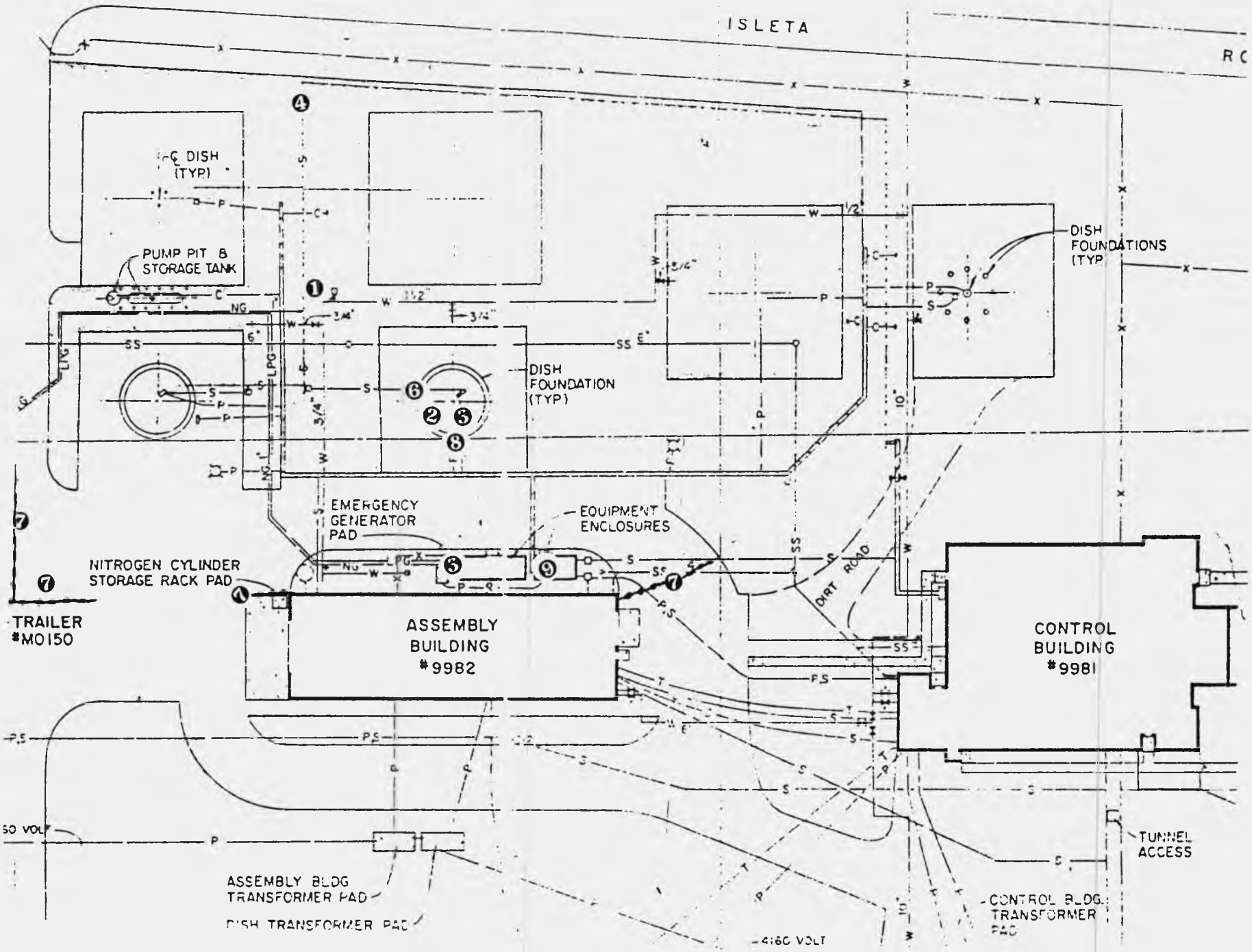
ISLETA
℄ DISH (TYP)
PUMP PIT & STORAGE TANK
DISH FOUNDATION (TYP)
DISH FOUNDATIONS (TYP)
EMERGENCY GENERATOR PAD
EQUIPMENT ENCLOSURES
NITROGEN CYLINDER STORAGE RACK PAD
TRAILER #M0150
ASSEMBLY BUILDING #9982
CONTROL BUILDING #9981
DIRT ROAD
TUNNEL ACCESS
ASSEMBLY BLDG TRANSFORMER PAD
DISH TRANSFORMER PAD
CONTROL BLDG. TRANSFORMER PAD
4160 VOLT

APPENDIX K

DISTRIBUTED RECEIVER TEST FACILITY SAFE OPERATING PROCEDURE FOR REFLUX HEAT-PIPE RECEIVER TESTING

ADDENDUM 11

SOP Number 22702 8810
Org 6222

DISTRIBUTED RECEIVER TEST FACILITY
SAFE OPERATING PROCEDURE
FOR
REFLUX HEAT-PIPE RECEIVER TESTING

August 4, 1988

This SOP applies to the testing of reflux heat-pipe solar receivers at the Distributed Receiver Test Facility (DRTF); the DRTF is part of the Solar Thermal Test Facility (STTF). The DRTF's chief function is to support research and development of distributed receiver solar technologies.

Sandia and outside contractors are involved in the development and evaluation of reflux heat-pipe solar receivers. In the reflux heat-pipe receiver, sodium is used as an intermediate heat transfer fluid to interface concentrated solar flux with Stirling engines and other heat removal devices. This SOP applies to the testing of sodium reflux heat-pipe solar receivers on the Test Bed Concentrators (TBCs). All personnel involved in the testing of reflux heat-pipe solar receivers at the DRTF shall read this procedure.

A P P R O V A L S

t. Scott Rawlinson	8/5/88	A.L. Parker	9-16-88
DRTF Task Leader	date	Industrial Hygiene	date
C.P. Cameron	8-17-88	Vernon L. Duke	9/27/88
DRTF Project Leader	date	Fire Protection	date
		D. Joe	10/11/88
Division Supervisor	date	Safety Engineering	date
W.D. Schuelke	8-19-88	B. Reed	10-12-88
Department Manager	date	Safety Eng. Supervisor	date

R E V I E W S

DRTF Project Leader	date	Division Supervisor	date

Distribution:
Industrial Hygiene
Fire Protection
Safety Engineering
Solar Thermal Test Facility File
DRTF Project Leader
DRTF Control Room
ETF Control Room

ADDENDUM 11

DISTRIBUTED RECEIVER TEST FACILITY
SAFE OPERATING PROCEDURE
FOR
REFLUX HEAT-PIPE RECEIVER TESTING

August 4, 1988

1. INTRODUCTION

1.1 DESCRIPTION OF THE FACILITY

The Distributed Receiver Test Facility (DRTF) is located at the Solar Thermal Test Facility of Sandia National Laboratories in Albuquerque, New Mexico, and is operated by Sandia's Solar Thermal Test Facility Division (STTF) for the Department of Energy (under contract DE-AC04-76DP00789) as part of the Solar Thermal Program.

The objective of the Distributed Receiver Test Program is to further the research and development of solar distributed receiver technologies.

The chief activity of the DRTF is testing the performance and reliability of the distributed receiver systems and sub-systems of both line-focus (trough) and point-focus (dish) technologies. The DRTF also conducts experiments for a variety of reimbursable customers.

1.2 SCOPE OF THE SOP

Sandia and outside contractors are involved in the development of reflux heat-pipe solar receiver technology. In the reflux heat-pipe receiver, sodium is used to interface concentrated solar flux with a Stirling cycle engine or other heat removal devices. This SOP applies to the testing of sodium reflux heat-pipe receivers on the Test Bed Concentrators (TBCs). All personnel participating in reflux heat-pipe receiver testing shall read this procedure. Only personnel who have read and signed this and the Test Bed Concentrator addenda as well as the DRTF SOP may be authorized to participate in receiver testing operations.

1.3 DESCRIPTION OF EQUIPMENT

Reflux heat-pipe solar receivers under development are prototypes designed to operate on the Test Bed Concentrators. They contain a quantity of sodium ranging from approximately 1 pound (0.5 kg.) to approximately 25 pounds (11 kg.) inside a hermetically sealed stainless steel or Inconel shell. During operation the sodium is passively circulated between a condenser section (engine heater tubes or calorimeter) and an evaporator section (the solar absorber).

The receivers will be designed to operate on the Test Bed Concentrators (TBC) which are described in Addendum 5. Their design operating temperature is in the range of 700 to 800 deg C.

For receiver testing, the delivered heat will be absorbed by a cold water gas-gap calorimeter. Variable thermal conductance is provided by an adjustable helium-argon mixture in a narrow gap between the receiver's condenser section and a steady-flow cold water calorimeter. Receiver temperature is established by the relative rates in which heat is delivered to and removed from the receiver. Receivers will eventually be tested with Stirling engines with which temperature will be established by adjusting the electrical load.

A small electric heater will be built into the receiver to preheat the sodium above its melting point before startup.

1.4 Scope of Testing

The goals of testing are to verify operation during the normal range of operating conditions and to characterize subsystem and component performance. Tests will therefore be conducted in two stages. Stage I tests will establish hardware limitations and will verify design specifications. In Stage II, performance will be characterized in detail.

2. GENERAL HAZARDS

2.1 Sodium

Sodium is a flammable metal which reacts violently with water and chlorinated hydrocarbons. Its melting point is 97 deg C and it has a vapor pressure of one atmosphere at 883 deg C. When exposed to air , sodium may ignite spontaneously at a temperature as low as 115 deg C depending on such conditions as humidity, dispersion, etc. Burning sodium will react violently with almost all common fire extinguishing materials. A sodium fire can be recognized by a very low flame with many bright yellow nodes. Sodium fires produce a dense white smoke which contains highly alkaline materials, sodium monoxide (NaO), and sodium hydroxide (NaOH), which can cause irritation and rapid tissue destruction through chemical and thermal burns. If a sodium fire contacts a concrete surface, chemical reactions can occur and the heat may vaporize moisture in the concrete, causing the surface to spall.

The sodium is hermetically contained inside the receiver and will not normally come in contact with air. A pressure transducer in the receiver will monitor for excessive pressures and leaks. When operating with the gas-gap calorimeter, sodium is separated from the water in the calorimeter by two walls, thus making the possibility of sodium contacting the water in the calorimeter very unlikely.

2.2 HIGH TEMPERATURES AND PRESSURES

As noted above, the receiver is operated at temperatures in the range of 700 to 800 deg C. Pressures within the receiver are slightly subatmospheric. The receivers will at no time be allowed to exceed a temperature of 850 deg C to insure that the internal pressure is less than ambient. The receiver is hot during operation and remains hot for several hours after shutdown.

2.3 ELECTRICAL HAZARDS

The receiver is equipped with a small electric heater for melting the sodium before going on sun. The heater operates at 110 volts which is hazardous to personnel.

3. GENERAL SAFETY PROCEDURES AND ACCESS REGULATIONS

3.1 GENERAL REGULATIONS

The immediate area surrounding a reflux heat-pipe solar receiver which is operating or undergoing maintenance is designated an EXCLUSION AREA and shall be marked by a rope or other suitable means along the perimeter. Only personnel who have read and signed this addenda shall be authorized to enter an exclusion area. Authorization shall be obtained from the designated test operator or technician in charge.

3.2 REFLUX HEAT-PIPE RECEIVER INSTALLATION

An installation procedure must be prepared and followed during installation of a reflux heat-pipe receiver. The procedure shall be subject to prior approval by the DRTF Project Leader and Safety Engineer. The procedure shall address lifting equipment requirements, mounting interfaces, and personnel access during the lifting operation. If possible, rubber hoses containing water will be protected from direct contact with sodium to provide safety in the event of a receiver leak.

3.3 REFLUX HEAT-PIPE RECEIVER SAFETY

3.3.1 RECEIVER/TBC INTERFACE

The reflux heat-pipe receivers will have an interlock capability which shall be implemented with the TBCs. The receiver provides a relay closure indicating to the TBC that the receiver is ready. The receiver control system monitors all receiver parameters and automatically shuts the receiver down and removes the interlock closure if any parameter is outside of its permissible range. Loss of the interlock closure at any time shall automatically close the shutter, isolating the incident energy from the receiver. The receiver control system will be checked periodically to verify that any excessive temperature or pressure signal will automatically shutdown the test.

3.3.2 REGULATIONS PRECEDING AND DURING TESTING

Prior to receiver testing, the following items must be checked:

(1) Calorimeter and shutter are operational
(2) TBC emergency slew systems have been tested
(3) Communications established with field observer
(4) Safety equipment is in place (see section 3.4.2)
(5) Safety shower has been tested
(6) TBC mirror and cable protection is in place
(7) No water present under TBC and in hub section
(8) "Test in Progress" light on
(9) Alarms set
(10) Checklist completed and initialed

A light warning system has been implemented at the DRTF. During periods of testing or other hazardous operations, these warning lights shall be on, and the following regulations pertaining to the exclusion area shall be strictly observed:

3.3.2.1 The exclusion area shall be under the direct control of an authorized operator designated by the DRTF project leader. The operator shall be the responsible safety officer for the duration of the test. He shall be thoroughly knowledgeable of the equipment under test, its operation, the purpose of the test, and all safety policies and precautions.

3.3.2.2 In preparation for testing, the warning light shall be turned on, signaling the "ON" condition. Prior to initiating testing or other hazardous operation, the authorized operator shall sound an audible alarm to inform all personnel in the area that the light has been turned on. Initiation and termination of test/operations shall be announced on radio channels 1, 3, & 4.

3.3.2.3 Only personnel authorized by the operator shall enter the exclusion area and then only by an explicitly designated safe entry path. Receivers mounted on a TBC cannot be approached during operation because of the presence of concentrated sunlight.

3.3.2.4 Protective clothing (see section 3.4.2) shall be available. During Stage I tests (initial receiver checkout), a field monitor will insure compliance, look for failures, and be prepared to fight a sodium fire. A supply of safety equipment and a MET-L-X fire extinguisher shall be maintained in the DRTF control room and shall be available during Stage I tests.

3.3.3 RECEIVER MAINTENANCE

Before maintenance of any reflux heat-pipe receiver which contains sodium, the system must be allowed to cool to ambient temperature.

Power shall be removed from the heater before all maintenance activities.

3.4 EMERGENCY PROCEDURES

3.4.1 SODIUM SPILLS

In the event of an emergency that requires that the control area be cleared of personnel, the operator will sound an audible alarm. All personnel shall clear the area until informed by the operator that the area may again be entered safely. If the emergency is a breach in the receiver which causes a sodium fire, the control building, the assembly building, and the ETF ventilation systems shall be turned off. Dial 117 and report fire immediately. Pull the fire alarm auxiliary box to ring the bells and send a signal to the Fire Department and alert the site fire team. Personnel shall stay clear of the smoke from the fire, and attempts to fight the fire should only be attempted with appropriate safety equipment and MET-L-X fire extinguishers. If the fire is limited to the receiver, no attempt will be made to extinguish the fire.

In case of contact with sodium, any sodium clinging to the skin or clothing should initially be brushed off. Affected areas should then be washed with large amounts of water. All clothing should be removed as soon as possible in case sodium is trapped in it. Water dilutes the caustic reaction products and will limit skin or wound damage. In the case of eye contact, use the eye-wash to flush the eyes with large amounts of water, then see an ophthalmologist immediately.

3.4.2 PROTECTIVE CLOTHING AND EQUIPMENT

The following protective clothing should be on hand for sodium receiver tests:

- Coveralls, flame retardent, quick removal (sized for personnel involved)
- Face shield
- Goggles
- Hard hats
- Gloves, PVC, loose fitting and discardable with a rapid arm motion
- Leather shoes or rubber overshoes

Note: Contact lenses cannot be worn by any personnel who may be near the receiver during testing.

In addition, the following equipment will be available:

- MET-L-X fire extinguishers
- Dry MET-L-X and shovels

SIGNATURE PAGE

I have read the DRTF SOP and the REFLUX HEAT-PIPE RECEIVER TESTING SOP and shall adhere to the safe practices and regulations specified therein.

NAME	SIGNATURE	DATE
K. Scott Ramaekers	K. Scott Ramaekers	10/17/88
Michael A. Quintana	Michael A. Quintana	10/18/88
John M. Stomp, Jr.	John Milt Stomp, Jr.	10/18/88
Walter M. Einhorn	Walter M. Einhorn	10/18/88
James B. Moreno	James B. Moreno	10/19/88
Charles E. Andrews	Charles E. Andrews	10/19/88
Vernon E. Dudley	Vernon E. Dudley	10/19/88
Richard R. Padilla	Richard R. Padilla	10/19/88
Jim Dudley	Jim Dudley	10/21/88
Doug Adkins	Doug Adkins	10/21/88
C P Cameron	C P Cameron	10/21/88
Daniel Ray	Daniel Ray	11/23/88
Kevin Linker	Kevin Linker	11/23/88
Richard B Diver	Richard B Diver	11/23/88
W. C. Ginn	W. C. Ginn	11-28-88
Roy Hogan	Roy Hogan	10/18/89
Gregory A Smith	Gregory A Smith	1/15/90
Timothy A. Moss	Timothy A. Moss	6/6/90

NSTTF OP #019

REFLUX RECEIVER TESTING

Distribution: **NSTTF CONTROLLED DOCUMENT**

DRTF Control Rm. - Copy #1 (Rawlinson/Andraka)
ETF Control Rm - Copy #2
Extra File - Copy #3
Extra File - Copy #4

APPROVED PLANS AND PROCEDURES

FOR

REFLUX RECEIVER TESTING

System Description

The attached plans comprise the required documents for testing reflux receivers at the Distributed Receiver Test Facility (DRTF). The receivers are to be tested on the Test Bed Concentrators which are controlled by personnel in the DRTF control room.

Required Documents

Test Plan	✓ ATTACHED	___ NOT REQUIRED
Test Plan Addendum	✓ ATTACHED	___ NOT REQUIRED
Test Procedure	✓ ATTACHED	___ NOT REQUIRED
Environmental Protection Plan	✓ ATTACHED	___ NOT REQUIRED
Failure Response Plan	✓ ATTACHED	___ NOT REQUIRED
Training Requirements Signoffs	✓ ATTACHED	___ NOT REQUIRED

APPROVALS

Experimenter	date
K. Scott Peabody	2/15/90
STTF Test Engineer	date
John T. Hall	2/15/90
STTF Division Supervisor	date

Note: Minor changes can be initialed by the STTF test engineer.
Major revisions require approval by supervisor.

STANDARDIZED TEST PLAN ADDENDUM

This addendum describes additional tests not discussed in the standardized plan.

A.1. X-ray Cinematography tests.

An attempt will be made to define bubble sizes and void fractions in real time using non-destructive evaluation with X-ray cinematography. Division 7551 will provide all necessary equipment. The X-rays will be at safe levels outside the exclusion area, and will be monitored by 7551 personnel. The X-ray source will have a remote shutoff located in the control room. The test will look at boiling at various power levels and temperatures, but only at conditions previously outlined in the test plan.

A.2. 1000 hour testing.

After the objectives of the test plan are met and the receiver is fully characterized, continued full-day testing may continue up to 1000 hours on-sun. These tests are contingent on further materials evaluation currently in progress. These tests will demonstrate that steady boiling is not a transient phenomena, and will provide some information on materials interaction with boiling sodium.

TEST PROCEDURES

The test procedures and checklists for the reflux receiver tests are included in the attached test plan.

The reflux receivers will be tested on the TBC-1 concentrator at the STTF. The site data and control systems are used where appropriate, and are described in the test site literature. This section will discuss the layout and operation of the control system for the on-sun testing of the receivers (Figs 1 & 2).

The control system monitors the operation of the receiver, controls the thermal conductance of the gas-gap calorimeter, and closes the shutter if a fault is detected. The system is based on an HP-9845 computer, which reads the selected channels approximately every 3 seconds. In addition a number of hardware displays provide rapid response to some thermocouple channels and the pyrometer channel. The particular channels to be monitored are determined by the project engineer, and are selected at the plugboard behind the computer.

The gas-gap calorimeter (fig 3) draws heat out of the receiver into city water. The water flow rate, temperature, and change in temperature are monitored. The flow rate and exit temperature can cause a shutdown if limits are exceeded. A 50 psi burst disk provides protection for the calorimeter in the case of flow failure and subsequent rapid boiling of the water. A shutoff valve can be actuated manually from the control computer (relay 001) in the case of a sodium spill. The calorimeter shell is stainless steel to minimize the possibility of sodium mixing with water.

A mixture of helium and argon flows in the gap between the water jacket and receiver. The ratio of the gases in the mixture determines the power extracted, and is controlled by a PID controller monitoring the condenser section temperature. The output "heat" signal of the controller proportionally drives the argon flow control valve, while the signal is inverted to drive the helium valve. The gas flows may be monitored by the data computer at transducer outputs FT201 and FT202. The control computer monitors pressure at the bottles with pressure switches PS201 and PS202, and sounds an alarm at 300 psi bottle pressure. The regulated pressure is monitored by PT201 and PT202. If the regulated pressure drops below 15 psi, the shutter is shut. The control computer also overrides the PID controller with relays 3 and 4 during an emergency shutdown. The relays demand full helium flow and no argon, providing the fastest possible cool-off. The water temperatures inside the calorimeter are also monitored and compared against limits.

In addition to the calorimeter system, up to 48 total type K thermocouples may be included. Standard thermocouple locations are outlined in the test plan. Up to 6 thermocouples may be monitored in hardware for almost instantaneous response. It is recommended that these include the pool temperature on a pool boiler, and several absorber thermocouples. Up to 12 additional thermocouples may be monitored by the 9845 computer. All thermocouples are monitored by the test site data recording system.

In addition, a solar blind pyrometer views a large portion of the absorber surface to supplement the absorber thermocouples. The pyrometer is monitored by a hardware display/shutdown device.

A first-out failure indicator displays what instrument first sensed a failure in the case of multiple alarms. Figure 4 shows a schematic of the indicator. A red light indicates first failure. No light indicates subsequent failure. A green light indicates safe conditions for that instrument. 16 instruments may be monitored at once.

An emergency stop (panic) button is included on the front panel. It lights red when the control computer is active, all systems are ready, and the shutter circuit is energized. Actual shutter operation is manually controlled at the dish control panel, and is only enabled when the control system circuit is energized (uses "engine ready" input signal). A reset button is included to clear failure indications. A silence button will silence the alarm siren when the failure is acknowledged. The computer activates a time-delay relay each time through the program loop, providing a deadman stop in the case of a computer failure. The shutter activation relay is latching, providing protection (manual reset required) after momentary power interruptions.

The preheat wiring is shown in figure 5. Three switches are provided on the front panel. The computer relay #5 provides 24V supply to the switches. These in turn pull down relays at the base of the dish, providing 120V power to the variacs. The variacs are set to provide uniform heating and prolonged heater life.

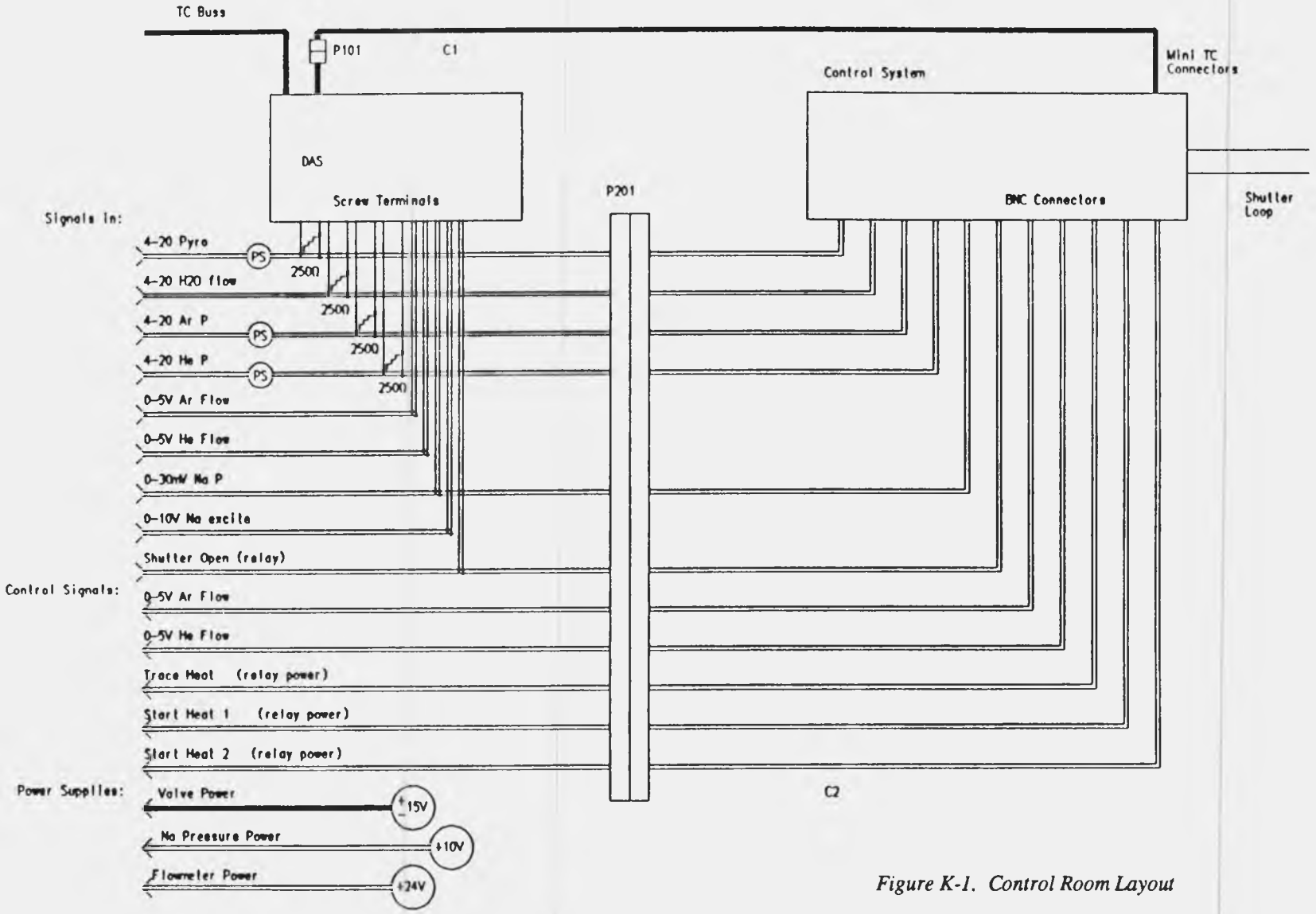

Figure K-1. Control Room Layout

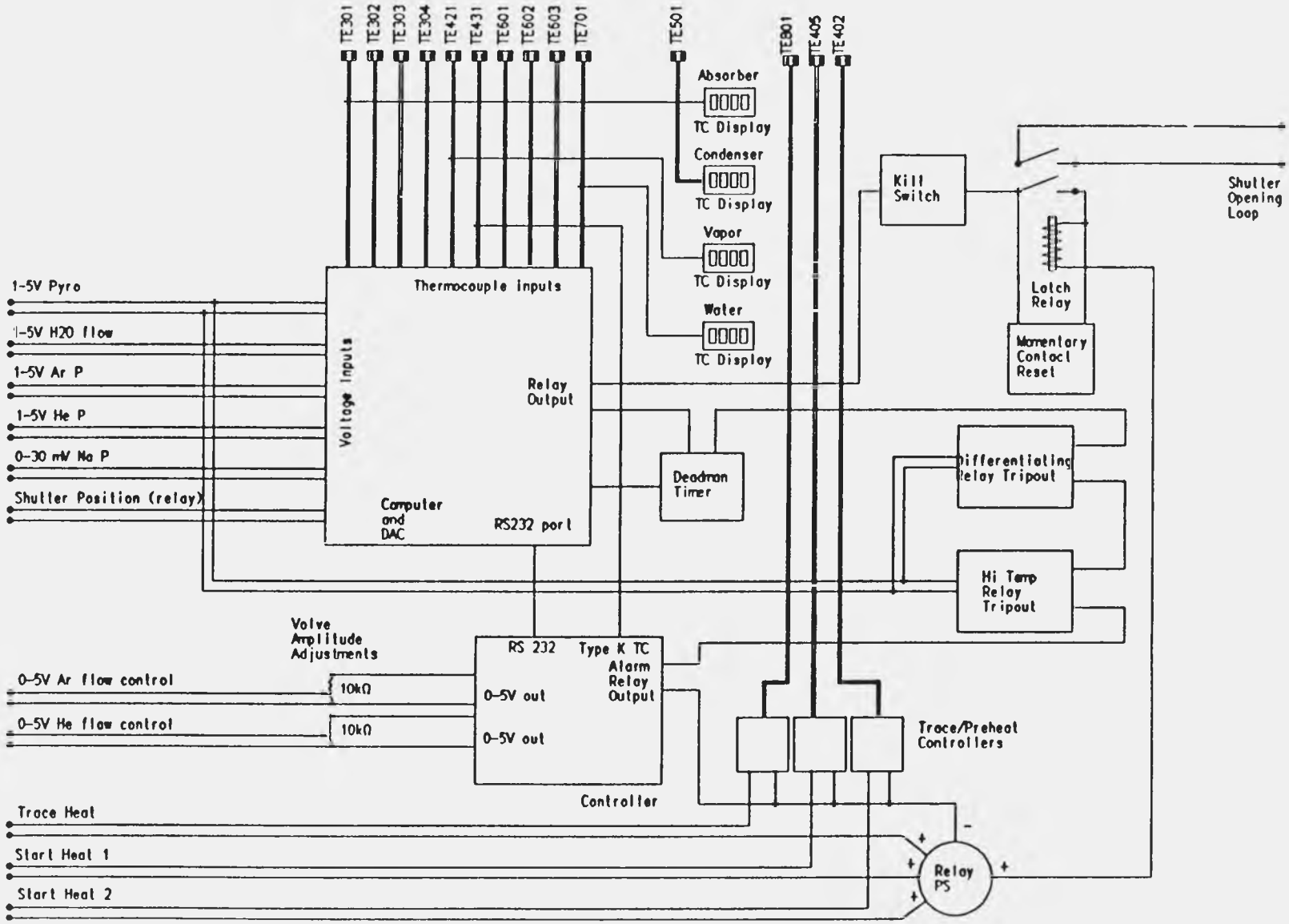

Figure K-2. Safety/Control System

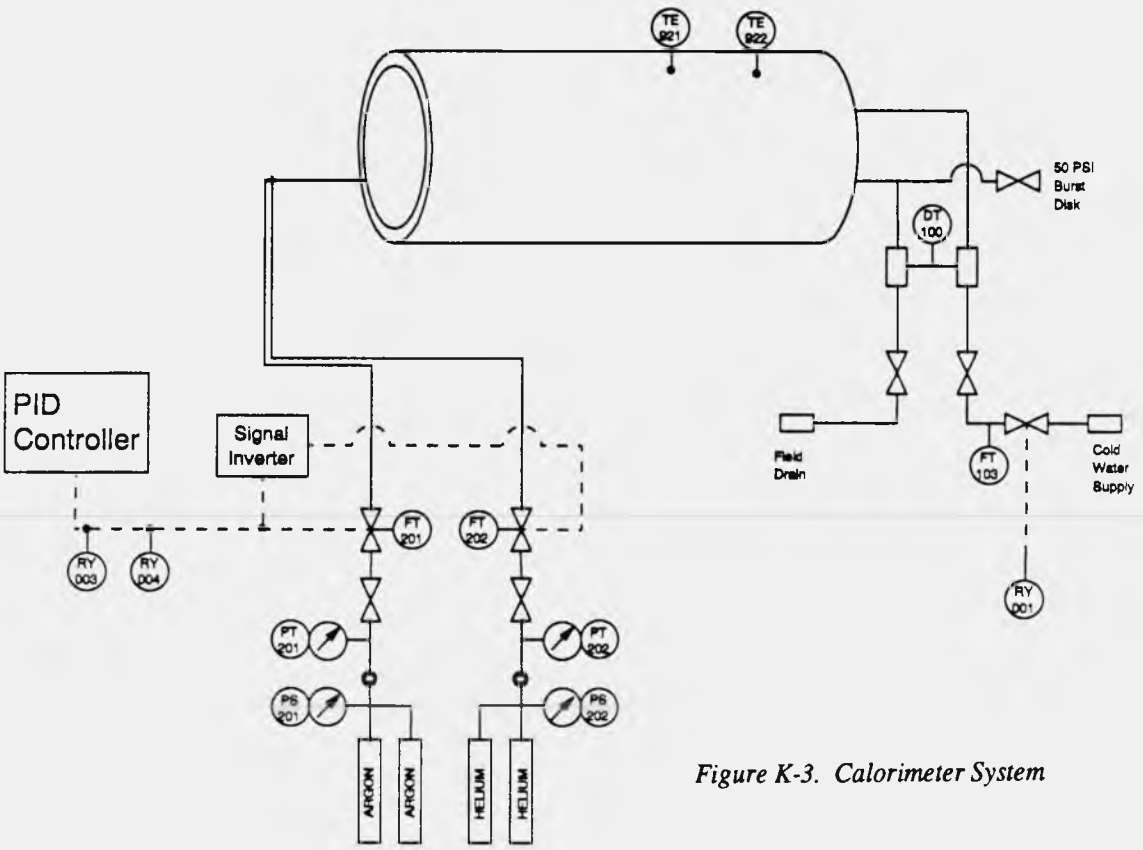

Figure K-3. Calorimeter System

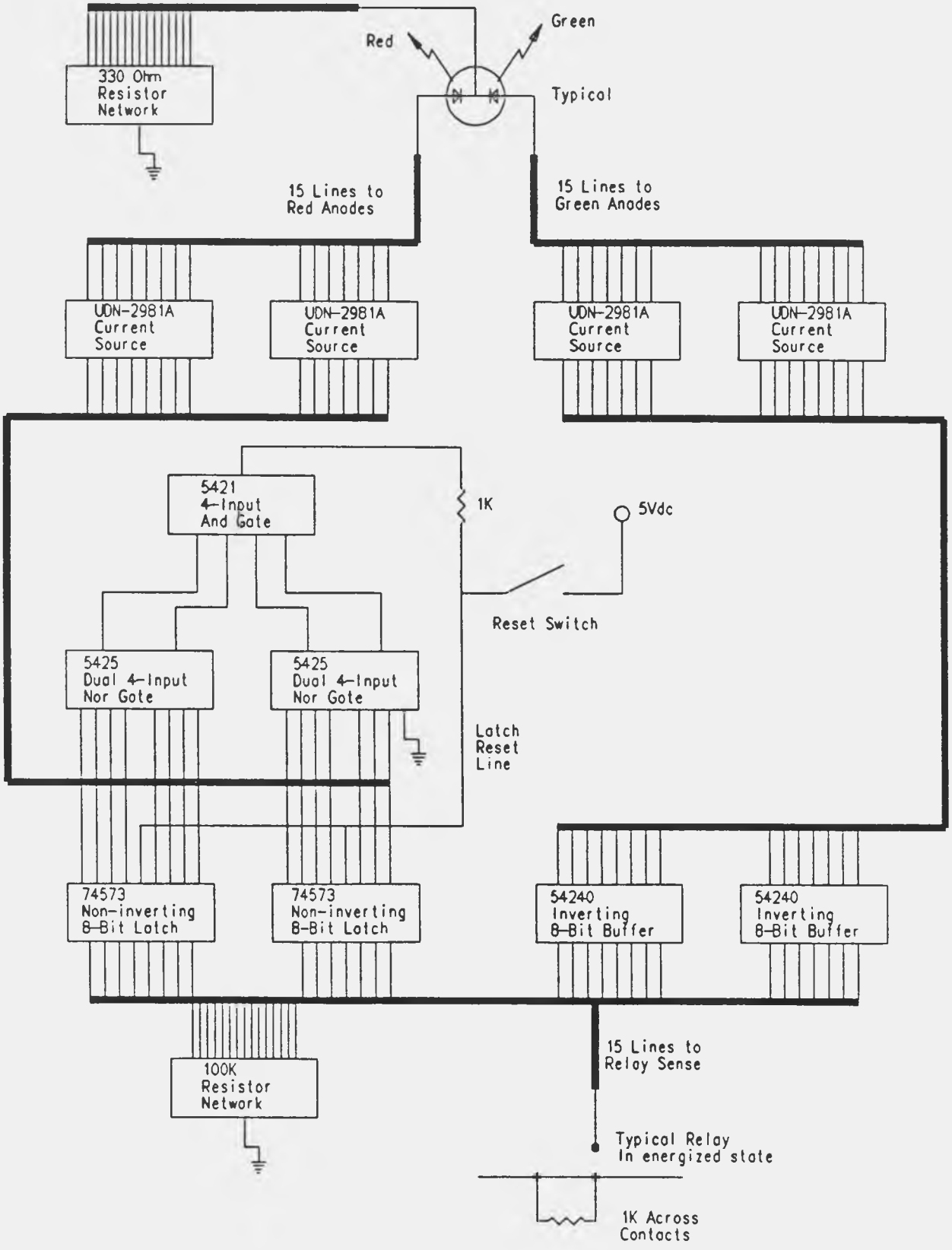

Figure K-4. Firstout Failure Indicator

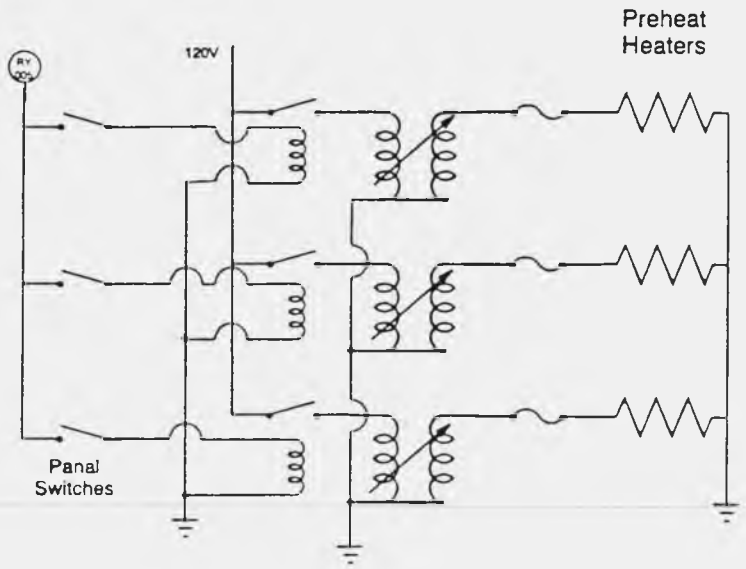

Additional Thermocouple
and instrumentation locations
identified in test
and instrumentation plan

Figure K-5. Preheater System

ENVIRONMENTAL PROTECTION PLAN

This document describes the potential environmental hazards associated with the Reflux Receiver testing on TBC-1. The Material Safety Data Sheets are attached.

The receivers may contain up to 25 pounds of sodium or NaK. The receiver shell is stainless steel, inconel, or related alloys. The receiver is elevated up to 15 meters. A typical failure could result in a rupture of the absorber surface at or below the surface of the liquid metal. In the case of the pool-boiler, liquid metal would then run out, reacting with the atmosphere. In the case of the heat pipe, the liquid metal is suspended in the wick structure, but may react with the admitted air. A leak on the absorber surface will not be contained by the structure. Failure elsewhere on the receiver, while unlikely, would cause a leak into the large volume of vermiculite insulation, effectively containing the leak.

The high temperature of the liquid metal will cause rapid reaction with the air and moisture in the air, creating sodium oxide, sodium hydroxide, and eventually sodium carbonate (soda ash Na_2CO_3). The sodium hydroxide is caustic but eventually decomposes to the carbonate.

Personnel should avoid contact with sodium and its products. Protective equipment is discussed in the SOP. Environmental Protection (Div 3202) will be notified for any necessary cleanup.

Sodium has many special handling precautions and protective equipment. They are discussed in detail in the DRTF SOP, Addendums 10 and 11.

A 50/50 water glycol mix is used for closed loop cooling of the aperture plate and shutter. The pump, surge tank, and emergency cooling tank are located in a hazardous material trailer (secondary containment built into the trailer floor) near the TBC. A cooling tower for the system is located adjacent to the trailer - it is mounted on a concrete pad with a curbing for secondary containment. The coolant lines run to the TBC and are then routed to the receiver ring. There is no secondary containment for the TBC, but the risk of a catastrophic leak in these lines is considered to be low.

RMI TITANIUM

RMI Company

SODIUM PLANT

P. O. BOX 560
ASHTABULA, OHIO 44004
216/997-5141 TWX 810-427-2937

MATERIAL SAFETY DATA SHEET

IDENTIFICATION

NAME
Sodium Metal

GRADES
Chemical Pure

SYNONYMS
Sodium, Natrium

MANUFACTURER
RMI Company

ADDRESS
Sodium Plant
Ashtabula, OH 44004

CHEMICAL FAMILY
Inorganic Metal

FORMULA
Na

PRODUCT INFORMATION PHONE NUMBER
(216) 997-5141

MEDICAL EMERGENCY PHONE NUMBER
(216) 998-1212 or 998-3111

TRANSPORTATION EMERGENCY PHONE
CHEMTREC (800) 424-9300

PHYSICAL DATA

Melting Point: 98°C (208°F) @ 1 atmosphere.

Appearance And Odor: Pinkish silver when freshly cut, turns white/gray when exposed to air.

FIRE AND EXPLOSION HAZARD DATA

Flammable solid. Reacts violently with water and certain organics, releasing hydrogen gas which will ignite and explode. Do not use water or chemical fire extinguishers (other than Class D) for fighting sodium fires. Sodium autoignites at 120 to 125°C (248 to 257°F).

REACTIVITY DATA

Reacts violently with any material containing water and many materials containin oxygen, halides, or active hydrogen.

Code No. 021-M
Original Issue Date: 7-26-85
Revised: 11-26-86

INGREDIENTS AND RECOMMENDED OCCUPATIONAL EXPOSURE LIMITS

INGREDIENTS	CAS NO.	% WEIGHT	EXPOSURE LIMITS OSHA PEL	EXPOSURE LIMITS ACGIH TLV
Sodium	7440-23-5	>99%	NS	NS
Other		< 1%		
NOTE: Sodium reacts with water to form sodium hydroxide.			$2mg/M^3$ as NaOH	$2mg/M^3$ as NaOH

HEALTH HAZARD DATA

NOTE: Persons handling sodium should be thoroughly familiar with hazards and proper first aid procedures. Do not get in eyes, on skin, or on clothing, and avoid contact with water.

Effects Of Overexposure

MAJOR EXPOSURE HAZARD
Skin Contact

Causes severe caustic burns. Sodium is very corrosive to animal skin or eyes by reactive formation of sodium hydroxide. Human health effects may include: skin burns, or ulceration; eye corrosion with corneal or conjunctive ulceration; and irritation of the upper respiratory passage.

Neither product nor its ingredients are considered to be a carcinogen according to the National Toxicology Program, International Agency for Research on Cancer or United States Occupational Safety and Health Administration.

Emergency And First Aid Procedures

If fumes from sodium reactions are inhaled, remove to fresh air immediately. If not breathing, give artificial respiration. If breathing is difficult, give oxygen. Call a physician. If swallowed, do not induce vomiting, give large quantities of water. Call a physician immediately. Never give anything by mouth to an unconscious person. In case of contact with skin or clothing, immediately remove sodium and flush eyes or skin with plenty of water for at least 15 minutes while removing contaminated clothing and shoes. Call a physician.

SPILL OR LEAK PROCEDURES

Cover with DRY soda ash or salt (if soda ash is unavailable), shovel into a dry metal container and cover again with soda ash or salt, and dispose of properly. Avoid putting wet sodium in a covered container because a hydrogen explosion may occur.

SPECIAL PROTECTION INFORMATION

Respiratory: When handling liquid sodium, a self-contained breathing apparatus is needed if large amounts of sodium smoke are present; a toxic dust disposable respirator can be used for smaller amounts.

Ventilation: Good general ventilation should be provided.

PERSONAL PROTECTIVE APPAREL

Solid Sodium

Use chemical splash goggles, dry moleskin mitts which are oversized for easy removal and which extend up the arm. Wear a long sleeve shirt and full length pants. Also a full face shield and a flameproof apron are desirable.

Molten Sodium

Full protective flameproof clothing should be used including long underwear, shirt and pants (or coveralls), hood or neck shroud, chemical splash goggles, spats and heavy duty work shoes. A flameproof apron and face shield are also desirable.

SPECIAL PRECAUTIONS

Firefighting:

1. Smother with DRY soda ash or use Type D extinguisher.
2. Less preferably use DRY salt or DRY sand.
3. DO NOT USE: water, soda acid, CO_2, or chlorinated organic extinguishers.

MATERIAL SAFETY DATA SHEET
Complies with 29 CFR 1910.1200,
OSHA Hazard Communication Standard.
Substance is subject to the PA
Worker & Community Right-to-Know Act.

CALLERY CHEMICAL COMPANY
DIVISION OF MINE SAFETY APPLIANCES COMPANY
P.O. Box 429, Pittsburgh, PA 15230
Phone: 412/538-3510 Telex: 86-6312

CHEMICAL IDENTITY

LABEL IDENTITY	Sodium Potassium Liquid Alloy
PRODUCT DESCRIPTION	Sodium potassium liquid alloy in metal container with dry nitrogen cover gas
CHEMICAL NAME/SYNONYMS	Sodium potassium alloy, NaK
FORMULA	NaK
FORMULATION	22% Na, 78% K

PHYSICAL AND CHEMICAL PROPERTIES

COLOR, FORM, ODOR	Silver liquid metal, no odor
MELTING POINT	9.3°F (-12.6°C)
BOILING POINT	1445°F (785°C)
SPECIFIC GRAVITY @ 212°F (100°C)	0.855
SOLUBILITY IN WATER	Reacts violently
STABILITY IN AIR	May ignite spontaneously; may form yellow potassium superoxide after long exposure to air

PHYSICAL HAZARD INFORMATION

PHYSICAL HAZARD(S)..... Water reactive solid, may be pyrophoric

CONDITIONS OR MATERIALS TO AVOID..... Water, air, oxygen and oxidizing materials, CO_2, halogenated hydrocarbons including Teflon and similar materials, halogens, acids

UNUSUAL FIRE AND EXPLOSION HAZARDS..... NaK reacts violently with water, liberating and igniting hydrogen, perhaps explosively. NaK may ignite spontaneously if exposed to air or oxygen. On concrete, burning may be more vigorous and accompanied by spattering.

NaK reacts violently with a wide variety of chemicals and can cause fires or explosions. NFPA Fire Protection Guide on Hazardous Materials (1975) lists specific reactions under sodium potassium alloy, potassium, and sodium.

FIRE EXTINGUISHER..... Dry soda ash, dry sodium chloride, Ansul's MET-L-X. Never use water, foam, carbon dioxide (CO_2), or dry chemical fire extinguishers.

SPECIAL FIRE FIGHTING PROCEDURES..... Wear pressure demand self-contained breathing apparatus with full facepiece and full protective clothing. Burning releases corrosive or highly irritating fumes and smoke. Work upwind if possible.

HEALTH HAZARD INFORMATION

HEALTH HAZARD(S)..... Causes caustic burns to eyes and skin. No information available on oral, dermal, inhalation toxicity or sensitization testing.

SIGNS AND SYMPTOMS OF EXPOSURE..... Burns may result from the reaction of NaK with the moisture in the skin. If skin is dry, caustic will slowly form and cause skin to redden and chemical burns to develop; pain may be delayed and will not provide a warning.

PRIMARY ROUTE(S) OF ENTRY..... Dermal

TARGET ORGANS..... Eyes, skin

MEDICAL CONDITIONS GENERALLY RECOGNIZED AS BEING AGGRAVATED BY EXPOSURE..... No information

EXPOSURE LIMITS (OSHA PEL, ACGIH TLV, OTHERS USED OR RECOMMENDED)..... None

CARCINOGENICITY DATA..... No information; chemical is not listed in National Toxicology Program (NTP) Annual Report on Carcinogens, not found to be a potential carcinogen in the International Agency for Research on Cancer (IARC) Monographs, not listed by OSHA.

EMERGENCY AND FIRST AID PROCEDURES..... CAUSES CAUSTIC BURNS! Eyes - Immediately flush eyes with plenty of water for at least 15 minutes, holding eyes open. Skin - Immediately shake or brush any material from skin, remove any contaminated clothing, then flush skin with plenty of water for at least 15 minutes. Wash clothing and thoroughly clean shoes before reuse. CALL A PHYSICIAN IN ALL CASES.

SAFE HANDLING AND USE

HYGIENIC PRACTICES..... Do not get in eyes, on skin, on clothing. Wear recommended protective equipment. Do not ingest.

PROTECTIVE MEASURES DURING REPAIR AND MAINTENANCE OF CONTAMINATED EQUIPMENT..... Wear recommended protective gear. Do not attempt repair or maintenance of contaminated equipment until it has been cleaned. Eliminate ignition sources. Remove as much material as possible from equipment. Remove contaminated sections to separate area, if possible. Clean (see waste disposal) before repairing or discarding. If contaminated sections of equipment cannot be removed, be sure to provide adequate venting for hydrogen gas generated during cleaning. Control the reaction rate by controlling the rate of addition of steam and/or water.

STORAGE..... Store under dry nitrogen or dry argon cover gas in metal container. Keep tightly closed. Maintain cover gas pressure. DO NOT STORE METAL UNDER OIL OR HYDROCARBONS. Store away from heat, sparks, and flames. Store away from any water source including sprinkler systems. Floor drains should be covered and not trapped.

SPILL OR LEAK CLEANUP PROCEDURES..... Wear recommended protective gear. Cover with dry soda ash, dry sodium chloride, or Ansul's MET-L-X. Scoop into DRY metal container with additional extinguisher powder. Cover loosely. Transport immediately to a chemical disposal area for disposal by trained personnel.

WASTE DISPOSAL..... Waste NaK should be treated in a well ventilated area to vent any hydrogen gas generated during treatment. Purge container with dry nitrogen gas. Remotely add dry superheated steam at a rate to control the reaction. When confident that all NaK has been reacted (heavy smoking ceases), continue adding steam at an increased rate for an additional thirty (30) minutes to ensure a complete reaction of the NaK. Then carefully and remotely fill container with water. Resulting solution will be extremely caustic. Alternatively, waste NaK may be incinerated.

CONTROL MEASURES

PERSONAL PROTECTIVE EQUIPMENT
WHEN EXPOSURE IS POSSIBLE..... Chemical protective goggles, dry leather gloves or moleskin mitts, fire retardant hat and long-sleeved coveralls without cuffs (pants should be long enough to cover top of shoes). A faceshield may be used in addition to the goggles. Showers and eye wash stations should be available in an adjacent room.

WORK PRACTICES..... Keep away from water, air, and incompatible materials. Handle under vacuum or dry nitrogen or dry argon atmosphere in dry equipment. Store under a dry nitrogen or dry argon gas cover. Dispose of all reaction residues immediately. If superoxide contamination is suspected, do not add to organics. Extinguishers should be readily available.

ENGINEERING CONTROLS..... Steel curbing and flooring should be used in areas where NaK is handled; concrete may spall with burning NaK. No sprinkler system should be installed and floor drains should be covered and not trapped. An exhaust fan is recommended to remove fumes in case of fire.

DATE OF PREPARATION..... 7/27/87

MATERIAL SAFETY DATA SHEET OHS09400

CUPATIONAL HEALTH SERVICES, INC.
50 SEVENTH AVENUE, SUITE 2407
NEW YORK, NEW YORK 10123
(800) 445-MSDS (212) 967-1100

EMERGENCY CONTACT:
JOHN S. BRANSFORD, JR. (615) 292-1180

SUBSTANCE IDENTIFICATION

CAS-NUMBER 107-21-1
RTEC-NUMBER KW2475000

SUBSTANCE: **ETHYLENE GLYCOL**

TRADE NAMES/SYNONYMS:
1,2-DIHYDROXYETHANE: 1,2-ETHANEDIOL: ETHYLENE ALCOHOL: GLYCOL:
GLYCOL ALCOHOL: MONOETHYLENE GLYCOL: DOWTHERM SR 1: ETHANE-1,2-DIOL:
LUTROL-9: MACROGOL 400 BPC: M.E.G.: TESCOL: 2-HYDROXYETHANOL:
ETHYLENE DIHYDRATE: DOWTHERM SR: C2H6O2: OHS09400

CHEMICAL FAMILY:
GLYCOL

MOLECULAR FORMULA: H-O-C-H2-C-H2-O-H MOLECULAR WEIGHT: 62.07

ERCLA RATINGS (SCALE 0-3): HEALTH=2 FIRE=1 REACTIVITY=0 PERSISTENCE=0
FPA RATINGS (SCALE 0-4): HEALTH=1 FIRE=1 REACTIVITY=0

COMPONENTS AND CONTAMINANTS

COMPONENT: ETHYLENE GLYCOL PERCENT: 100

OTHER CONTAMINANTS: NONE

EXPOSURE LIMIT:
ETHYLENE GLYCOL:
50 PPM (125 MG/M3) OSHA CEILING
50 PPM (125 MG/M3) ACGIH CEILING (VAPOR AND MIST)

SUBJECT TO SARA SECTION 313 ANNUAL TOXIC CHEMICAL RELEASE REPORTING

PHYSICAL DATA

DESCRIPTION: ODORLESS, COLORLESS, HYGROSCOPIC LIQUID WITH A SWEET TASTE.

BOILING POINT: 388 F (198 C) MELTING POINT: 10 F (-12 C)

SPECIFIC GRAVITY: 1.1088 SOLUBILITY IN WATER: SOLUBLE

VAPOR DENSITY: 2.14 VAPOR PRESSURE: 0.05 MMHG @ 20 C

OTHER SOLVENTS (SOLVENT - SOLUBILITY):
SOLUBLE IN ALCOHOL, ACETONE, GLYCEROL, ACETIC ACID,
ALDEHYDES, KETONES, PYRIDINE; SLIGHTLY SOLUBLE IN ETHER; PRACTICALLY INSOLUBLE
IN BENZENE, PETROLEUM ETHER, OILS, CHLORINATED HYDROCARBONS.

OTHER PHYSICAL DATA
SCOSITY: 21 CPS @ 15 C

FIRE AND EXPLOSION DATA

FIRE AND EXPLOSION HAZARD
SLIGHT FIRE HAZARD WHEN EXPOSED TO HEAT OR FLAME.

FLASH POINT: 232 F (111 C) (CC) UPPER EXPLOSION LIMIT: 5%

LOWER EXPLOSION LIMIT: 3.2% AUTOIGNITION TEMP.: 748 F (398 C)

FLAMMABILITY CLASS (OSHA): IIIB

FIREFIGHTING MEDIA:
DRY CHEMICAL, CARBON DIOXIDE, HALON, WATER SPRAY OR ALCOHOL FOAM
(1987 EMERGENCY RESPONSE GUIDEBOOK, DOT P 5800.4).

FOR LARGER FIRES, USE WATER SPRAY, FOG OR ALCOHOL FOAM
(1987 EMERGENCY RESPONSE GUIDEBOOK, DOT P 5800.4).

FIREFIGHTING:
MOVE CONTAINER FROM FIRE AREA IF POSSIBLE. DO NOT SCATTER SPILLED MATERIAL
WITH HIGH PRESSURE WATER STREAMS. DIKE FIRE CONTROL WATER FOR LATER DISPOSAL
(1987 EMERGENCY RESPONSE GUIDEBOOK, DOT P 5800.4, GUIDE PAGE 31).

USE AGENTS SUITABLE FOR TYPE OF SURROUNDING FIRE. AVOID BREATHING HAZARDOUS
VAPORS, KEEP UPWIND.

WATER OR FOAM MAY CAUSE FROTHING (NFPA FIRE PROTECTION GUIDE ON HAZARDOUS
MATERIALS, EIGHTH EDITION).

ALCOHOL FOAM (NFPA FIRE PROTECTION GUIDE ON HAZARDOUS MATERIAL, EIGHTH
EDITION).

TOXICITY

ETHYLENE GLYCOL:
IRRITATION DATA: 12 MG/M3/3 DAYS EYE-RAT; 555 MG OPEN SKIN-RABBIT MILD;
100 MG/1 HOUR EYE-RABBIT MILD; 500 MG/24 HOURS EYE-RABBIT MILD;
12 MG/M3/3 DAYS EYE-RABBIT; 1440 MG/6 HOURS EYE-RABBIT MODERATE.
TOXICITY DATA: 10000 MG/M3 INHALATION-HUMAN TCLO: 9530 MG/KG SKIN-RABBIT LD50;
5500 MG/KG ORAL-CHILD TDLO; 786 MG/KG ORAL-HUMAN LDLO;
398 MG/KG ORAL-HUMAN LDLO: 4700 MG/KG ORAL-RAT LD50;
7500 MG/KG ORAL-MOUSE LD50; 6610 MG/KG ORAL-GUINEA PIG LD50;
5500 MG/KG ORAL-DOG LD50; 1650 MG/KG ORAL-CAT LD50;
00 MG/KG SUBCUTANEOUS-RAT LD50; 2700 MG/KG SUBCUTANEOUS-MOUSE LDLO;
3000 MG/KG SUBCUTANEOUS-GUINEA PIG LDLO: 2000 MG/KG SUBCUTANEOUS-CAT LDLO;
3260 MG/KG INTRAVENOUS-RAT LD50: 3000 MG/KG INTRAVENOUS-MOUSE LD50;
5 GM/KG INTRAVENOUS-RABBIT LDLO; 5010 MG/KG INTRAPERITONEAL-RAT LD50;
5614 MG/KG INTRAPERITONEAL-MOUSE LD50; 1000 MG/KG INTRAPERITONEAL-RABBIT
LDLO: 3300 MG/KG INTRAMUSCULAR-RAT LDLO: 5500 MG/KG INTRAMUSCULAR-RABBIT
LDLO; 1637 MG/KG UNREPORTED ROUTE-MAN LDLO:

MUTAGENIC DATA (RTECS); REPRODUCTIVE EFFECTS DATA (RTECS).
ARCINOGEN STATUS: NONE.
AL EFFECTS: IRRITANT- INHALATION, SKIN, EYE.
CUTE TOXICITY LEVEL: MODERATELY TOXIC BY INGESTION; SLIGHTLY TOXIC BY DERMAL ABSORPTION.
ARGET EFFECTS: CENTRAL NERVOUS SYSTEM DEPRESSANT; NEPHROTOXIN; NEUROTOXIN. POISONING MAY AFFECT THE LUNGS, HEART, BLOOD, BRAIN AND LIVER.

HEALTH EFFECTS AND FIRST AID

NHALATION:
THYLENE GLYCOL:
RRITANT.
ACUTE EXPOSURE- INHALATION IS UNLIKELY AT ROOM TEMPERATURE, DUE TO THE LOW VAPOR PRESSURE. AEROSOLS AT 140 MG/M3 WERE IRRITATING, AND 200 MG/M3 WERE INTOLERABLE CAUSING A BURNING SENSATION OF THROAT AND COUGHING. EXPOSURE TO HIGH CONCENTRATIONS OF MISTS OR AEROSOLS MAY RESULT IN EFFECTS ON THE HEMATOPOIETIC SYSTEM AND CENTRAL NERVOUS SYSTEM WITH HEADACHE, DIZZINESS AND DROWSINESS.
CHRONIC EXPOSURE- HUMANS EXPOSED TO AEROSOLS FROM 3-67 MG/M3 CONTINUOUSLY FOR 1 MONTH REPORTED IRRITATION OF THE RESPIRATORY TRACT, OCCASIONALLY SLIGHT HEADACHE AND LOW BACKACHE, BUT NO OTHER SIGNIFICANT ADVERSE EFFECTS. CONTINUED EXPOSURE TO VAPORS FROM A PROCESS UTILIZING A MIXTURE OF ETHYLENE GLYCOL, BORIC ACID AND AMMONIA HEATED ABOVE 100 C RESULTED IN NYSTAGMUS, LYMPHOCYTOSIS AND SUDDEN LOSS OF CONSCIOUSNESS FOR 5-10 MINUTES. NYSTAGMUS OCCURRED 2-3 TIMES WEEKLY UNTIL EXPOSURE CEASED. REPEATED EXPOSURE TO SATURATED ETHYLENE GLYCOL VAPORS PRODUCED SLIGHT NARCOSIS IN RATS. EFFECTS ON THE FETUS HAVE BEEN REPORTED IN RATS AND MICE FOLLOWING EXPOSURE DURING GESTATION. THERE WAS A LIKELIHOOD THAT AT LEAST A PORTION OF THE EFFECTS RESULTED FROM INGESTION SINCE ANIMALS GROOMED CONSTANTLY BEFORE AND AFTER EXPOSURE.

IRST AID- REMOVE FROM EXPOSURE AREA TO FRESH AIR IMMEDIATELY. IF BREATHING HAS STOPPED, PERFORM ARTIFICIAL RESPIRATION. KEEP PERSON WARM AND AT REST. TREAT SYMPTOMATICALLY AND SUPPORTIVELY. GET MEDICAL ATTENTION IMMEDIATELY.

KIN CONTACT:
THYLENE GLYCOL:
RRITANT.
ACUTE EXPOSURE- LIQUID MAY DEFAT THE SKIN AND CAUSE MINOR IRRITATION. ANIMAL STUDIES INDICATE THAT LETHAL AMOUNTS MAY BE ABSORBED THROUGH INTACT SKIN. ONE CASE HAS BEEN REPORTED OF COMA ACCOMPANIED BY MIOSIS AND SLOWED PULSE 4 HOURS AFTER MASSIVE APPLICATION OF AN ECZEMA REMEDY CONTAINING ETHYLENE GLYCOL. SENSITIZATION REACTIONS MAY OCCUR IN PREVIOUSLY EXPOSED PERSONS.
CHRONIC EXPOSURE- A SLIGHT MACERATING ACTION ON THE SKIN MAY RESULT FROM VERY SEVERE, PROLONGED EXPOSURE. REPEATED OR PROLONGED CONTACT MAY RESULT IN SENSITIZATION.

IRST AID- REMOVE CONTAMINATED CLOTHING AND SHOES IMMEDIATELY. WASH AFFECTED EA WITH SOAP OR MILD DETERGENT AND LARGE AMOUNTS OF WATER UNTIL NO IDENCE OF CHEMICAL REMAINS (APPROXIMATELY 15-20 MINUTES). GET MEDICAL ATTENTION IMMEDIATELY.

YE CONTACT:
THYLENE GLYCOL:
RRITANT.

ACUTE EXPOSURE- VAPORS MAY CAUSE REDNESS, AND CONTACT WITH THE LIQUID MAY CAUSE CONJUNCTIVITIS AND IRIDOCYCLITIS, BUT NO PERMANENT DAMAGE.
CHRONIC EXPOSURE- VAPOR OR SPRAY AT 17 MG/M3/4 WEEKS PRODUCED NO ILL EFFECTS IN HUMANS. RATS EXPOSED CONTINUOUSLY TO 12 MG/M3 FOR SEVERAL DAYS SOMETIMES SHOWED SEVERE EYE IRRITATION, EDEMA OF THE EYELIDS, CORNEAL OPACITY AND APPARENT BLINDNESS, WITHOUT SIGNS OF SYSTEMIC INTOXICATION.

FIRST AID- WASH EYES IMMEDIATELY WITH LARGE AMOUNTS OF WATER OR NORMAL SALINE, OCCASIONALLY LIFTING UPPER AND LOWER LIDS. UNTIL NO EVIDENCE OF CHEMICAL REMAINS (APPROXIMATELY 15-20 MINUTES). GET MEDICAL ATTENTION IMMEDIATELY.

INGESTION:
ETHYLENE GLYCOL:
NARCOTIC/NEPHROTOXIN/NEUROTOXIN.
ACUTE EXPOSURE- THE ESTIMATED LETHAL DOSE FOR ADULTS IS 100 MILLILITERS. THERE ARE THREE STAGES OF INTOXICATION FOLLOWING INGESTION OF ETHYLENE GLYCOL: CENTRAL NERVOUS SYSTEM STIMULATION FOLLOWED BY DEPRESSION; CARDIORESPIRATORY FAILURE; AND RENAL FAILURE. AN ACUTE CENTRAL NERVOUS SYSTEM STAGE MAY FOLLOW SHORTLY AFTER INGESTION AND LAST SEVERAL HOURS WITH SYMPTOMS OF NAUSEA, VOMITING, ABDOMINAL PAIN, DEHYDRATION, VISUAL DIFFICULTY, CONFUSION, PERSONALITY CHANGES, HALLUCINATIONS, CONVULSIONS, COMA, MENINGISM, MYOCLONUS, FIXED PUPILS, DECREASED OR LOSS OF VISION, LOSS OF ACCOMMODATION, PAPILLEDEMA, DIPLOPIA, NYSTAGMUS, STRABISMUS, ABNORMAL EYE MOVEMENTS, OPTIC NERVE ATROPHY, CRANIAL NERVE PALSIES, ATAXIA, TREMORS, MYOSITIS, MUSCLE TWITCHING, TETANY, HYPERREFLEXIA, AND AREFLEXIA. LIFE-THREATENING COMPLICATIONS WHICH MAY OCCUR IN THIS PERIOD INCLUDE RESPIRATORY FAILURE, SECONDARY TO CENTRAL NERVOUS SYSTEM DEPRESSION, CARDIOVASCULAR COLLAPSE, PULMONARY EDEMA AND SEVERE METABOLIC ACIDOSIS. WITHOUT TREATMENT, DEATH MAY OCCUR IN 8-24 HOURS. IF DEATH DOES NOT OCCUR EARLY, LUMBAR PAIN, ALBUMINURIA, HEMATURIA AND OLIGURIA PROGRESSING TO ANURIA ARE PROBABLE. ACUTE RENAL FAILURE WITH UREMIA, PERIPHERAL EDEMA, ASCITES, PULMONARY EDEMA, DROWSINESS, CYANOSIS, COMA AND DEATH IN 7-10 DAYS IS POSSIBLE. METABOLISM TO OXALIC ACID RESULTS IN PRECIPITATION OF CALCIUM OXALATE CRYSTALS IN SOFT TISSUES. CAPILLARY DAMAGE MAY RESULT IN EXUDATIVE, CONGESTIVE OR HEMORRHAGIC DAMAGE TO THE BRAIN, PERICARDIUM AND LIVER. MILDER INTOXICATION MAY RESULT IN INEBRIATION FOLLOWED BY AN ASYMPTOMATIC PERIOD OF SEVERAL DAYS BEFORE THE ONSET OF RENAL FAILURE. OLIGURIA MAY BE PERSISTENT, BUT EVENTUAL IMPROVEMENT IN RENAL FUNCTION IS ANTICIPATED IN SURVIVORS. PERMANENT CEREBRAL DAMAGE MAY OCCUR IN SURVIVORS OF PROLONGED COMA OR CONVULSIONS.
CHRONIC EXPOSURE- REPEATED DAILY INGESTION OF 15-30 ML MAY CAUSE OLIGURIA WITHIN 24-72 HOURS, WHICH MAY PROGRESS RAPIDLY TO ANURIA AND UREMIA. REPEATED ADMINISTRATION TO ANIMALS RESULTED IN SHORTENED LIFE SPAN, CALCIUM OXALATE BLADDER STONES, SEVERE RENAL INJURY, PARTICULARLY OF THE TUBULES, AND CENTRILOBULAR DEGENERATION OF THE LIVER. MATERNAL EFFECTS, EFFECTS ON FERTILITY, FETAL DEVELOPMENTAL ABNORMALITIES AND EFFECTS ON THE EMBRYO AND FETUS HAVE BEEN REPORTED FROM REPEATED ADMINISTRATION TO RATS AND MICE DURING GESTATION; ADMINISTRATION TO LACTATING MICE PRODUCED DELAYED EFFECTS ON THE NEWBORN.

FIRST AID- REMOVE INGESTED MATERIAL BY GASTRIC LAVAGE OR EMESIS. GIVE ARTIFICIAL RESPIRATION WITH OXYGEN IF RESPIRATION IS DEPRESSED. (DREISBACH HANDBOOK OF POISONING, 11TH ED.). GET MEDICAL ATTENTION IMMEDIATELY. ADMINISTRATION OF GASTRIC LAVAGE SHOULD BE PERFORMED BY QUALIFIED MEDICAL PERSONNEL.

ANTIDOTE:
THE FOLLOWING ANTIDOTE(S) HAVE BEEN RECOMMENDED. HOWEVER, THE DECISION AS TO WHETHER THE SEVERITY OF POISONING REQUIRES ADMINISTRATION OF ANY ANTIDOTE AND ACTUAL DOSE REQUIRED SHOULD BE MADE BY QUALIFIED MEDICAL PERSONNEL.

FAILURE RESPONSE PLAN

The anticipated failure modes of the receivers are discussed in the SOP (Addendum 11) and the control system plan. Specific hazards are also discussed. Most failure modes are quickly and automatically sensed, the shutter is automatically closed, and an alarm sounds. In addition, an observer in radio contact with the control room (or physically in the control room) will report any anomalies. The control room personnel will respond by pressing the emergency stop button, and then following any additional procedures spelled out in the SOP.

In the case of a sodium leak, the dish will not be approached until the smoke has cleared. Personnel will be cleared of the area downwind of the incident.

APPENDIX L

BAKEOUT AND FILL OPERATION

APPENDIX L
BAKEOUT AND FILL OPERATION

The final welds on the first pool-boiler receiver were completed in June, 1989. The receiver was helium leak-checked using a commercial diffusion-pump leak detector at Sandia's furnace-brazing facility. No leaks were detected, and the receiver was backfilled with argon and moved to the Engine Test Facility at Sandia's National Solar Thermal Test Facility, where it was mounted in its housing. Metal-sheathed trace heaters (to be used to preheat the receiver during on-sun testing) were attached.

Bakeout

For the vacuum bakeout, supplemental glass-tape heaters and mineral-wool insulation were temporarily applied. The receiver was connected to a 50-liter/second (s) turbo-molecular pump station and was evacuated without heating for 24 hours (hrs). It was then vacuum baked at about 520°C for 8 hrs and at 600°C for 48 hrs. At the end of the bakeout, before cooling, the pressure measured just upstream of the pump was 2×10^{-6} torr. Several additional days of cold pumping were carried out while other activities proceeded. Further reduction in pressure would have taken a very long time because of the size of the vacuum line to the receiver. A residual gas analyzer was used to determine that the dominant specie after the bakeout was argon (see Table L-1). With the vacuum pump valved off, pressure in the receiver was observed to remain stable at 8×10^{-3} torr over a 9-day period. This permitted the leak rate to be bounded as not greater than 2×10^{-8} atm-cm^3/s.

The gas contamination of the receiver's sodium charge has been estimated based on (1) the final pressure and (2) the leak-rate bound. The total volume of the receiver was taken to be approximately 1 cubic foot (ft^3) and the mass of sodium was 12.7 pounds (lb). To begin, the contamination was (conservatively) considered to be pure air. In the first case, the mass of air that would fill 1 ft^3 of volume at the final pressure is $(8 \times 10^{-3}$ torr)/(760 torr/atm) x 1 ft^3 x 0.077 lb air/atm-ft^3 = 8.1×10^{-7} lb, or 0.064 ppm. In the second case, the leak rate over one year amounts to $(2 \times 10^{-8}$ atm-cm^3/s) $(365 \times 24 \times 3600$ s)$(1.225 \times 10^{-3}$ gm air/atm-cm^3) = 7.7×10^{-4} gms, or 0.13 ppm. To determine the amount of oxygen contamination, these results should be divided by about five. If the contaminant was assumed to be pure water vapor instead of air, the results would be multiplied by 16/28.8 = 0.56. In either case, the contamination was much less than the stated impurity level in the as-delivered sodium. The sodium was Callery Chemical's (Callery, Pennsylvania) high-purity grade certified to contain 16 ppm oxygen.

Fill

The receiver and vacuum-pump station were connected to the sodium fill system illustrated in Figure L-1. The fill system was vacuum-baked at about 200°C for 24 hrs, and the sodium was melted and held at 150°C for 24 hrs. Sodium was then pushed from the shipping container into the defined volume, using purified argon. After the defined volume was full (as indicated by its pressure gauge) the contents were drained into the receiver. While the sodium was still molten, the receiver was rotated to its lowest operating elevation, and the fill was confirmed using gamma radiography.

TABLE L-1. PUMPED GASES AT END OF RECEIVER BAKEOUT

Molecular weight	Peak at 600°C (arb. units)	Peak at 20°C (arb. units)	20°C, receiver valved off
2	8.5	0.40	0.20
18	6.0	1.6	2.0
28	6.0	1.2	0.60
32	2.0	0.05	0.04
40	10.0	3.5	0.10
44	1.0	0.20	0.20

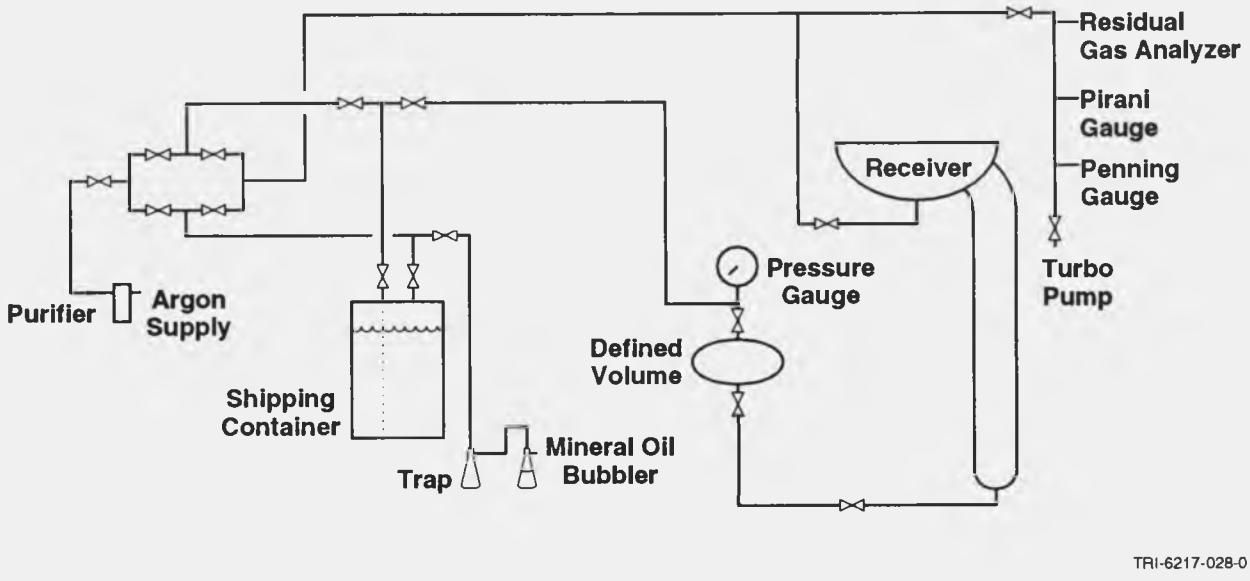

Figure L-1. Schematic of the sodium fill system for the pool-boiler receiver.

APPENDIX M

TEST RESULTS OVERVIEW

APPENDIX M
TEST RESULTS OVERVIEW

The pool-boiler receiver was tested on eighteen separate days between August 31, 1989 and May 30, 1990, for a total of about 48 hours (hrs) above 700°C. Tests were performed at various power levels and operating temperatures. A large portion of the tests was dedicated to solving the hot-restart over-temperature problem. Additional characterization tests were performed using an infrared camera and x-ray equipment. One performance test was performed essentially from horizon-to-horizon. Table M-1 summarizes the history of receiver testing.

TABLE M-1. POOL-BOILER OPERATION SUMMARY

Date	Description	Minutes >600°C	Minutes at 800°C	Hot Restarts	Safety Tripouts	Notes
8/31/89	1/2-power test	105.2	13.6	2	3	Boiled; cloud cover ended test
9/7/89	3/4-power test	214	193.8	2	1	Auto control Face TCs deteriorating
9/8/89	Full power test	162.9	148.2	3	4	Several real cloud transients, failed TCs
9/13/89	Hot restart tests	320.8	80.5	40	19	Established repeatable hot restart trouble
9/14/89	More hot restart tests	353.2	174.5	58	41	Test software (control) solution to restarts
10/2/89	Attempt xenon addition	0	0	0	0	WD-40 smoke; did not reach boiling before clouds
10/3/89	Xenon addition	169.9	76.4	16	3	Baseline restarts followed by Xenon addition Reduced condenser performance noted
10/12/89	Xenon "removed"	219.4	125.8	21	0	Attempt to re-establish hot-restart problem baseline with most of xenon removed Problem not reproduced
10/19/89	All day performance	604.5	593.3	1	0	Test within 5° of each horizon. Some shadows on dish and NIP
11/15/89	Dirty/clean compare	190.6	184.4	1	0	Bucket/Scale flow measurements disagree with flowmeter Test terminated to investigate
12/21/89	X-ray camera test	61.9	9.0	5	1	One offtrack caused melt on aperture x-ray camera looking at elbow area
5/9/90	X-ray array test	103.1	49.5	14	3	Multiple x-ray detectors looking at midway up the domes New TC channel assignments aperture protected with TCs Several simulated hot restarts Restart problem re-appeared
5/10/90	Low elevation hot restarts	7.7	0	0	0	Low insolation cancelled test
5/15/90	Low elevation hot restarts	159	108.2	33	1	Restart problem returned above about 55° elevation Fall tests did not reach that elevation
5/18/90	IR camera/performance	91.8	82.7	1	0	IR camera debugging Auto control tuning adjustments water flow rate verification
5/22/90	IR camera	22.2	14.9	1	0	
5/23/90	Wispy cloud performance	148	134.1	4	1	Clouds ended the test Struggles with de-track sensors
5/30/90	Demo/performance	23.1	0.3	1	2	Failure occurred during restart
	Totals	2957.1 (49.3 h)	1989.2 (33 h)	203	79	

The objective of the first three tests was to demonstrate well-behaved boiling at 1/2, 3/4, and full power. The power was attenuated by covering selected mirror facets on Test Bed Concentrator #1 (TBC-1). Figure M-1 shows the mirror coverage for the 1/2-power test. The mirror coverage patterns are specified in the standardized test plan (Appendix J of this report). Two specific concerns in these initial tests were boiling instabilities and flooding limits (Moreno and Andraka, 1989). Test #1 totaled 96 minutes (min) at 1/2 power, with eight minutes of steady operation at 800°C condenser temperature. In tests #2 and #3, nearly all test time was at 800°C. Time totaled 204 min at three-quarter power and 180 min at full power. Figures M-2 through M-4 show the solar insolation, pool temperature, and power throughput histories for these three tests. Figure M-5 shows extracted power and temperatures measured during a steady-state portion of the full power test. This figure demonstrates the stability of the boiling, with temperature fluctuations on the absorber surface of less than 10°C. Receiver thermal efficiency was about 90% when the input power and sodium temperature were at their maximum tested values. The temperature was quite steady and nearly isothermal within the receiver, indicating that stable nucleate boiling was achieved. The absorber temperature shown was measured with a flattened thermocouple brazed to the air side of the absorber. Because the thermocouple was about as thick as the absorber, this temperature was estimated to be as much as 15° to 20°C higher than at the surface of the absorber, and was considered to be dependent on the local heat flux. Qualitatively similar temperature results were obtained at 1/2 and 3/4 power, and in brief runs at 700° and 750°C at 1/2 and full power.

Figure M-1. Mirror coverage on TBC-1 during the 1/2-power test. This mirror coverage provides a reduced power level with a qualitatively similar flux distribution to the full-power testing.

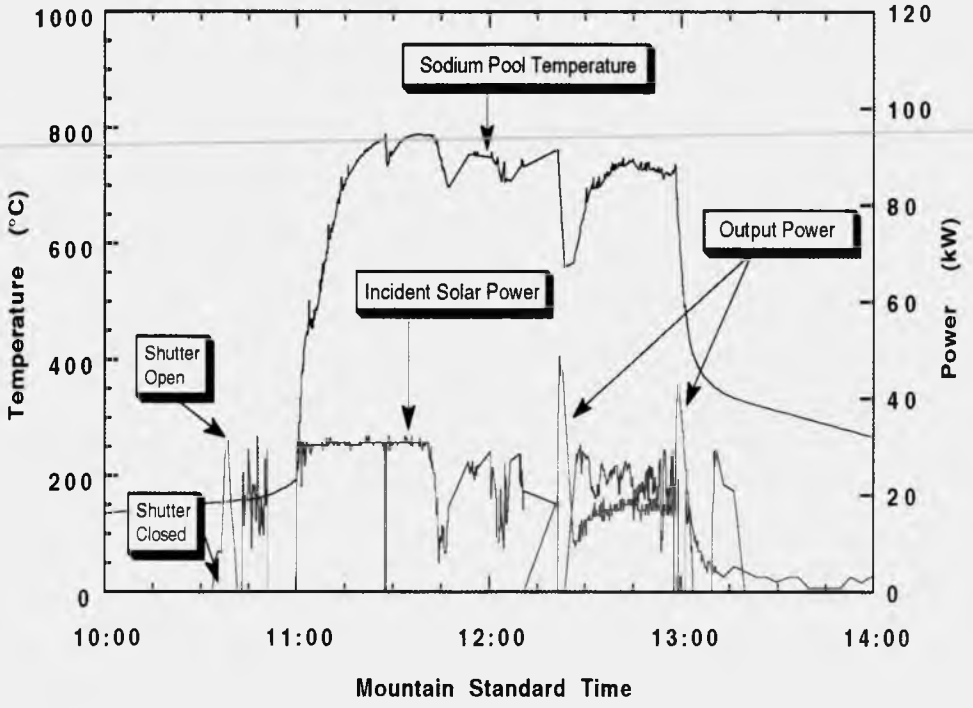

Figure M-2. Insolation, pool temperature, and power extracted during the 1/2-power initial test of the pool-boiler receiver (August 31, 1989).

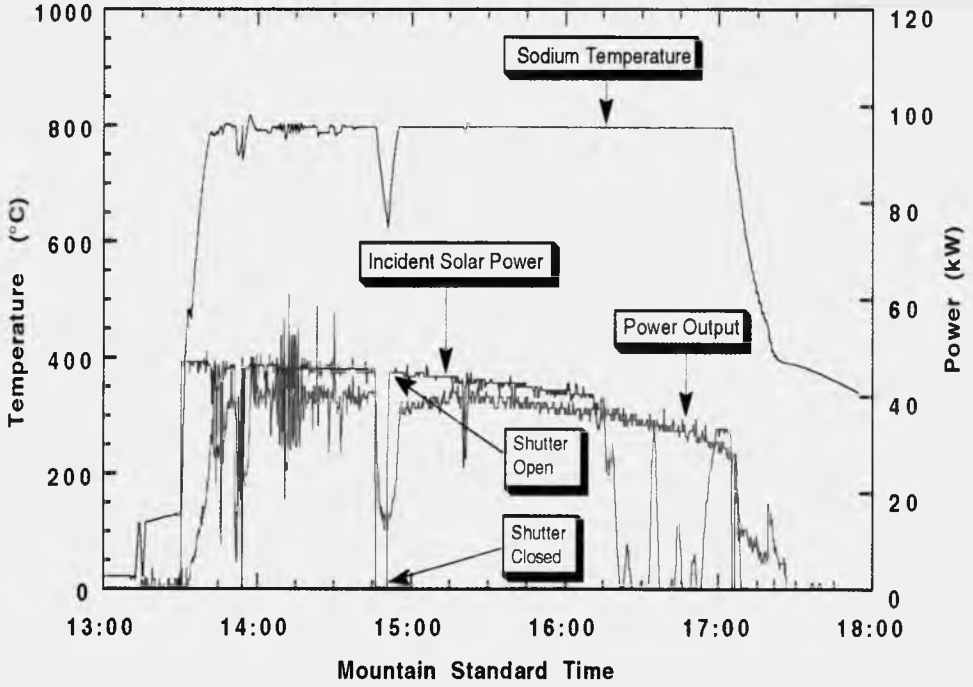

Figure M-3. Insolation, pool temperature, and power extracted during the 3/4-power test of the pool-boiler receiver (September 7, 1989).

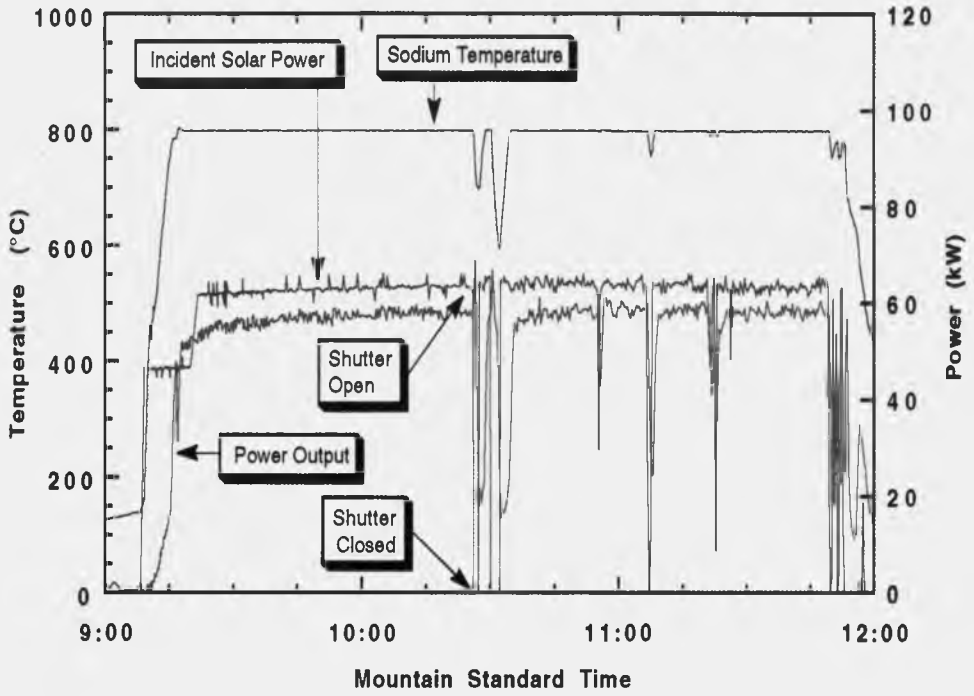

Figure M-4. Insolation, pool temperature, and power extracted during the first full-power test of the pool-boiler receiver (September 8, 1989).

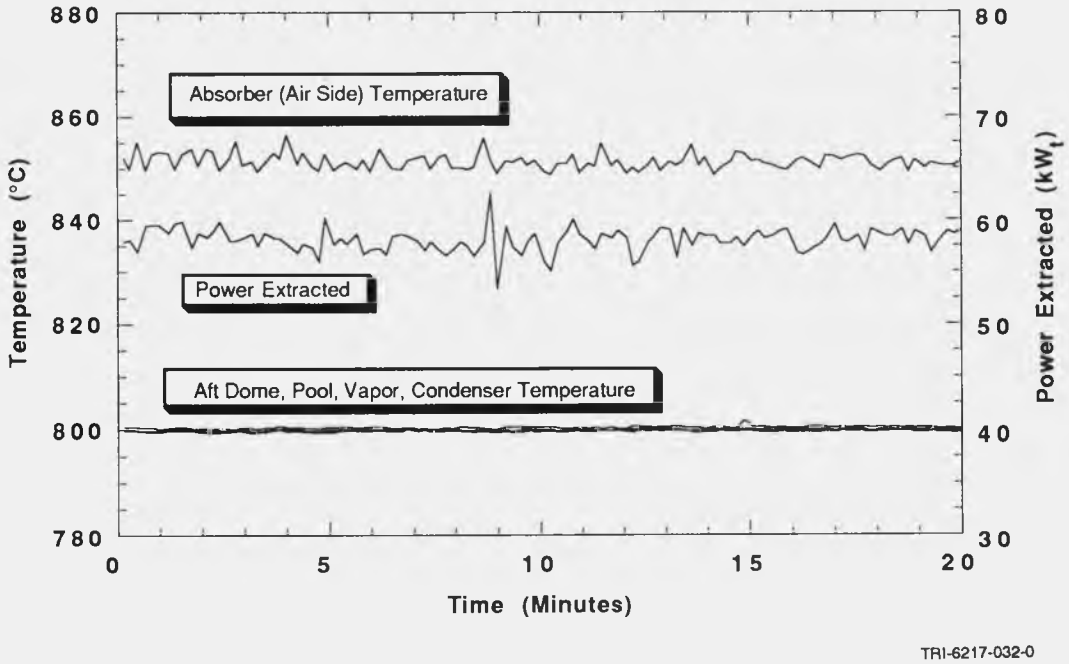

Figure M-5. Temperatures and extracted power during a 20-minute portion of a full-power steady-state test (September 8, 1989), demonstrating the isothermal and steady nature of the two-phase boiling system. The absorber thermocouples are brazed to the surface in the flux, and therefore read higher than the surface temperature because of conduction of a high flux through the sheath.

Figure M-6 shows a typical full-power startup on a clear day. The sodium was electrically preheated to just above melting (about 100°C) and then solar flux was applied. Boiling initiated at a pool temperature between 450° and 500°C, as evidenced by the condenser temperature response. This was significantly below boiling start temperatures experienced on prior bench testing at Sandia (600°C) (Moreno and Andraka, 1989). The target temperature of 800°C was reached in 7 min and "steady state" (as evidenced by the output power reaching nominally full power) was reached in 9 min.

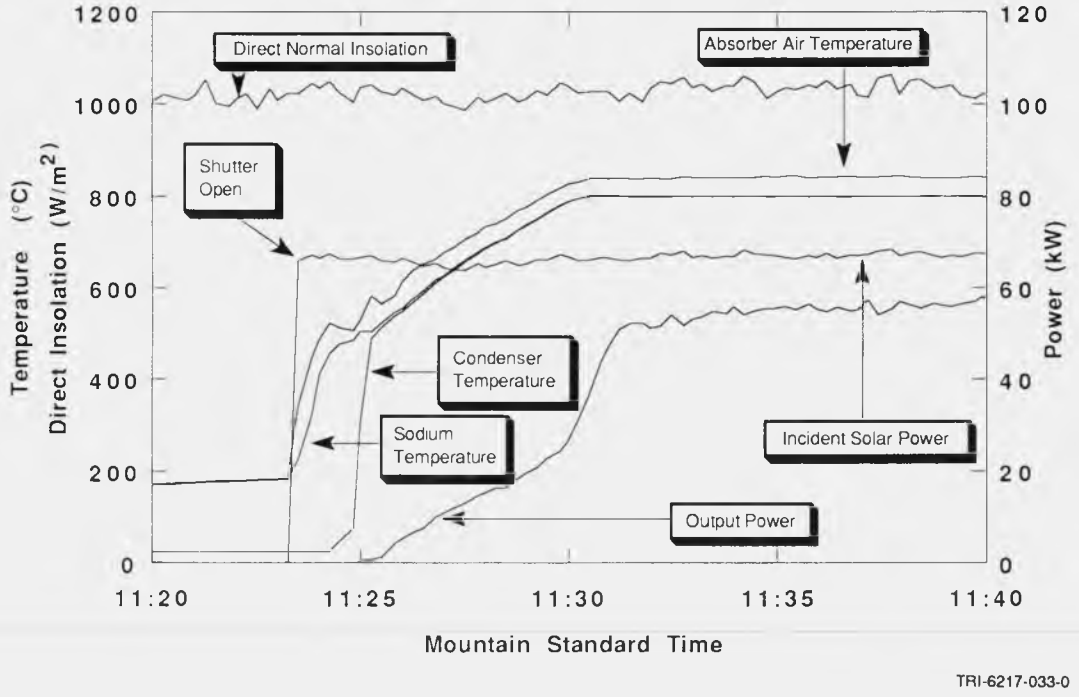

Figure M-6. A typical full-power startup of the receiver, demonstrating the ability to provide power shortly after going on-sun.

Figure M-7 illustrates the temperature distributions along vertical and horizontal diameters of the absorber during startup and near steady state, at full power. The temperatures were indicated by flattened thermocouples brazed to the air side of the absorber. As expected, the temperature distributions were qualitatively similar to the calculated flux distributions (Figure M-8). However, sodium conduction and convection tended to moderate the effect of the flux nonuniformities, resulting in relatively uniform temperatures even during startup. The temperature distribution on the rear dome (not shown) was even more uniform. These absorber temperatures were always consistent with conduction of the incident solar flux through the absorber into the sodium pool. This seemed to confirm that the boiler design was adequate to avoid a flooding limit (heat transfer crises) (Moreno and Andraka, 1989) at all tested orientations and input power levels.

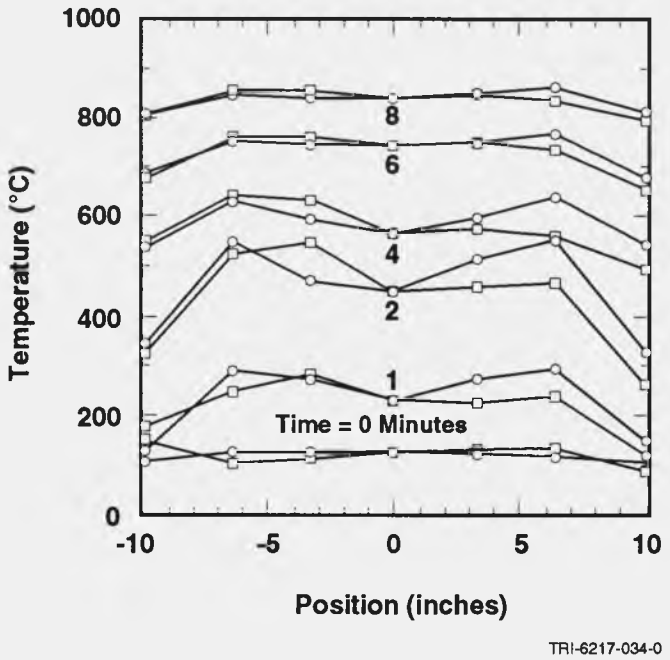

Figure M-7. Temperatures indicated by the thermocouples brazed to the air side of the absorber along the horizontal (circles) and vertical (squares) bisectors during a full-power startup. The zero position corresponds to the center of the receiver.

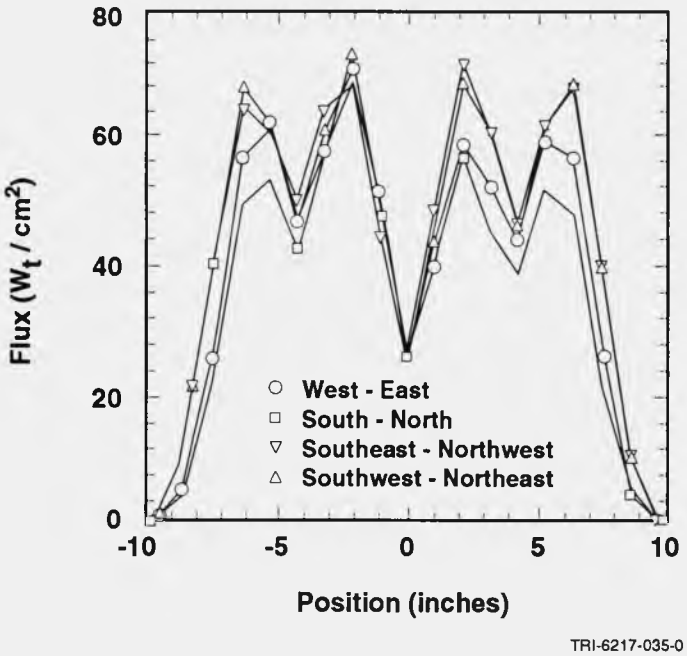

Figure M-8. Design incident solar flux on the receiver as calculated by CIRCE2. Flux distribution as a function of position along bisectors of the absorber is shown for four compass directions as viewed from the concentrator. Negative positions on the X-axis correspond respectively to west, south, southeast, and southwest of the center of the absorber.

The objective of the 4th and 5th tests was to study the "hot restart problem" identified during simulated cloud transients in the bench-scale tests (Moreno and Andraka, 1989; Andraka and Moreno, 1989). In those tests, power was interrupted, pool temperature was allowed to drop into the range of 680° to 720°C, and then power was re-applied. Temperatures indicated by thermocouples brazed to the heated surface quickly exceeded 900°C, causing safety-system automatic shutdowns. In the subject tests, cloud transients were simulated using the receiver shutter. More than 80 hot restarts were studied during these two tests. Figures M-9 and M-10 present the insolation, pool temperature, condenser temperature, and shutter position histories for these two tests. It was found that the system had to be "conditioned" before an over-temperature would occur. Once an over-temperature occurred, it would repeat on every succeeding cycle. Conditioning amounted to repeating a cloud cycle several times without steady operation between cycles. A typical example showing two cycles of conditioning followed by a third cycle with an over temperature is presented in Figure M-11. Figure M-11 shows that the condenser and absorber temperatures diverged during the third cycle cool-down. The divergence and the simultaneous observation that the sounds of boiling had stopped were taken as evidence that boiling had stopped. Significantly, in every case of over-temperature, boiling had stopped by the time the shutter re-opened. Such behavior was consistent with the fact that it takes a much larger wall-to-pool temperature difference to initiate boiling (incipient boiling superheat) than to maintain boiling (nucleate boiling superheat) (Dwyer, 1976). These observations suggested several remedies that are discussed in this overview.

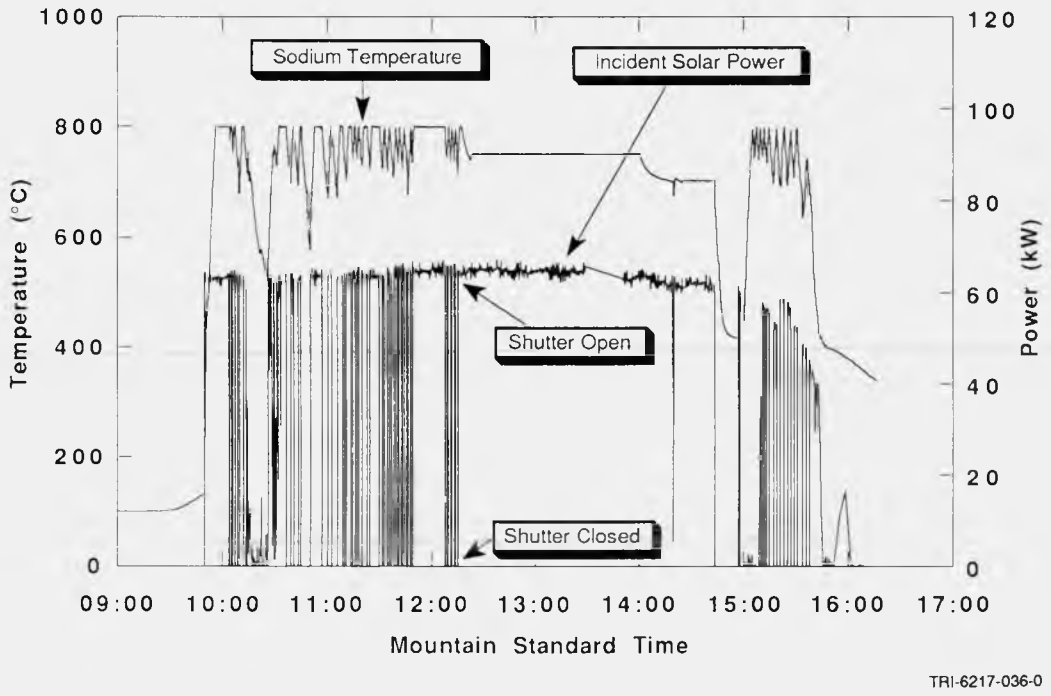

Figure M-9. Sodium pool temperature and incident power during the first hot-restart test series (September 13, 1989). Hot restarts were attempted at many orientations and power levels, and some steady state testing was also performed. Over-temperatures due to failure to restart boiling occurred very rapidly compared to the data rate, and therefore do not appear on this plot.

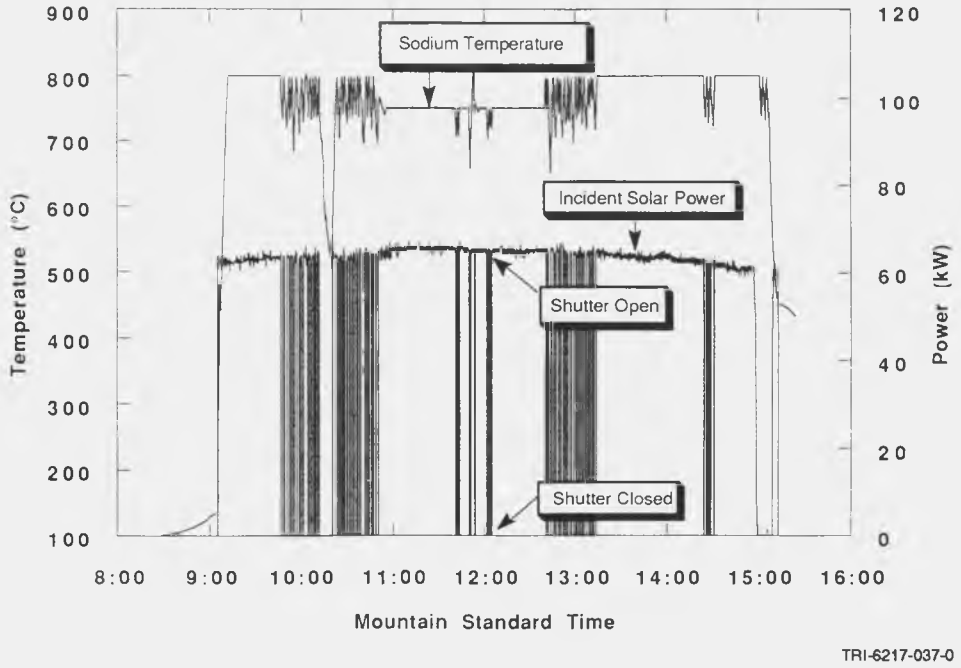

Figure M-10. Sodium pool temperature and incident power during the second day of hot restart characterization (September 14, 1989). Hot restarts were attempted at several operating temperatures, and a repeatable sequence was developed. Active control of the pool-to-condenser temperature difference was attempted during these tests.

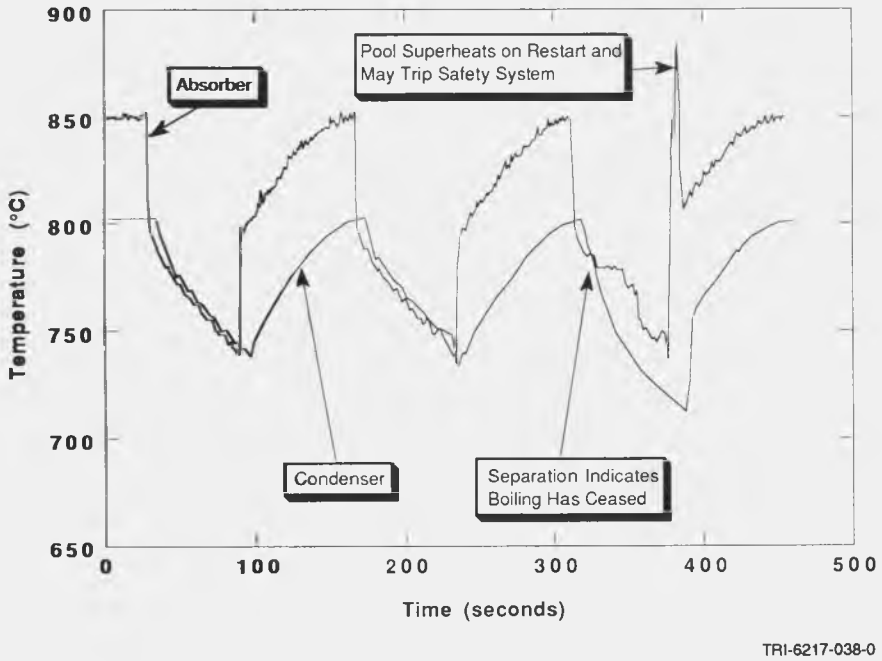

Figure M-11. This stripchart recording of the absorber and condenser temperatures during hot restarts demonstrates the repeatable sequence of three hot restarts that leads to separation upon cool-down and a failure to start boiling upon reapplication of power. The very rapid temperature spike was usually not detected by the data system, but caused automated emergency shutdowns to be initiated.

An active-control solution to the hot-restart problem was successfully demonstrated in test #5. During closed-shutter cool-downs, whenever signs of boiling cessation occurred, boiling was forced to continue by immediately adding helium to the calorimeter gas gap. The effect of the helium was to lower the condenser temperature (and thus to lower the system pressure), thereby assisting bubble inflation at the heated surface. This procedure was automated so that helium was added whenever the pool and condenser temperatures diverged by more than 10°C. Repeated tests suggested that this control strategy is a way to eliminate the hot restart problem in most cloud-transient situations. In a receiver-engine combination, the same effect during cool-down could be produced by increasing the engine load whenever the absorber and heater-head temperatures diverged.

A passive solution to the hot restart problem was suggested by Elric Saaski (Saaski, 1989). This involved introducing a small amount of inert gas into the vapor space in the boiler. Xenon was chosen because of its reported high solubility in sodium (Reed and Droher, 1970). The possible beneficial effect of dissolved gas on incipient-boiling superheat has been discussed by others (Singer and Holtz, 1969) and has been tried in a bench-scale device (Proceedings of the Solar Stirling Heat Transport System Workshop, 1989). The purpose of tests #6 and #7 was to try this idea in the full-scale receiver. In test #6 about 128 standard cm^3 (3.7 torr) of xenon was added to the receiver. Following the addition, the hot-restart problem could not be reproduced using the previously repeatable procedure. However, the xenon had an adverse effect on heat transfer. Before the addition, with pure helium in the calorimeter gas gap and the pool at 700°C, about 60 kW_t could be extracted. After the addition, the same conditions required a pool temperature of 760°C. To correct this problem, most of the xenon was pumped out when the boiler was cold. A turbo-molecular vacuum pump was attached to a 1/4-inch (in.) pumpout line overnight. The remaining pressure, assumed to be xenon, was measured after closing the vacuum pump valve. About 1.5 cm^3 (0.09 in^3) of free xenon remained, plus an estimated 0.9 cm^3 (0.05 in^3) or less dissolved in the sodium (Appendix N of this report). In the next test, this change restored the heat transfer characteristics to their initial values, but the hot restart problem could not be repeated. Apparently, the small amount of remaining xenon was enough to affect the hot-restart mechanism. Figure M-12 shows the effect of the small amount of xenon on typical test results for this time period. In contrast to the cycles shown in Figure M-11, these results show repeated cycles made without over temperature. This particular plot is a portion of about 20 repeating hot restarts. It can be seen that the absorber and condenser temperatures quickly converged and remained close during cool-down, indicat-

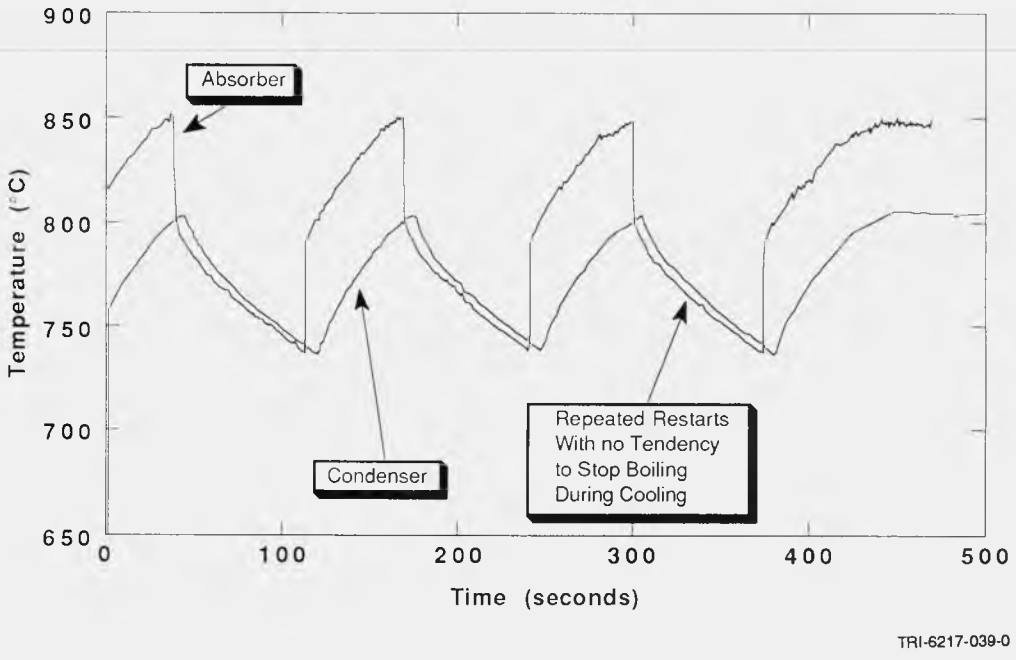

Figure M-12. This stripchart recording, when compared to Figure M-11, demonstrates the positive effect of the addition of xenon to the sodium vapor space of the receiver. After numerous consecutive restart attempts, there is no evidence of separation of the absorber and condenser temperatures during cool-down, and no temperature spike upon reapplication of the solar flux.

ing that cessation of boiling did not occur. These results show that the hot restart problem can be controlled by the addition of a very small amount of xenon into the boiler. This passive solution is preferable to the active control method because of its simplicity and low cost.

The next test in the series was run to determine receiver behavior over the full range of orientations for a typical day, and to collect data for comparison with existing performance models. The test was run on a clear day with operation nearly from horizon-to-horizon. Figure M-13 shows power levels and representative temperatures for the day-long test. The very steady temperatures show that boiling stability and automatic temperature control were not a problem. The insolation data from 14:45 to 16:15 MST were corrected with a curve fit because of shadowing of the Normal Insolation Pyrheliometer (NIP) during the test. No clouds were observed during this period, and no shadowing affected the concentrator, so this correction to the data was reasonable. Daily receiver efficiency, determined from the total energy input to the receiver and extracted by the calorimeter, was about 89%. This result demonstrated the potential of the pool-boiler receiver for high efficiency at the high temperatures needed for Stirling engine operation. It was in part attributable to the small size of the receiver cavity, which minimized the loss to air convection. The small size in turn was possible because of the excellent internal heat transfer characteristics of the receiver.

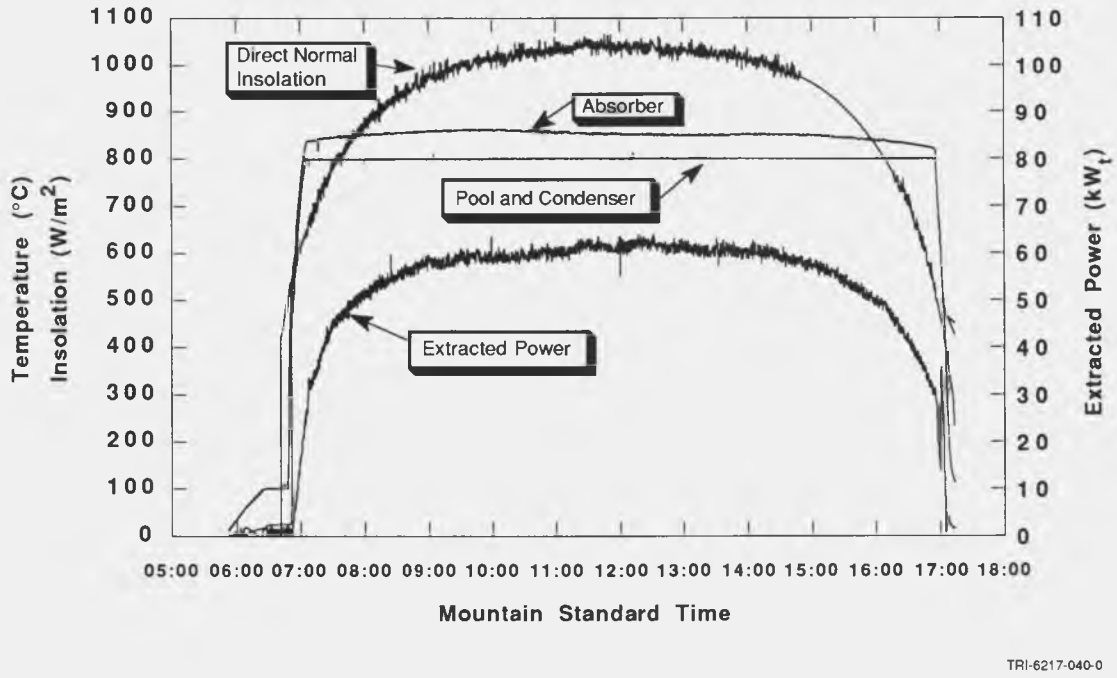

Figure M-13. Power input, output, and temperatures during the all-day performance test of the receiver (October 19, 1989). Steady operation was flawless in all tested orientations and power levels.

The November 15 test was intended to study the performance difference between dirty and clean mirrors. The dish was operated with the dirty mirrors for about three hrs. During this time, a careful flow measurement indicated a 4% error in the calorimeter flowmeter reading. Cloudy weather in the afternoon prevented completion of the "clean mirror" test. Figure M-14 shows the insolation, pool temperature, and power throughput history during this test. Appendix Q of this report discusses the performance testing results in detail, and Appendix R of this report compares the results to numerical models developed at Sandia.

The next test performed involved real-time x-ray cinematography of the boiling sodium. Because of physical constraints around the receiver housing, only a small portion near the top of the pool could be viewed. The fluorescent plate intensity was measured before the sodium was melted (through structure and vacuum), after it had melted and

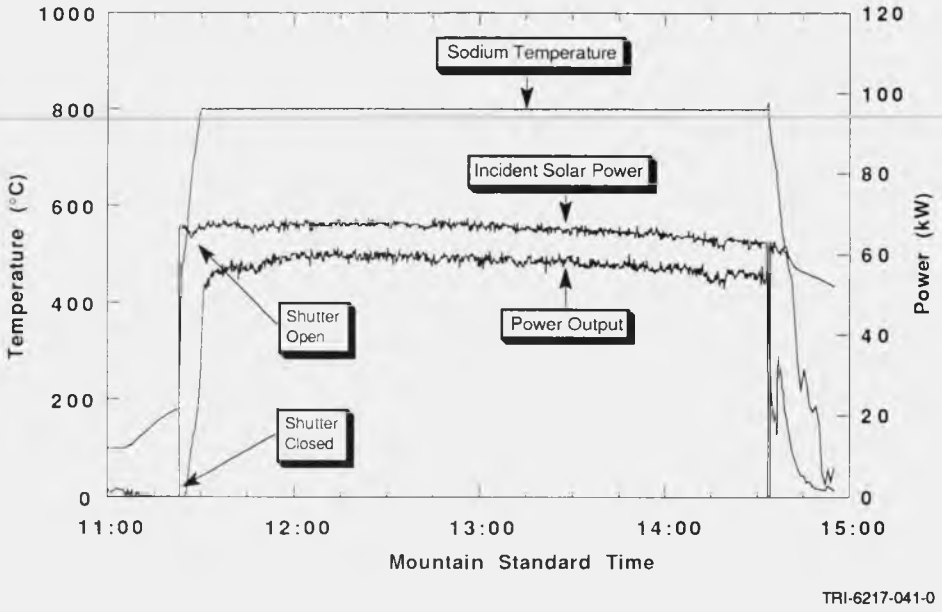

Figure M-14. Insolation, pool temperature, and power throughput during the first performance verification test (November 15, 1989). A 4% error in the water flowrate measurement was discovered during this test. The test was discontinued because of clouds.

thermal expansion had occurred (through structure and sodium liquid), and while it boiled (through structure, liquid, and voids). The void fraction during boiling could then be inferred from these measurements. Light leaks and background skewing caused some apparent negative void fractions. When corrections were applied for these effects, void fractions of 33 to 46% were calculated at 800°C and 60 kW_t. Appendix O of this report discusses the x-ray results in more detail.

The calorimetry system was filled with glycol to prevent freezing during the winter, and the x-ray data was reviewed. An alternative method of x-ray analysis, based on an array of discrete sensors rather than a camera, was implemented and installed near the midpoint (vertically) of the domes. Difficulties with preventing freezing in the cooling system and delays with the x-ray setup delayed further testing until May 1990.

The first test in May was the x-ray detector array test, described in Appendix O. During the test, several hot restarts were attempted to observe void fractions under all operating conditions. Most of the restarts were performed around mid-day, and several caused over temperature tripouts when the solar flux was re-applied. A number of theories explaining the tripouts were discussed; the leading theory indicated elevation as the critical factor. The fall tests were late enough in the year that the elevation was limited to less than 45 degrees, while the May test included restarts at elevations of over 60 degrees. Additional hot restart tests were planned for May following the completion of the x-ray studies, and results are presented later.

The May 10 test was aborted because of clouds. On May 15 hot restarts were performed, starting early in the morning, and repeating for approximately every 5 degrees of elevation. Figure M-15 shows the dish elevation, solar insolation, shutter position, and pool and condenser temperature histories during this test. Much to our relief, the fall results (problem solved) were repeated. However, at 55 degrees elevation, there was notable separation of the condenser and pool temperatures upon cool down, and at 60 degrees, the hot restart problem became repeatable. Based on these results, it was theorized that the small amount of xenon was compressed into the condenser endcap, and was then entrained by sodium splashing from the pool. Small entrained bubbles of xenon then provided nucleation sites to cause boiling to continue during the cloud transient. At the higher elevations, and because of the long condenser section, the sodium simply did not get thrown high enough to entrain the small pocket of xenon. If this mechanism has been correctly

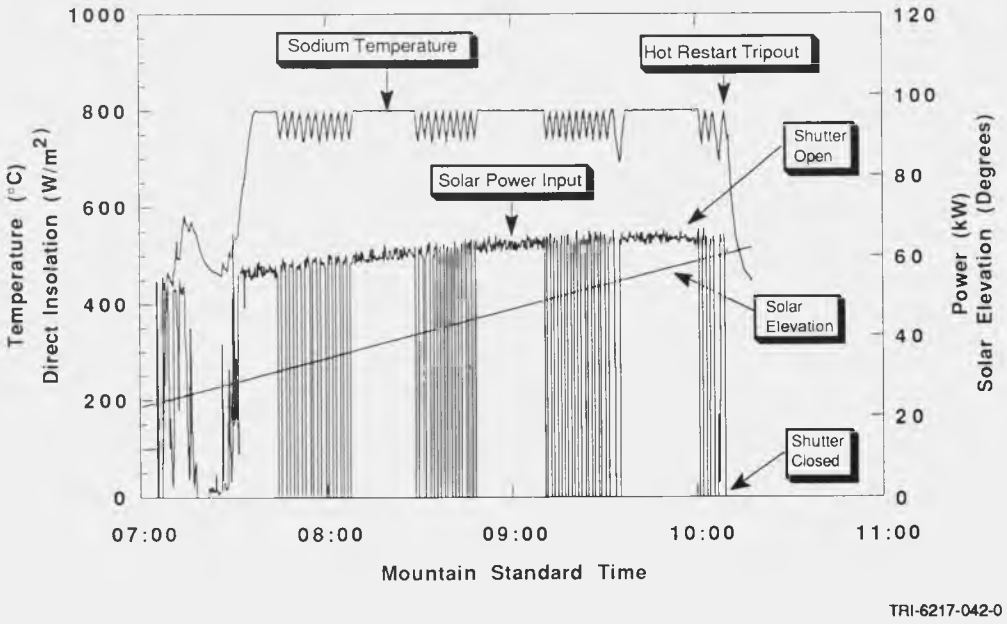

Figure M-15. Sodium pool temperature, power input, and solar elevation during continued hot restart testing of the receiver (May 10, 1990). As the elevation reached 60 degrees above the horizon, the hot restart problem began to emerge again, suggesting new mechanisms for the function of xenon in the receiver. The October testing after the addition of xenon included hot restarts to elevations of 45 degrees only.

understood, a receiver with an engine (which would have a shorter condenser section) should resolve the elevation problem. The elevation-dependence issue will be studied further in bench-scale tests at Sandia.

The next pair of tests were designed to get IR (infrared) video images of the receiver during startup and operation. The ceramic aperture was widened to 26 cm (10.2 in.) to allow a greater view of the absorber. The first test (May 18) was used for camera debugging, controls tuning, and water flow verification. The water flow measured with the factory calibration on a new flowmeter disagreed with bucket measurements by 1.5%. In the next test, on May 22, the IR camera image was recorded during a startup and through steady state. The test was stopped to retrieve the camera, and afternoon clouds prevented further testing. The IR camera results are discussed in more detail in Appendix P of this report.

On May 23, the receiver was run with a high wispy cloud cover. Several thermocouples had been added to the aperture because of tracking problems encountered earlier. The thermocouples caused several inadvertent shutdowns and hot restarts until their positions and temperature limits were adjusted. A heavier cloud cover ended the test after several hours.

On May 30, which was a clear day, a performance testing and a demonstration of capabilities were scheduled. During the startup, a face thermocouple failed and caused a shutdown (Figure M-16). By this time, such a failure was a "normal" occurrence. After the data was reviewed (abnormal and off-scale readings) and the thermocouple resistance was checked to verify that there was an instrumentation problem rather than a receiver problem, the thermocouple was removed from service and the shutter was opened. The pool had reached a peak of 670°C prior to the thermocouple failure and had cooled to 450°C during the investigation. As evidenced by the microphone sounds, boiling started almost immediately and continued smoothly for about 30 seconds. The boiling sounds then stopped and smoke issued from the receiver. The shutter was closed and the emergency procedures were followed. The postmortem analysis continued over the next several months, and indicated that the most likely cause of failure was local film boiling or exceeding the flooding limit, although other possible causes could not be conclusively ruled out. The sequence of events, particularly the low temperature restart, was unique to this particular test, and could have contributed to the failure in either of these scenarios. A postmortem analysis of these factors is presented in Appendix S of this report.

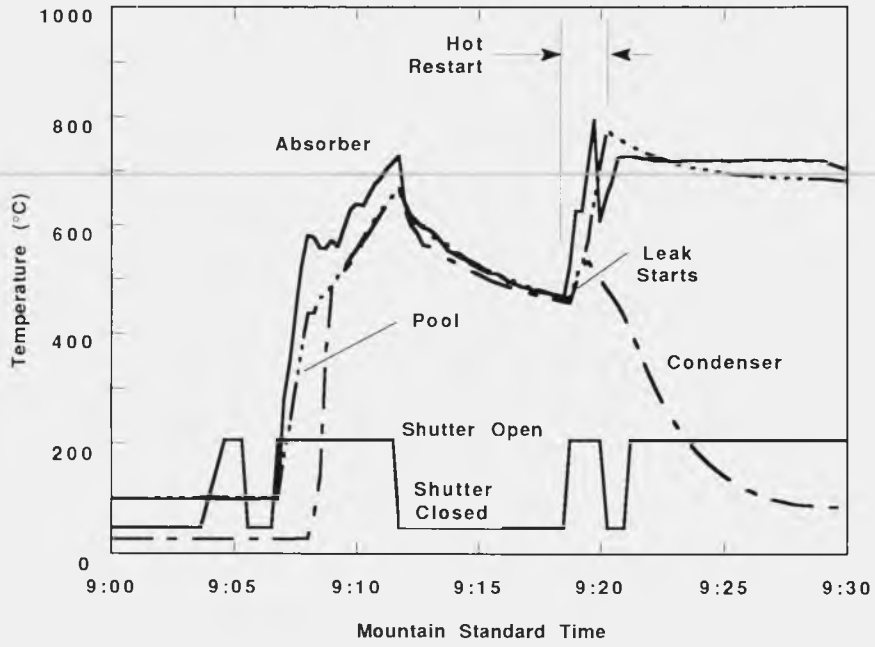

Figure M-16. Temperatures and shutter positions during the May 30, 1990 test leading to the failure of the receiver.

The receiver was tested for a total of 2957 minutes (49 hrs) at or above 600°C, and 1989 min (33 hrs) at or near 800°C. Some of the lower temperature periods at 700° and 750°C were planned operations intended to characterize the receiver for lower temperature Stirling engines. The receiver experienced 18 cold starts and about 200 hot restarts initiated with shutter-simulated clouds. There were a total of 79 shutdowns triggered by the safety system, mostly during the simulated hot restarts. About 11 hrs of cloudy-weather operation also contributed to the thermal cycle loading of the receiver.

References

Andraka, C. E., and J. B. Moreno. 1989. "Pool-Boiler Reflux Solar Receiver for Dish-Electric Systems," paper no. 899462. *Proceedings of the 24th IECEC, Washington, DC, August, 1989.* SAND89-1311C. Albuquerque, NM: Sandia National Laboratories.

Dwyer, O. E. 1976. *Boiling Liquid-Metal Heat Transfer.* Hinsdale, IL: American Nuclear Society.

Moreno, J. B., and C. E. Andraka, 1989. *Test Results from Bench-Scale Sodium-Pool-Boiler Solar Receiver.* SAND89-0899. Albuquerque, NM: Sandia National Laboratories.

Proceedings of the Solar Stirling Heat Transport System Workshop, Lancaster, PA, September 27-28, 1989.

Reed, E. L., and J. J. Droher. 1970. *Solubility and Diffusivity of Inert Gases in Liquid Sodium, Potassium, and NaK.* LMEC-69-36. Canoga Park, CA: Atomics International.

Saaski, E. 1989. "Advanced Solar Conversion System (ASCS) Heat Transport System Working Group Meeting." Albuquerque, NM: Sandia National Laboratories.

Singer, R. M., and R. E. Holtz. 1969. "On the Role of Inert Gas in Incipient Boiling Liquid Metal Experiments." *International Journal of Heat and Mass Transfer.* 12: 1045-1060.

APPENDIX N

XENON ADDITION

APPENDIX N
XENON ADDITION

A description of the hot-restart problem is given earlier in Appendix M of this report. The problem is characterized by a very-high incipient-boiling wall superheat when heat is reapplied to the pool boiler after a brief interruption. The problem is believed to be a result of deactivation of all but the smallest nucleation sites during cool down. A passive solution to this problem was suggested by Elric Saaski (Saaski, 1989) and tested in a bench-scale device (Proceedings of the Solar Stirling Heat Transport System Workshop, 1989). The solution involves adding inert gas to the receiver vapor space. Several mechanisms have been proposed to explain how this might solve the hot restart problem. One rationale is that gas that has dissolved in the sodium during high-temperature operation will precipitate out on the absorber at the lower temperatures that occur during cloud transients. This might prevent nucleation-site deactivation that otherwise would occur. Another rationale is that the inert gas will be entrained in the sodium as small bubbles as a result of two-phase turbulence in the condenser section. Some of these bubbles would persist during cool down and serve as nucleation sites on restart.

Xenon was chosen to be added to the receiver because of its estimated high solubility in sodium (Reed and Droher, 1970). At 800°C, this value is approximately 2×10^{-4} (mole of xenon per mole of sodium per atm). Using this value, the amount of xenon that could be dissolved in the sodium pool was calculated. There were about 250 moles of sodium in the receiver. During operation, it was expected that the xenon not dissolved in the sodium would be swept to the rear of the condenser, where it would form a gas cap equal in pressure to the sodium vapor pressure (approximately 0.5 atmosphere [atm]). In the interface between the sodium vapor and the gas cap, xenon would be driven into solution in the liquid sodium forming on the walls. As the liquid refluxed to the pool, it would move out of the high-pressure xenon area, and thus could lose some of its dissolved gas. The amount of xenon in the pool could therefore be bounded by 2×10^{-4} (mole of xenon per mole of sodium per atm) x 250 (moles of sodium) x 0.5 (atm) = 0.025 moles. In our estimates, this amount was doubled to provide for an equal amount of gas in the condenser. At one atmosphere and room temperature, 0.05 moles of xenon fill a volume equal to $0.05 \times 8.31 \times 10^7 \times 300\ (K)/(1.01 \times 10^6) = 1234\ cm^3$. This is about 5% of the total receiver volume. Because excess xenon could adversely affect heat transfer by blanketing the condenser wall, it was decided to add xenon in 10% increments of this amount, checking the hot-restart behavior and heat-transfer characteristics after each addition.

The original plan was to introduce the xenon through the receiver's 3/4-inch (in.) pumpout valve, with the receiver still mounted on the Test Bed Concentrator (TBC). The sodium in the 3/4-in. tube between the valve and the aft dome would be melted by operating the receiver at 800°C for a short period, and then xenon at 30 psia in a 60-cm^3 defined-volume manifold would be bubbled through the sodium into the receiver. A fill manifold was fabricated for this purpose. One problem with the plan was that access to the 3/4-in. line was extremely limited. This distraction contributed to an incorrect tightening specification. When the manifold was attached to the 3/4-in. valve, overtightening resulted in failure of the weld between the valve and the 3/4-in. tube that connected it to the aft dome. This necessitated removal of the receiver from the TBC. A new valve was installed, using a compression-type connection. Before the valve was closed and capped, it was connected to a turbomolecular pump station, leak checked, and evacuated for 24 hours. Because the end of the solid sodium plug in the 3/4-in. tube was contaminated by air, a water-cooling coil was installed on the tube to keep the plug frozen and thus prevent migration of the contamination into the sodium pool. Next, it was decided to carry out the xenon addition through the receiver's 3/8-in. fill tube. A metal-sheathed heater was attached to the fill tube to enable the sodium to be melted or, if desired, evaporated out of the tube. A new xenon fill manifold was made, connected to the tube, and evacuated, and the receiver was mounted on the TBC.

With the sodium in the fill tube melted, tests confirmed continued existence of the hot-restart problem. Then 128 standard cm^3 of xenon was added to the receiver. The tests that followed (described in detail in Appendix M) indicated that the hot-restart problem was apparently cured. However, the temperature data showed that the xenon was interfering with heat transfer at the condenser. It was decided to evaporate the sodium out of the fill tube in order to pump the xenon out of the receiver. The condenser end cap and the fill tube were heated for approximately six hours. Temperatures at the top and midpoint were above 500°C, but the temperature only reached 280°C at the valve. Temperature changes in the vicinity of the valve were used to decide when evaporation was complete. Using an aerial work platform, the turbomolecular pump station was attached to the fill manifold, and the manifold was evacuated. With the pump valved out of the system, the fill valve was opened. The pressure indicated by the Pirani gauge stabilized at 1.7 torr. Because a calibration of this gauge for xenon was unavailable, the result was taken only as an indication that communication with the receiver was established. The receiver was evacuated for about three hours. By then, the pressure with

the pump valved out was equilibrating at about 2×10^{-2} torr. A rough bound on the amount of xenon remaining in the receiver could be made by including the quantity frozen into the sodium plus whatever remained in the vapor space. The xenon solubility at the sodium freezing point is 2.3×10^{-5} (mole of xenon per mole of sodium per atm) (Reed and Droher, 1970) (Reed and Droher, 1970). Assuming a 1-ft^3 vapor space, the xenon pressure corresponding to 128 standard cm^3 at the sodium freezing point is 4.5 torr. The frozen-in xenon is thus 2.3×10^{-5} (mole of xenon per mole of sodium per atm) x 250 (moles of sodium) x 4.5 (torr) / 760 (torr/atm) = 3.4×10^{-5} moles, or $3.4 \times 10^{-5} \times 8.31 \times 10^{7} \times 300$ (K)/(1.01×10^{6}) = 0.9 standard cm^3. The xenon remaining in the vapor space is at most 128 (standard cm^3) x 2×10^{-2} (torr)/ 1.7 (torr) = 1.5 standard cm^3. A rough bound on the xenon remaining in the receiver is thus 2.4 standard cm^3.

The tests that followed (detailed in Appendix M) indicated that the hot restart problem remained cured even with this extremely small amount of xenon present. The xenon present is approximately 0.2% of that expected to solve the problem based on the solubility argument. This small amount of xenon had no apparent affect on the condenser heat transfer. May testing (Appendix M) indicated an elevation angle dependence for this solution method.

References

Proceedings of the Solar Stirling Heat Transport System Workshop, Lancaster, PA, September 27-28, 1989.

Reed, E. L., and J. J. Droher. 1970. *Solubility and Diffusivity of Inert Gases in Liquid Sodium, Potassium, and NaK.* LMEC-69-36. Canoga Park, CA: Atomics International.

Saaski, E. 1989. "Advanced Solar Conversion System (ASCS) Heat Transport System Working Group Meeting." Albuquerque, NM: Sandia National Laboratories.

APPENDIX O

X-RAY TESTING

APPENDIX O
X-RAY TESTING

The present x-ray tests are reported in full in Moreno et. al., 1991. The tests were motivated by the need to improve our understanding of the internal dynamics of the pool-boiler receiver. Specifically, we wanted to determine locations and frequencies of bubble formation on the absorber, departing bubble sizes, bubble rise velocities, paths followed by bubbles as they rise, and the resultant time-averaged void fraction distribution within the pool. The poor state of knowledge of boiling dynamics in liquid metals is well-documented by Dwyer (Dwyer, 1976). Dwyer reports only one x-ray study of boiling liquid metals (Bobrovich et. al., 1967). In that reference, bubble growth rates, departure diameters, and bubble rise velocities were observed in boiling potassium. The reported bubble diameters were nearly independent of pressure, in conflict with predictions presented by Dwyer and experimental results from ordinary liquids (Dwyer, 1976).

The present tests were conceived after the pool-boiler on-sun test was well underway. As a result, the x-ray views were limited by the existing physical arrangement. In particular, only observations normal to the receiver symmetry plane were attempted. Two different types of observations were made: (1) x-ray cinematography, and (2) path-averaged void-fraction measurements. The same x-ray source was used in both instances.

In the first case, the transmitted x-rays were observed using a fluorescent plate, a mirror, and a video camera mounted in a (nominally) light-tight box. The size of the box limited observations to an area near the pool surface roughly the size of a 45-degree right triangle with 3.5-inch legs (Figure O-1). Oscillations in the pool surface were clearly visible before the receiver was put on sun. However, once boiling began, the free surface was no longer discernable, and the video recording could only be interpreted as suggestive of chaotic motion. Attempts to extract quantitative information from the recording were not successful because of light leaks and "fogging." Rough estimates of void fraction obtained from this effort range from 33 to 46%.

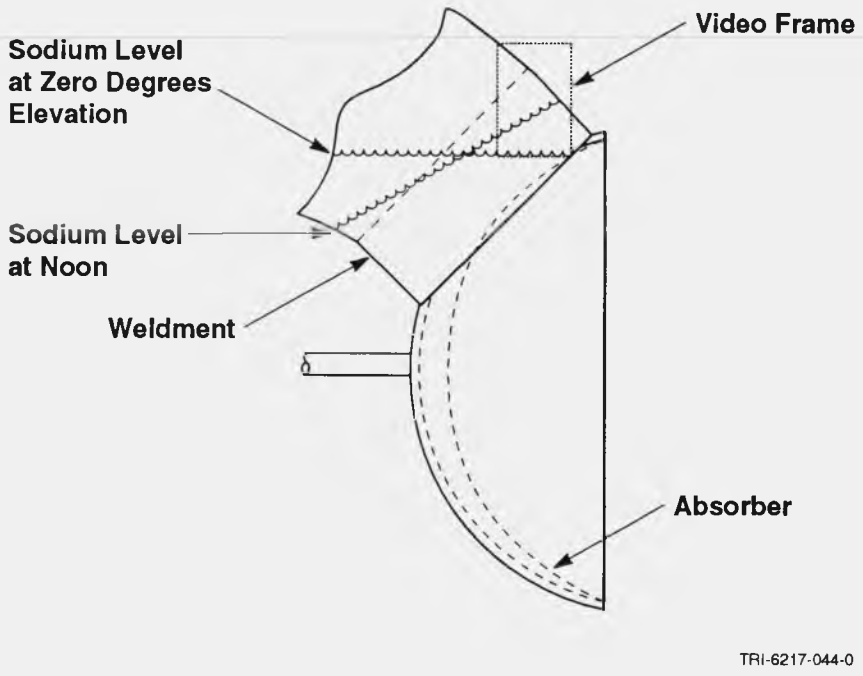

Figure O-1. Side view of pool-boiler receiver showing area viewed during x-ray cinematography, and sodium level at the time of the test (noon, December 21, 1989).

In the second case, we used an array of scintillator-crystal/photomultiplier-tube combinations to observe the transmitted x-rays. The size of the array permitted observations at eight locations between the front and aft domes (Figures O-2, O-3). Poor collimation of the detectors resulted in loss of all useful information on five of the eight detectors. On the remaining three detectors, the path-averaged and time-averaged void fraction was determined to be in the range of 60 to 80% when the receiver operating temperature was above 700°C. A void fraction this high brings into question the adequacy of the Kutataladze heat-transfer safety factor. Unfortunately, at this time we do not have an analytical model to make a connection between the measured void fraction and the Kutataladze safety factor. In our opinion, such a model should be developed as soon as possible. Also, additional x-ray studies should be carried out on the next-generation pool-boiler receiver, capitalizing on lessons learned on the first one.

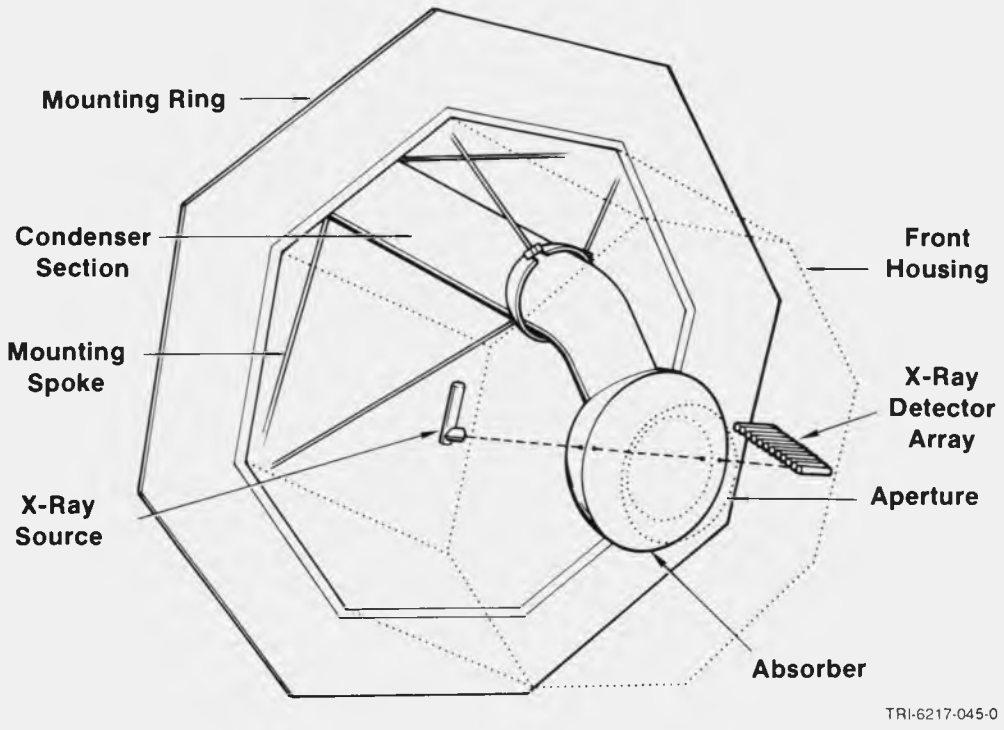

Figure O-2. Arrangement of x-ray source and detector array relative to the pool-boiler receiver.

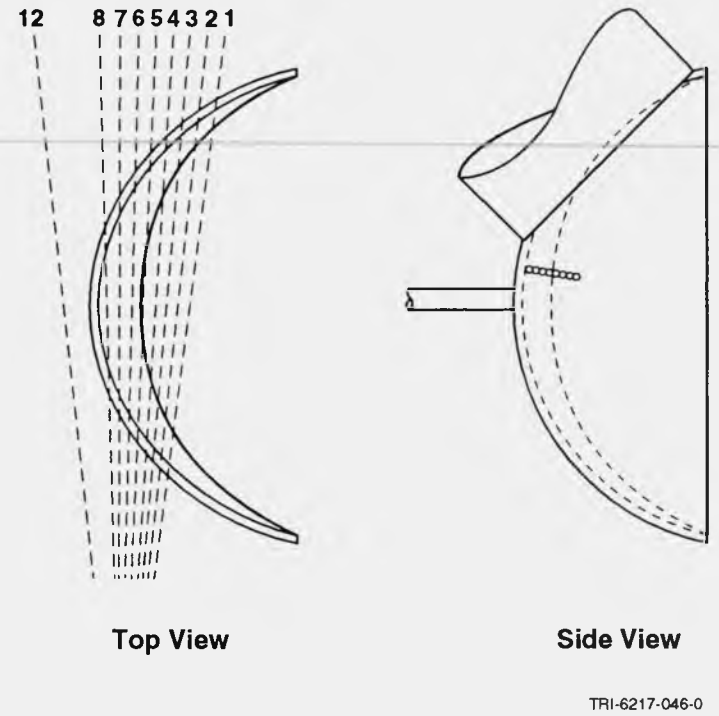

Figure O-3. Approximate locations of pool-boiler-receiver volumes probed by the x-ray detector array.

References

Bobrovich, G. I., B. P. Avksentyuk, and N. N. Mamontova. 1967. "On the Mechanisms of Boiling of Liquid Metals." *Proceedings of the Semi-International Symposium on Heat Transfer, Tokyo, September, 4-8, 1967.* p. 71.

Dwyer, O. E. 1976. Boiling Liquid-Metal Heat Transfer. Hinsdale, IL: American Nuclear Society.

Moreno, J. B., G. C. Stoker, and K. T. Thompson. 1991. *X-Ray Observations of Boiling Sodium in a Solar Reflux Pool-Boiler Receiver.* SAND91-1538. Albuquerque, NM: Sandia National Laboratories.

APPENDIX P

INFRARED THERMOGRAPHY

APPENDIX P
INFRARED THERMOGRAPHY

Infrared thermography of the reflux pool-boiler receiver was performed on May 18 and 22, 1990, to map the absorber temperature distribution (within the field of view limited by the aperture). In addition, we wanted to compare, in qualitative terms, the temperature distributions of reflux receivers with the temperature distributions of directly-illuminated tube receivers as observed by the Jet Propulsion Laboratory.

Instrumentation

An Inframetrics Model 525 infrared camera was used with a 3X telescope and 14- by 18-degrees field-of-view lens. The resulting field of view was therefore 4.7 degrees x 6 degrees. The camera senses radiation in the spectral range 8 to 12 μm, which is essentially free of solar radiation (reflection). Surface thermocouples on the receiver provided calibration for the camera. The infrared video signal was recorded on a VHS video cassette. The microphone mounted inside the receiver added boiling sounds to the May 22 video sound track. A date and time stamp synchronized with the facility data acquisition system was also added.

The camera was mounted on-axis with the concentrator on a unistrut beam cantilevered approximately 3 meters (m) (10 feet [ft]) from the dish vertex. The distance from the camera to the receiver was approximately 4.3 m (14 ft). In order to keep the camera tilt relatively level while the concentrator tracked the sun (to avoid spilling the liquid nitrogen that was used to keep the camera's HgCdTe detector cool), a flat, front-surfaced aluminized mirror mounted a few inches in front of the camera's lens was used to bias the tilt. With the dish axis horizontal, the camera pointed away from the receiver and upward at about a 30-degree angle. The video image was therefore reversed left-to-right.

For the infrared thermography test the receiver aperture was expanded to 0.26-m diameter (10.2 inches [in.]). This was the maximum allowed by the stainless steel conical side wall.

Because of the limited length of the remote-control cable for the camera, the camera operator (Mark Nissen, Sandia Division 7556) had to stand just behind the dish. The equipment was set on one of the main beams that form the TBC alidade.

Procedure

The test on May 18 served primarily as a shakedown. Since the primary test objective was to visualize temperature distributions during steady-state operation, the camera's operating range was set for measurements in the temperature range 700° to 800°C (500°C range). As expected, the resulting video, showed a uniform receiver absorber temperature when operating at elevated temperatures (>600°C). During startup, however, interesting temperature fluctuations, apparently associated with boiling, were observed.

On May 22, it was decided to set the camera on the 200°C range to better observe and record startup behavior. A microphone mounted inside the receiver added boiling sounds to the video sound track. A date and time stamp synchronized with the facility data acquisition system was also added. After the absorber surface temperature reached approximately 700°C, the camera was switched to the 500°C range. Following about 10 minutes of steady-state operation, the Test Bed Concentrator (TBC) was tracked off in each azimuth and elevation direction in turn. Shortly afterward, the shutter was closed, the dish was tracked off sun, the shutter was opened, and cool-down was recorded.

Steady-State Results

Steady-state operation, as discussed earlier, revealed a uniform temperature distribution across the observable part of the absorber surface. Figure P-1 shows a typical steady-state video image. In this photograph, the black and white image has been color-enhanced to better show temperature variations. The corresponding thermocouple readings are centered over their approximate locations on the figure. Comparisons of thermocouple readings with the infrared video are consistent for all steady-state and transients conditions. Relatively cool dark regions are apparent on the figure and in the colorized video. Their locations correspond to braze stop-off marks on the absorber which were left when the front surface absorber thermocouples were attached. They appear cooler because they have a lower emissivity than the surrounding oxidized 316L stainless steel. The track-off tests revealed no unexpected results.

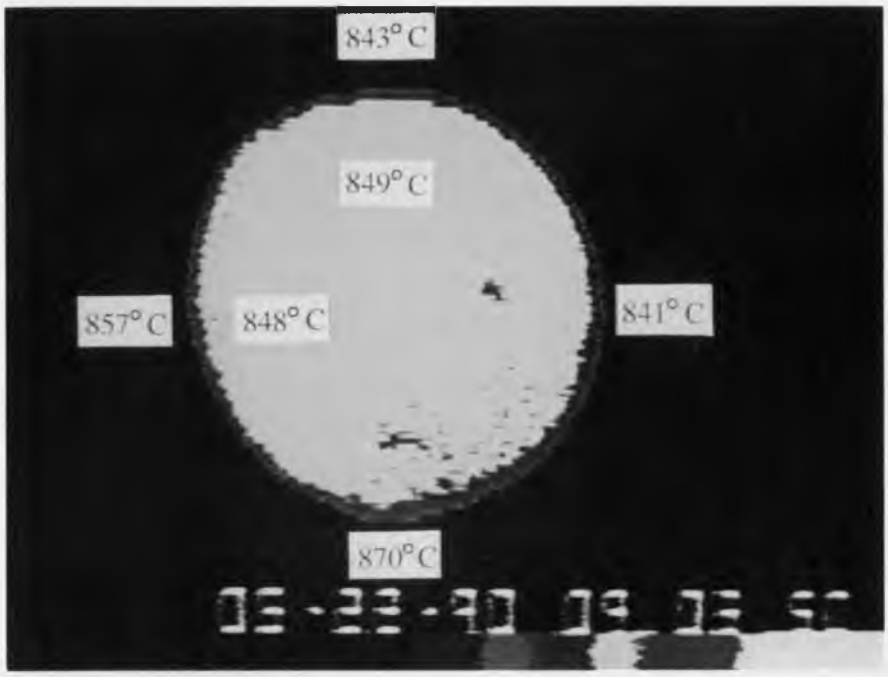

Figure P-1. Typical steady-state infrared video image of the Sandia pool-boiler receiver. The aperture restricted the field-of-view to 10.2 inches. The image is a reversed left-to-right (by the mirror) view of what an observer, standing at the concentrator and looking at the receiver, sees. Functioning absorber thermocouple readings in their approximate locations are shown on the figure. Each change in color represents approximately 50°C.

For comparison to directly-illuminated tube receivers, Figure P-2 shows a colorized infrared video image of a United Stirling receiver taken with an Inframetrics 525 and 3X telescope during November 1982 on a TBC at the Edwards Air Force Base test site (Nelving, 1983). Measured temperature variations along tubes were typically about 150°C, temperature variations between the four heater-head quadrants were typically 50° to 100°C (Livingston, 1985).

Quantitative analysis of the steady-state video images was conducted to see whether boiling sites could be detected in the video images. Over a 1.86-second (s) period of steady-state boiling, 56 consecutive video images (video frames are taken every 1/30th s) were subtracted from the average of the 56 images. The image of the sum of the absolute value of the 56 differences did not reveal a pattern. Calculations suggest that temperature fluctuations caused by boiling at the nucleation sites should be on the order of 1°C or less (air-side surface). Because the thermal resolution of the camera was about 3.1°C, and the spatial resolution of the camera was limited to about 0.7 cm (0.3 in.), it was not surprising that temperature fluctuations of less than 1°C at the artificial cavity nucleation sites were not revealed with this analysis.

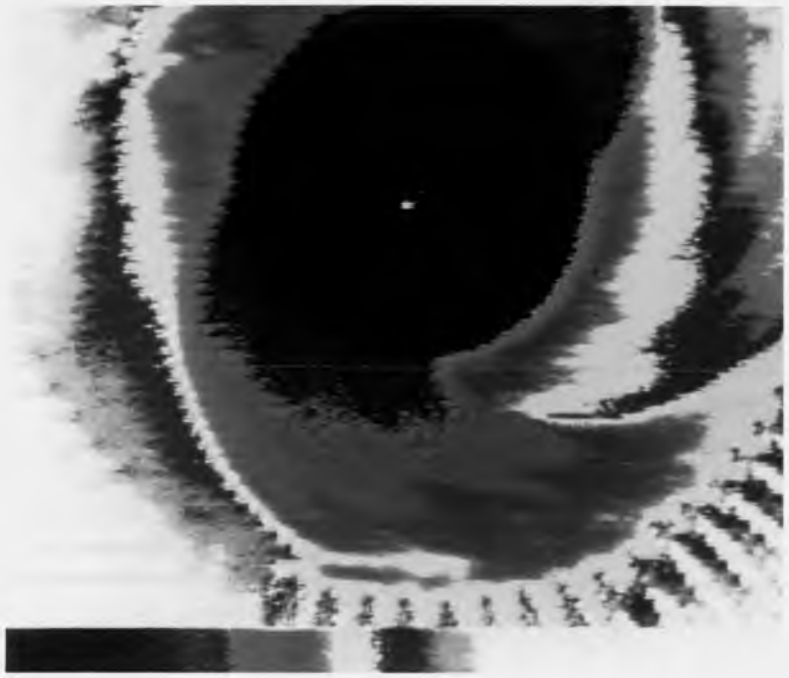

Figure P-2. Infrared video image of a United Stirling receiver taken during November 1982.

Startup Results

The most interesting pool-boiler data occurred during start-up. For the May 22 test, the receiver was preheated to approximately 200°C before going on-sun. During the first minute, before boiling initiated, receiver operation was characterized by conduction and natural convection heat transfer to the sodium. As might be expected during this relatively quiescent period, the temperature distribution observed on the absorber was proportional to the flux distribution incident on it. Figure P-3 (the temperature distributions 15 s into startup) shows the high flux inner ring predicted by CIRCE2 (see Figure G-4, Appendix G of this report). Figure P-3 indicates that there was a slight mistrack in azimuth. The high flux/temperature inner ring was shifted to the left in the photograph (the image was reversed by the mirror), and the intensity was reduced on the left-hand side. Good qualitative agreement between the CIRCE2 prediction and the infrared video was obtained by introducing a 3-mrd azimuth pointing error in the CIRCE2 simulation. This tracking error also placed high flux in the vicinity of the receiver's eventual point of failure.

Figure P-3. Infrared video image taken 15 seconds after startup. The high flux inner ring predicted by CIRCE2 appears to be offset to the left indicating a 3 milliradian concentrator mistrack. The image is a reversed left-to-right (by the mirror) view of what an observer, standing at the concentrator and looking at the receiver, sees.

After approximately one minute of testing, audible indications of boiling were observed and, significant temperature fluctuations were evident in the infrared video and the thermocouple data. In general, these temperature fluctuations were characterized by relatively cool salients moving from the top of the receiver towards the center (see Figure P-4). In the thermocouple data, this transition to boiling is characterized by temperature swings with decreases of 30° to 40°C between measurements (Figure P-5). Thermocouple data was taken every 15 s. The video suggests that this was a result of relatively cool liquid sodium refluxing from the condenser to the top of the absorber. Another explanation is that the top of the absorber may have become depleted of sodium (due to vapor entrainment) and that cooling resulted from the relatively high heat transfer rates associated with evaporation on a thin liquid film on the back of the absorber. No evidence of excessively high absorber temperatures is detectable in the video, however.

At the same time as boiling began, the hottest side of the receiver shifted from the right side to the left side of the image, Figure P-4. Visually there was an indication that the internal flow, driven by the vapor, was biased to the left. This observation was consistent with the apparent shift in flux distribution caused by azimuth mistracking. The left side of the receiver remained hotter for the duration of the startup. The temperature difference eventually became imperceptible when the receiver approached operating temperature.

During the early stages of boiling, because the receiver was relatively cool and the vapor density was relatively low, the receiver was closest to the critical heat flux and flooding limits. The rapid increase and shift in temperature associated with boiling that are seen in the infrared video suggest that the receiver may have been in the "transition" boiling region.

Dwyer describes transition boiling as follows:

"In this regime, the heating surface is essentially blanketed with vapor, but because of Taylor instability, the liquid-vapor interface is ruptured (periodically in time and uniformly in space) to release slugs of vapor and admit spikes of liquid. The liquid spikes are generally believed to make transient contact with the heating surface" (Dwyer, 1976).

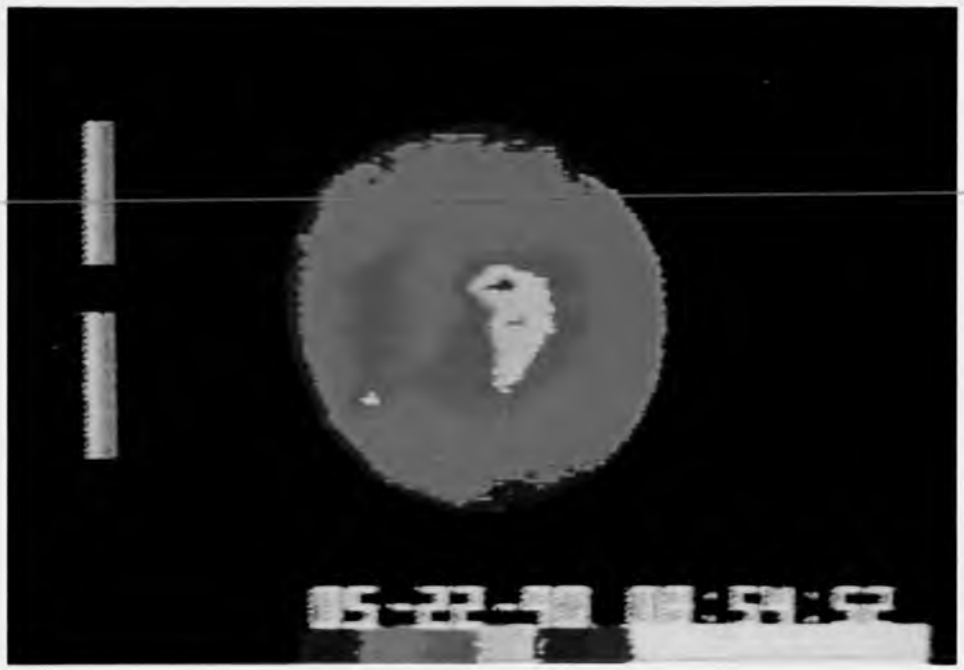

Figure P-4. Infrared video image taken seconds after boiling began. Both a relatively cool salient from the top of the receiver and the temperature shift (the left side of the image is now the hottest) can be seen in the figure. The thermocouple temperature readings in their approximate locations are shown on the figure and are in agreement with the infrared camera.

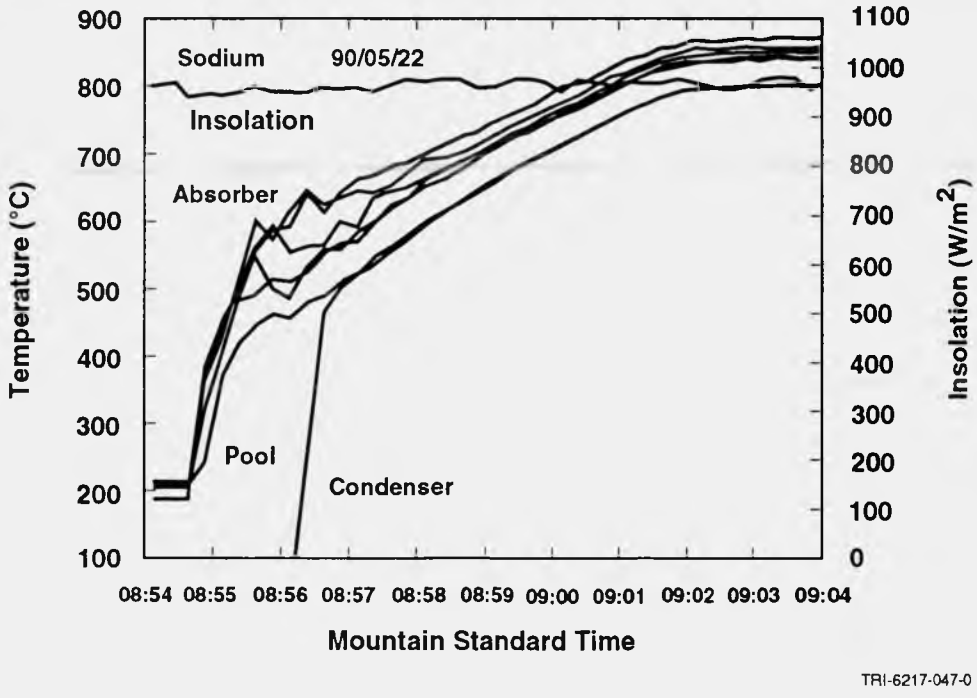

Figure P-5. Thermocouple startup data for May 22, 1990.

Unfortunately speculation about operation in the transition boiling regime during these tests cannot be proven with the data available. In addition, this test was not a controlled boiling experiment. Pressure gradually increased as the system heated, and the geometry was nonconventional. However, observations with the infrared camera were consistent with the qualitative discussions of transition boiling in Dwyer. If correct, they suggest that for the temperature at which boiling began in these tests (450° to 500°C), the receiver was near the film boiling or flooding limit.

Conclusions and Recommendations

1. During steady-state operation, the pool-boiler absorber temperature distribution was very uniform. Temperature variations were significantly less severe than previously observed in the United Stirling directly-illuminated tube receiver.

2. Temperature fluctuations associated with boiling at the artificial cavity nucleation sites could not be detected—even with a statistical analysis. This result was expected because temperature fluctuations associated with boiling should be too small to be detected with the limited thermal and spatial resolution of this infrared camera.

3. The absorber temperature distribution observed during startup (before boiling was initiated) was a good qualitative match to the CIRCE2-predicted flux distribution and suggested that the concentrator was mistracked. By assuming a 3mrd azimuth mistrack to match the infrared camera temperature distribution, we can place the location of a relative flux "hot spot" in the vicinity of the receiver failure.

4. Subsequent to boiling initiation, relatively cool salients were observed extending from the top of the receiver. The salients were probably associated with cool liquid refluxing from the condenser.

5. Subsequent to boiling initiation, the hottest part of the absorber shifted from the right side to the left side of the image. The infrared video suggested that vapor flow was biased to the left (consistent with the mistrack observation) and that operation during the early phase of boiling may have been near the flooding and/or film boiling limit.

6. Comparisons of thermocouple and infrared camera temperature measurements were consistent. Combined, they provide a comprehensive absorber temperature profile. The visualization of temperature distributions made possible by the infrared camera facilitates the interpretation of test results.

7. Future receiver tests should make use of infrared camera diagnostics, at least during the early stages of testing. The standard test plan should incorporate the expansion of the receiver aperture to increase the viewable area of the receiver. Development of a dedicated infrared camera with improved thermal and spatial resolution is recommended.

References

Dwyer, O. E. 1976. *Boiling Liquid-Metal Heat Transfer*. Hinsdale, IL: American Nuclear Society.

Livingston, F. R. 1985. *Activities and Accomplishments in Dish/Stirling Electric Power System Development*. DOE/JPL-1060-82. Pasadena, CA: Jet Propulsion Laboratory.

Nelving, H. G. 1983. "Testing of the United Stirling 4-95 Solar Stirling Engine on Test Bed Concentrator." *Proceedings of the Fifth Parabolic Dish Solar Thermal Power Program Annual Review, Indian Wells, CA, December 6-8, 1983*. DOE/JPL-1060-69. Pasadena, CA: Jet Propulsion Laboratory.

APPENDIX Q

PERFORMANCE MEASUREMENT

APPENDIX Q
PERFORMANCE MEASUREMENT

Reflux pool-boiler and heat-pipe solar receivers promise to be more efficient than directly-illuminated tube receivers that have previously been used in dish-Stirling systems. Compared to tube receivers, the reflux receiver has extremely high heat-transfer coefficients, has a high-flux capability, operates nearly isothermally, has minimal heat transfer area for convection loss, and permits designs with no direct incident flux on uncooled surfaces. The thermal performance of reflux receivers is being analyzed both experimentally and analytically to (1) assess performance, (2) to help make development and design trade-offs, and (3) to support systems analysis.

Receiver Heat Loss and Efficiency Measurements

The Sandia reflux pool-boiler receiver provided an opportunity to assess reflux receiver performance in a controlled experiment. Unlike other dish receivers, which have only been evaluated as part of a system, the Sandia pool-boiler receiver was designed to operate with a gas-gap cold-water calorimeter (CWC). Because the gas-gap CWC's instrumentation was identical to the CWC used to characterize the Test Bed Concentrator #1 (TBC-1), relatively accurate measurement of receiver heat loss and efficiency was feasible. Measured heat loss was determined by subtracting the power delivered by the receiver to the gas-gap CWC from the power provided by TBC-1 to a CWC with the same size aperture.

TBC-1 was characterized with a CWC between July 12 and August 3, 1989 (Rawlinson and Dudley, 1990). Measurements were made with the concentrator in various states of cleanliness and at low (1/2 power), intermediate (3/4 power), and full power. Normalized power delivered by TBC-1 through a 22-centimeter (cm) (8.7-inch [in.-]) diameter aperture ranged from 64.1 kW_t with dirty mirrors, about 65.0 kW_t with "intermediate" dirty mirrors, to 66.6 kW_t with clean mirrors. Opening the calorimeter aperture to 0.60 meters (m) (24 in.) increased input normalized power by only 0.3 kW. The stated accuracy of the Delta-T Company differential temperature transducer was 0.04°C, resulting in better than 1% accuracy for typical ΔTs of over 10°C. The accuracy of the Flow Technology Company turbine flow meter and Epply direct-normal-insolation pyrheliometer were each better than 1%. Periodic checks of the turbine flow meter's calibration during operation with a bucket, scale, and stop-watch confirmed the reported flow-meter accuracy. The overall power measurement accuracy was determined to be about 0.8 kW_t (Rawlinson and Dudley, 1990).

Unfortunately, as a result of the receiver failure, the pool-boiler receiver was not completely characterized for performance as outlined in the "Standard Reflux Receiver Test and Instrumentation Plan" (Appendix J of this report). In fact, the failure occurred during an early performance assessment test (Stage II). Although some of the early Stage I test results could have been used to assess thermal performance, there was significant uncertainty about the accuracy of the turbine flow meter. The bucket, scale, and stop-watch technique was not used to check the flow meter's calibration until November 15, 1989. In that check, the flow meter was found to be in error by about 4%.

The performance results presented in Table Q-1 are for conditions in which the receiver had been operated for at least one hour (to minimize the effect on results of start-up transient heating) and in which the receiver had generally operated stably for a period of at least 10 minutes (min). Each of the entries represents the average of 25 measurements over a 6-min period. The 13:04, May 9, 1990 condition was an exception. That entry was the mean of 18 data points over a 4-min period.

Estimating the level of mirror cleanliness was a source of input power uncertainty. Based on visual observations of mirror cleanliness, input power was estimated to be 64.4 kW_t normalized to 1-kW/m^2 direct normal insolation for the results in Table Q-1. Mirrors were not washed after August 2, 1989. For the 1989 data, the estimated uncertainty in normalized input power caused by mirror cleanliness was 0.6 kW_t. The root-sum-square method uncertainty in receiver input power was therefore about 1 kW_t. (1 $kW_t = (0.8^2 + 0.6^2)^{0.5}$, where 0.8 was the measurement uncertainty from the TBC-1 calorimetry (Rawlinson and Dudley, 1990). For the May 1990 results, input power uncertainty was assumed to increase to about 1.2 kW_t because of the additional time period following TBC calorimetry.

The "all day" test of October 19, 1989, using the November 15, 1989 calibration, provides four of the performance measurements presented in Table Q-1. Because of the flow measurement uncertainty in this data, the receiver output power uncertainty was estimated to be about 3.0 kW_t. Data taken during the period in which flow was calibrated on November 15, 1989 provided the most accurate heat-loss measurements. Heat loss during this period was just less than

TABLE Q-1. SANDIA POOL BOILER RECEIVER PERFORMANCE SUMMARY

Date (mm/dd/yy)	Time (MST)	Vapor Temp (Deg. C)	Aper. Diam. (m)	Input Power (kW)	Uncer. + or - (kW)	Output Power (kW)	Uncer. + or - (kW)	Heat Loss (kW)	Uncer. + or - (kW)	Wind Speed (m/s)	Elev. Angle (Deg.)	AEETES Heat Loss (kW)
10/19/89	10:03	800.9	0.22	65.4	1.0	56.5	3.0	8.8	3.2	1.5	38.1	6.9
10/19/89	12:03	801.0	0.22	66.9	1.0	58.7	3.0	8.2	3.2	1.6	44.8	6.4
10/19/89	14:03	800.9	0.22	65.1	1.0	58.1	3.0	7.0	3.2	1.8	35.1	7.0
10/19/89	16:33	800.5	0.22	44.8	1.0	38.8	3.0	6.0	3.2	1.0	9.8	7.4
11/15/89	14:23	800.6	0.22	63.1	1.0	53.2	1.0	9.9	1.4	5.2	25.4	7.5
11/15/89	14:30	800.4	0.22	62.5	1.0	52.6	1.0	9.9	1.4	6.0	24.5	7.5
05/09/90	12:03	800.7	0.26	68.5	1.2	61.0	1.2	7.5	1.7	4.1	72.5	6.9
05/09/90	12:20	750.4	0.26	68.5	1.2	62.2	1.2	6.3	1.7	5.6	72.0	6.2
05/15/90	13:04	800.7	0.26	66.9	1.2	60.2	1.2	6.7	1.7	3.3	67.7	7.0
05/15/90	08:23	800.7	0.26	60.5	1.2	51.9	1.2	8.6	1.7	7.5	39.2	8.2
05/15/90	09:03	800.1	0.26	62.7	1.2	54.7	1.2	8.0	1.7	7.7	47.3	7.8
05/15/90	09:56	800.6	0.26	64.1	1.2	56.0	1.2	8.1	1.7	1.5	57.8	7.2
05/18/90	09:07	799.7	0.26	60.3	1.2	52.2	1.0	8.1	1.6	2.3	48.5	7.6
05/18/90	09:24	800.7	0.26	61.2	1.2	53.0	1.0	8.2	1.6	4.0	51.9	7.4
05/23/90	09:06	800.4	0.26	61.4	1.2	51.9	1.2	9.5	1.7	3.7	48.7	7.5
05/23/90	09:20	800.5	0.26	57.0	1.2	47.7	1.2	9.3	1.7	3.1	51.5	7.2
05/23/90	10:23	800.7	0.26	63.4	1.2	55.0	1.2	8.4	1.7	2.1	63.8	6.9
05/23/90	10:37	800.7	0.26	65.7	1.2	57.3	1.2	8.4	1.7	2.9	66.3	7.0
05/23/90	11:03	800.7	0.26	59.8	1.2	51.6	1.2	8.2	1.7	7.0	70.5	6.6
					Average Heat Loss			8.16				7.17

10 kW_t. The low elevation angle (about 25°) and the high wind speed (over 5 m/second) probably contributed to the relatively high heat loss.

Tests in May of 1990, just prior to the receiver failure, provided additional performance data. In these tests a factory calibrated flow meter placed on the inlet line assured accurate and reliable water flow measurement. The aperture was opened to a 26-cm (10.2-in.) diameter. Despite the enlarged aperture diameter for these runs, heat loss was measured to be less than on November 15, 1989—probably because of the higher elevation angles and therefore lower convection loss. During the May 18 testing the inlet flow meter was calibrated with the bucket, scale, and stopwatch technique. All of the May performance test results were based on the May 18 calibration.

Numerical Model Predictions

Previous comparisons of the corrected pool-boiler receiver performance measurements for October 19, 1989 with a new reflux-receiver thermal performance numerical model, recently named AEETES (in Greek mythology Aeetes was the brother of Circe), indicated good receiver thermal performance, excellent agreement with a three-dimensional thermal model, and general agreement with measurements (Hogan, 1991). The results presented in Table Q-1 and plotted in Figure Q-1 also indicate reasonable agreement between measured and AEETES predicted heat loss. The Stine convection correlation was used in the simulations (Stine and McDonald, 1989). Discussion of the model and the assumptions used in the simulations can be found in Hogan (1991) and in Table R-1 in Appendix R of this report. Measured input power, condenser temperature, sun angle, and ambient temperature were used as inputs to AEETES. Increased convection loss caused by winds not accounted for in the convection correlation, AEETES's tendency to underpredict conduction loss (it uses a one-dimensional thermal resistance approach of just the side wall to calculate conduction loss), and possible degradation of TBC-1 during the winter of 1989-1990 are possible reasons for the higher measured heat losses.

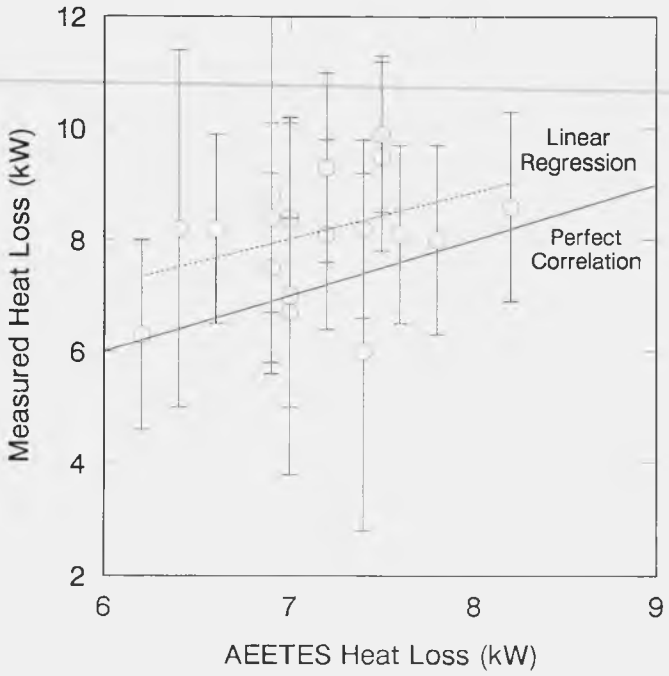

Figure Q-1. Comparison of AEETES-predicted heat loss with measurements.

Conclusions

Based on the results presented here, the high-performance potential of reflux receivers appears to be confirmed. The heat loss measurements of about 8 kW_t compare very favorably with the 7.4 kW_t heat loss estimated by Advanco (Washom, 1984). Accounting for the higher operating temperature (800°C versus 750°C) and the larger aperture diameters (22 and 26 cm [8.7 and 10.2 in.] versus 20 cm [7.8 in.]), the Sandia pool-boiler receiver performance was clearly at least comparable to the United-Stirling directly illuminated tube receivers used by Advanco and McDonnell Douglas. The Sandia pool-boiler receiver was also not an optimized design. Based on AEETES simulations it is reasonable to expect improved performance with better optical materials (See Appendix R).

The calorimetry procedures used to characterize the Sandia pool-boiler receiver's performance provided the most accurate assessment of dish-receiver performance to date. Accurate measurement devices for differential temperature, water flow, and solar insolation and consistent measurements with identical instruments of concentrator and receiver performance were key to accurate heat-loss measurements. Frequent calibration of the flow meter would have improved the measurement uncertainty. Calorimetry of TBC-1 following performance testing had been planned and would have further reduced heat-loss measurement uncertainty. Unfortunately, damage to the concentrator resulting from the receiver failure eliminated the benefit of follow-up calorimetry.

The recently developed reflux receiver thermal analysis model, AEETES, appears to reasonably predict performance. Differences between measurements and model predictions appear to be caused by increased cavity convection caused by the wind. Other possible contributions to the apparent discrepancy are an underprediction of cavity conduction loss and concentrator degradation during the winter.

References

Hogan, R. E., Jr. 1991. "Numerical Modeling of Dish-Stirling Reflux Solar Receivers." *Proceedings of the 13th Annual ASME Solar Energy Conference, Reno, NV, April, 1991.*

Rawlinson, K. S., and V. Dudley. 1990. *Test Bed Concentrator #1 Calorimetry Results.* SAND89-2840. Albuquerque, NM: Sandia National Laboratories.

Stine, W. B., and C. G. McDonald. 1989. "Cavity Receiver Convection Heat Loss." *Proceedings of the International Solar Energy Society, Solar World Congress 1989 Kobe. Kobe, Japan.*

Washom, B. J., 1984. *Vanguard I Solar Parabolic Dish-Stirling Engine Module Final Report.* DOE-AL-16333-2 (84-ADV-5).

APPENDIX R

PERFORMANCE ANALYSIS

APPENDIX R
PERFORMANCE ANALYSIS

The performance of solar receivers is dependent on a number of factors. In Table R-1 the variables that affect the performance of reflux receivers are categorized and listed. In general, receiver performance is a function of (1) receiver geometry, (2) receiver materials properties, (3) environmental parameters, and (4) system parameters, i.e., variables that are dictated by other components and/or system considerations.

The parameters used to characterize receiver performance are receiver efficiency (η_r) and heat loss (Q_ℓ). Receiver efficiency is a function of heat loss and input power (Q_i). Input power is defined here as the power delivered by the concentrator through the aperture. Output power (Q_o) is the power delivered to the engine.

$$\eta_r = \frac{Q_i - Q_\ell}{Q_i} = \frac{Q_o}{Q_i}$$

Because heat loss (Q_ℓ) is much less dependent on input power (Q_i) than receiver efficiency (η_r), it is the most useful performance parameter.

Heat losses from solar receivers are comprised of (1) solar energy reflected from the receiver (reflection loss), (2) infrared radiation emitted from the receiver (reradiation), (3) energy conducted through the insulation (conduction), and (4) energy convected from the receiver (convection). Of these, convection is the most difficult to predict.

TABLE R-1. REFLUX RECEIVER THERMAL PERFORMANCE PARAMETERS

RECEIVER GEOMETRY	OST Pool Boiler	Next Gen. Pool Boiler	Range Analyzed
Receiver Diameter (m)	0.414	0.458	0.356 to 0.610
Sphere Angle (degrees)	70	70	70
Side-Wall Angle (degrees)	45	45	52 to 35
Absorber Thickness (mm)	0.813	0.889	0.813 & 0.889
Insulation Thickness (cm)	15.24	15.24	15.24
RECEIVER MATERIALS	316L SS	Haynes 230	
Working Fluid h (W/m^2-K)	1×10^8	1×10^8	1×10^8
Absorber Conductivity (W/m-K)	24.5	24.4	24.5 & 24.4
Absorber Absorptance	0.87	0.91	0.87 to 0.95
Absorber Emittance	0.85	0.85	0.85
Side-Wall Absorptance	0.87	0.15	0.15 to 0.91
Side-Wall Emittance	0.85	0.8	0.8 to 0.85
Insulation Conductivity (W/m-K)	0.4	0.4	0.4
ENVIRONMENTAL PARAMETERS	Stine Convection	Stine Convection	
Ambient Temperature (K)	287	287	287
Sun Elevation Angle (degrees)	45	45	0 to 90
Wind Speed (mph)	0	0	0
Wind Direction	—	—	—
SYSTEM PARAMETERS			
Temperature (°C)	800	750	650 to 850
Flux Distribution	TBC-1	TBC-1	Several
Aperture Size (m)	0.22	0.22	0.18 to 0.36
Input Power (kW)	70	70	70

Numerical models have been developed at Sandia to evaluate the thermal performance of reflux receivers (Hogan et al., 1990; Hogan, 1991). A finite-control-volume (FCV) model was developed and used to evaluate thermal performance and potential weld overheating of the Sandia pool-boiler receiver (See Appendix G of this report). A simpler and easier-to-use thermal-resistance (TR) model was also developed to simulate reflux receiver performance and to make parametric studies.

The TR model, recently named AEETES (in Greek mythology Aeetes was the brother of Circe), has been used to explore the performance implications of some of the variables in Table R-1. The details of AEETES are presented in (Hogan, 1991 in the TR Model sections). The current AEETES model calculates surface temperature distributions and heat loss of axisymmetrical cavity receivers. Surface elements are specified as annular ring-shaped elements which form basic geometric shapes, e.g., conics, cylinders, spheres, and disks (consistent with CIRCE2). The analysis is therefore one-dimensional axisymmetric. Input incident flux from CIRCE2 is averaged over the azimuthal dimension to produce a one-dimensional radial distribution. Multiple reflection of the solar flux and reflection and reradiation of infrared (IR) energy between the ring shaped elements is taken into account. Surfaces are assumed to be diffuse and gray with separate solar and IR radiation properties. The aperture is treated as a black surface with a temperature 6°C less than ambient.

One-dimensional heat conduction models are used to calculate conduction heat loss (through the cavity side walls) and heat delivered to the sodium (through the absorber). Depending on the geometry, the one-dimensional conduction equation for each surface element is either cylindrical or planar. Cavity convection coefficients for each surface can be arbitrarily specified or determined from correlations. The correlation recommended by Stine (Stine and McDonald, 1989), which accounts for cavity geometry, aperture diameter, cavity and ambient temperatures, and sun-elevation angle was used for these analyses. Energy balance equations on each element are used to iteratively solve for the surface temperature distribution. An iteration conversion criterion of 0.001°C change per iteration was used.

Figure R-1 shows the temperature distribution and summarizes the efficiency and heat losses of the Sandia pool-boiler receiver used in the design point calculation and predicted by AEETES. Input parameters to AEETES are listed in Table R-1. The 16 side-wall and 40 absorber ring elements used in the calculations are evident in the figure.

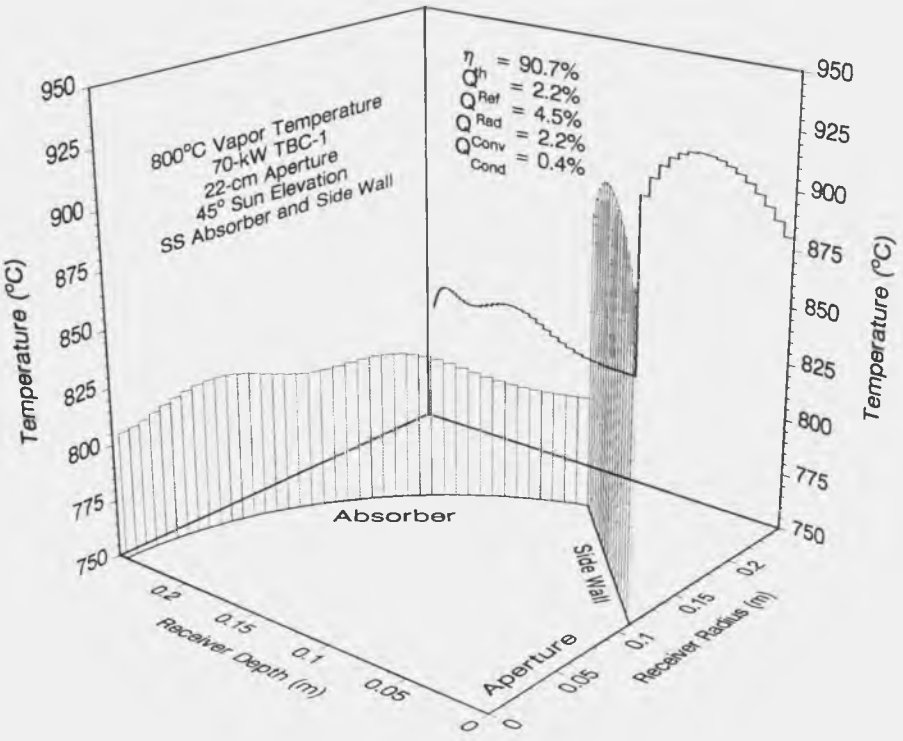

Figure R-1. Sandia pool-boiler receiver design point temperature distribution and performance prediction.

Insulation geometries for all of the analyses were assumed to be cylindrical on the outside diameter (surrounding the side wall), with a minimum thickness of 15.24 centimeters (cm) (6 inches [in.]) at the intersection of the absorber and side wall. The convection coefficient from the insulation housing to the surrounding air was assumed to be 20 watts per square meter per degrees K (W/m^2-K). The insulation conductivity was assumed to be 0.4 W/m-K. This value is approximately four times higher than published values to account for heat loss axially through the insulation adjacent to the aperture and heat loss though insulation surrounding the aft dome, and to better account for radiation heat transfer through the insulation. Conduction heat loss results (253 W in this case) should therefore be considered approximations. These test results and more rigorous analyses agreed that conduction is a relatively small loss component. By comparison the FCV model predicts conduction heat loss to be about 325 W for this condition.

Convection from the absorber to the sodium was assumed to be high (1×10^8 W/m^2-K), essentially forcing the sodium-side absorber temperature to be equal to the sodium vapor temperature. In actuality, wall superheats on the order of 10°C might be expected, but were not accounted for in these analyses. The absorber temperature distribution predicted by AEETES matched the one-dimensional CIRCE2 incident solar flux distribution. Side-wall temperatures of approximately 900°C agreed with the experimental data.

The total receiver heat loss for the design condition depicted in Figure R-1 is 6510 W. Radiation (3180 W) is the largest source. Cavity reflection (1530 W) and convection (1550 W) losses are also substantial. Comparison of AEETES results with experimental data (see Appendix Q of this report) show good general agreement, but a tendency for AEETES to underpredict heat loss. Convection losses higher than predicted by the Stine correlation, caused by wind effects, and possibly higher conduction losses were probable reasons for the differences.

Figures R-2 through R-9 show the results of parametric studies around the design point of some of the more important performance parameters. In general, the studies show that the parameters with the greatest effect on performance, e.g., sun elevation angle (Figure R-6), receiver temperature (Figure R-7), and aperture diameter (Figure R-9), are not within the control of the receiver designer. At the same time, the results suggest that the designer has substantial freedom to vary side-wall geometry and absorber size to minimize incident peak flux intensities without seriously affecting performance (Figures R-2 and R-3). The flux distribution on the absorber also had virtually no effect on heat loss (Figure R-8).

Figure R-4 shows that increasing the absorber solar absorptivity from 0.87 (measured value for the 316L stainless steel Sandia pool-boiler receiver) to 0.91 (measured value for oxidized Haynes 230) reduces overall heat loss by about 670 W. A high solar absorptivity paint could potentially reduce heat loss by about 1340 W. Even if the paint increases the thermal resistance of the absorber, performance improvements can be obtained. For example, the increased thermal resistance point on Figure 4 is based on a paint thickness of .00254 cm (0.001 in.) and a thermal resistance of 0.4 W/m^2-K. Even though the paint increases the area-weighted average absorber temperature by about 20°C, overall heat loss is reduced by about 1100 W compared with the design condition.

AEETES indicates that the use of a white side-wall material, such as an alumina-silica ceramic ($a_{solar} = 0.15$, $e_{ir} = 0.8$), instead of the 316L stainless steel side wall in the current design can reduce heat loss slightly (150 W). Perhaps more importantly, side-wall temperatures can be substantially reduced and construction simplified.

The AEETES predicted temperature distribution and performance summary for the next generation design is presented in Figure R-10. Because the receiver operates at a lower temperature and is constructed from Haynes 230, reradiation and convection losses are reduced. The white side-wall temperatures are also lower.

Conclusions

Thermal performance models have been developed at Sandia to assess the performance of reflux receivers and to quantify design tradeoffs. Results from a relatively simple thermal-resistance model, AEETES, have been found to compare well with a more sophisticated model and to agree reasonably well with measurements.

Parametric studies around the Sandia pool-boiler receiver design indicate that the parameters with the most impact on receiver performance are generally out of the control of the receiver designer. On the other hand, the receiver designer has freedom to alter absorber and cavity side-wall geometry and size in order to reduce peak incident solar flux without seriously affecting performance. AEETES and CIRCE2 quantify these design tradeoffs.

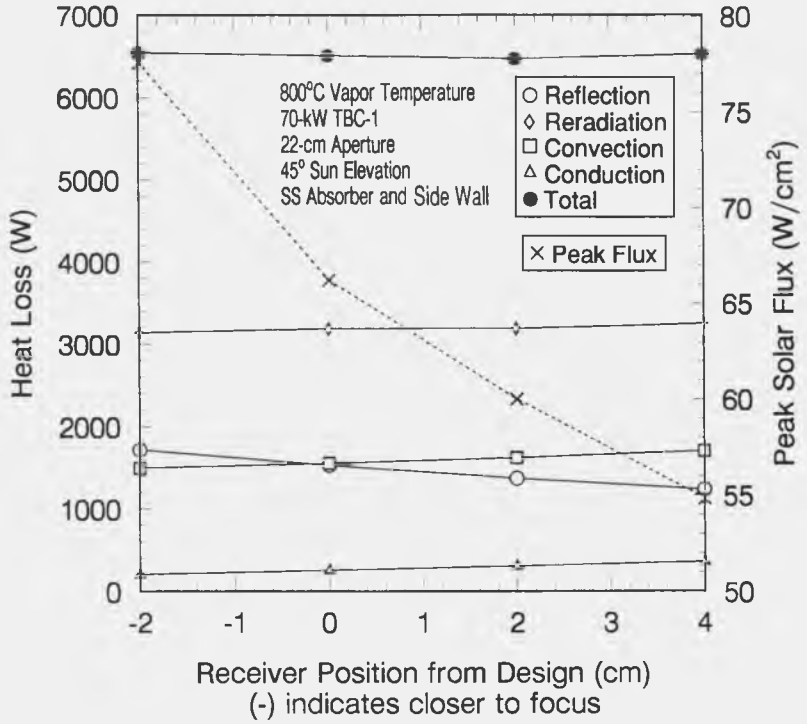

Figure R-2. Receiver heat loss and peak incident solar flux as a function of spherical absorber position.

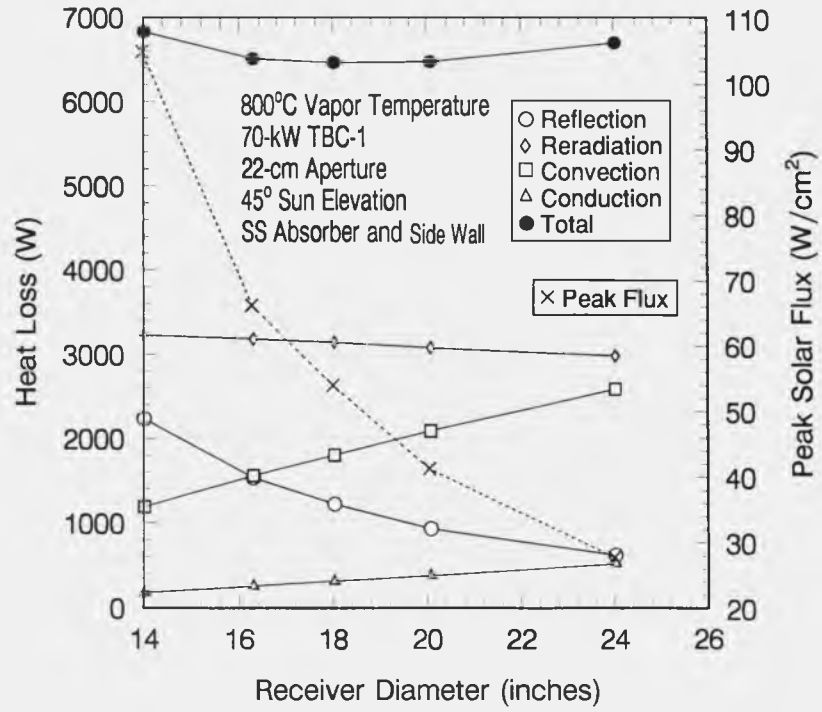

Figure R-3. Receiver heat loss and peak incident solar flux as a function of absorber diameter.

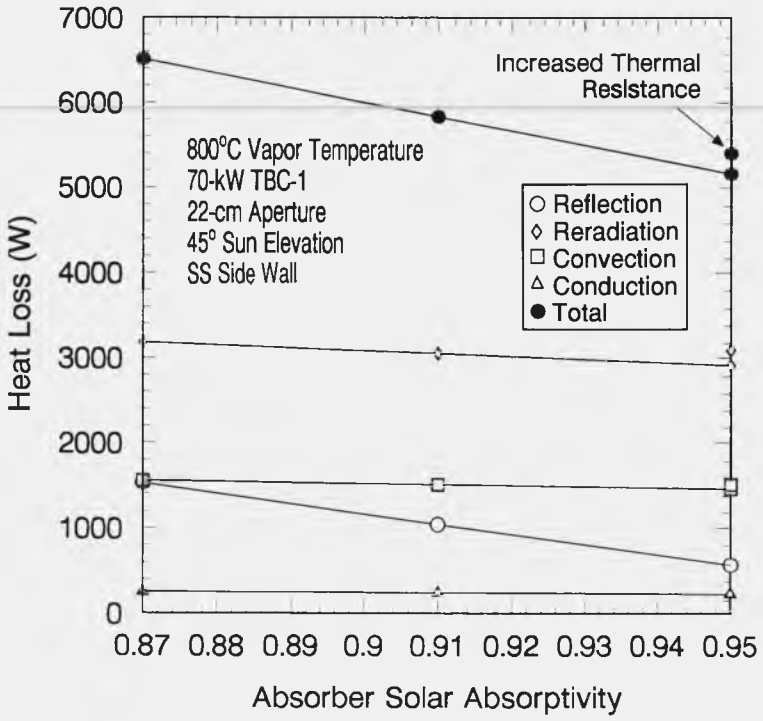

Figure R-4. Receiver heat loss as a function of absorber solar absorptivity.

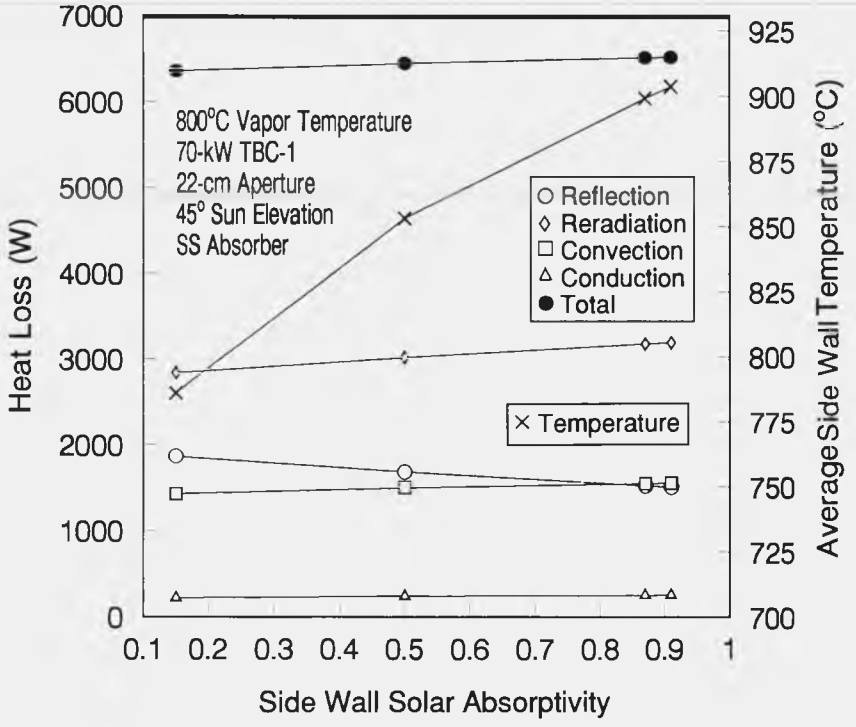

Figure R-5. Receiver heat loss and average side-wall temperature as a function of side-wall solar absorptivity.

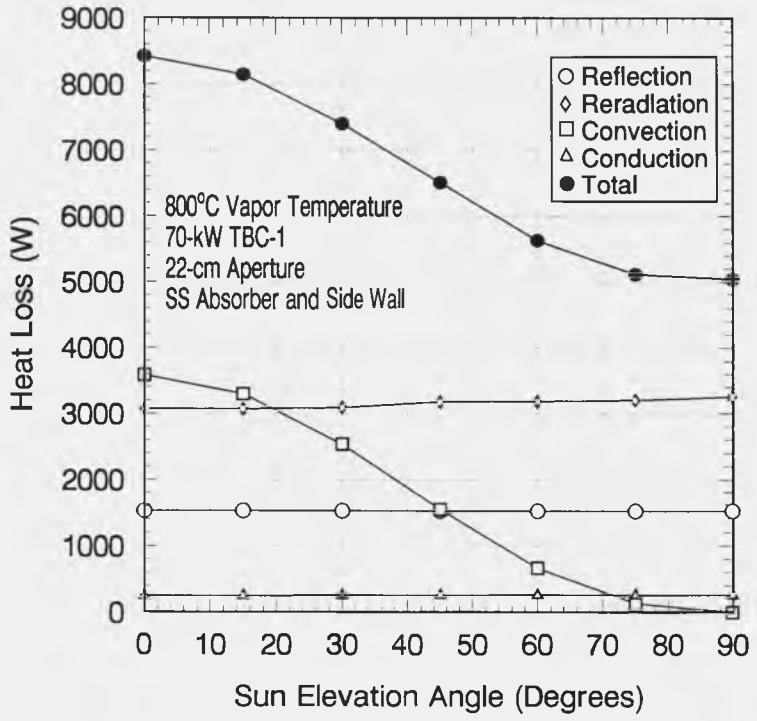

Figure R-6. Receiver heat loss as a function of sun elevation angle.

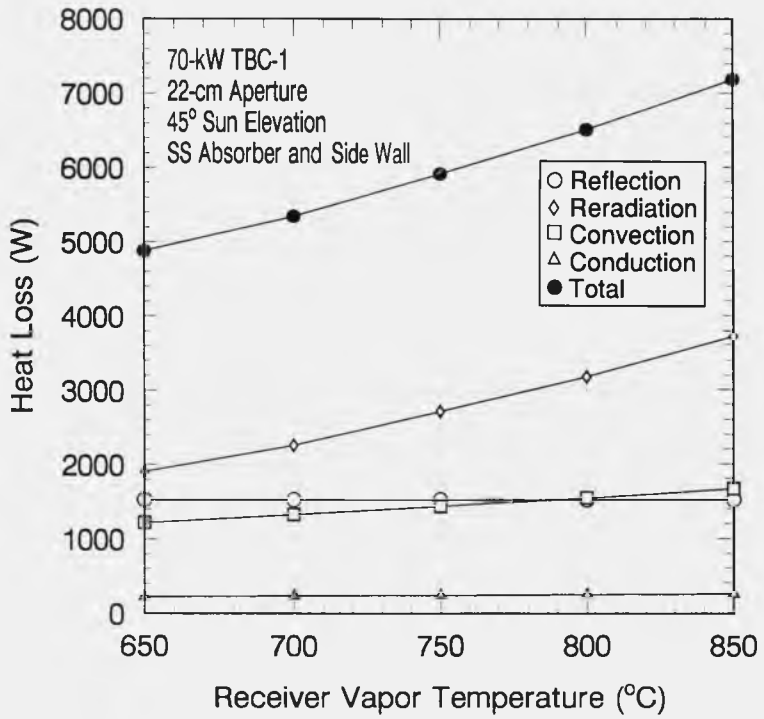

Figure R-7. Receiver heat loss as a function of sodium vapor temperature.

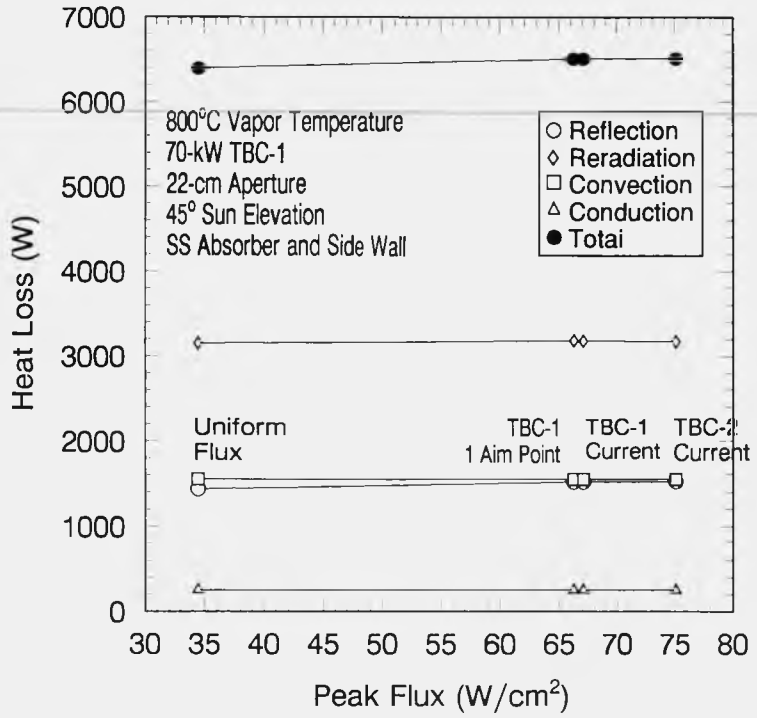

Figure R-8. Receiver heat loss as a function of incident flux distribution.

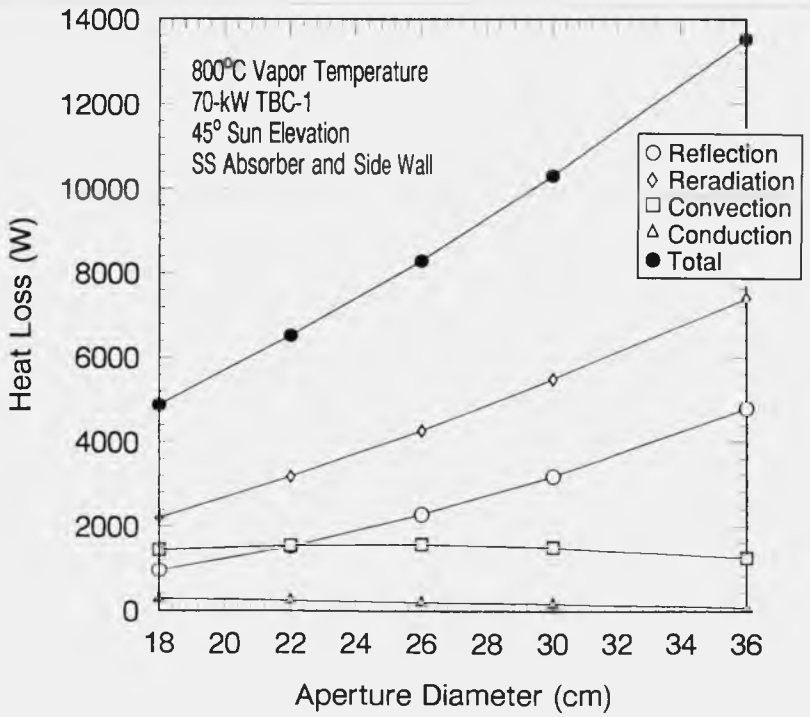

Figure R-9. Receiver heat loss as a function of aperture diameter.

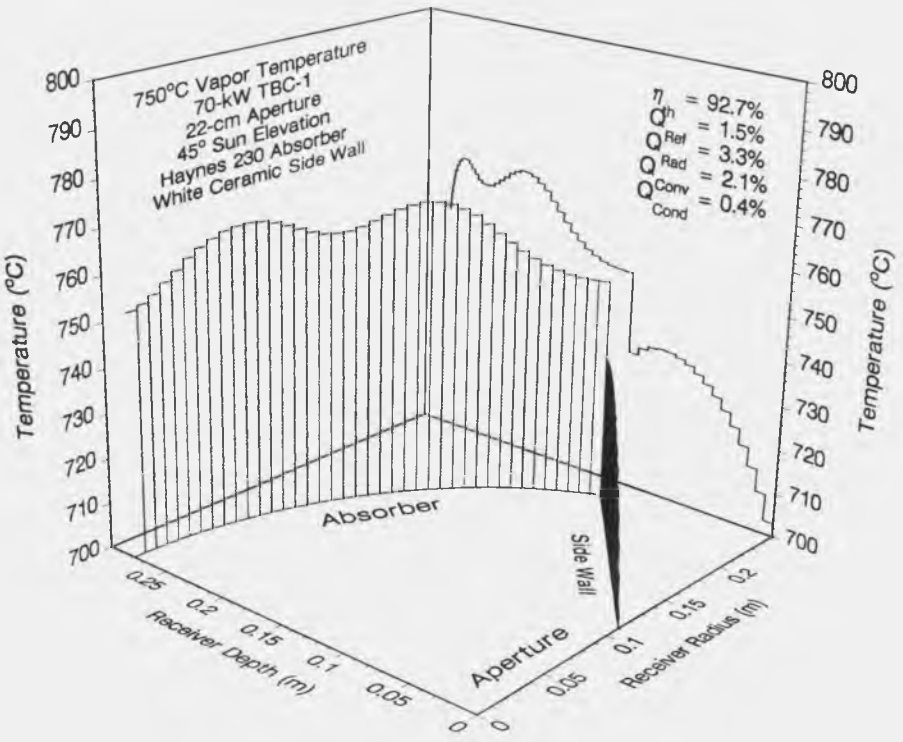

Figure R-10. Sandia next-generation pool-boiler receiver design point temperature distribution and performance prediction.

The parametric studies also indicate that significant improvements in receiver performance can be obtained with improved solar absorption of the absorber. The use of white side walls instead of black side walls also appear to be advantageous. Results from these performance analyses have been applied to the Sandia next-generation pool-boiler design.

References

Hogan, R. E., Jr., R. B. Diver, and W. B. Stine. 1990. "Comparison of a Cavity Solar Receiver Numerical Model and Experimental Data." *Journal of Solar Energy Engineering*. 112: 183-190.

Hogan, R. E., Jr. 1991. "Numerical Modeling of Dish-Stirling Reflux Solar Receivers." *Proceedings of the 13th Annual ASME Solar Energy Conference, Reno, NV, April, 1991.*

Stine, W. B., and C. G. McDonald. 1989. "Cavity Receiver Convection Heat Loss." *Proceedings of the International Solar Energy Society, Solar World Congress 1989 Kobe. Kobe, Japan.*

APPENDIX S

POST-TEST ANALYSIS

APPENDIX S
POST-TEST ANALYSIS

The post-test analysis concentrated on a physical examination of the failed pieces and on modeling of fatigue damage and loss-of-heat-transfer modes of failure. In addition, the flux distribution was analyzed and measured as outlined in Appendix G of this report. The peak fluxes measured were close to the 75 W/cm^2 predicted by CIRCE2. The physical examination looked for remaining evidence of the failure mode, as well as evidence of other impending failures or problems. The fatigue analysis was used to identify a number of sources of alternating stress and to examine their effects on the life of the receiver. The loss-of-heat-transfer study examined flooding and local film boiling as causes for the melting of the absorber metal.

Physical Examination

Metallurgical analysis of the pool boiler receiver was reported in detail in the July 22, 1991 memo (which is included in this Appendix) from Van Den Avyle to Moreno. A recounting of the leak aftermath and a brief overview of the metallurgical analysis is outlined below.

After the leak and the ensuing fire had stopped and the receiver had cooled, the receiver was removed from the Test Bed Concentrator (TBC). Most of the remaining sodium was melted and drained out, and an area of the absorber approximately 2 x 6 inches (in.) (0.05 x 0.15 meter [m]) surrounding the leak was cut out for immediate metallurgical examination. A patch was epoxied over the resulting hole. Further cleaning and dissection of the receiver did not occur until four months later. The delay was necessary to accommodate x-ray studies of the empty receiver that complemented on-sun x-ray studies of boiling in the receiver.

When the x-ray follow-up studies permitted, the remaining sodium in the receiver was removed by reaction with 2-propanol and water. The absorber along with a small amount of the aft dome was cut from the receiver as a unit to avoid disturbing the rim weld. The weldment joining the forward section of the condenser to the 8-in. pipe elbow was also removed for examination.

Metallurgical examination of the components has led to the following observations:

1. The leak occurred midway between two artificial cavities.
2. The absorber melted in the vicinity of the leak.
3. Metallurgical evidence at the site of the leak was insufficient to establish the cause of the leak.
4. No evidence of incipient mechanical damage or melting was found anywhere else on the absorber surface.
5. Most of the artificial cavities had lost material around their mouths so that they were chamfered.
6. There was no evidence of extension of the built-in crack in the dome rim weldment.

In addition, a dye-penetrant test of the weldment joining the 8-in. elbow and the condenser section (not reported in the memo) showed no evidence of cracks. Because the weldment was not a full-penetration joint, examination was limited to its external surface. The weldments joining the condenser section to its mounting rings were cracked. The cracks did not affect the receiver vacuum integrity or mounting system strength.

Fatigue Analysis

The stress analysis (Appendix H of this report) shows that the reflux pool-boiler receiver was subjected to a stress cycle for each startup/shutdown pair. The effect of this thermal cycle on receiver lifetime has been estimated from fatigue-life data, using the calculated strain range, the mean stress for the cycle, and the number of cycles. The Soderberg method (Viswanathan, 1989) was used to model the effect of mean stress. Creep relaxation of the mean stress was not taken into account, so the lifetime estimate was conservative.

The results of fatigue, with and without the mean stress effect, are shown in Figure S-1. The maximum stress calculated for the absorber was 100 MPa (14,500 psi), a condition which occurred during startup. The mean stress for a cycle was half this value, because the absorber was nearly stress-free before startup. The total strain at 100 MPa (14,500 psi) amounts to less than 0.1%. This would result in a fatigue life much greater than 10^6 startups if the mean stress had no effect (Aerospace Structural Materials, 1975). Applying the Soderberg method approximately halved the endurance limit. Applying this factor to fatigue-life strain-range data reduced the lifetime at 0.1% strain to somewhat more than 10^4 cycles. The largest class of starting transients that the receiver was intentionally subjected to was the 195 hot restarts—occasions when steady operation was interrupted and the receiver was allowed to cool and then was restarted. The stresses during hot restarts should be less than during a cold start, because temperature differences are smaller. The number of hot restarts plus the much smaller number of cold starts was so much less than 10^4 that fatigue can reasonably be discounted as a cause of failure.

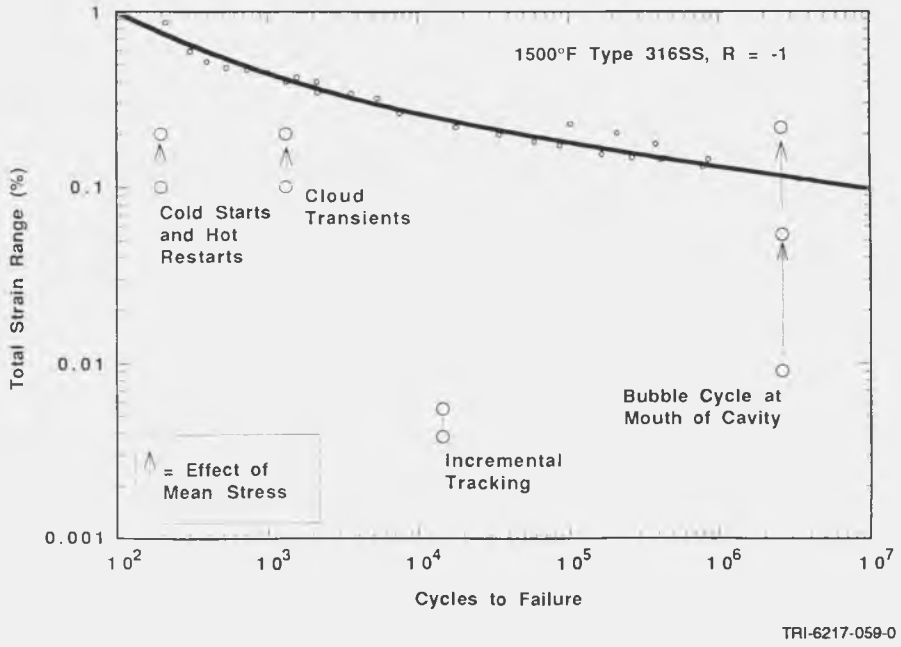

Figure S-1. Estimates of the number of cycles and the strain range for different oscillating phenomena for the pool-boiler receiver. The higher strain range in each case was after the addition of the effect of the mean stress. The third point for the cavity case was the increase that would be caused by a 15% error in the estimated mean stress at a cavity in the highest flux region. The failure did not occur at or near a cavity.

Three other cyclic phenomena have been identified that might produce larger numbers of cycles or greater strain ranges. These are, in decreasing order of potential number of cycles: (1) the bubble cycle at a nucleation site, (2) oscillations in the position of the flux distribution on the absorber, and (3) cloud transients.

The bubble cycle will produce many more cycles than the other possibilities (frequency x total test time @15 hertz x 48 hours (hrs) = 2.6 x 10^6 thermal cycles). Some damage was observed at the mouths of artificial cavities in the absorber. Stress analysis in the vicinity of the cavities indicated a total strain range associated with the bubble cycle of only 0.009%, but a mean local stress of about 68.9 MPa (10,000 psi) in the most highly stressed region of the absorber. Using the Soderberg model again, the endurance limit was now reduced by a factor of 6. Here, unlike the startup analysis, this factor was sensitive to error in the calculated local mean stress: it was nearly quadrupled by a 15% increase in the mean stress. If the larger factor was applied to the fatigue-data strain ranges, a lifetime of only about 20,000 cycles is predicted at 0.009% strain. Fatigue was a plausible explanation for the damage seen at artificial cavities located

where the absorber stresses were the highest. It is important to note, however, that cavity damage was limited in depth and localized to the neighborhood of the artificial cavities, whereas the leak occurred midway between the cavities. Thus, it was unlikely that the leak was a result of thermal fatigue associated with the bubble cycle. A side issue remained, however: what caused the damage at the cavity mouths? As mentioned above, the mean stress was only high enough for fatigue failure at the location of peak stresses. Another possibility was that pressure pulses associated with bubble dynamics caused the damage. We have not assessed this possibility because of lack of analytical tools and time. A third possibility was that the damage was actually done at the time that the holes were machined. At the time of delivery, we inspected the cavities for diameter and depth, but not specifically for the damage under discussion here. We do not, however have any recollection of this damage. On the contrary, we remember being impressed with the crisp, well-formed appearance of the cavities. Nevertheless, because the inspection was not specifically for chamfering, the preexistence of chamfering cannot be dismissed entirely.

Oscillation in the position of the flux distribution is the second possible cause of fatigue that has been identified, and is a result of stop and start motion in the dish tracking system. This behavior was not well-characterized. We have made a rough estimate that azimuthal tracking proceeded in steps of up to 0.05 degree. This produced approximately one cycle every 12 seconds (s), or a total of 14,400 cycles over the total test time. The position of the flux distribution shifted about 0.25 in. (0.006 m) on each cycle. Smaller azimuthal steps would result in more cycles of smaller shifts. Referring to Appendix H, it can be seen that a 0.25-in. (0.006-m) shift in the flux distribution would change the stress in the region of steepest gradient (which was about where the leak occurred) by 3.8 MPa (550 psi). Again, the strain range and number of cycles were too small for fatigue failure to have occurred.

Cloud transients are the third possible cause of fatigue that has been considered. A review of the data for the 18 separate days on which the receiver was tested showed that cloud transients were present during about 11 hrs of test time. The total number of cycles was easily bounded by realizing that a cloud transient was typically much longer than 30 s. This resulted in a gross overestimate of about 1320 cycles. Most of these cycles amounted to hot restarts, and the associated stresses should have been well below those seen during a cold start. Thus, the strain range and number of cycles again fell short of what was necessary to cause a fatigue failure.

Because the failure occurred at a local maxima in the calculated two-dimensional flux distribution, we have considered the following additional areas: (1) the possibility that the flux in the vicinity of the failure was much greater than calculated, and (2) the effect of non-axisymmetric features of the calculated flux distribution on the stresses. Either of these could increase our estimates of total cyclic strain range at the failure site. We have measured the flux level in the vicinity of the failure, as described in Appendix G of this report. It was in good agreement with our calculations. We have not attempted to calculate the non-axisymmetric stress field for the absorber, but experience suggests that strain range estimates at the failure site would not be significantly increased.

Our understanding of the part that fatigue may have played in the pool-boiler failure was less than satisfactory, primarily because a detailed analysis, including all of the factors that affect fatigue, was not possible. A list of these factors would include the effect of creep, mean stress, temperature, hold time between cycles, absorber size, surface condition, stress concentrations, and manufacturing defects (Viswanathan, 1989). Instead, effort was focused on lifetime predictions for the next-generation receiver, which will use Haynes Alloy 230 instead of 316L stainless steel. Thus, at this time, although our judgement was that the absorber probably did not fail as a result of fatigue, we have not conclusively ruled out the possibility.

Loss-of-Heat-Transfer Analysis

This section will discuss the possibility that the receiver failure was caused by a loss of liquid metal cooling, leading to a rapid temperature rise and subsequent melting of the receiver housing material. Loss of cooling could be localized (film boiling) or global (flooding limit). The receiver failure occurred at or near a local peak in the input heat flux, which would be the most likely region for local film boiling to occur, or the most likely area to melt in the case of a general failure of cooling (flooding limit). Failures in heat pipes which experience loss of cooling have typically resulted in melt-through with similar characteristics. The pool boiler bench test also terminated in a loss-of-cooling failure, in which frozen sodium was trapped at the wrong end of the pipe because of an experimental error. Although a large area of the surface was not cooled by the sodium, only a small spot at the peak flux melted, with melt characteristics similar to the present receiver.

As liquid metal boils in the receiver, the vapor must travel up to the condenser along the same path where the returning liquid flows down to the absorber. If enough vapor has been generated, the liquid can no longer return, and a "flooding limit" is reached, resulting in burnout of the absorber dome. The Kutataladze flooding criterion, developed for flow in vertical cylindrical tubes, was modified by Stirling Technology Corp (1988) to account for a flow angle other than vertical. While the present geometry was not a cylindrical tube, the modified Kutataladze criterion could be used for a *relative* measure of safety factor. Here, safety factor was defined as heat input producing burnout divided by actual heat input. Figure S-2 shows the dependence of the flooding limit on temperature in the present design for thermal inputs of 43.5 kW_t and 65 kW_t. Increasing the elevation angle of the receiver reduced these factors slightly. While the receiver normally operated at throughput of 65 kW_t, during startup, some of the energy heated the absorber end of the receiver and its contents, and thus did not create vapor that must flow to the condenser. A comparison of the measured startup temperature ramp before and after boiling initiates indicated that about 43.5 kW_t was transferred out of the pool immediately after boiling began. The measured gap between the domes at the apex was only 1.2 in., compared to a design gap of 1.5 in. This reduced the flooding limit further by reducing cross-sectional flow area, but did not change the relative results.

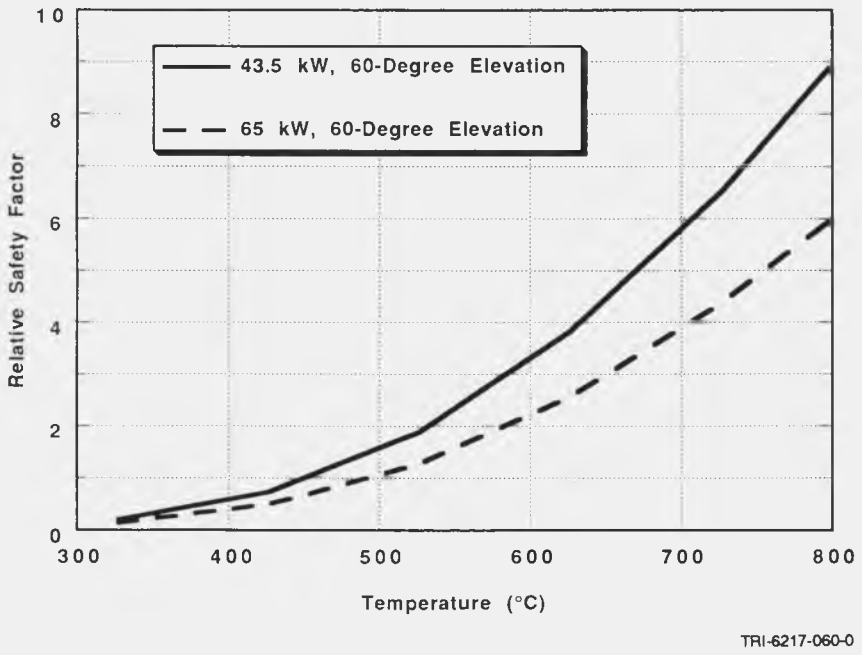

Figure S-2. Dependence of the flooding limit on temperature, power level, and elevation. The Kutataladze relationship was modified for use at different elevation angles by STC. During an initial startup, about 43.5 kW of the 65-kW input heat was actually transported by vapor to the condenser, while the remaining input heat provided sensible heat to the receiver materials.

The pool boiler bench tests (Moreno and Andraka, 1989) typically initiated boiling at 600°C. These conditions would result in a calculated flooding safety factor of about 4 for the full-scale receiver. However, during on-sun tests, the boiling typically initiated at about 480°C, resulting in a calculated flooding safety factor of slightly less than 2 for the 43.5 kW_t case. No satisfactory explanation has been found about why boiling initiated at a lower temperature in the full-scale test. The pool boiler survived approximately 20 normal starts prior to failure. Hot restarts were limited to above 600°C until the final test.

During the startup of the final test, the sodium pool reached about 650°C, and then the receiver was taken off-sun to investigate a thermocouple failure. The temperature history of the test is shown in Figure M-9 in Appendix M of this report. The receiver was brought back on-sun with the pool at less than 500°C, a unique condition not previously encountered. It was possible that, because of the pre-heating during the first attempt at starting, less than the normal thermal energy was required to heat the receiver at the absorber end (pool was less subcooled). These conditions would result in a vapor volumetric flow rate through the pool and to the condenser greater than previously encountered and possibly exceeding the flooding limit. This problem could be resolved by increasing the cross-sectional flow area

between domes, at the expense of a greater liquid metal inventory. Methods of delaying the start of boiling could also be investigated.

Figure S-3 shows the dependence of the film-boiling critical heat flux (CHF) on temperature. These data were extrapolated from horizontal flat plate data (Saaske, 1989), and so are only good for relative comparisons. The peak flux, as stated earlier, was around 75 W/cm^2. Again, the argument can be made that the receiver experienced a unique condition of less subcooling during this startup, possibly leading to localized film boiling. The CHF has been noted to decrease with less pool subcooling (Dwyer, 1976). The receiver may have failed because the CHF was exceeded when the pool was less subcooled than during a normal startup. This problem could be resolved by reducing the flux (enlarge dome or move back from focus) or by delaying the start of boiling.

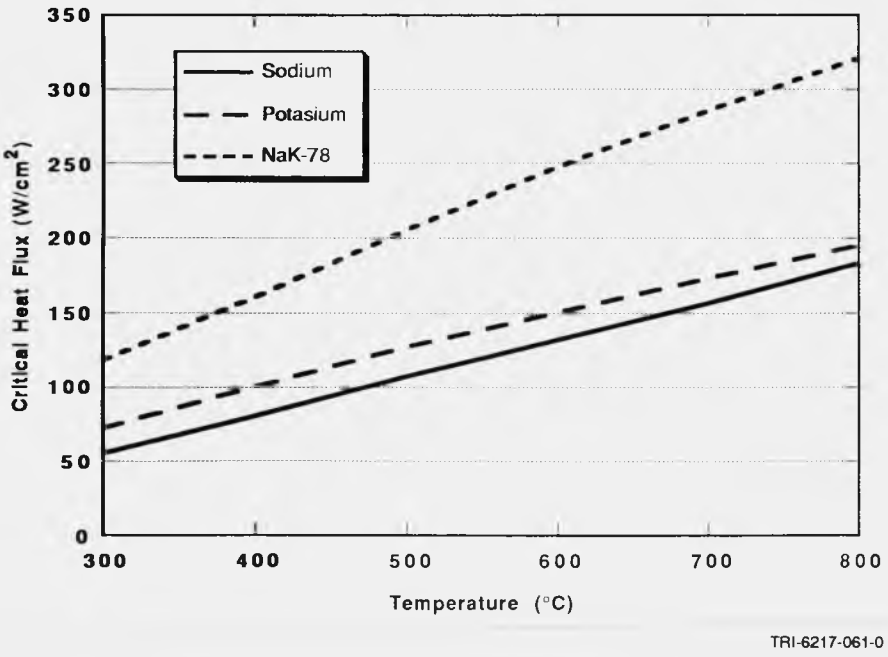

Figure S-3. Dependence of the critical heat flux (CHF) on temperature for different working fluids. These data were extrapolated from experimental data to the 300°-800°C range using a 1/8-power relation on the saturated vapor pressure.

Conclusions

The following conclusions have been drawn from the postmortem analysis:

1. The leak did not occur at an artificial cavity.

2. Metallurgical evidence at the site of the leak is insufficient to establish the cause of the leak.

3. The number and magnitude of thermal-strain cycles is too small to have likely caused a fatigue-failure leak.

4. The leak was at or near a flux "hot spot" predicted by CIRCE2 and confirmed experimentally.

5. The "hot restart" underway at the time that the leak occurred was different than all others that the receiver had experienced, in that it had a greater potential to cause either transition to film boiling or flooding.

6. The leak was most probably caused by either transition to film boiling or exceeding the flooding limit.

7. Although the absorber did not fail at an artificial cavity, there was loss of material around the mouth of most cavities, creating a chamfered appearance. This damage is probably fatigue-related.

8. The weldment joining the receiver elbow and condenser section, which is subjected to the passage of a thermal front on startup, showed no evidence of cracking. However, the weldments joining the condenser section to its mounting rings were cracked.

9. The next-generation pool-boiler design will incorporate a larger dome to reduce the flux and a larger gap between the domes to improve the flooding limit.

References

Aerospace Structural Materials Handbook. 1975. Code 1307, Belfour Stulen, Inc.

Dwyer, O. E. 1976. *Boiling Liquid-Metal Heat Transfer*. Hinsdale, IL: American Nuclear Society.

Moreno, J. B., and C. E. Andraka, 1989. *Test Results from Bench-Scale Sodium- Pool-Boiler Solar Receiver.* SAND89-0899. Albuquerque, NM: Sandia National Laboratories.

Saaski, E. 1989. "Thermal Modeling Overview." *Proceedings of the Advanced Solar Conversion System (ASCS) Heat Transport Workshop NASA LeRC/Thermacore, Lancaster, PA: September 27-38, 1989.*

Stirling Technology Company, 1988. 25-kWe Solar Thermal Stirling Hydraulic Engine System, Final Conceptual Design Report. DOE/NASA/0371-1, NASA CR- 180889. Cleveland, OH: National Aeronautics and Space Administration, Lewis Research Center.

Viswanathan, R. 1989. *Damage Mechanisms and Life Assessment of High-Temperature Components.* Metals Park, OH: ASM International.

Sandia National Laboratories

Albuquerque, New Mexico 87185

date: July 22, 1991

to: J. B. Moreno, 6217

from: J. A. Van Den Avyle, 1832

subject: Metallurgical Post-Test Analysis of Sodium Reflux Pool-Boiler

refs: 1. memo J. B. Moreno, 2542 to J. A. Van Den Avyle, 1832; dtd. 7/17/90; subject: "Post Mortem for Full-Scale Solar Sodium Receiver".
2. memo J. B. Moreno, 2542 to C. E. Andraka, 6217; dtd. 8/1/90; subject: "Status of Post-Mortem and Other Materials Questions".

Summary:

This memo reports on the results of a destructive post-mortem analysis of the subject solar boiler. It addresses a number of questions and concerns listed in the two references. The boiler, made of 316L stainless steel sheet, developed a small leak after approximately 48 hours operation above 600°C with temperatures as high as 800°C. The hole and surrounding areas were examined by scanning electron microscopy and by cross-sectioning. Small areas of localized melting at the leak were found, but there was no remaining evidence of cracking due to creep or fatigue damage. The entire interior and exterior absorber wall surfaces were examined for evidence of local melting or cracking (none found) as well as for corrosion and dissolution. The liquid sodium-exposed side was unaffected, but the air side was oxidized to a depth of 0.001 inch. The artificial cavities EDM-drilled into the inner wall were damaged by metal loss near the surface, resulting in chamfered hole openings. The damaged areas appeared to be fatigue fracture surfaces; fatigue cracking was likely caused by cavitation-induced stresses or localized thermal cycling during boiling. Metallographic examinations of the receiver rim weld found no evidence of weld cracking. (case 2216.330)

This investigation had several goals. The major one was to try to determine whether the boiler leak was caused by thermo-mechanically induced damage, i.e. fatigue cracking or creep-fatigue cracking, or by localized overheating leading to melting through the boiler wall. Other features to examine included a) the condition of the artificial cavities put in the sodium side wall to promote boiling, b) any oxidation of the outer wall or sodium attack of the inner wall, and c) the chemical composition of unidentified metal nodules attached to the inner wall

Examinations of the Leak Area

The section which contained the leak was cut out of the pool boiler and examined both through an optical microscope and in a scanning electron microscope (SEM). A photograph of this piece showing the inside surface is given in Fig. 1. Approximate dimensions of the hole are 0.21 inch x 0.07 inch. The staining and circular marks around the leak are due to light corrosion of the stainless steel by the entering air which reacted with the sodium to form sodium hydroxide. Visible on Fig. 1 are the locations of two artificial cavities, marked #1 and #2. The leak location was not associated with any of the artificial cavities or thermocouple attachment points. The area marked #3 is the location of an unknown metal nodule deposited on the inner wall. These are described later.

A SEM view of the leak from the inner wall side (Fig. 2a) shows that material flowed inward, resulting in an inner lip. From the hole volume it is evident that significant metal has been removed, probably sucked inward as air rushed in through the leak. At higher magnification (Fig. 2b) near the left edge of the hole, no cracking of the stainless steel wall is visible. The two small spherical particles located approximately 0.09 inch from the hole edge were identified as melted wall material that had reattached to the surface. High magnification inspections around the entire edge of the hole on the inner surface found no cracks.

The features of the leak from the outer wall side are shown in Fig. 3a-c. On this side, shallow oxide-filled grooves extend from the ends of the hole (Fig. 3b and c). No real cracks were noted in the metal at these locations, and metallurgical cross-sections made below the ends of the hole also did not reveal cracking. Some light scratches, probably due to cleaning of the part, are visible at the hole ends. High magnification inspections around the entire edge of the hole on the outer surface also found no cracks.

A through-wall cross-section of the leak showed that the material which formed the lip on the inner wall had been melted and flowed inward as a liquid (Fig. 4). The microstructure of this flowed metal was dendritic, confirming that it had solidified from liquid. The extent of microstructural rearrangement caused by exposure to near-melt temperatures is limited to about one wall thickness away from the hole edge. This indicates that the melting zone was very localized.

Examinations of the Post-Test Inner and Outer Boiler Surfaces

Since the leak occurred after a relatively short period of operation at temperature (approximately 48 hours above 600°C with few thermal cycles), little time was available to accumulate fatigue or creep damage. For such mechanically-driven damage to have occurred, stresses would have to have been high to account for the short life. If similar high level stresses were present at other locations on the boiler, evidence of mechanical damage, such as surface rumpling or crack initiation, should have been visible. Likewise, if other small areas of incipient melting occurred they could possibly have been visible as glazed-over (melted) or distorted wall surfaces.

The complete inner and outer walls of the boiler were inspected in detail visually at 20X to check for any other damage sites. No cracks or areas roughened by deformation were found. Numerous assembly-caused defects were noted on both surfaces; these included scrapes, scratches, small pits, braze deposits, and ground-off braze deposits. No cracks were detected at any of these assembly-caused surface defects.

Damage to Artificial Cavities

These cavities were EDM drilled into the inner wall to provide stable boiling nucleation sites. Visual examination of the two cavities located in Fig. 1 showed that the top of the holes had lost material and were chamfered in appearance. They were examined in the SEM (Fig. 5 and 6), and the one marked #2 was metallographically cross-sectioned (Fig. 7). The surfaces of the damaged hole corners do not appear dissolved, but instead look most like fracture surfaces. The intersections of the chamfered edges with the wall surfaces are generally sharp. At higher magnifications, Figs. 5b and 6b, the damaged areas are oxidized, but have features similar to fatigue fractures in this stainless steel, with possible fine fatigue crack growth striations. In the cross-section the damage is localized to the top 30% of the hole. (From these examinations the hole dimensions are approximately 0.0055 inch diameter by 0.022 inch deep.) No other secondary cracks running from the hole are present.

The other artificial cavities on the boiler were examined visually and had experienced the same damage. These features are consistent with micro-fatigue cracking caused by local alternating stresses. Two possible sources of alternating stress are thermal cycling and/or cavitation at the hole during sodium boiling. The source of cavitation stress is bubble formation and collapse, which can generate shock waves at the adjacent hole edges. Rapid temperature fluctuations can also generate thermal shock. These stress pulses can cause fatigue crack initiation and growth.

Identification of Nodules on the Boiler Inner Wall

A number of metal lumps or nodules were found by visual inspection on the inner wall surface; they were well attached and could not be removed by scraping. Many, such as the example identified as area #3 in Fig. 1, were thin, flat particles (Fig. 8a), while others were more spherical in shape. Fig. 8b shows a polished and etched cross-section of the flat example. Its microstructure is unlike the base alloy, and an elemental analysis done by wavelength dispersive X-ray analysis in the electron microprobe found it to be nickel. These results indicate that the particles are fragments of braze alloy used to attach thermocouples to the internal wall. The braze alloy was BNi-3, which contains boron -- a low atomic number element which is not detectable in a routine microprobe analysis.

Condition of the Boiler Inner and Outer Wall Surfaces

The inner wall in contact with liquid sodium was relatively unaffected by the exposure. This is evident in areas around the artificial cavities, Figs. 5a and 6a, and in the cross-sections in Fig. 7 and 8. Except where corroded near the leak, the stainless steel surfaces remained clean, and original finishing marks were visible. The cross-sections did not reveal any grain boundary attack or evidence of significant metal transport on the sodium side.

Outer wall surfaces exposed to air experienced oxidation, with formation of approximately 0.001 inch oxide thickness. Oxide penetration was greatest at the grain interiors, while the grain boundaries protruded above the surface into the oxide layer (Figs. 7, 8b, and 9). The nonuniform attack outlines the grain boundaries as seen in the SEM view (Fig. 10). This amount of oxidation was not large, but the exposure times were short. Longer exposures could cause significant wall thinning, given that only a 0.010 inch depth remained below the artificial cavities (Fig. 7). Oxide growth rates for longer tests (with this alloy) would depend on the adherence of the oxide layer. The oxide acts as a diffusion barrier for the oxidation reaction, and if it periodically scaled off, the rate would increase. It is possible

that thermal cycling could accelerate oxide loss due to thermal expansion mismatch or due to mechanically induced straining.

Cause of the Leak

The physical evidence does not give a certain cause of formation for this leak. Two potential mechanisms were considered:

The first was that elevated temperature exposure, combined with thermal cycles (both global and local), could have induced cyclic thermal stresses which produced a short creep-fatigue crack. Once the crack perforated the wall, air would enter and decrease heat transfer locally. Melting in the vicinity of the crack could have occurred, resulting in the observed hole shape and features. Such melting could erode the initial crack and make it impossible to verify this mechanism. This scenario is not directly supported. As stated above, for the short operating life, stresses would have to be very high to initiate cracking, and other small cracks would be expected in different locations. None were found. Second, no evidence for a prior existing crack remained at the melted hole, although the evidence could have been destroyed.

The second mechanism was direct localized melting at the leak location caused by loss of heat transfer on the inside surface. The observations support this scenario in that melting did occur. Again, no other incipient melting sites were noted during the inspection, but there is low confidence that these incipient sites would necessarily be easily detected. Possible mechanisms for local loss of heat transfer are beyond the scope of this discussion.

Examination of Receiver Rim Weld

Manual TIG welding procedures were used to join the fore and aft spherical sections of the receiver. This weld geometry forms a crack-like joint where the two spherical segments join tangentially. A concern is that cyclic thermal stresses could induce fatigue crack growth into the weld fusion zone. Metallographic analyses were performed on four sample sections cut out at 90° intervals around the outer rim. Resulting cross-sections are shown in Figure 11. In these micrographs the thicker section is the receiver rear wall, and the thin section is the front absorber. The dendrictic weld fusion zone is darker. There are substantial differences in weld geometries and gap size among there four examples. There is no evidence of extension of the crack-like joints in any of the cross-sections.

Conclusions:

1. The physical evidence does not unambiguously determine the cause of leaking. Local melting did occur, and the scenario best supported is local loss of heat transfer leading to melt-through. No other incipient failure sites were detected.

2. Damage to artificial cavities was likely due to boiling cavitation-induced fatigue cracking.

3. Metal nodules attached to the boiler inner wall were identified as a nickel-based thermocouple braze alloy BNi-3. No other metal transfer was noted on the inner liquid sodium side of the boiler.

4. The boiler inner wall surface was substantially unaffected by the short time high temperature exposure to liquid sodium; the outer wall exposed to air was oxidized to a

depth of 0.001 inch. This oxidation rate could be excessive, particularly if the oxide was non-adherent during thermal cycling.

5. No cracking was observed at the roots of sections taken from the outer receiver rim weld.

1832:jav

copies to:
1830 A. D. Romig
1831 M. J. Cieslak
1832 W. B. Jones
1833 J. L. Jellison
1834 A. K. Hays
1832 file

Fig. 1 Photograph of segment containing leak cut from boiler front wall, 0.75X.

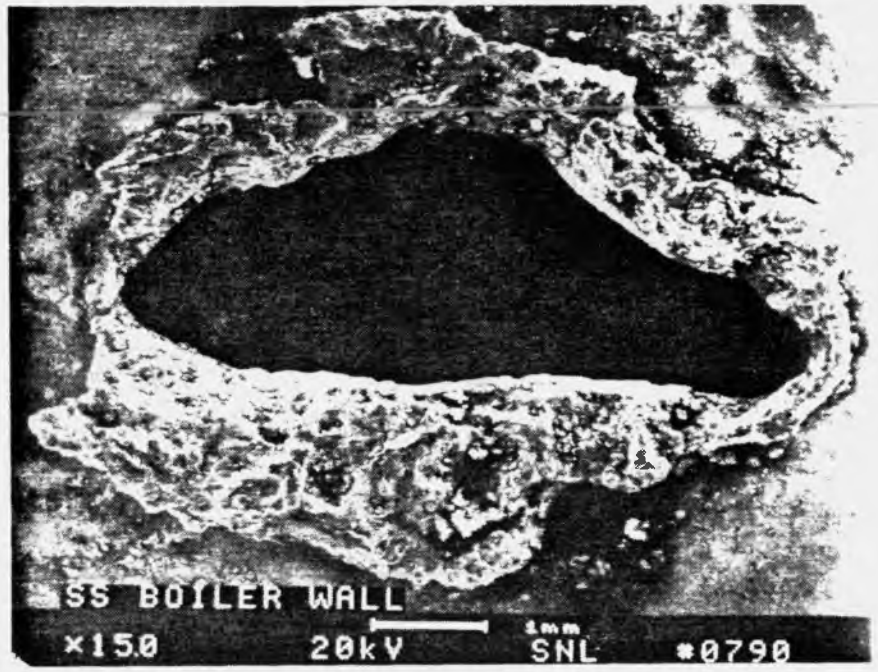

(a)

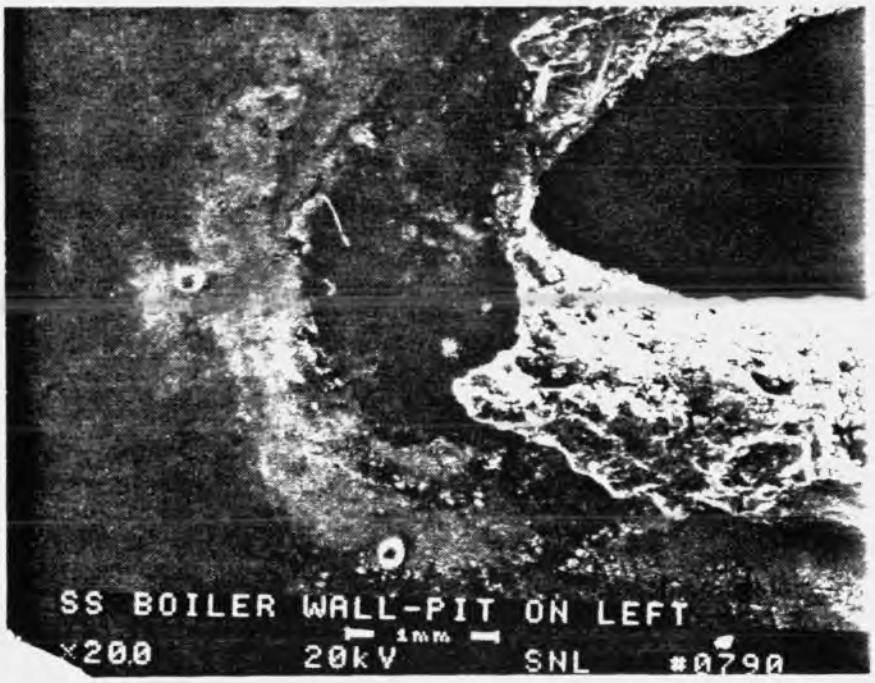

(b)

Fig. 2 SEM micrographs of leak viewed from the inside showing lip of metal; a) 15X; b) left side of hole with melted metal balls, 20X.

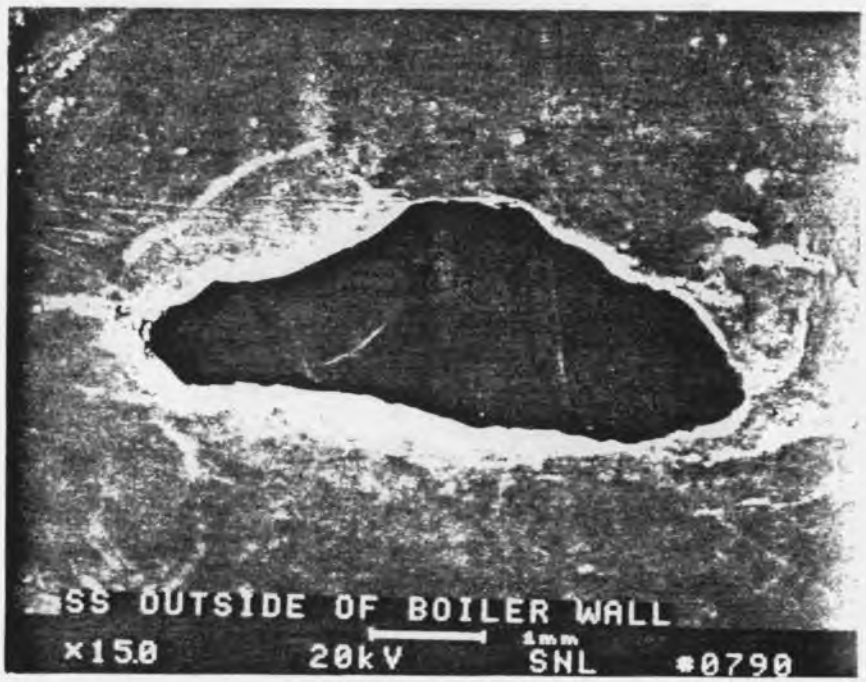

(a)

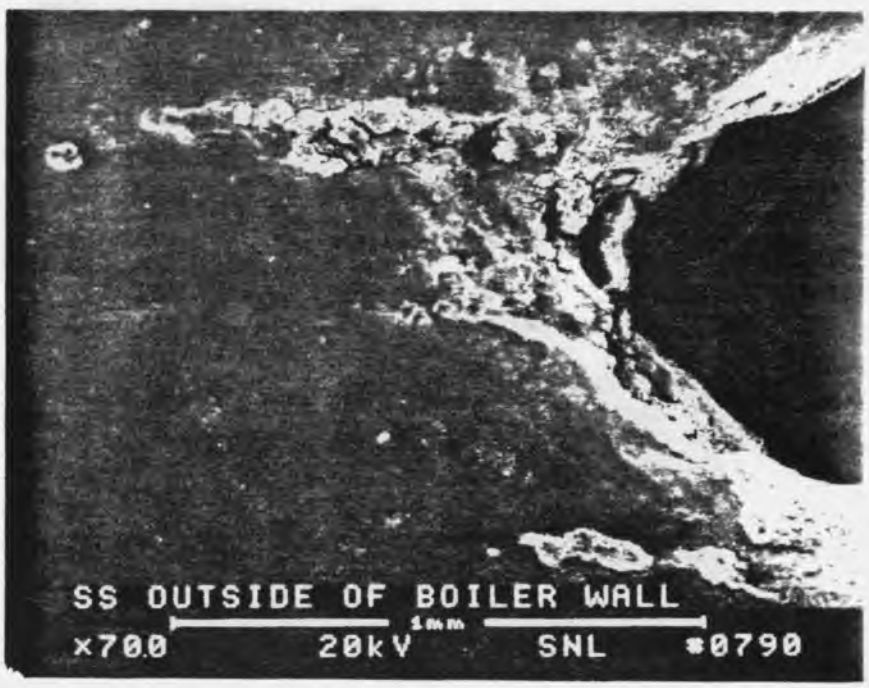

(b)

Fig. 3 SEM micrographs of leak viewed from the outside; a) 15X; b) 70X; c) same hole edge as Fig. 2b, 15X.

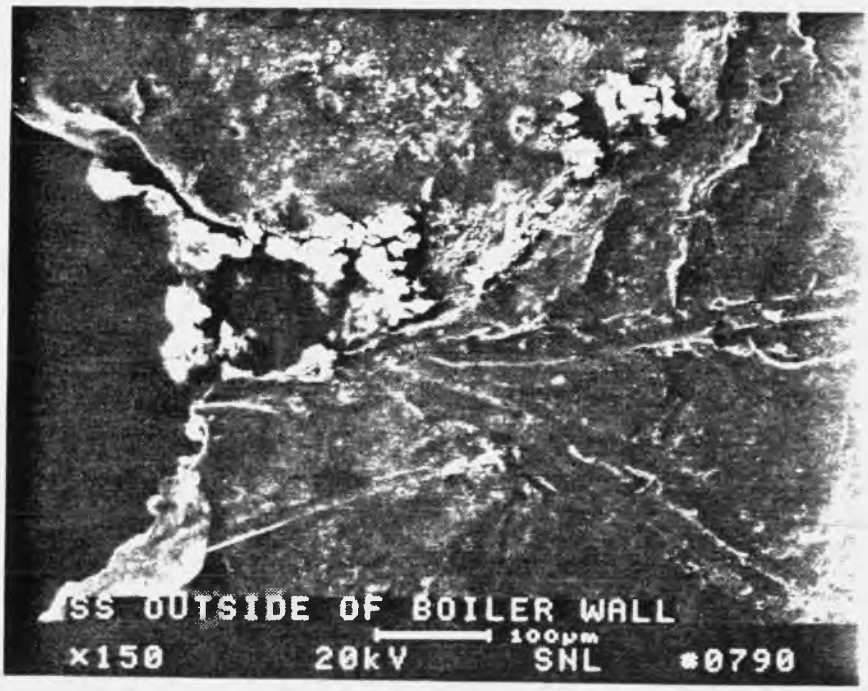

(c)

Fig. 3 cont. SEM micrographs of leak viewed from the outside; a) 15X; b) 70X; c) same hole edge as Fig. 2b, 15X.

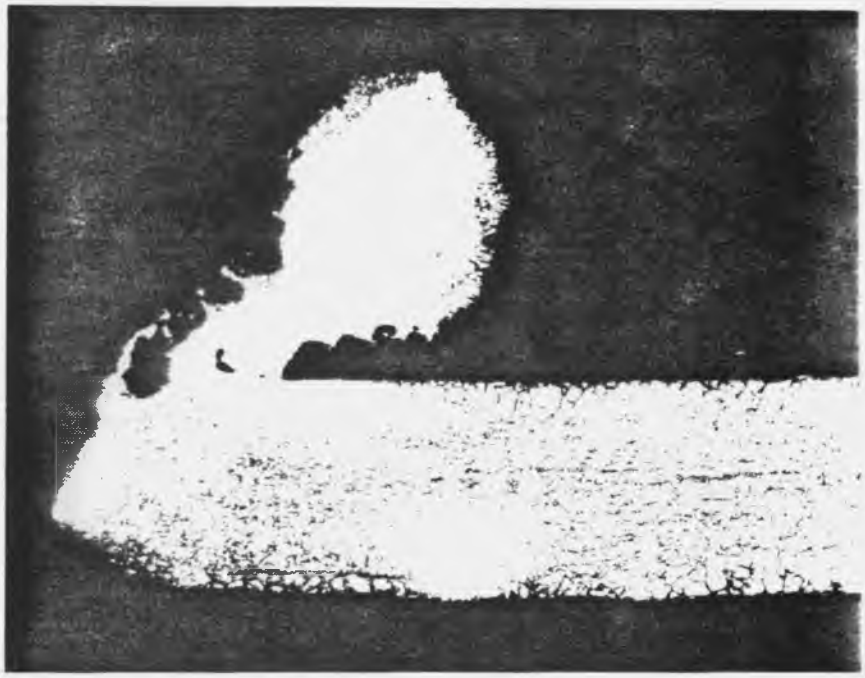

Fig. 4 Polished and etched cross-section through leak showing metal flow toward inside of boiler; re-deposited metal is dendritic, indicating it was melted and solidified, 35X.

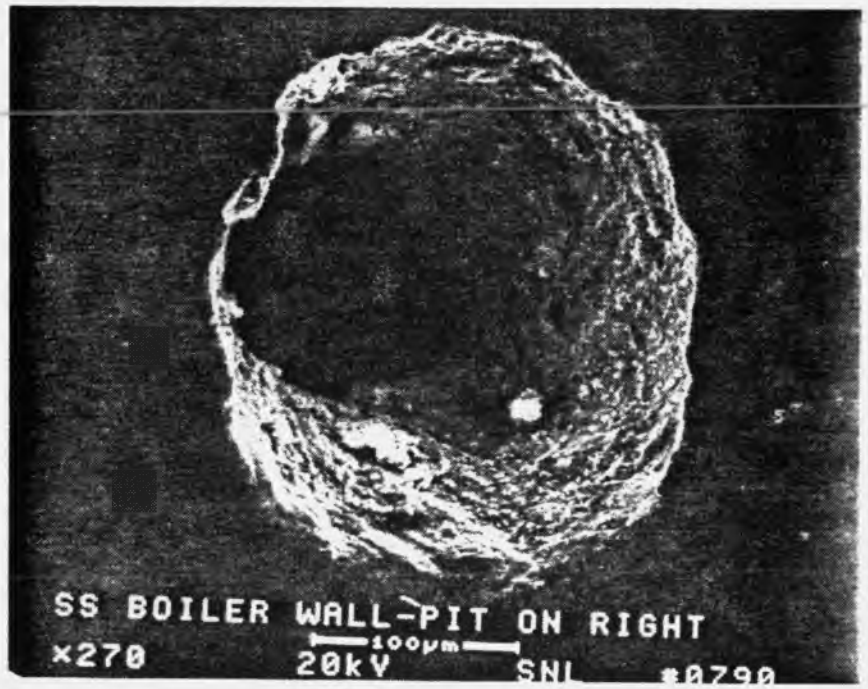

(a)

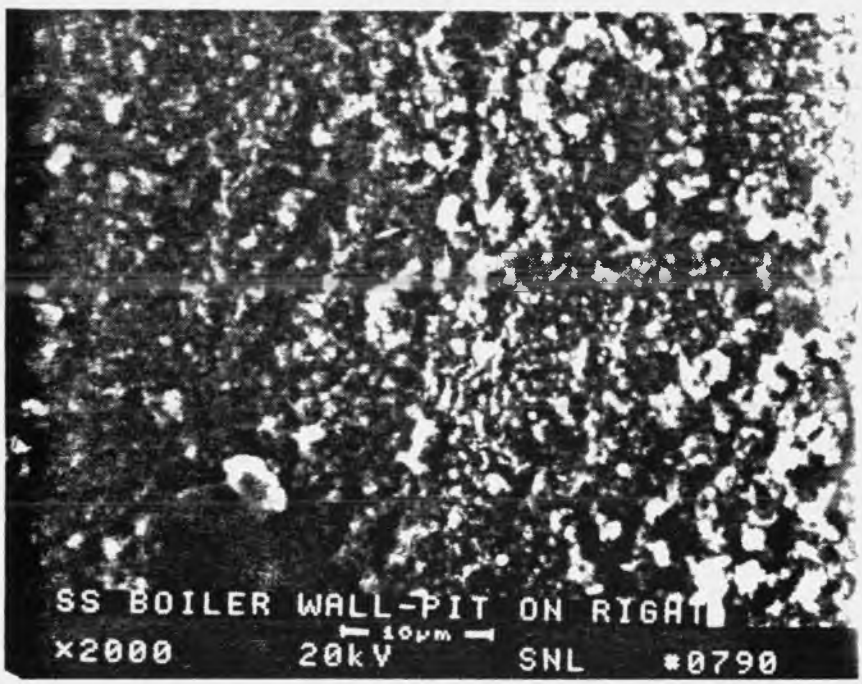

(b)

Fig. 5 SEM micrographs of artificial cavity, area #2; a) 270X; b) high magnification view of damaged surface, 2000X.

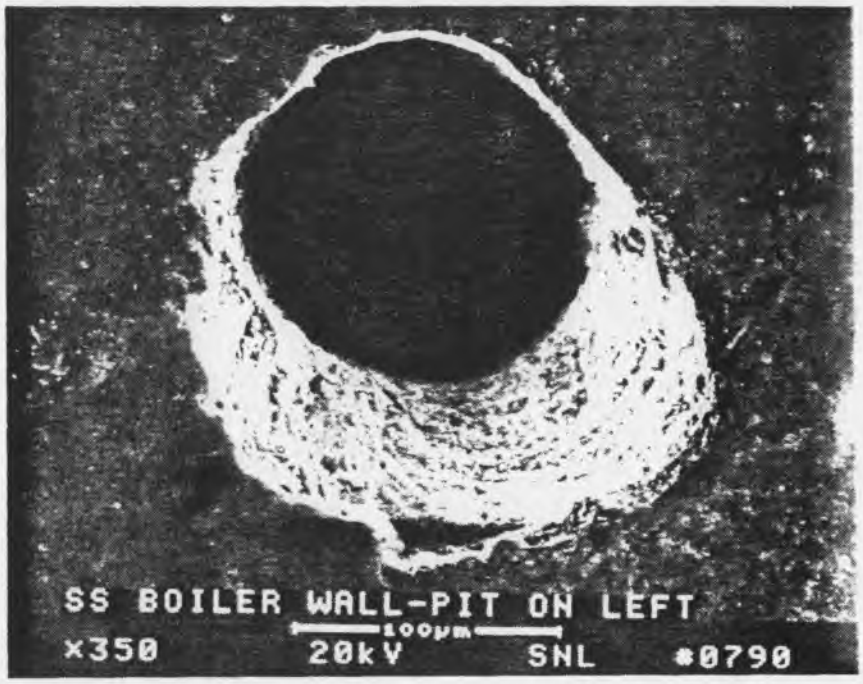

(a)

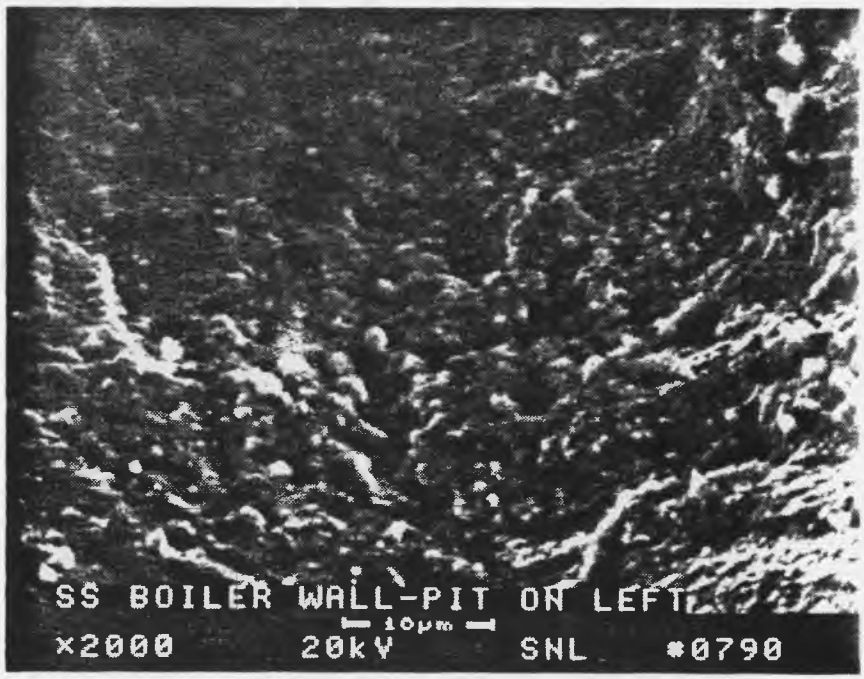

(b)

Fig. 6 SEM micrographs of artificial cavity, area #3; a) 350X; b) high magnification view with possible fatigue striations, growth direction vertical, 2000X.

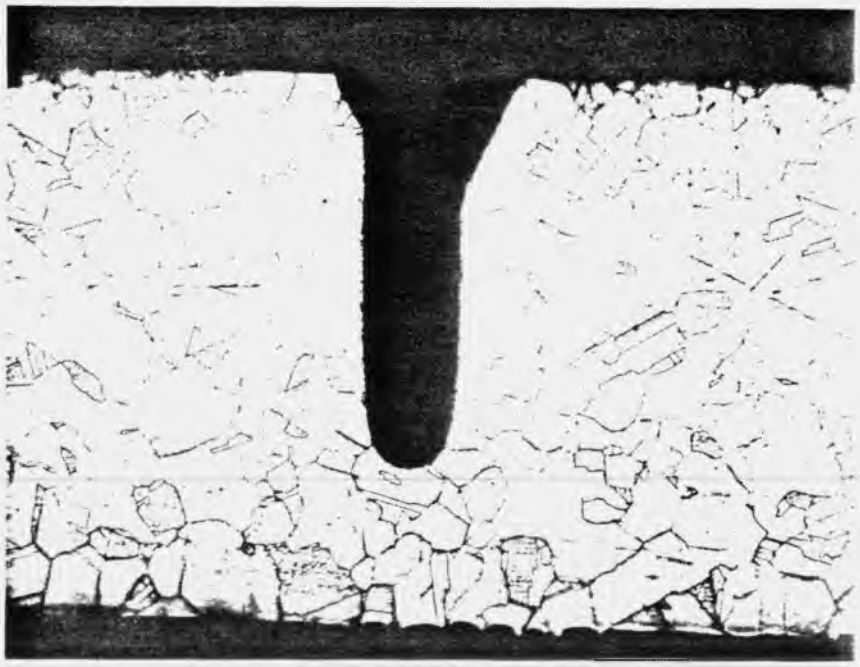

Fig. 7 Polished and etched cross-section through artificial cavity showing damage near top surface, 90X.

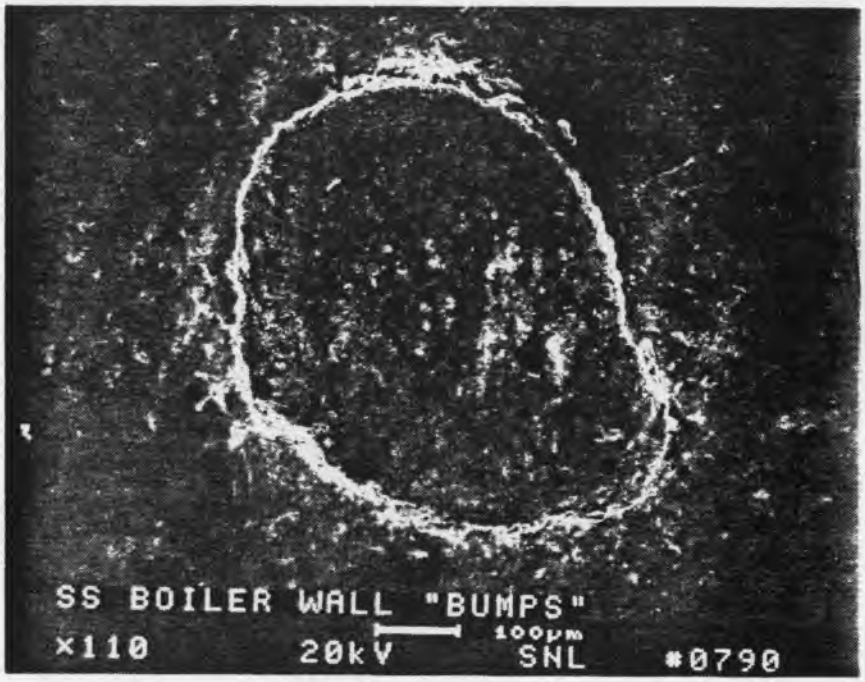

(a)

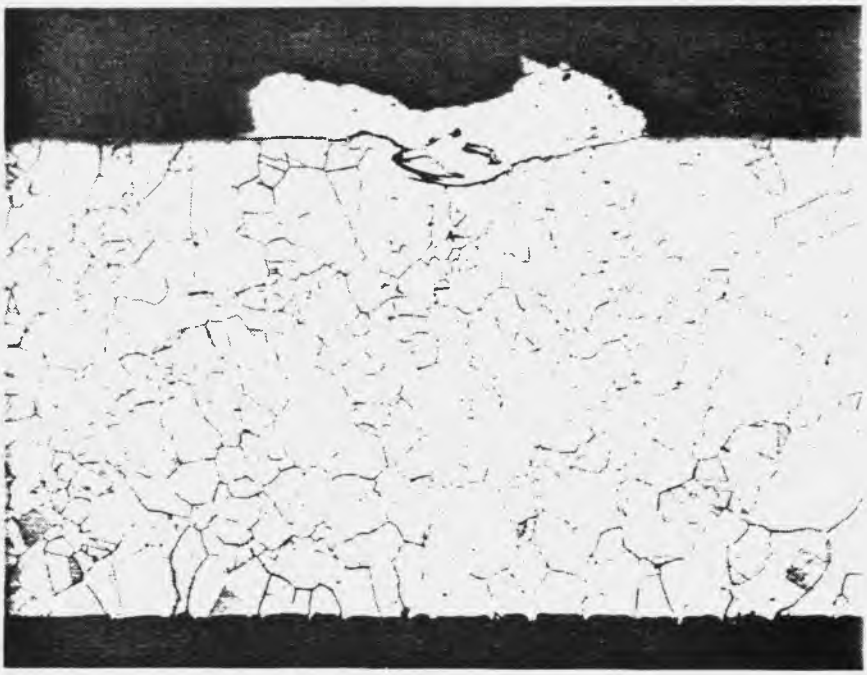

(b)

Fig. 8 Nickel braze alloy nodule deposited on inner wall surface; a) SEM micrograph, 110X; b) polished and etched cross-section showing flat nodule attached to inner wall, 80X.

Fig. 9 Oxidation of air-exposed outer wall showing penetration within grains and protrusions at grain boundaries. Dark inclusion stringer noted within wall. 500X.

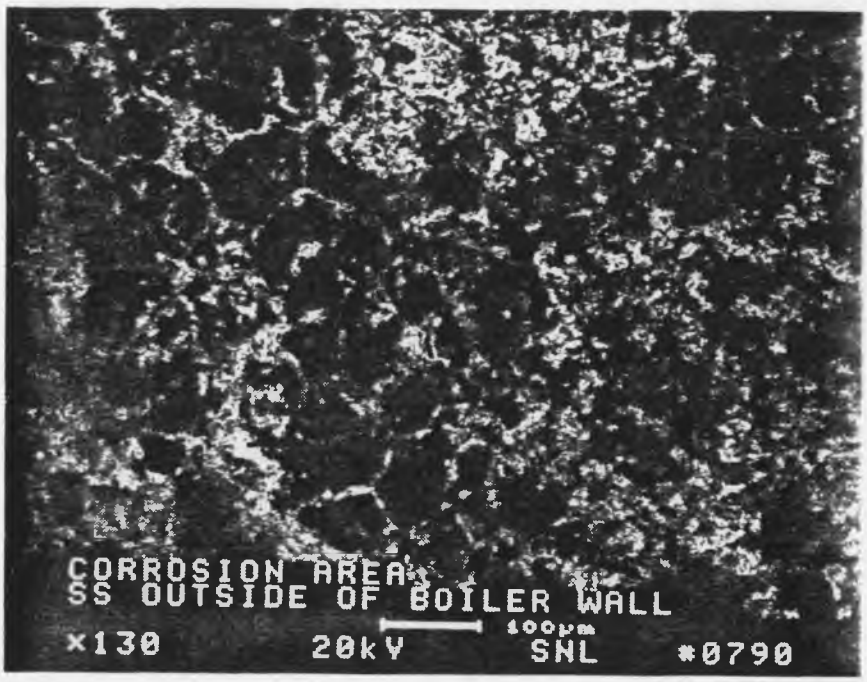

(a)

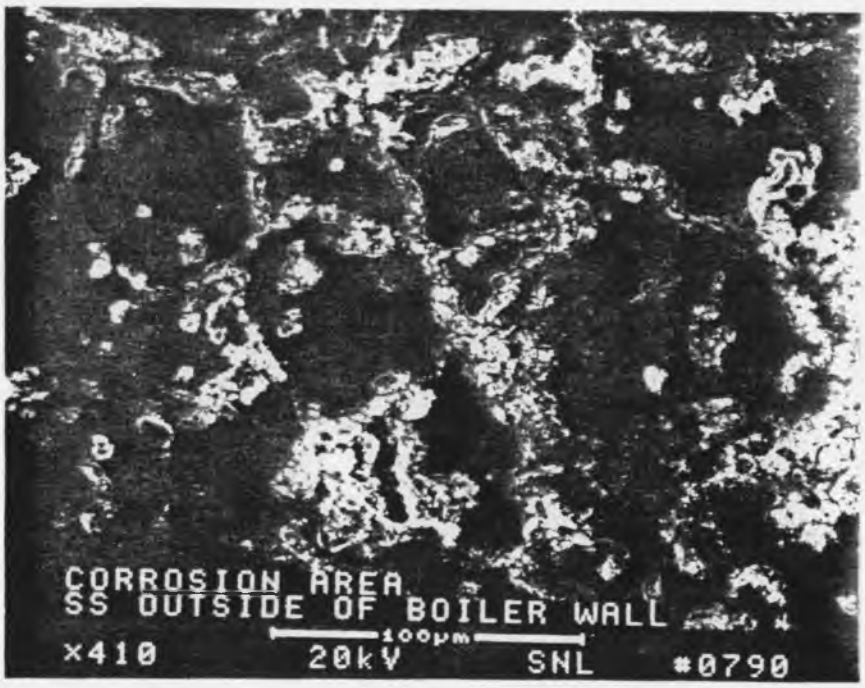

(b)

Fig. 10 SEM micrographs of oxidized outer surface of boiler wall showing grain boundaries; a) 130X; b) 410X.

(a)

(b)

Fig. 11 Metallographic cross-sections of samples taken at 90° intervals around the receiver rim weld; a) 40X; b) 32X;

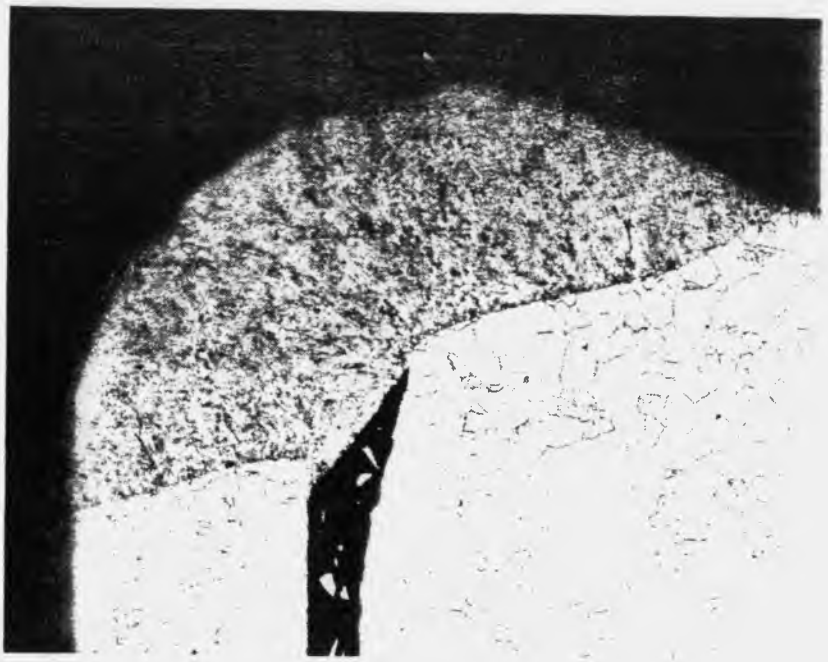

(c)

(d)

Fig. 11 cont. Metallographic cross-sections of samples taken at 90° intervals around the receiver rim weld; c) 40X; d) 32X.

DISTRIBUTION:

U.S. Department of Energy (5)
Forrestal Building
Code CE-132
1000 Independence Avenue, SW
Washington, DC 20585
Attn: G. Burch
S. Gronich

U.S. Department of Energy (2)
Forrestal Building
Code CE-13
1000 Independence Avenue, SW
Washington, DC 20585
Attn: R. Annan

U.S. Department of Energy (2)
Albuquerque Operations Office
P.O. Box 5400
Albuquerque, NM 87115
Attn: G. Tennyson
N. Lackey

U.S. Department of Energy
San Francisco Operations Office
1333 Broadway
Oakland, CA 94612
Attn: R. Hughey

Arizona Solar Energy Office
Dept. of Commerce
1700 W. Washington, 5th Floor
Phoenix, AZ 85007
Attn: F. Mancini

Battelle Pacific Northwest Laboratory
P.O. Box 999
Richland, WA 99352
Attn: D. Brown

California Polytechnic
University Dept. of Mechanical Engineering
3801 West Temple Avenue
Engineering
Pomona, CA 91768
Attn: W. Stine

Clever Fellows
Innovation Consortium, Inc.
R.D. 1, Box 410, River Road
Melrose, NY 12121
Attn: J. A. Corey, P.E.

Cummins Power Generation (2)
MC 60125
P. O. Box 3005
Columbus, IN 47202-3005
Attn: R. Kubo

Cummins Power Generation South
150 Tannehill Drive
Abilene, TX 79602
Attn: M. McGlaun

Dynatherm Corporation
1 Beaver Court
P.O. Box 398
Cockeysville, MD 21030
Attn: David Wolf

Electric Power Research Institute
P.O. Box 10412
Palo Alto, CA 94303
Attn: J. Schaeffer

Energy Technology Engr. Center (2)
Rockwell International Corp.
P. O. Box 1449
Canoga Park, CA 91304
Attn: W. Bigelow
R. LeChevalier

Florida Solar Energy Center
300 State Road, Suite 401
Cape Canaveral, FL 32920
Attn: Library

Georgia Power
7 Solar Circle
Shenandoah, GA 30265
Attn: W. King

Institute of Gas Technology
34245 State Street
Chicago, IL 60616
Attn: Library

Jet Propulsion Laboratory
4800 Oak Grove Drive
Pasadena, CA 91109
Attn: M. Alper

Karl Thomas Feldman, Jr. Ph.D., P.E.
Mechanical Engineering Consultant
1704 Stanford Dr. NE
Albuquerque, NM 87106

Lawrence Berkeley Laboratory
MS 90-2024
One Cyclotron Road
Berkeley, CA 94720
Attn: A. Hunt

Los Alamos National Laboratory
MS-E13
Los Alamos, NM 87545
Attn: M. Merrigan

McDonnell-Douglas Astronautics Company
5301 Bolsa Avenue
Huntington Beach, CA 92647
Attn: R. L. Gervais,
J. Rogan,
D. Steinmeyer

Mechanical Technology, Inc. (2)
968 Albany Shaker Road
Latham, NY 12110
Attn: G. Dochat
J. Wagner

NASA Lewis Research Center (4)
21000 Brook Park Road
Cleveland, OH 44135
Attn: R. Shaltens
J. Schrieber

National Renewable Energy Laboratory (6)
1617 Cole Boulevard
Golden, CO 80401
Attn: T. Williams
L. M. Murphy
G. Jorgensen
T. Wendelin
A. Lewandowski
M. Bohn

Northern Research and Engineering Corp.
39 Olympia Avenue
Woburn, MA 01801-2073
Attn: J. Kesseli

Power Kinetics, Inc.
415 River Street
Troy, NY 12180-2822
Attn: W. E. Rogers

Research International
18706 142nd Avenue NE
Woodinville, WA 98072
Attn: E. Saaski

Science Applications International Corporation
10343 Roselle Street, Suite G
San Diego, CA 92121
Attn: K. Beninga

Science Applications International Corporation
Mail Stop 32
10260 Campus Point Court
San Diego, CA 92121
Attn: B. Butler

Solar Energy Industries Assoc. (2)
777 North Capitol St. NE
Suite 805
Washington, D.C. 20002
Attn: S. Sklar
K. Sheinkopf

Solar Kinetics, Inc. (2)
P.O. Box 540636
Dallas, TX 75354-0636
Attn: J. A. Hutchison
P. Schertz

Stirling Technology Company (3)
2952 George Washington Way
Richland, WA 99352
Attn: Mr. Maurice A. White

Stirling Thermal Motors (2)
2841 Boardwalk
Ann Arbor, MI 48104
Attn: Lennart Johansson

Stirling Machine World
1823 Hummingbird Court
West Richland, WA 99352-9542
Attn: Brad Ross

Sunpower, Inc.
6 Byard Street
Athens, OH 45701
Attn: W. Beale

Tech Reps, Inc. (2)
5000 Marble NE, Suite 222
Albuquerque, NM 87110
Attn: J. Stikar

Thermacore, Inc. (2)
780 Eden Road
Lancaster, PA 17601
Attn: Mr. Donald Ernst

University of Houston
Solar Energy Laboratory
4800 Calhoun
Houston, TX 77704
Attn: J. Richardson

University of Minnesota
Dept. of Mechanical Engineering
111 Church St., SE
Minneapolis, MN 55455
Attn: E. A. Fletcher

Australian National University
Department of Engineering
Physics
P. O. Box 4
Canberra ACT 2600 AUSTRALIA
Attn: S. Kaneff

Energy Research Centre
R. S. Phy. Sc.
Australian National University
Canberra ACT 2601 AUSTRALIA
Attn: K. Inall

DLR
Pfaffenwaldring 38-40
7000 Stuttgart 80 GERMANY
Attn: R. Buck

Schlaich, Bergermann & Partner
Hohenzollernstr. 1
D - 7000 Stuttgart 1 GERMANY
Attn: W. Schie.

1513 D. R. Adkins
1513 R. E. Hogan
1513 V. J. Romero
1513 R. D. Skocypec
1514 E. L. Hoffman
1514 C. M. Stone
1832 J. A. VanDenAvyle
2756 G. S. Phipps
3141 S. A. Landenberger (5)
3145 Document Processing for DOE/OSTI (8)
3151 G. C. Claycomb (3)
4313 J. F. Muir
6000 D. L. Hartley
6200 B. W. Marshall
6215 C. P. Cameron, Actg
6215 K. S. Rawlinson
6215 Library (5)
6216 C. E. Tyner
6216 T. R. Mancini
6217 P. C. Klimas
6217 C. E. Andraka (20)
6217 R. B. Diver (5)
6217 J. B. Moreno (5)
6217 D. F. Menicucci
6217 T. A. Moss
6217 Library (5)
6220 D. G. Schueler
6221 A. R. Mahoney
6315 W. C. Ginn
8523-2 Central Technical Files

☆ U.S. GOVERNMENT PRINTING OFFICE: 1992—673-122/60164